Technische Universität München

Department Chemie

Protein Interactions Studied by

Biochemical and NMR Spectroscopic Methods

Alexander Dehner

Vollständiger Abdruck der von der Fakultät für Chemie der Technischen Universität München zur Erlangung des akademischen Grades eines

Doktors der Naturwissenschaften

genehmigten Dissertation.

Vorsitzender: Univ.- Prof. Dr. St. J. Glaser

Prüfer der Dissertation:
        1.   Univ.- Prof. Dr. H. Kessler
        2.   Univ.- Prof. Dr. W. Hiller
        3.   Univ.- Prof. Dr. J. Buchner

Wenn ich einmal im Lebensland,
im Gelärme von Markt und Messe -
meiner Kindheit erblühte Blässe:
meinen ernsten Engel vergesse -
seine Güte und sein Gewand,
die betenden Hände, die segnende Hand, -
in meinen heimlichsten Träumen behalten
werde ich immer das Flügelfalten,
das wie eine weiße Zypresse
hinter ihm stand.

Rainer Maria Rilke, aus Engellieder

meinen Eltern

Danksagung / Acknowledgments

Publications

The following publications have been written during the PhD thesis or are in preparation:

- Frenzel, E., Dehner, A., Meinlschmidt, B., Kessler, H., Haslbeck, M., Buchner, J. (2004) Hsp12 from *S. cerevisiae* is a natively unfolded protein
  in preparation

- Dehner, A., Klein, C., Hansen, S., Schwaiger, M., Kessler, H. (2004) p53 Dimerization Mutants lack DNA Binding via missing Cooperativity
  submitted

- Dehner, A., Klein, C., Tomita, Y., Pan, Hongguang, Schweiger, M., Kessler, H., Erster, S., Palacios, G., Pancoska, P. Moll, M. U. (2004) Mapping the binding sites for Bcl-xL and Bcl2 on the p53 DNA binding domain.
  submitted

- Klein, C., Hesse, F., Dehner, A., Engh, R.A., Schwaiger, M. and Hansen, S. (2004) In vitro folding and characterization of the p53 DNA binding domain.
  Biol. Chem., **385**, 95-102.

- Dawson, R., Müller, L., Dehner, A., Klein, C., Kessler, H. and Buchner, J. (2003) The N-terminal domain of p53 is natively unfolded.
  J. Mol. Biol., **332**, 1131-1141

- Dehner, A., Furrer, J., Richter, K., Schuster, I., Buchner, J. and Kessler, H. (2003) NMR Chemical Shift Perturbation Study of the N-Terminal Domain of Hsp90 upon Binding of ADP, AMP-PNP, Geldanamycin, and Radicicol.
  ChemBioChem, **4**, 870-877.

- Furrer, J., Enthart, A., Kühlewein, A., Dehner, A., Klein, C., Hansen, S., Schwaiger, M., Kessler, H. and Gemmecker, G. (2003) Backbone 1H, 13C and 15N resonance assignments for the 25.8 kDa DNA binding domain of the human p63 protein.
  J. Biomol. NMR, **26**, 377-378.

- Dehner, A., Planker, E., Gemmecker, G., Broxterman, Q.B., Bisson, W., Formaggio, F., Crisma, M., Toniolo, C. and Kessler, H. (2001) Solution structure, dimerization, and dynamics of a lipophilic alpha/3(10)-helical, C alpha-methylated peptide. Implications for folding of membrane proteins.
  J. Am. Chem. Soc., **123**, 6678-6686.

1 Contents

2 Abbreviations

53BP1	p53 Binding Protein 1
%(w/v)	weight percent
%(v/v)	volume percent
Å	Angstrøm (10^{-10} m)
aa	amino acid
AIDS	Acquire Immunodeficiency Syndrome
AIR	Ambiguous Interaction Restraint
AMP-PNP	Adenylyl-imido-diphosphate
APS	Ammoniaperoxodisulfate
ATP	Adenosine Triphosphate
APAF-1	Apoptotic Protease-Activating Factor 1
Bax	Bcl-2-associated X protein
Bcl-2	B-cell lymphoma 2
Bid	BH3-interacting death agonist
BPP	Bipolar Pulse Pairs
BLAST	Basic Local Alignment Search Tool
bp	base pair
BMRB	Biomagnetic Research Bank
BSA	Bovine Serum Albumin
CCT	Group-II-Chaperonins
CD	Circular Dichroism
CDK	Cycline-Dependent Kinase
Cpn	Group-I-Chaperonins
cDNA	complementary DNA
Caspace	Cystein-Aspartate Proteases
CHK2	Checkpoint 2 Protein
COSY	Correlation Spectroscopy
CON1x5	pentameric Consensus-1x5 p53 DNA-Oligonucleotide
CON2x5	decameric Consensus-2x5 p53 DNA-Oligonucleotide
CON4x5	dodecameric Consensus-4x5 p53 DNA-Oligonucleotide
CPD	Composite Pulse Decoupling
CRINEPT	Cross Relaxation-Enhanced Polarization Transfer
CRIPT	Cross Relaxation-Induced Polarization Transfer
CSD	Cambridge Structural Database
CSI	Chemical Shift Index
CT	Constant Time
CTD	C-terminal Domain
CTRD	C-terminal Regulatory Domain
1D	One-dimensional
2D	Two-dimensional
3D	Three-dimensional
Da	Dalton
DBD	DNA Binding Domain
DNA	Desoxyribonucleic Acid
dNTP	Desoxynucleotidetriphosphate
DOSY	Diffusion Ordered Spectroscopy
DPC	Dodecyl Phosphocholine
DPFGE	Double Pulsed Field Gradient Echo
DQC	Double Quantum Coherence
DSC	Differential Scanning Calorimetry
DSTE	Double Stimulated Echo
dsDNA	Double-Stranded DNA
DTT	1,4-Dithiothreitol

elec	electrostatic (interactions)
ε	Molar Extinction Coefficient
ECM	Extracellular Matrix
E. coli	Escherichia coli
EMSA	Electrophoretic Mobility Shift Assay
f	Femto
FAK	Focal Adhesion Kinase
Fig.	Figure
f.l.	full-length
FID	Free Induction Decay
FPLC	Fast Protein Liquid Chromatography
FT	Fourier Transformation
GA	Geldanamycin
GdnCl	Guanidiumhydrochloride
GCC	Gradient Calibration Constant
GCSTE	Gradient Compensated Stimulated Echo
GCSTESL	Gradient Compensated Stimulated Echo Spin Lock
GST	Gluthation-S-Transferase
h	hour
HDM2	Human MDM2 Oncoprotein
HMQC	Heteronuclear Multi-Quantum Correlation
HSQC	Heteronuclear Single-Quantum Correlation
HTS	High-throughput Screening
Hsp	Heat Shock Protein
Hsp90	Heat Shock Protein, 90 kDa
Hsp12	Heat Shock Protein, 12 kDa
IAPs	Inhibitor of Apoptosis Proteins
IB	Inclusion Bodies
ILT	Inverse Laplace Transformation
IPTG	Isopropyl-β-D-thiogalactopyranosid
IUP	Intrinsically Unfolded Protein
K_D	Apparent dissociation constant
kb	Kilobases
LB	Luria Bertani
LED	Longitudinal Eddy Current Recovery Delay
LT	Laplace Transformation
MAPK	Mitogen Activated Protein Kinase
MCS	Multiple Cloning Site
MDM2	Mouse Double Minute, murine oncoprotein
mRNA	messenger RNA
mt	mutant
Nhsp90	N-terminal domain of Hsp90 (residues 1-210)
NLS	Nuclear Localization Signal
NMR	Nuclear Magnetic Resonance
NOE	Nuclear Overhauser Effecct
NOXA	*Latin* for "harm" or "damage"
Np53	N-terminal domain of p53 (residues 1-93)
NTA	Nitrilotriaceticacid
NTD	N-terminal Domain
OD	Optical Density
p53	Human Tumor Suppressor Protein p53
p63	Human p63, p53 homologous protein
p73	Human p73, p53 homologous protein
p.A.	pro Analysis
PAb	Polyclonal Antibody
PAGE	Polyacrylamide Gelelectrophoresis
PASTA	Protein Assignment by Threshold Accepting
pBS	pBluescript

PBS	Phosphate Buffer Saline
PDI	Protein-Disulfid-Isomerase
PCR	Polymerase Chain Reaction
PDB	Protein Data Bank
PG	Polygrip, p53 specific DNA oligonucleotide
PFG	Pulsed Field Gradients
PIGs	p53-Inducible Genes
PPI	Peptidy-Prolyl-cis/trans-Isomerase
PUMA	p53-Upregulated Modulator of Apoptosis
ppm	parts per million $(=10^{-6})$
rf	radiofrequency
R_1	Longitudinal Relaxation Rate
R_2	Transversal Relaxation Rate
RMSD	Root Mean Square Deviation
RNA	Ribonucleic Acid
ROE	Rotating Frame Nuclear Overhauser Effect
RT	Room Temperature (20 – 25 °C)
RP	Reversed Phase
S	Signal (intensity)
SAR	Structure-Activity Relationship
SH3	src Homology Domain 3
SHR	Steroid Hormone Receptor
SDS	Sodium dodecyl sulfate
SE	Spin Echo
STE	Stimulated Echo
SUMO	Small Ubiquitin-like Modifier
sHsp	small Heat Shock Protein
src	Sarcoma
ssDNA	Single-stranded DNA
T_1	Longitudinal Relaxation Time
T_2	Transversal Relaxation Time
τ_R	Molecular Correlation Time
Tab.	Table
TAD	Transactivationdomain
TAE	TRIS/Acetat/EDTA buffer
TBE	TRIS/Borate/EDTA buffer
TEMED	N,N,N´,N´-Tetramethylethylendiamine
TG	TRIS/Glycine buffer
TNF	Tumor Necrosis Factor
TOCSY	Total Correlation Spectroscopy
TRAIL	Tumor Necrosis Factor-Related Apoptosis-Inducing Ligand
TRIS	Trishydroxymethylaminoethan
Triton X-100	t-Octylphenoxypolyethoxyethanol
TROSY	Transverse Relaxation Optimized Spectroscopy
U	Units (enzyme activity)
UV	Ultraviolet
[U-	Uniformly
vdW	van der Waals
v/v	volume per volume
w/v	weight per volume
wt	wild type
ZQC	Zero Quantum Coherence

3 Summary

This work is mainly concerned with protein–protein (p53-Bcl-xL), protein–DNA (p53-DNA) and protein–ligand (Hsp90; Hsp12-SDS) molecular interactions studied by biochemical and NMR spectroscopic methods:

In pulsed field gradient NMR experiments the molecular motion is measured by the attenuation of a spin-echo signal which is related to the diffusion coefficient (section 5). Furthermore the diffusion coefficient depends on the molecular weight and shape. Therefore, if the shape is already know independently from electron microscopy or X-ray crystallography or can be estimated in terms of a model (section 5.4), measured diffusion coefficients yield information about possible oligomerization and interactions.

The induction of apoptosis by transcriptional activation of pro-apoptotic target genes in response to cellular stress is the most conserved function of p53. The N-terminal domain of p53 (residues 1-93) compromises a transactivation region (residue 1-63) and an adjacent proline-riche SH3-target subdomain modulating the transcription activation function of p53.

The analysis of the entire N-terminal domain of p53 by diffusion NMR experiments and hydrodynamic calculations shows features of an intrinsically unstructured protein which is in agreement with a variety of transactivation domains (section 6.3).

Recent studies have demonstrated that a cooperative binding to DNA is crucial for the tumor suppressor function of p53, as most of the oncogenic mutations observed in human cancer map to the highly conserved sequence-specific DNA binding domain.

The dimerization interface of the p53 DNA binding domain was identified by a mutational study of solvent-exposed residues. The results demonstrate the existence of two intermolecular E180 – R181 salt bridges which are the driving force for DNA binding cooperativity. *Vice versa*, mutations hindering the formation of this salt bridges, e.g., E180R or R181E, might belong to a new class of p53 core mutations which lack DNA binding by abolishing cooperativity (section 6.2). The essential role of the identified H1 helix dimerization interface for a proper p53 function is demonstrated by the germline p53 E180K mutation which is associated with the Li-Fraumeni syndrome and a lost transcriptional activation.

Although the sequential assignment of the p63 DNA binding domain indicates the existence of the H1 helix also in p63 (section 6.5), its different DNA binding behavior

can be explained by a E180L mutation in p63 which does not support the necessary cooperativity in DNA binding.

In addition to its transcription-dependent function, p53 can directly induce mitochondrial membrane permeabilization by complexation of the DNA binding region of p53 with the anti-apoptotic proteins Bcl-xL and Bcl-2.

In this thesis a specific binding interface between the human p53 DNA binding domain (DBD) and Bcl-xL is identified by using a combination of solution NMR and molecular docking calculations. An integrative structural model of an oligomeric p53/Bcl-xL complex is presented in the context of the mitochondrial membrane. The oligomeric structural model has an implication for the efficacy of p53-mediated activation of pro-apoptotic proteins such as Bax, Bak and Bid (section 6.4).

Hsp90 is one of the most abundant chaperone proteins in the cytosol. In an ATP-dependent manner it plays an essential role in the folding and activation of a range of client proteins involved in signal transduction and cell cycle regulation. Heat shock proteins can inhibit apoptosis by conformational regulation of apoptotic molecules and are overexpressed in several tumor cells. Due to the specific ATP-binding site of Hsp90, targeting Hsp90 became a central attraction in Hsp-related tumor inhibition.

In this thesis NMR shift perturbation experiments were used to obtain information on the structural implications upon binding of AMP-PNP (a nonhydrolysable ATP analogue), ADP and the competitiv inhibitors Radicicol and Geldanamycin. Analysis of ^{1}H-^{15}N correlation spectra showed a specific pattern of chemical shift perturbations at Nhsp90 (Hsp90, residues 1-210) upon ligand binding. All ligands show specific interactions in the binding site known from the crystal structure of Nhsp90. For AMP-PNP and ADP, additional shift perturbations of residues outside the binding pocket were observed which can be considered as a result of conformational rearrangement upon binding. According to the crystal structures, these regions are the first α-helix and the "ATP-lid" ranging from amino acids 85 to 110 (section 7.2).

Hsp12 was classified to the family of small heat shock proteins, however, it does not show the typical α-crystallin domain, nor form oligomeric complexes. To clarify its potential role, Hsp12 was further investigated by NMR spectroscopic methods. Hsp12 shows features of an intrinsically unstructured protein as demonstrated by diffusion experiments and hydrodynamic calculations. Furthermore addition of SDS-micelles induces a helical secondary structure which was further studied by hydrogen exchange and spin label experiments. The sequential assignments of unfolded and SDS-folded Hsp12 localize the SDS-induced secondary structure to at least two amphiphilic helices that "swim" in the SDS-membrane (section 7.3).

4   Introduction and Aims

Nuclear magnetic resonance spectroscopy is a versatile biophysical technique with a wide range of applicability (Ernst, 1992). Besides X-ray crystallography, NMR spectroscopy can be used as a tool for the determination of macromolecular three-dimensional structures at atomic resolution (Wüthrich, 2003). Given the widening gap between the number of protein structures currently solved by either of these techniques and the number of available protein sequences from the Human Genome Sequencing Project, it is obvious that rapid and robust methods for the determination of protein folds and structures are required, as many of these gene products still have an unknown function.

However, an understanding of protein function does not end with the identification of their folds or structures, but leads on to an intriguing challenge in modern biology: How do cells respond to, and distinguish between different stimuli? How does a network of signaling pathways extending from the membrane to the core of the nucleus transmit environmental changes into a graded transcriptional response?
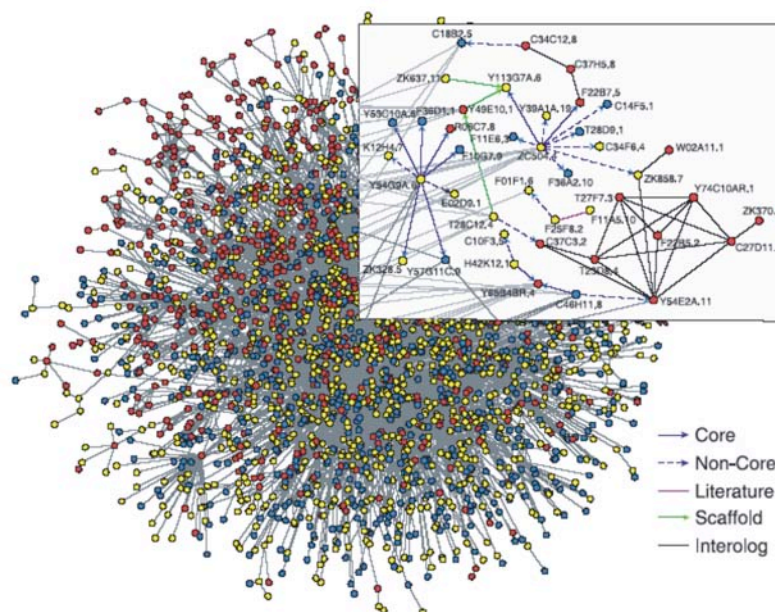
Figure 1: Mapping the *C. elegans* interactome. Interactome maps aid navigation of the proteome. They describe the cell's molecular complexes, formed by protein-protein interactions. The interactome map of *C. elegans* contains approximately 3000 proteins (nodes) linked by nearly 5000 potential interactions. The color of the nodes indicates evolutionary conservation. Red: conserved in yeast; yellow: conserved in other multicellular species; blue: no clear orthologs. The inset highlights a small part of the network (Adapted from (Li et al., 2004)).

In fact, protein-protein networks are probably amongst the most ubiquitous types of interactions in biological systems and play a key role in all cellular processes. Determining the interaction network of whole organisms has therefore become a major goal of functional genomics efforts. Several studies in recent years have identified hundreds of potentially interacting proteins and their complexes in yeast and other organisms (**Figure 1**) (Aloy et al., 2004; Gavin et al., 2002; Gavin and Superti-Furga, 2003; Giot et al., 2003; Ho et al., 2002; Huynen et al., 2003; Ito et al., 2001; Uetz et al., 2000; Li et al., 2004).

In this context NMR spectroscopy particularly represents its full versatility, as it is not solely a tool for structure determination, but can also be applied in a broader scope combining in a unique fashion the three-dimensional structure, the identification and characterization of molecular interactions, their flexibility and induced conformational changes; In fact, this has long been recognized: back in 1965, Jardetzky et al. detected and characterized penicillin binding to serum albumin using NMR spectroscopic methods similar to the ones currently employed (Fischer and Jardetzky, 1965); and many investigations have followed in which protein–ligand, protein–protein and protein–nucleic acid interactions were identified and characterized on an atomic level. All of these investigations rely mainly on two aspects of a binding event: the protein resonances experience a chemical shift perturbation upon complexation with the ligand, which is due to either direct protein–ligand interactions or to an induced conformational rearrangement. The changes can also affect the internal flexibility of each partner, e.g., a flexible linker or loop region of a multi-domain protein or an unstructured domain might become rigid or even more flexible upon binding – which is called "induced fit". The second effect may be studied by NMR spectroscopic relaxation measurements in more detail, yielding time-dependent correlation functions which can be interpreted in dynamic models (Lipari and Szabo, 1981).

Hence NMR spectroscopy has evolved on the one hand as a fundamental technique in understanding detailed biochemical functions on structural and dynamical grounds and on the other hand it can also be integrated in all phases of a drug discovery program (Shuker et al., 1996) including HTS and combinatorial chemistry. The ability to deal with weak interactions between potential ligands and a macromolecule and to structurally characterize them are unique features of NMR spectroscopy. Besides chemical shift changes of the target protein there are several more NMR parameters that are commonly exploited in the investigation of protein–ligand binding. During the time when a ligand is bound to a protein, the ligand temporarily does not behave like a small molecule, but like the large protein: it

tumbles more slowly. This has several consequences, as protein properties are transferred to the ligand including faster relaxation, large and negative NOEs and a slower diffusion. In the last decade, pulsed field-gradient (PFG) NMR spectroscopy has become a convenient method for measuring diffusion in solution (Price, 1997b; Price, 1998). As the diffusion coefficient of a certain molecule under given conditions is proportional to its effective molecular weight, size and shape, it is evident that diffusion can be used to map intermolecular interactions or aggregation events. Nevertheless the applications of diffusion NMR spectroscopy as a tool for studying molecular interactions only started in the last few years. However, gradient NMR spectroscopy is a powerful tool not only for studying diffusion and aggregation, it also provides structural information of cavities in cells or zeolites in the range of $0.1 - 100$ µm when the diffusion is restricted on the NMR time scale (Basser, 1995; Moseley et al., 1990). Thus diffusion can be added to the standard NMR observables of chemical shift and relaxation times.

This work is mainly concerned with a variety of protein – protein molecular interactions studied by biochemical and NMR spectroscopic methods focusing the applicability of diffusion NMR experiments. The thesis is divided into three major chapters:

In the following, chapter 5, a theoretical introduction to pulsed-field gradient diffusion NMR spectroscopy is given, including hydrodynamic calculations which yield "theoretical" values for experimentally determined diffusion coefficients.

In chapter 6 the cooperative DNA binding of p53 DNA binding domain is studied by site-directed mutation of solvent-exposed residues within a proposed dimerization interface. Dimerization behavior and cooperativity in DNA binding of each mutant was examined by electrophoretic mobility shift assays and NMR spectroscopic diffusion measurements. The aim of this work was to explain the cooperative DNA binding of p53 DBD in contrast to p63 DBD on structural grounds. Furthermore this chapter is concerned with a new model complex of p53 DBD-Bcl-xL based on NMR spectroscopic titration data, followed by NMR spectroscopic investigation on the N-terminal domain of p53 which shows properties of a natively unfolded protein and closes with the sequential backbone assignment of the DNA binding domain of p63. Therefore this chapter also includes the cloning, expression and purification of wild-type p53 DBD and dimerization mutants as inclusion bodies, as well as their *in vitro* refolding and the expression and purification of Bcl-xL and p63 DBD.

Chapter 7 is concerned with two heat shock proteins namely Hsp90 and Hsp12. For Hsp90 its interaction with AMP-PNP, ADP, Radicicol and Geldanamycin is

examined by ^{15}N HSQC titration and relaxation experiments in order to gain insight into conformational rearrangements within the so-called "ATP-lid" and within the first H1 helix upon ligand binding. Hsp12 is a natively unfolded protein; however, interaction with SDS micelles induces a helical secondary structure, which is studied in more detail by NMR spectroscopic diffusion, hydrogen exchange and spin label experiments.

5 Pulsed-Field Gradient Spin-Echo and Diffusion

5.1 Translational Diffusion

5.1.1 Translational Diffusion in Isotropic Systems

Translation diffusion is one of the most important modes of molecular transport. Brownian motion in the absence of an applied force is the origin of self-diffusion; in this case no external force acts on the molecular particles and, consequently, no net displacement is observed. However, external fields can be applied to force additional translational motion. These fields include gravity or angular acceleration in sedimentation or ultracentrifugation experiments and electric fields in electrophoresis (Crank, 1975; Cussler, 1984; Cantor and Schimmel, 1980).

The simplest possible system of biological interest will contain two components: a solvent (1), which is usually water, and a dissolved macromolecule (2). As most measurements are done in closed systems, any changes in location of component 1 must be compensated for by a corresponding change in position of component 2. The flux J of the solute (component 2) defined as the rate of mass transport across a surface of unit area is given by,

$$J_2 = dm_2 / dt \quad [\text{g sec}^{-1} \text{ cm}^{-2}] \qquad\qquad 5\text{-}1$$

where m_2 is the number of grams of solute on one side of the surface.

Consider a small zone of fluid bounded by unit area surfaces at x and $x+dx$. The flux from one side to the other through the zone dx ought to be proportional to the concentrations $c_2(x)$ and $c_2(x+dx)$, respectively, and inversely proportional to the thickness of the zone, dx. Thus, transport in one direction is proportional to $c_2(x)/dx$ and in the other direction proportional to $c_2(x+dx)/dx$. Defining the proportionality constant D, the net rate of mass transport is the difference between these two individual rates:

$$J_2 = \left[Dc_2(x) - Dc_2(x + dx) \right] / dx = -D\left(\partial c_2 / \partial x \right) \qquad\qquad 5\text{-}2$$

The right-hand side of equation 5-2 was originally proposed by A. Fick in the nineteenth century and is known as Fick´s first law of diffusion. With increasing concentration c_2 from left to right (with increasing x), J_2 will become negative and mass will flow from right to left. If the flux across the surface at x, $J_2(x)$, is not equal

to the flux across the surface at $x+dx$, $J_2(x+dx)$, then the concentration c_2 in the volume element dx must change as function of time t:

$$(dc_2/dt)_x = [J_2(x) - J_2(x+dx)]/dx = -(\partial J_2/\partial x)_t \qquad\qquad 5\text{-}3$$

Combining equation 5-2 and 5-3 yields Fick´s second law of diffusion:

$$(dc_2/dt)_x = -\left(\partial(-D\partial c_2/\partial x)\ /\partial x\right)_t = D(\partial^2 c_2/\partial x^2)_t \qquad\qquad 5\text{-}4$$

These equations are fundamental to all hydrodynamic studies and are true regardless of what forces are acting on the system, as long as the concentration of the solute is very low. D depends on frictional properties of the solute molecules and these are concentration-dependent, thus the value of D might also vary. By dimensional analysis of equation 5-4 one yields cm^2/s for D as dimension and therefore the net distance moved by a diffusing molecule is time-dependent and must be proportional to $(Dt)^{1/2}$. As given by the Einstein equation the root mean square displacement $(<X^2>)^{1/2}$ is consequently

$$(<X^2>)^{1/2} = (nDt)^{1/2} \qquad\qquad 5\text{-}5$$

where n is 2, 4 or 6 for the case of a one-, two- or three-dimensional diffusion. Thus in an isotropic case of free diffusion the mean displacement increases linearly with the square root of the diffusion time t.

Fick´s second law of diffusion (equation 5-4) can be solved (Cantor and Schimmel, 1980) using boundary conditions, which describe a diffusion process starting with an initial thin band of solute (e.g. gel exclusion chromatography or band sedimentation) at $x_0 = 0$ and $t_0 = 0$ in the absence of any external forces by applying the Fourier operator to both sides of Equation 5-4. The conditional probability $P(x,t)$ of finding a molecule initially at position $x_0 = 0$ at a position x after a time t is then given by:

$$P(x,t) = (4\pi Dt)^{-3/2} \exp^{-\left(\frac{(x-x_0)^2}{4Dt}\right)} \qquad\qquad 5\text{-}6$$

This means that the initial thin volume zone occupied by a molecule at position $x_0 = 0$ becomes a Gaussian shape, which is broadening with increasing diffusion time t according to $(4\pi Dt)^{-3/2}$ in every dimension. Furthermore $P(x,t)$ does not depend on the initial position, x_0, but depends only on the net displacement $(x-x_0)$. This reflects the Markovian nature of Brownian motion (Lenk, 1986; Van Kampen, 1981).

5.1.2 Restricted and Anisotropic Translational Diffusion

As shown in the last part, for the case of free isotropic diffusion the mean displacement of a molecular species increases linearly with the square root of the diffusion time, which is expressed in Einstein´s equation (Equation 5-5). Thus, plotting the mean displacement against the square root of the diffusion time, one obtains a linear increasing graph with its slope representing the diffusion coefficient.

However, in systems where any kind of barrier prevents an unhindered free diffusion, an increasing diffusion time will not yield a linear increase in the mean displacement of the diffusing species, but will reach a point of saturation, which reflects the maximum mean displacement possible. Such a restriction will occur when the diffusion time t will be larger than $l^2/2D$, where l is the length of the compartment and D the diffusion coefficient of the diffusing molecular species. In these systems the restricted diffusion prevails and instead of the diffusion coefficient only apparent diffusion coefficients can be extracted (Basser, 1995; Moseley et al., 1990). In addition these diffusion barriers and compartments might not be uniformly distributed; in this case anisotropic translational diffusion may be found. In heterogeneous systems such as porous material or biological systems these kinds of diffusion have to be taken into account. As diffusion times during an NMR diffusion experiment range in the order of 10^{-3} seconds, one can handle and obtain structural information from heterogeneous systems (Callaghan et al., 1991; Callaghan et al., 1998; Callaghan et al., 2003) in the order of 10^{-6} meters, assuming a diffusion constant of 10^{-6} cm^2/s.

5.1.3 Molecular Interpretation of the Diffusion Constant

In solution each molecule will undergo Brownian motion (Woessner, 1996), as it is accelerated and decelerated by collisions with other molecules. Assuming that all solute molecules (component 2) are moving with the same average velocity $<v_2>$, the flux according to equation 5-1 given in g s^{-1} cm^{-2} across a surface element will be $J_2 = c_2<v_2>$, where c_2 is the concentration. A molecule moving in this way will feel a total frictional force given by $<v_2>f$ and thus the force per gram solute molecules will be $N_A<v_2>f / M_2$, where N_A is Avogadro's number and M_2 the molecular weight of the solute. This force must be opposed by an equal force if there is no net acceleration. As shown in section 5.1.1, concentration gradients $-(d\mu_2/dx)_t$ produce a diffusion force that leads to molecular transport of solute. In the case of a free diffusion, where no external forces are applied, the diffusion force and the frictional force can be set equal: $N_A<v_2>f / M_2 = -(d\mu_2/dx)$. Multiplication of both sides with c_2 yields the observed flux across a surface element due to Brownian motion:

$$J_2 = c_2 \langle v_2 \rangle = - \left(\frac{c_2 M_2}{N_A f} \right) (\partial \mu_2 / \partial x)_t \qquad \text{5-7}$$

Recalling that the chemical potential of μ_2 is given by its activity coefficient γ_2 via $\mu_2 = \mu_2{}^0 + (RT/M_2) \ln a_2 = \mu_2{}^0 + (RT/M_2) \ln (\gamma_2 c_2)$ and substituting the value of Bolzmann´s constant k for R/N_A one obtains:

$$J_2 = - \frac{kT}{f} \left(1 + \frac{\partial(\ln \gamma_2)}{\partial(\ln c_2)} \right) \frac{\partial c_2}{\partial x} \qquad \text{5-8}$$

Comparing equation 5-8 with Fick´s first law of diffusion (Equation 5-2) and setting corresponding terms in these equations equal, the diffusion constant has to be:

$$D = - \left(\frac{kT}{f} \right) \left(1 + \frac{\partial(\ln \gamma_2)}{\partial(\ln c_2)} \right) \qquad \text{5-9}$$

In an infinite dilution the activity coefficient γ_2 is 1.0 and therefore the differential $d(\ln \gamma_2) / d(\ln c_2) = 0$ and the diffusion constant D_0 at infinite dilution becomes:

$$D_0 = - \left(\frac{kT}{f} \right) \qquad \text{5-10}$$

The equations 5-9 and 5-10 were first derived by A. Einstein and they are called Einstein-Sutherland equations. Thus the diffusion constant of a molecule will be a function of the temperature and it will also depend on the solvent viscosity, as the translational friction f is proportional to the radius of the diffusing particle r and to the solvent viscosity η, which is themselves a function of temperature.

$$f \propto \eta \cdot r \quad [\text{g sec}^{-1}] \qquad \text{5-11}$$

For molecular species of different geometries, different theories are needed to describe the hydrodynamic frictional coefficient, f. If a spherical particle interacts strongly with the fluid molecules, resulting in strong frictional forces one obtains the so-called Stokes law under sticky boundary conditions:

$$f_{sph,sticky} = 6\pi \cdot \eta \cdot r \qquad \text{5-12}$$

The other extreme is, if there are no interactions between particles and the fluid, resulting in so-called slip boundary conditions:

$$f_{sph,slippy} = 4\pi \cdot \eta \cdot r \qquad\qquad 5\text{-}13$$

Most macromolecules of biological interest are not spheres but appear to be compact, globular or irregular rigid bodies and therefore an ellipsoid is a more realistic model. For equal volumes, the surface area of an ellipsoid is larger than that of a sphere, following that they will have larger frictional coefficients compared to an equivalent sphere. The dependence of the frictional coefficient of an ellipsoid on the axial ratio $p_r = a/b$, where a and b are the long and short semiaxes, respectively, can be calculated for sticky boundary conditions. For a prolate ellipsoid this yields:

$$F = \frac{f_{eli}}{f_{sph}} = \frac{\sqrt{1-p^2}}{\sqrt[3]{p^2} \cdot \ln\left\{\left[1+\sqrt{1-p^2}\right]\Big/ p\right\}}; \quad p = b\big/a = 1\big/p_r \qquad 5\text{-}14$$

The translational frictional coefficient ratio F is often called a shape factor or Perrin factor. With increasing axial ratio this factor increases gradually. This equation indicates that a measured self-diffusion coefficient of a given molecular species under controlled conditions, e.g., a free isotropic diffusion, provides in principle information on the effective size or weight of a diffusing species; and even though a single value of F is consistent with many possible shapes it is in addition sensitive to structural properties.

Unfortunately, real solutions do not show such a simple behavior, as proteins interact with a substantial number of water molecules. The term hydration refers to effects ranging from specific entrapment of structural water molecules in internal cavities, e.g., observed in crystal structures, to the generic perturbation of the water layer covering the external protein surface. Protein – water interactions play an essential role in the folding, stability and function of proteins. Since the primary events of biological processes, such as enzymatic catalysis, association, and recognition, take place at the protein – water interface, the dynamics of the hydration layer is of special interest. Much of the experimental information about protein hydration dynamics has come from NMR relaxation experiments using two different techniques: First, the magnetic relaxation dispersion relies on the fact that water molecules in the bulk solution and in the hydration layer exhibit different rotational correlation times giving rise to characteristic frequency dependencies in the longitudinal relaxation rate R_1 (Halle and Denisov, 2001; Modig et al., 2004). Secondly, as NOEs are effectively observed only for distances shorter than 4 – 5 Å, protein – water intermolecular NOEs report on direct interactions between the protein and the water molecules in the first shell of hydration (Otting, 1997; Wüthrich et al.,

1996). A recent report could show that 95 % of the water molecules in contact with the protein surface is no more than two-fold motionally retarded as compared to the bulk water (Modig et al., 2004). Furthermore, calorimetric studies show that, when a protein solution is frozen, about 0.4 g of water per gram protein remain unfrozen (Cantor and Schimmel, 1980) and thus clearly perturbed by the presence of the protein.

In addition, this water interacts and will move with the protein and therefore contribute to the proteins apparent size, also altering its hydrodynamic properties. Usually, a very simple model of hydration is constructed: Different classes and spheres of bound water are merged together into a net weight of bound water per weight of macromolecule, assuming that water occupies all internal spaces and covers the surface of the macromolecule. Then the hydrated radius of an equivalent sphere, r_h, can be calculated from the hydrated volume V_h,

$$V_h = (M/N_A)(\overline{V}_2 + \delta_1 \overline{V}_1) \qquad\qquad 5\text{-}15$$

$$r_h = \left[(3/4\pi)(M/N_A)(\overline{V}_2 + \delta_1 \overline{V}_1)\right]^{1/3} \qquad\qquad 5\text{-}16$$

where $\overline{V}_2$ and $\overline{V}_1$ are the partial specific volumes of the macromolecule and the solute, respectively, and δ_1 is the hydration given in grams of bound water per gram of macromolecule (Cantor and Schimmel, 1980).

Therefore, if the shape is already known independently, e.g., from electron microscopy or X-ray crystallography measured frictional coefficients can yield either the molecular weight and consequently its possible aggregation, or yield the hydration, if the other quantity is available independently or can be estimated in terms of a model.

5.2 Studying Diffusion by Pulsed-Field Gradient Spin-Echoes

5.2.1 Relaxation Data Analysis versus Pulsed-Field Gradients

In recent years, NMR spectroscopic diffusion measurements have replaced the traditional way to determine self-diffusion coefficients by radioactive tracers, due to the noninvasive nature of NMR spectroscopy. In addition the simultaneous determination of diffusion coefficients in multi-component systems is possible. In principle there are two ways in which NMR spectroscopy may be used to study self-diffusion: first, the analysis of relaxation data (Orekhov et al., 1999; Palmer, 1997) and secondly, pulsed-field gradient NMR techniques (Price, 1997b; Price, 1998). Even though a translational diffusion coefficient can be derived in both cases, they will only agree under certain circumstances (Price et al., 1990). This is because the two methods report on motions on very different time-scales. The relaxation method is in fact sensitive to rotational diffusion which is in the picosecond to nanosecond timescale, according to atomic reorientational correlation motions, whereas the PFG method measures translational diffusion on the millisecond to second timescale.

Figure 2 illustrates the principle procedure of the methods. Relaxation data are analyzed in order to determine rotational correlation times, τ_c, which again can be related to the viscosity of the solution by using the Debye equation, and finally applying Stokes-Einstein´s equation yields the translational diffusion coefficient. One major disadvantage of the relaxation method for the evaluation of diffusion coefficients is the number of serious assumptions which need to be made depending on the system being studied: (a) The relaxation mechanism of the species needs to be known. (b) Intermolecular contributions to the relaxation must be separable from intramolecular contributions. (c) Only if the molecule is spherical the rotational correlation times can be properly characterized by single correlation of the whole molecule. (d) One basic requirement for the validity of the Debye equation is a continuous bulk solution, which depends on the size of the probe molecules compared to the solute. (e) The Stokes radius of the diffusing species has to be known in advance (Price, 1997b).

In pulsed-field gradient methods molecular motion is measured by the attenuation of a spin-echo signal due to the dephasing of coherent magnetization, resulting from a combination of translational motion of spins (including diffusion, convection or any other flux) and spatially well-defined gradient pulses. In contrast to the above discussed relaxation methods, no additional assumptions are needed; however, in order to determine the "true" diffusion coefficient, as against an apparent

diffusion coefficient (see section 5.1.2) the effect of structural boundaries and barriers hindering the natural diffusion of the probe molecules has to be considered.

Relaxation Method   ## Pulsed-Field Gradient Method

Relaxation Measurements T_1, T_2, NOE

↓ Relaxation Mechanism

Correlation time τ_c

↓ Debye Equation
$\tau_c = 4\pi\eta r_s^3 / (3kT)$

Viscosity η

↓ Stokes-Einstein Equation
$D = kT / (6\pi\eta r_s)$

Diffusion Coefficient D

Spin-Echo Attenuation

Relationship between
phase change and
molecular displacement
in the presence of magnetic
gradients

Diffusion Coefficient D

Figure 2: Schematic illustration of relaxation and pulsed-field gradient NMR methods for the determination of self-diffusion coefficients. Adapted from (Price, 1997b).

5.2.2 Magnetic Gradients as Spatial Label

The basis for diffusion measurements is that magnetic field gradients can be used to label the spatial position of nuclear spins through their Larmor frequency,

$$\omega_0 = \gamma \cdot B_0 \qquad\qquad 5\text{-}17$$

given in radians per second and with the gyromagnetic ration γ in radT^{-1}s^{-1} or HzG^{-1}. B_0 is the strength of the static magnetic field and since B_0 is spatially homogeneous throughout the sample ω_0 is the same over the whole sample, thus equation 5-17 is valid for single quantum coherence ($n=1$). If in addition to B_0 there is a spatially dependent magnetic field G in T/m, ω becomes also spatially dependent,

$$\omega_{eff}(n,r) = n\big(\omega_0 + \gamma(\mathbf{G}\cdot\mathbf{r})\big) \qquad\qquad 5\text{-}18$$

where n accounts for the possibility of more than single quantum coherence ($n = 1$). $\mathbf{G}$ is defined by the *grad* of the gradient field component parallel to B_0, where $\mathbf{i}$, $\mathbf{j}$ and $\mathbf{k}$ are the unit vectors in the x, y and z direction of the laboratory frame of reference:

$$\mathbf{G} = \nabla B_0 = \frac{\partial B_z}{\partial x}\mathbf{i} + \frac{\partial B_z}{\partial y}\mathbf{j} + \frac{\partial B_z}{\partial z}\mathbf{k} \qquad\qquad 5\text{-}19$$

If a homogeneous gradient of known magnitude is applied, the Larmor frequency yields an additional phase shift depending on the spatial position of the spin and the direction of the gradient. In imaging systems, which can produce equally strong magnetic field gradients along the x, y and z direction, it is possible to measure diffusion along any of these directions (Price, 1997a; Talagala and Lowe, 1991; Xia, 1996). In principle it is also possible to apply B_1 radiofrequency gradients instead of magnetic B_0 gradients and the theoretical aspects are generally analogous (Canet, 1997; Canet and Décorps, 1995; Cante, 1996). In the case of a single magnetic gradient oriented along the z axis parallel to B_0, as defined in equation 5-19, the magnitude of G is only a function of the position in this direction. Furthermore from equation 5-18 follows, that the higher the homonuclear quantum transitions are, the more sensitive are the effects of gradients, whereas zero quantum transitions are unaffected by the presence of gradients (section 5.3.5).

For a single quantum coherence the cumulative phase shift for a single spin is given by:

$$\phi(t) = \underbrace{\gamma B_0 t}_{\text{static field}} + \underbrace{\gamma \int_0^t G(t') \cdot z(t')dt'}_{\text{applied gradient}} \qquad\qquad 5\text{-}20$$

The first term corresponds to the acquired phase shift due to the static B_0 field and the second term belongs to the effect of an applied gradient with duration t. Thus the degree of an additional dephasing of magnetization due to the gradient is proportional to the gyromagnetic ratio, γ, the strength of the gradient, G, the duration of the gradient, t, and the displacement of the spin during the time t in the direction of the gradient, z. The strength of the gradient G may or may not be a function of time: When applying rectangular gradient pulses this is not the case; however, under certain circumstances it might be more convenient to apply for example sine-shaped gradient pulses, which are obviously time-dependent (section 5.3.2.5).

5.2.3 Measuring Diffusion with Magnetic Field Gradients

From section 5.2.2 it is clear that a well-defined magnetic gradient can be used to label the position of spins. In order to measure translational spin motion a simple modification (Stejskal, 1965; Stejskal and Tanner, 1965; Tanner and Stejskal, 1968) of the Hahn spin-echo pulse sequence (Carr and Purcell, 1954; Hahn, 1950) is needed, with two equal gradient pulses of duration δ are inserted into each τ period. This pulse

sequence is called the "Stejskal and Tanner sequence" or "PFG spin-echo (SE) sequence".

The traditional Hahn spin-echo method is a steady gradient experiment which shows a number of experimental limitations (Stejskal and Tanner, 1965) compared to the application of field gradient pulses. The advantages of PFG NMR are: (a) There is no gradient during acquisition and thus the line width is not broadened by the gradient. Therefore it is possible to measure diffusion coefficients of more than one species simultaneously. (b) There is no need to increase the radiofrequency pulses to cope with broadened spectra. (c) PFG experiments allow the use of stronger gradients (pulses), and thus measuring smaller diffusion coefficients (under favorable circumstances down to 10^{-17} m^2s^{-1}). (d) Due to the use of pulses the diffusion time is well defined. (e) With the use of gradient pulses it is possible to separate the effects of diffusion and spin-spin relaxation, respectively. (f) Background gradients resulting from differences in susceptibility in the sample or inhomogeneities in the B_0 field can be neglected for the analysis, due to comparably very strong gradient pulses.

In **Figure 3** the "Stejskal and Tanner sequence" is shown and its effect on diffusion and flow of the spins is illustrated schematically. A 90° rf-pulse is applied which rotates the macroscopic magnetization in its thermal equilibrium from the z-axis to the x-y plane. The first gradient pulse of duration $t = \delta$ and magnitude G is applied and the spins experience a phase shift according to equation 5-20, with the integral ranging over the duration δ. In the middle of 2τ the 180° rf-pulse reverses the sign of the precession, equivalent to an inversion of the sign of the applied gradients and static field. In addition the chemical shifts and frequency dispersions due to residual B_0 inhomogeneities and susceptibility effects in heterogeneous samples are refocused. In fact, this is an additional advantage of PFG spin-echo sequences compared to gradient-echo pulse sequences, which do not include this refocusing 180° rf-pulse. The second gradient is equal in magnitude and duration and thus, if the spins have not undergone any translational motion with respect to the z-axis, this second gradient will refocus the magnetization of all the spins dephased by the first gradient. However, if the spins have moved during the time period Δ between the two gradient pulses, the degree of dephasing due the applied gradients is proportional to the displacement in the direction of the gradients. Thus in the presence of diffusion, the winding by the first gradient to a "magnetization helix" and the unwinding by the second gradient is scrambled by the diffusion process, resulting in a disruption of coherent magnetization and therefore in a signal loss. The larger the diffusion, the poorer is the refocusing effect of the second gradient and the smaller is the resulting signal. In the absence of any background gradient, diffusion processes before and after

the diffusion delay Δ do not affect the signal attenuation. In the presence of flow along the direction of the gradients with a constant velocity for all spins present in the sample, the Stejskal and Tanner pulse sequence will yield the same net phase shift for all the spins. If both diffusion and flow processes are present, the whole diffusion-induced phase shift will receive an additional net phase shift. This flow-induced net phase shift can be compensated (Jerschow, 2000; Jerschow and Müller, 1997), by applying the sequence twice with inverted gradient sets, so that the second inverted gradient sets result in the corresponding negative net phase shift, which can be added to the first and thus cancels, leaving the diffusion process only (section 5.3.3).
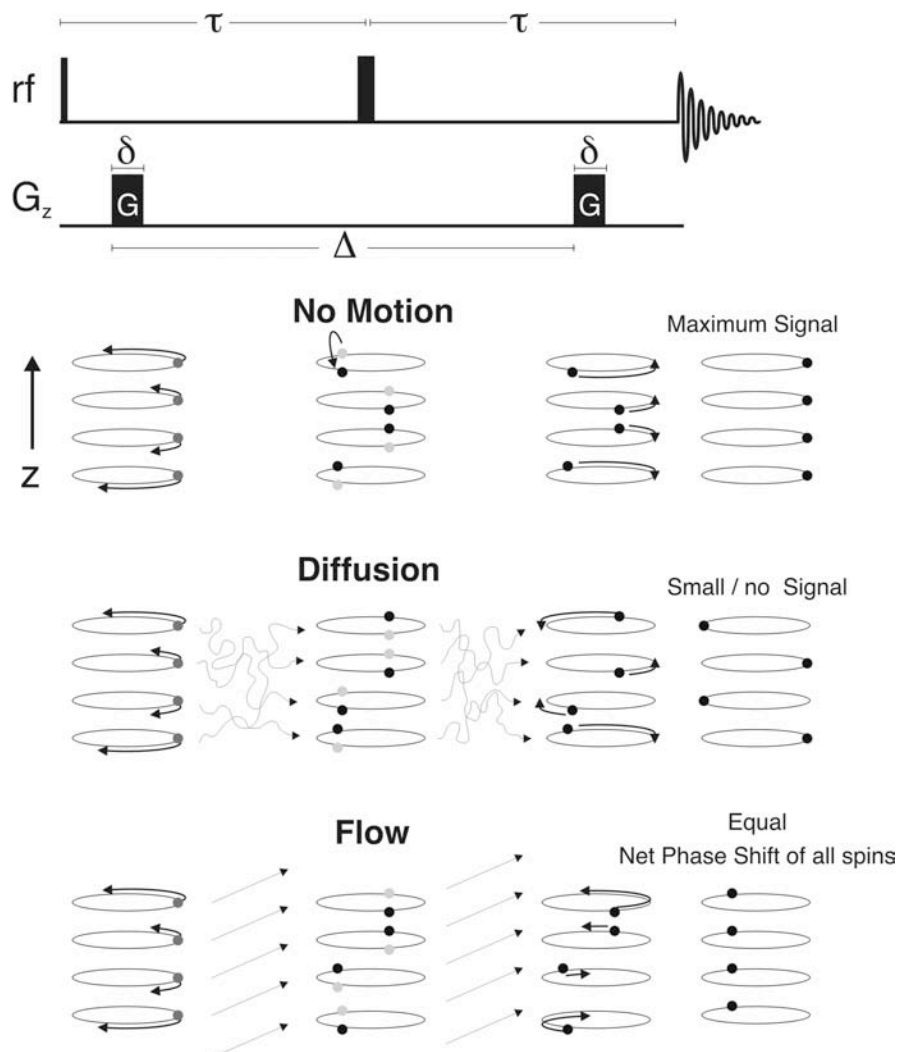
Figure 3: Schematic representation of the Stejskal and Tanner pulse sequence, measuring diffusion and flow. In each delay τ a gradient pulse of duration δ and magnitude G is inserted. The separation between the gradient pulses is denoted by Δ. Only the precession due to gradients is considered in a rotating reference frame rotating at ω_0. As the center of the gradient coincides with the center of the sample, the two spins above and below acquire phase shifts in opposite senses.

In addition to the signal attenuation due to diffusion and flow, relaxation processes during $t = 2\tau$ have to be considered. As the attenuation due to relaxation and due to diffusion and flow are independent, one obtains,

$$S(2\tau) = S(0) \cdot \underbrace{\exp\left(-\frac{2\tau}{T_2}\right)}_{\substack{\text{attenuation} \\ \text{due to relaxation}}} \cdot \underbrace{f(\delta, G, \Delta, D)}_{\substack{\text{attenuation} \\ \text{due to diffusion}}} \qquad \text{5-21}$$

where S is the signal intensity and $f(\delta, G, \Delta, D)$ represents a function for the attenuation due to diffusion. Hence, if τ is kept constant during all the experiments, relaxation-induced signal attenuation can be separated from diffusion-induced attenuation, and one can normalize equation 5-21 as follows:

$$E = \frac{S(2\tau)}{S(2\tau)_{G=0}} = f(\delta, G, \Delta, D) \qquad \text{5-22}$$

where $S(2\tau)_{G=0} = S(0)\ exp\text{-}(2\tau/T_2)$ represents the signal attenuation due to relaxation only.

5.2.4 Signal Attenuation due to Diffusion: Macroscopic Approach

For free, unrestricted diffusion it is possible to derive the relationship between diffusion and the observed signal attenuation analytically using Bloch equations including the effect of diffusion (Abragam, 1961; Torrey, 1956). In the case of restricted diffusion this macroscopic approach becomes mathematically intractable and one is forced to use different approximations. The so-called GPD approximations start with the Gaussian Probability Density of diffusion processes (Price, 1997b); there are several other approximations like SGP (Short Gradient Pulse) (Blees, 1994; Linse and Södermann, 1995; Wang et al., 1995a) and others (Caprihan et al., 1996; Sheltraw and Kenkre, 1996). However, even when using approximations, analytical solutions are generally not possible and numerical methods must be used. A detailed discussion and derivations of the GPD and the SGP approximations applying free and restricted diffusion are given elsewhere (Price, 1998).

The Bloch equations for the macroscopic nuclear magnetization, $\mathbf{M}(\mathbf{r},t) = M_x + M_y + M_z$, including the diffusion of magnetization, are given by Torrey et al. (Torrey, 1956),

$$\frac{\partial \mathbf{M}(\mathbf{r},t)}{\partial t} = \gamma \mathbf{M} \times \mathbf{B}(\mathbf{r},t) - \frac{M_x\mathbf{i} + M_y\mathbf{j}}{T_2} - \frac{(M_z - M_0)\mathbf{k}}{T_1} + D\nabla^2\mathbf{M} \qquad \text{5-23}$$

where $\mathbf{i}, \mathbf{j}$ and $\mathbf{k}$ are the unit vectors in the x, y and z direction of the laboratory frame of reference. For an anisotropic diffusion the last term in equation 5-23 has to be replaced by $\nabla \mathbf{D} \cdot \nabla \mathbf{M}$. Considering that $\mathbf{B}_0$ is along the z-axis superimposed by a parallel gradient $\mathbf{G}$ one can write in analogy to equation 5-18:

$$
\begin{aligned}
B_x &= 0 \\
B_y &= 0 \\
B_z &= B_0 + (\mathbf{G} \cdot \mathbf{r}) = B_0 + G_x x + G_y y + G_z z
\end{aligned}
$$

5-24

Substitution of equation 5-24 into 5-23 and considering that Cartesian product $\mathbf{M} \times \mathbf{B}$ is defined as

$$
\mathbf{M} \times \mathbf{B} = \left(M_x B_y - M_y B_x \right)_z + \left(M_y B_z - M_z B_y \right)_x + \left(M_z B_x - M_x B_z \right)_y
$$

5-25

and considering only transverse magnetization, including equation 5-17 and defining the complex transverse magnetization as $M_+ = M_x + iM_y$ one obtains:

$$
\frac{\partial M_+}{\partial t} = \underbrace{-i\omega_0 M_+}_{\text{static field}} \underbrace{-i\gamma(\mathbf{G} \cdot \mathbf{r})M_+}_{\text{gradient}} \underbrace{-\frac{M_+}{T_2}}_{\text{relaxation}} \underbrace{+D\nabla^2 M_+}_{\text{diffusion}}
$$

5-26

5.2.4.1 Stejskal and Tanner Sequence in the Absence of Motion

In the absence of any motion the transverse magnetization M_+ relaxes exponentially with the time constant T_2 as follows

$$
M_+ = \psi \exp^{-i\omega_0 t - t/T_2}
$$

5-27

where ψ is the amplitude of magnetization unaffected by relaxation. Setting $D = 0$ and substituting equation 5-27 into 5-26 one obtains a first-order differential for the amplitude ψ,

$$
\frac{\partial \psi}{\partial t} = -i\gamma(\mathbf{G} \cdot \mathbf{r})\psi
$$

5-28

and its solution is,

$$
\psi(r,t) = S \exp\{-i\gamma \mathbf{r} \cdot \mathbf{F}\}, \text{ where } \mathbf{F}(t) = \int_0^t \mathbf{G}(t')dt'
$$

5-29

$F(t)$ is the integral over all gradient pulses within the sequence. Thus, defining the starting point of the first gradient pulse as time point a, one calculates for the pulse sequence given in **Figure 3**:

$$F(t) = \int\limits_{0}^{a} 0\,dt + \int\limits_{a}^{a+\delta} G\,dt + \int\limits_{a+\delta}^{a+\Delta} 0\,dt + \int\limits_{a+\Delta}^{t} G\,dt = G \cdot (t + \delta - a - \Delta) \qquad \text{5-30}$$

From the 90° pulse until the 180° pulse equation 5-29 is valid. The effect of the 180° is to set back the phase of ψ by twice the amount that it had during the first τ period (**Figure 3**) and thus for the second half one yields:

$$\psi(r,t) = S\exp\{-i\gamma\mathbf{r} \cdot (\mathbf{F} - 2\mathbf{f})\}, \text{ where } \mathbf{f} = \mathbf{F}(\tau) \qquad \text{5-31}$$

Equations 5-29 and 5-31 can be combined, describing the whole sequence using the Heaviside step function $H(x)$:

$$\psi(r,t) = S\exp\{-i\gamma\mathbf{r} \cdot (\mathbf{F} - H(t-\tau)2\mathbf{f})\} \qquad H(x) = \begin{cases} 0 & x < 0 \\ 0.5 & x = 0 \\ 1 & x > 0 \end{cases} \qquad \text{5-32}$$

Equation 5-32 is also valid for the Hahn spin-echo pulse sequence.

5.2.4.2 Stejskal and Tanner Sequence in the Presence of Diffusion

Starting from equation 5-28 and including the diffusion term from equation 5-26 one obtains:

$$\frac{\partial\psi}{\partial t} = -i\gamma(\mathbf{G} \cdot \mathbf{r})\psi + D\nabla^2\psi \qquad \text{5-33}$$

Assuming a solution of equation 5-33 to be of the form of equation 5-32 one can substitute equation 5-32 into 5-33, but accounting for the time dependent diffusion process S will be a function of time, $S(t)$, and one obtains for the time-dependence of S:

$$\frac{\partial S}{\partial t} = -\gamma^2 D[\mathbf{F} - H(t-\tau)2\mathbf{f}]^2 S(t) \qquad \text{5-34}$$

Stepwise integration according to the Heaviside step function of equation 5-34 from $t = 0$ to $t = 2\tau$ yields:

$$\ln\left[\frac{S(2\tau)}{S(0)}\right] = \ln(E(2\tau))$$
$$= \int\limits_{0}^{\tau} -\gamma^2 D\mathbf{F}^2\,dt + \int\limits_{\tau}^{2\tau} -\gamma^2 D[\mathbf{F} - 2\mathbf{f}]^2\,dt \qquad \text{5-35}$$

Integration of equation 5-35, using $F(t)$ as given in equation 5-30, will yield the result (Stejskal and Tanner, 1965):

$$\ln(E) = -\gamma^2 G^2 \delta^2 D \left(\Delta - \frac{\delta}{3} \right) \qquad \text{5-36}$$

The resulting equation 5-36 is not a function of a, the starting point of the first gradient pulse, and therefore the placement of the gradient pulses within the sequence is of no matter, nor have they to be placed symmetrically around the 180° rf pulse. Besides the gyromagnetic ration, γ, this equation provides three experimental parameters which can be varied during a diffusion measurement: G, the gradient strength, δ, the gradient duration or Δ, the time between dephasing and refocusing of magnetization. Increasing one if these parameters will lead to increased signal attenuation. The term $(\Delta - \delta/3)$ is called diffusion time, where $\delta/3$ accounts for the finite gradient duration.

In addition, if the Bloch equations 5-23 are supplemented with an additional term representing unidirectional flow with a constant velocity v $(-\nabla v M)$, a similar analysis will yield the signal attenuation due to diffusion and flow in the direction of the gradients:

$$\ln(E) = \underbrace{-\gamma^2 G^2 \delta^2 D \left(\Delta - \frac{\delta}{3} \right)}_{\substack{\text{attenuation} \\ \text{due to diffusion}}} \quad \underbrace{+ i\gamma\delta G \Delta \cdot v}_{\substack{\text{net phase shift} \\ \text{due to flow}}} \qquad \text{5-37}$$

Whereas the diffusion results in a loss of echo intensity with increasing parameters G, Δ or δ, the flow induces only a phase shift, which is equal for all spins in the sample as long as v is constant and equal for all spins.

5.3   Experimental Aspects of Diffusion Measurements

5.3.1   The Stimulated Echo Sequence (STE)

Spin echo pulse sequences containing two and three 90° rf pulses were studied by Hahn (Hahn, 1950). He found that the three-pulse sequence can generate up to five echoes and the first echo after the third rf pulse was named by Hahn "stimulated echo" (STE). The effects of diffusion of the STE have been studied using both, the steady gradients (Woessner, 1961) and the pulsed gradients (Burstein, 1996; Tanner, 1970). In **Figure 4** the pulse sequence of a standard PFG-STE diffusion experiment is shown. The signal intensity for rectangular gradient pulses can be derived by an application of equation 5-33 to the sequence and yields (including relaxation attenuation):

$$S(2\tau_1 + \tau_2) = \frac{S(0)}{2} \cdot \underbrace{\exp\left[-\left(\frac{2\tau_1}{T_2}\right) - \left(\frac{\tau_2}{T_1}\right)\right]}_{\text{relaxation attenuation}} \cdot \underbrace{\exp\left[-\gamma^2 G^2 \delta^2 D\left(\Delta - \frac{\delta}{3}\right)\right]}_{\substack{\text{Stejskal} - \text{Tanner} \\ \text{factor}}} \qquad 5\text{-}38$$
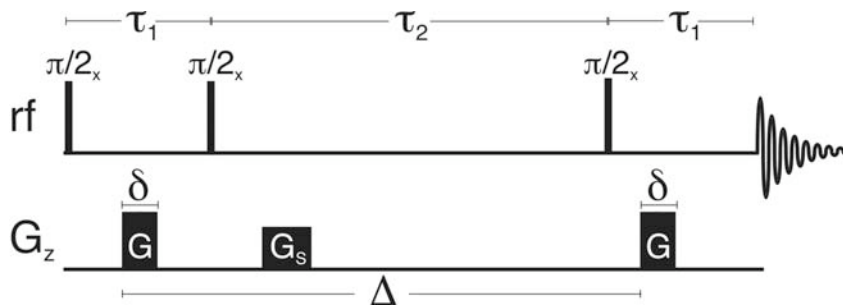
Figure 4: The stimulated echo (STE) pulse sequence with pulsed field gradients. During τ_2 magnetization is stored along the z-axis and therefore subjected only to longitudinal T_1 relaxation. G_S indicates a spoil gradient.

From equation 5-38 it is obvious that the signal amplitude of the PFG-STE experiment is reduced by a factor of two, compared to the PFG-SE experiment (Stejskal-Tanner experiment). This is a result of the second $90°_x$ pulse, which stores the magnetization by rotating only the y-components into the $\pm z$-axis and the remaining x components are eliminated by phase cycling or spoil gradients (**Figure 4**). After the storage period τ_2 the third $90°_x$ pulse returns the z-components to the $\pm y$-directions, where the second gradient refocuses the magnetization so that the STE signal appears at $t = 2\tau_1 + \tau_2$. However, at the time of the echo, the refocused isochromates are no longer coplanar, but their projection onto the xy-plane define a

circle which is tangential to the xz-plane. Yet the PFG-STE sequence has one major advantage compared to the PFG-SE sequence. The major part of Δ can be contained in the τ_2 period, where the magnetization is aligned along the z-axis and therefore subjected only to longitudinal T_1 relaxation. Since for most macromolecules $T_1 \gg T_2$ is valid, the STE sequence is generally preferred to the SE sequence as long $\tau_1 \ll \tau_2$. The ratio of the signal obtained from the stimulated echo (STE) sequence compared to that obtained from the Stejskal and Tanner (SE) sequence can be calculated using equations 5-21 and 5-38. In performing these calculations it was assumed that $2\tau = T_1$ in the case of the Stejskal and Tanner sequence and that $2\tau_1 + \tau_2 = T_1$ in the case of the STE sequence. In **Figure 5** the signal amplitude ratio $S(\text{STE}) / S(\text{SE})$ is plotted against the ratio T_1 / T_2 in a logarithmic scale for three cases of $\tau_1 = \tau_2/2$; $\tau_1 = \tau_2/4$ and $\tau_1 = \tau_2/8$. As expected, when $T_1 / T_2 = 1$, the stimulated echo sequence gives only half the intensity of the spin echo sequence. However, assuming typical value for macromolecules with $T_1 / T_2 = 10$ and $\tau_1 = \tau_2 / 4$, the enhancement factor for the STE sequence is greater than 200, and thus more than compensates for the 50% smaller coefficient.
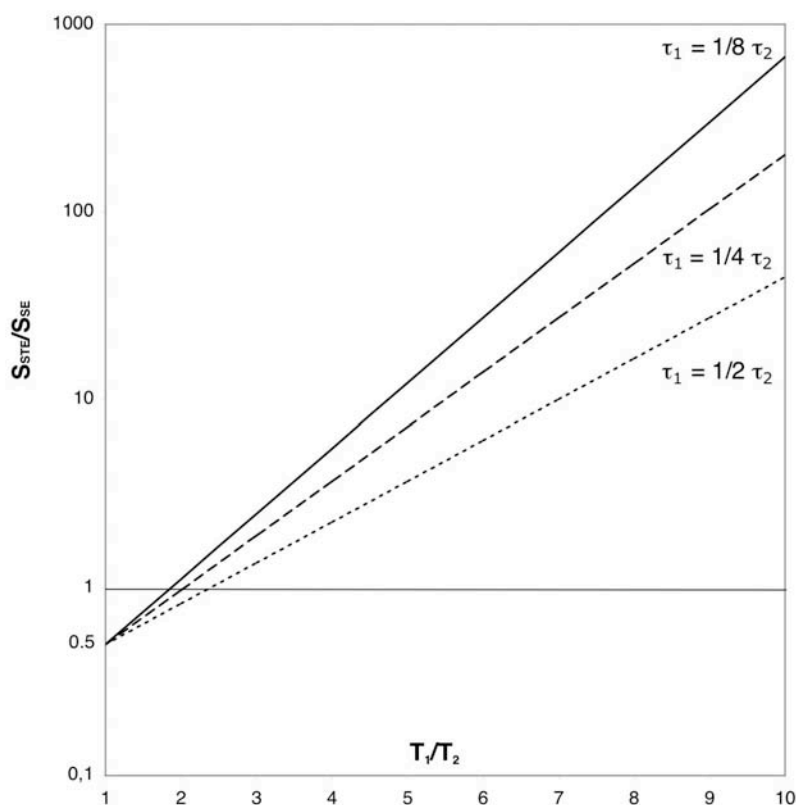
Figure 5: Logarithmic signal ratio of the stimulated echo sequence (STE) and the Stejskal and Tanner (SE) sequence versus the ration T_1/T_2 for three cases as indicated. In performing the calculation it was assumed that $2\tau = T_1$ for the SE sequence and that $2\tau_1 + \tau_2 = T_1$ for the STE sequence.

Another important point is that after the first 90° pulse of the STE sequence chemical shifts are encoded, which may seriously affect the signal amplitude. For a spin with offset frequency ω_A and position z the component $cos(\omega_A\tau_1 + \gamma Gz\delta)$ will be stored by the second 90° pulse. The third 90° pulse brings this component back into the xy-plane and after an additional time τ_1 the amplitude of the y-component will be $cos^2(\omega_A\tau_1 + \gamma Gz\delta)$, neglecting the effect of diffusion. For a sample of length L the amplitude of the peak at ω_A, neglecting relaxation, is given by the integral over the whole sample and thus:

$$\frac{1}{L}\int_{-L/2}^{L/2}cos^2(\omega_A\tau_1 + \gamma Gz\delta)dz = \frac{1}{2} + \frac{1}{2}cos(2\omega_A\tau_1)\cdot sinc(L\gamma Gz\delta/\pi) \qquad 5\text{-}39$$

The sinc-function is oscillating around zero for all values of G, except those close to $G = 0$, there the sinc-function becomes unity. Consequently the signal amplitude is as expected 1/2 (equation 5-38), however, when the gradient vanishes or $q = \gamma Gz\delta$ is zero, the signal amplitude depends on the frequency offset ω_A, encountering the modulation factor $(1/2)\,cos(2\omega_A\tau)$. Therefore, in STE experiments the echo amplitude $S_0(2\tau_1 + \tau_2)$ for $G \approx 0$ should be avoided in data analysis.

5.3.2 Eddy Current Reduction

Rapid changes in gradient pulses can generate eddy currents in surrounding conducting materials. The induced eddy currents, and thus their associated magnetic fields which interfere with the main magnetic field, are proportional to the strength of the gradient and are especially sensitive to rapidly rising and falling gradient pulses, such as rectangular pulse shapes. If the eddy current tail from the first gradient pulse in the Stejskal and Tanner sequence extends in to the second τ-period, then the total field gradient during the second τ-period is not equal to the first and the situation is analogous to mismatched or non-reproducible gradient pulses. Thus, even if a spin has not undergone any motion, there will be a residual phase shift, resulting in the following effects: (a) phase changes in the observed spectra, (b) anomalous signal attenuation, (c) gradient-induced broadening of signals, and (d) wiggles in the spectrum due to time-dependent B_0 shifts.

5.3.2.1 Shielded Gradient Coils

There are several methods of handling eddy current effects. The most effective solution is to use shielded gradient coils. The design of gradient coils is out of the scope of this thesis and can be found elsewhere (Buszko and Maciel, 1994; Price, 1996; Price et al., 1994); however, the commonly used geometry for producing

gradients along the *z*-axis are so-called Maxwell pairs of coils which contain two sets of windings at either end of the coil in opposite handedness. The shielding of this (primary) gradient coil is achieved by placing a second shield gradient coil outside the primary one. These coils were originally proposed by Mansfield, Chapman (Chapman and Mansfield, 1986; Mansfield and Chapman, 1986) and Tuner (Turner, 1986; Turner and Bowley, 1986) and are designed to cancel the radiation of the main gradient coil outwards, whereas the gradient generated within the sample volume would be unaffected by the presences of the shielding coils. Thus, using shielded gradient coils, generated eddy currents can be reduced typically to < 1% (Burl and Young, 1996); in return they also yield a decrease in strength and linearity of the primary gradient coil (Jasinski et al., 1992), which is, however, tolerable for many experiments (Hurd et al., 1996).

5.3.2.2 *Pre-Emphasis*

Another commonly used approach is based on the requirement that the sign of generated eddy current fields is opposite to the change which induced them.
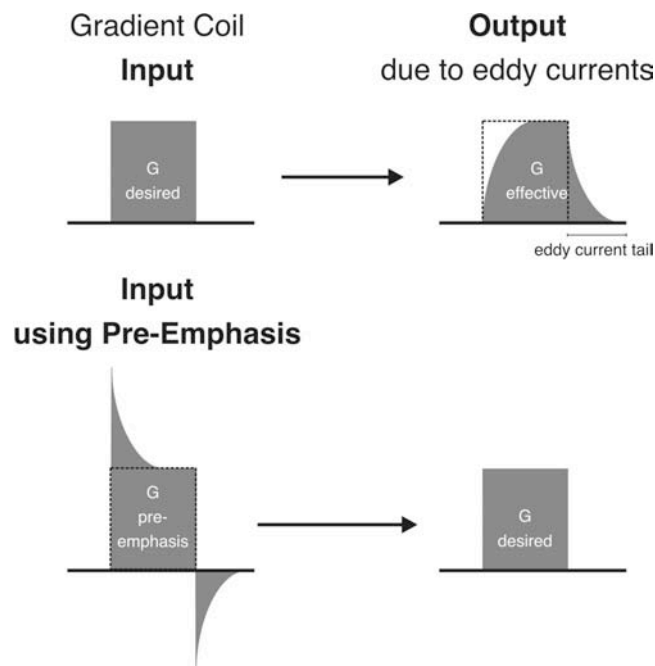
Figure 6: Illustration of the pre-emphasis method to yield the desired gradient shape against eddy currents.

Therefore, overdriving the currents at the leading and tailing edges of the gradient pulses will self-compensate for induced eddy current fields. This method is called pre-emphasis and is performed by adding small exponential corrections of different

amplitude to the desired waveform (Jehenson et al., 1990; Majors et al., 1990; Van Waals and Bergman, 1990). In **Figure 6** the conceptual idea of pre-emphasis is illustrated. Owing to the generation of eddy currents the ideal input waveform into the gradient coil will not produce an identical gradient shape, but will result in a distorted waveform. Thus the input waveform has to be shaped counteracting the eddy current effects. In practice this method is not perfect, since the spatial distribution of fields produced by eddy currents in the surrounding is rather different from those generated by the gradient coils. However, this method is often used in combination with shielded gradient systems to improve performance.

5.3.2.3   *Longitudinal Eddy Current Delay (LED) Sequence*

The LED pulse sequence is a modification by Gibbs of the STE sequence as shown in **Figure 7** (Gibbs and Johnson, 1991). The major change is an additional fourth 90° pulse at the center of the stimulated echo which stores the magnetization in the longitudinal direction, while the eddy currents of the second gradient decay. After the period T_e, the magnetization is recalled by the fifth 90° pulse and acquired. However, the LED sequence does not cope with the eddy current tails of the first gradient. This can be encountered, by adding a train of three gradient pre-pulses to yield a train of five equally spaced (Δ) gradient pulses (Hrovat and Wade, 1981a; Hrovat and Wade, 1981b; Von Meerwall and Kamat, 1989).
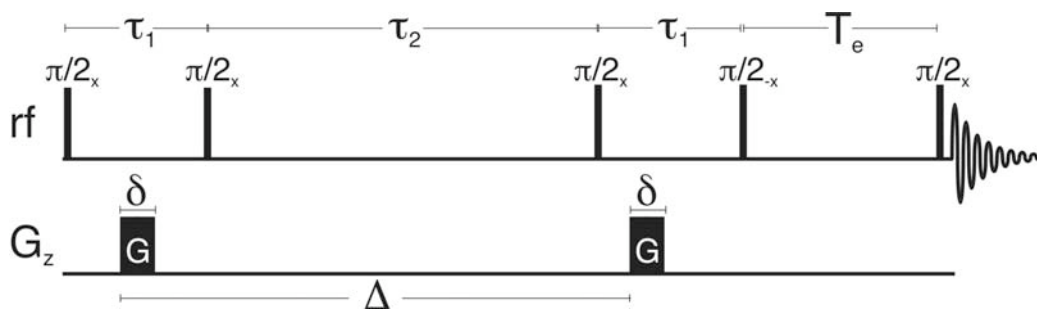
Figure 7: The LED pulse sequence stores the decoded magnetization prior to acquisition along the *z*-axis, until eddy currents have decayed. (Gibbs and Johnson, 1991)

This ensures that the induced magnetic fields, resulting from previous gradients, are equal after the first and third 90° pulse; however, they also introduce additional heat which might yield convection artifacts. Phase cycling to +*z*/-*z* is essential for the last two 90° pulses, in order to remove effects of longitudinal relaxation during T_e. The composite pulse sandwich 90°$_x$ G_z 90°$_{-x}$ is equivalent to encoding the spatial position in longitudinal magnetization by a single B_1 gradient pulse and the decoding is done in

the same manner (Canet, 1997; Cante, 1996; Counsell et al., 1985; Raulet et al., 1997). Thus, LED may also hold for "longitudinal encoded decoded" which is analogous to B_1 gradient experiments.

5.3.2.4 Bipolar Pulse Pair Gradients (BPP)

One of the best solutions to diminish eddy current effects is the use of self-compensating, bipolar gradient pulses. In this method the gradient pulse δ is replaced by a composite bipolar gradient combination *(G)-180°-(-G)*, where *G* has a duration of $\delta/2$ (Wider et al., 1994).
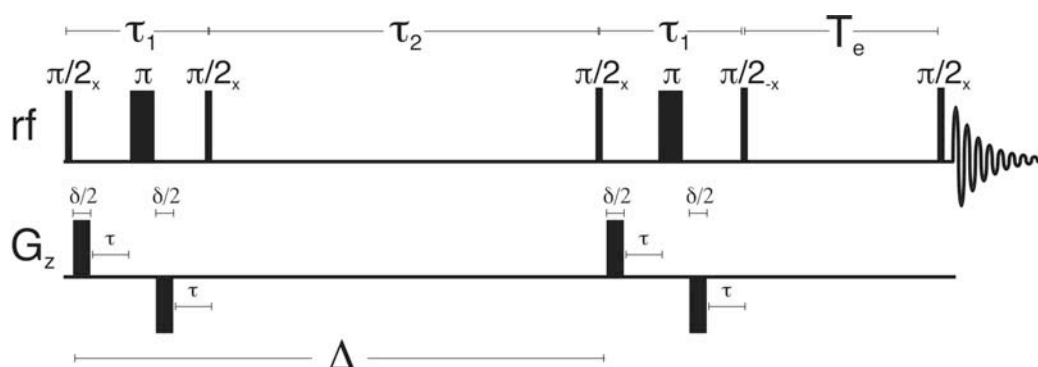
Figure 8: Pulse sequence of the BPP-LED experiment. The self-compensating effect of the bipolar gradient pulse sandwiches largely cancel the generation of eddy currents.

In **Figure 8** the LED sequence is shown using bipolar gradients to encode and decode the magnetization. The two gradient pulses are of opposite sign and the 180° pulses between them compensates the induced phase shift of the first gradient pulse within the pulse sandwich such that, taken as a whole, the effective gradient is equivalent to a single gradient pulse of duration δ. In addition, eddy currents induced by a positive polarity of the first gradient pulse are cancelled out by an equivalent negative polarity of the second gradient pulse, providing self-compensation of induced eddy currents. The attenuation factor for the BPP-LED sequence as given in **Figure 8** can be corrected for each gradient pair and yields:

$$\ln(E) = -\gamma^2 G^2 \delta^2 D\left(\Delta - \frac{\delta}{3} - \frac{\tau}{2}\right)$$

5-40

    Gradient pulse sequences with alternating polarity were introduced into PFG NMR spectroscopy originally by Karlicek and Lowe (Karlicek and Lowe, 1980), in order to take advantage of the fact that the 180° rf pulse refocuses static magnetic

gradients and the effects of background gradients (Cotts et al., 1989). In high resolution NMR spectroscopy two other effects are encountered that are also sensitive to refocusing. In the absence of the 180° rf pulse, chemical shifts are encoded along with the position dependent phase information during the τ_1 period of the STE experiment (section 5.3.1) which affect the amplitude of the STE signal (Chen et al., 1998; Pelta et al., 1998). In addition unrefocused chemical shifts in a coupled spin system generate zero quantum coherence after the second 90° pulse of a STE experiment, and phase errors due to different relaxation properties of zero quantum coherence and longitudinal magnetization may occur for long values of the storage time τ_2 (Straubinger et al., 1995). However, the pulse sandwich *(G)-180°-(-G)* eliminates chemical shift, exchange and zero quantum problems and thus increases the quality of the collected data. A potential disadvantage of the BPP-STE or BPP-LED experiment is that the amount of time to complete the composite gradient pulse pair exceeds the time required for a single gradient pulse, thus, when T_2 relaxation times are very short in macromolecular systems, the extra amount of time in transverse magnetization may lead to a loss of signal (Johnson, 1999).
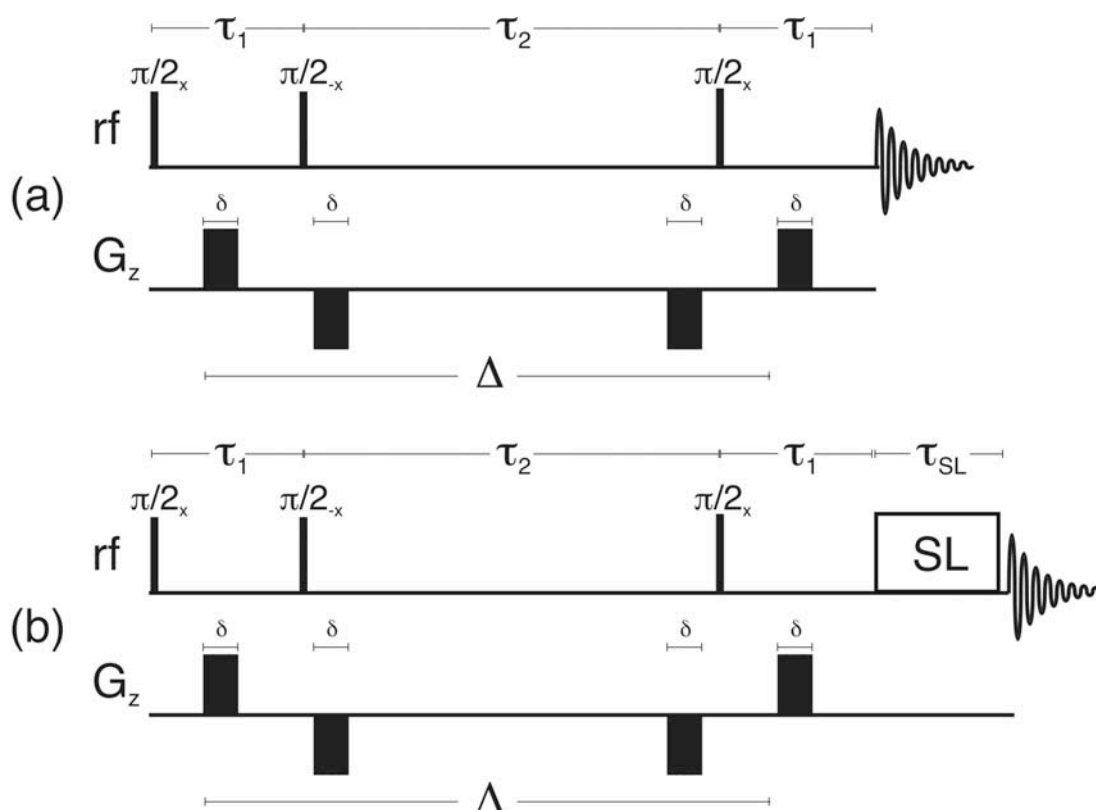
Figure 9: Gradient compensated pulse sequences (a) GCSTE and (b) GCSTESL with a reduced phase cycle due to the homospoil effect during τ_2 (Pelta et al., 1998).

Pelta et al. have suggested two additional pulse sequences with self-compensating gradient pairs (Pelta et al., 1998), which are known as gradient compensated stimulated echo (GCSTE) and gradient compensated stimulated echo spin lock (GCSTESL). Both of these pulse sequences, illustrated in **Figure 9** feature bipolar gradient pulse pairs in which one of the pulses is placed in the storage interval τ_2 providing a homospoil effect.

This pulse arrangement avoids the extra 180° pulses required when the BPPs are placed within the transverse interval τ_1. The major advantage is a reduction in the required phase cycling. Disadvantages are (1) a doubled amount of heating for the same $q = \gamma\delta\Delta G$; (2) for coupled spin systems phase errors occur due to the generation of ZQCs; and (3) due to chemical shift evolution amplitude modulation may occur. The GCSTESL sequence with an additional spin lock interval τ_{SL} corrects the line shape for ZQCs, but not for chemical shift or exchange effects.

5.3.2.5 *Shaped Gradients*

As already mentioned above, the severity of eddy currents is proportional to *dG/dt*, the rise and fall times of the gradient pulses. Hence reducing eddy currents is possible by slowing down these rise and fall times using shaped pulses instead of rectangular pulses (Stejskal and Tanner, 1965); commonly used are sine or trapezoidal gradient pulses. For the case of nearly rectangular shaped pulses solutions for the signal attenuation from diffusion can be determined by applying the macroscopic approach (section 5.2.4). Furthermore it can be shown that the precise shape is unimportant as long as the product, $G \cdot \delta$, gradient strength times gradient duration is equal to that of the ideal rectangular pulse (Price and Kuchel, 1991). A detailed discussion and derivation can be found elsewhere (Price, 1998; Price and Kuchel, 1991); however, the ratio $G \cdot \delta$ between a rectangular and a sine shaped gradient pulse is $2/\pi$ and for a squared-sine shape this ratio is 0.5. Thus, compared to a rectangular gradient pulse of duration δ, a sine shaped gradient pulse applies an effective gradient $G \cdot \delta_{sine}$ which is reduced to $2/\pi$, and a squared-sine shape is reduced to 0.5. This has to be taken into account when analyzing the data of a diffusion experiment, e.g., in a non-linear least square regression of the exponential signal decay against the gradient strength.

5.3.3 Temperature Gradients and Convection

Convection currents are induced in non-viscous samples by temperature gradients. These temperature gradients are easily possible along the z-axis, since temperature regulation in NMR probes is normally performed by flowing heated or cooled (nitrogen) gas through the base of the probe. Assuming that the induced convective compensation currents are planar along the z-axis, the convection will transport equal amounts of sample in opposite directions along the temperature gradient. As already outlined in section 5.2.3 and **Figure 3**, unidirectional flow will cause a net phase shift which is equal for all the spins in the sample; however, convection is, considering the z-axis only, a bidirectional flow with a distribution of velocities canceling all imaginary parts over the sample volume (equation 5-37). Therefore convection causes a corresponding damping factor, resulting from a vector addition of positive and negative phase changes which interfere with the attenuation due to diffusion and thus increases the measured diffusion coefficient. In addition a non-exponential signal decay can be observed: convection artifacts are characterized by a downward curvature in plots of the logarithm of the spin-echo amplitude against q^2, where q is defined as $q = \gamma\delta G$. For longer diffusion times, Δ, one can observe an increasing oscillation of the signal amplitude which is a sensitive detector for convection artifacts.

5.3.3.1 *The Double-Stimulated Spin-Echo Experiment*

To scope with convection a modification of the PFG diffusion experiment can be used which relies on gradient moment nulling. This means that a second gradient set of opposite effective polarity is applied during the sequence, inducing an opposite handedness of the "magnetic helix" and therefore resulting in an opposite net phase shift and thus canceling the overall acquired phase shifts. The mathematical requirement is therefore that the first moment of effective gradients G^* over the entire pulse sequence is zero, while p is the coherence order (Callaghan, 1993):

$$\int_0^t G^*_z(t')t'dt' = 0$$

where   5-41

$$G^*_z = p \cdot G_z$$

The phase shift at time t of a nuclear spin following a path **r** in a gradient **G** is given by:

$$\phi(t) = \gamma \int_0^t \mathbf{G}(t') \cdot \mathbf{r}(t') dt'$$

5-42

The component of the spin's motion which is along the direction of the gradient $z(t)$ is relevant and can be expanded in Taylor series:

$$z(t) = z_0 + \underbrace{\left(\frac{\partial z}{\partial t}\right)_{t=0}}_{\substack{\text{velocity} \\ v_0}} t + \frac{1}{2} \underbrace{\left(\frac{\partial^2 z}{\partial t^2}\right)_{t=0}}_{\substack{\text{acceleration} \\ a_0}} t^2 + \dots$$

5-43

Therefore one can write for the phase shift at time t:

$$\phi(t) = \gamma z_0 M_0 + \underbrace{\gamma v_0 M_1}_{\text{velocity}} + \underbrace{\frac{1}{2}\gamma a_0 M_2}_{\text{acceleration}} + \dots$$

where

5-44

$$M_n = \int_0^t G^*{}_z(t')(t')^n \, dt'$$

M_n is the nth moment of $G^*{}_z$ and is set to zero for $n = 1, 2,\dots$ and higher moments, thus the Stejskal and Tanner attenuation factor (equation 5-37) becomes independent of a constant velocity v, leaving the attenuation due to diffusion only. However, the method does not compensate for turbulent convection. **Figure 10** illustrates the most simple velocity-compensated gradient sequence, where during the first half (2δ) the magnetic winding is of opposite handedness than in the second half and overall the first moment over all gradients is zero.
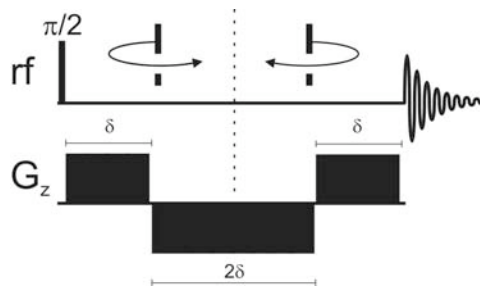
Figure 10: Simple gradient spin echo pulse sequence with a zero first moment of the gradients. The handedness of magnetic winding is indicated above the sequence.

The flow-compensated double stimulated echo sequence as proposed by Jerschow and Müller (Jerschow and Müller, 1997) is shown in **Figure 11**, using bipolar gradients and an eddy current delay at the end of the sequence which also allows both coherence-transfer pathways of opposite signs during the precession

period to be converted to observable magnetization (dashed and full lines). The first moment of the effective gradient over the whole sequence is zero and the winding during each diffusion period $\Delta/2$ is of opposite handedness and therefore refocuses all constant velocity effects. In addition, chemical shifts are also refocused if the delay $\Delta/2$ is equal to τ_1. A proper coherence pathway selection as indicated in **Figure 11** is essential, as the effective gradient is proportional to the coherence order (equation 5-42). The gradients in the center of the DSTE experiment might be merged together; however, due to different rise and fall times, discrete identical gradients, such as during τ_1 yield better refocusing. Since chemical shifts are refocused separately in each precession period by 180° pulses, the delays τ_a and τ_b need not to be equal. The diffusion-dependent signal attenuation for the bipolar double stimulated spin-echo experiment is given by

$$\ln(E) = -\gamma^2 G^2 \delta^2 D \left(\Delta - \frac{4\delta}{3} - \frac{5\tau_a}{2} - \frac{\tau_b}{2} \right)$$

5-45

where Δ, δ, τ_a and τ_b are defined as in **Figure 11**.
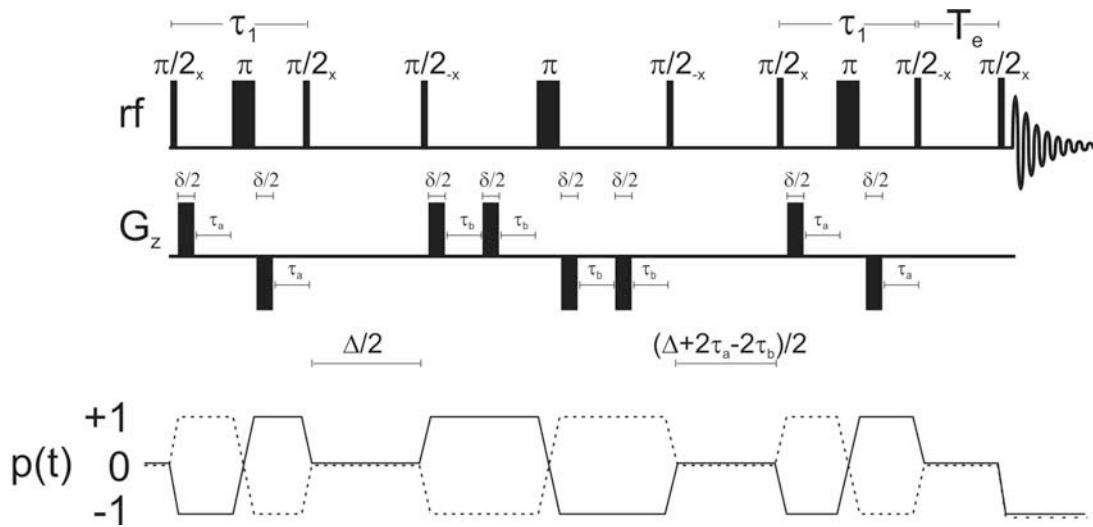
Figure 11: Double stimulated spin-echo experiment with bipolar gradient pulses and an eddy current delay at the end of the sequence. The selected coherence transfer pathways $p(t)$ are given beneath the sequence.

5.3.4   J Modulation, Cross Relaxation and Chemical Exchange

5.3.4.1   *J Modulation*

In coupled homonuclear spin systems the precession frequencies and thus the refocusing depend on the magnitude of the spin coupling constant, *J*. In addition, the echo sequence used for measuring diffusion exchanges the spin states of coupled nuclei and echo maxima occur when,

$$\tau = n/J$$

and negative maxima occur when

$$\tau = n/(2J)$$

5-46

where *J* is the coupling constant in Hertz and *n* is an integer. Thus to obtain a good signal-to-noise ratio it is important to consider the pulse sequence delays with respect to *J*, and it is preferable to keep $\tau_1 << 1/J$. This is of special importance in PFG experiments where the magnetization is not stored along the *z* axis during diffusion. Decoupling of coupled spin systems can cause anomalous changes in signal intensity, especially in systems with large coupling constants which is due to an incomplete decoupling during gradient pulses.

5.3.4.2   *Cross Relaxation in STE-type Experiments*

Diffusion measurements of macromolecular systems in water can cause cross relaxation. The problem of cross relaxation does not apply to the original Stejskal and Tanner experiment; however, for STE pulse sequences (section 5.3.1) the situation is as follows: After the first 90° rf pulse, both the macromolecule and water magnetization are in the xy-plane. The transverse T_2 relaxation time of the macromolecule is much less than that of water, such that by the end of the τ_1 period the macromolecules are fully relaxed, whereas the relaxation of the water magnetization is more or less insignificant. Thus, after the second 90° rf pulse, the longitudinal *z* magnetization of the macromolecule is zero, as it was entirely aligned along the *z* axis due to relaxation prior to the pulse. In contrast, the water *z* magnetization is proportional to $cos(qz)$, where $q = (2\pi)^{-1}\gamma\delta G$, as the gradient pulse creates a "magnetization helix" along the direction of the gradient with a period of $2\pi / (\gamma\delta G)$. However, as qz ranges over many periods within the sample, the net *z* magnetization of water over the whole sample is zero. During τ_2 cross relaxation results from local equilibrium differences between both magnetizations and thus cross relaxation will depend on $q = (2\pi)^{-1}\gamma\delta G$ and thus *G*. A detailed discussion including equations accounting for this cross relaxation in a two-phase system can be found elsewhere (Peschier et al., 1996). Under certain conditions it is also possible to

determine the exchange parameters, allowing *D* to be calculated correctly (Peschier et al., 1996).

5.3.4.3   Effects of Chemical Exchange

Chemical rate processes have been studied by NMR spectroscopy for decades and the ways that chemical exchange affects NMR spectra are very diverse, such as line broadening and coalescence, or lack of coupling to exchangeable protons or cross-peaks in a NOESY-type spectrum. However, the underlying mechanism is much the same (Bain, 2003; Johnson, 1965). In the standard model for chemical exchange, nuclei or groups of nuclei explore a number of sites in a Markovian random process. These sites are associated with a different chemical environment and thus characterized by different spin Hamiltonians. Examples are basic groups which may accept a proton or conformational rearrangements or different molecular configurations, such as *cis* and *trans* isomers. Chemical exchange processes are defined by their rate relative to the NMR timescale and can be grouped in slow exchange, which is defined by a situation where characteristic individual sites can be observed in the spectra by individual signals, and fast exchange, which yields an time-averaged spectrum over the different sites. The path from slow exchange to fast exchange consists of line broadening, coalescence and motional narrowing as the mean lifetimes for the occupation of different sites decrease. These exchange rates, i.e., inverse lifetimes, can be manipulated by changes in temperature or concentration of participating species for intermolecular interactions.

With the use of diffusion NMR spectroscopy arise new possibilities, as it is of no matter whether the spin Hamiltonian is different in different sites or not, as long as the hydrodynamic properties of the species are different. In addition, as the variable is q^2 rather than time, there is nothing analogous to lifetime-dependent line broadening in diffusion measurements. Nevertheless a variation of the storage time τ_2 in STE-type diffusion measurements sometimes permits the observation of slow and fast exchange limits without changing the physical properties of the sample (Johnson, 1993); (Chen et al., 1998).

5.3.4.3.1   Two Site Exchange and Effects in Diffusion Spectra

The effect of chemical exchange on the longitudinal magnetization during the diffusion time interval τ_2 in an STE experiment (**Figure 4**) can be calculated, assuming that $\tau_1 \ll \tau_2$, so that $\tau_2 \approx \Delta$. Taking into account diffusion, flow and chemical exchange, the rate of change of the nuclear magnetization $M_n(r,\tau_2)$ for the nth species with spatial coordinates *r* is given by Bloch equations:

$$\frac{\partial \mathbf{M}(\mathbf{r},\tau_2)}{\partial \tau_2} = -\frac{M_n(\mathbf{r},\tau_2)}{T_{1n}} + \nabla \cdot J_n(\mathbf{r},\tau_2) + \sum_m K_{nm} M_m(r,\tau_2)$$

where rate the constants are

$$k_n = -K_{nn} \text{ and } k_{nm} = K_{nm}$$

and the flux is defined by

$$J_n(\mathbf{r},\tau_2) = -D_n \nabla M_n(r,\tau_2) + M_n(r,\tau_2) \cdot v_n(r,\tau_2)$$

5-47

In equation 5-47 D_n and $v_n(r,\tau_2)$ are the diffusion coefficient and the velocity of the nth species, respectively. These equations and their solution taking the spatial Fourier transform have been discussed by Kräger et al (Kräger et al., 1988); and similar equations for nuclear magnetic relaxation in multiple phase systems were previously treated by Zimmermann and Brittin (Zimmerman and Brittin, 1957).

Real applications often involve a two-site exchange, and for this case analytical solutions can be carried out, neglecting flow,

$$\frac{\partial \mathbf{M}(K,\tau_2)}{\partial \tau_2} = \mathbf{L}\mathbf{M}(K,\tau_2)$$

where

$$\mathbf{L} = \begin{pmatrix} L_{AA} & L_{AB} \\ L_{BA} & L_{BB} \end{pmatrix} = \begin{pmatrix} -k_A - R_A & k_B \\ k_A & -k_B - R_B \end{pmatrix}$$

5-48

where $R_n = (1/T_{1n}) + D_n q^2$, describing relaxation and $\mathbf{L}$ describes the exchange using the rate constants k_A and k_B at either site.

For the case that the chemical shift difference between the sites is much larger than the exchange rate the required matrix elements are available in literature (Ernst et al., 1987):

$$M_A = \left[\frac{M_{A0}}{2} - \frac{(\beta M_{A0} - k_B M_{B0})}{2\chi}\right] \exp\left[(-\alpha + \chi)\tau_2\right]$$

$$+ \left[\frac{M_{A0}}{2} + \frac{(\beta M_{A0} - k_B M_{B0})}{2\chi}\right] \exp\left[(-\alpha - \chi)\tau_2\right]$$

$$M_B = \left[\frac{M_{B0}}{2} + \frac{(\beta M_{B0} - k_A M_{A0})}{2\chi}\right] \exp\left[(-\alpha + \chi)\tau_2\right]$$

5-49a

$$+ \left[\frac{M_{B0}}{2} - \frac{(\beta M_{B0} - k_A M_{A0})}{2\chi}\right] \exp\left[(-\alpha - \chi)\tau_2\right]$$

where

$$M_{A0} = M_A(q,0);\ M_{B0} = M_B(q,0)$$

and

$$\alpha = \frac{1}{2}\left[k_A + k_B + D_A q^2 + D_B q^2\right]$$

$$\beta = \frac{1}{2}\left[k_A - k_B + D_A q^2 - D_B q^2\right]$$ 5-49b

$$\chi = \sqrt{\beta^2 + k_A k_B}$$

and

$$q = \gamma\delta G$$

When considering the special case in which the chemical shift difference is zero or much less than the exchange rate so that a single line is observed in the NMR spectra, the diffusion spectrum is calculated by the sum $M(q,\tau_2) = M_A(q,\tau_2) + M_B(q,\tau_2)$ and thus yields:

$$M(q,\tau_2) = \left[\frac{M_0}{2} + \frac{\Lambda}{2\chi}\right]\exp\left[(-\alpha + \chi)\tau_2\right]$$

$$+ \left[\frac{M_0}{2} - \frac{\Lambda}{2\chi}\right]\exp\left[(-\alpha - \chi)\tau_2\right]$$ 5-50

where

$$M_0 = M_{A0} + M_{B0}$$

and   5-51

$$\Lambda = \beta\left[M_{B0} - M_{A0}\right] + M_{A0}k_A + M_{B0}k_B$$

The probability of occupation of the nth site (n = A, B) is p_n and the mean lifetime of a spin in this site is $\tau_n = 1/k_n$. Therefore $p_A = \tau_A/(\tau_A + \tau_B)$ and $N = k\tau_2/2$ is the mean number of times that a spin changes sites during the longitudinal storage period τ_2, when $k = k_A/p_B = k_B/p_A = 1/\tau$. If t_A and t_B are the total amounts of time that a spin occupies the sites A and B, the longitudinal storage period is given by $\tau_2 = t_A + t_B$ and the equilibrium constant is then $K_{eq} = t_B / t_A$.

In addition, from equation 5-50 it is clear that chemical exchange in diffusion spectra does not yield a simple sum of exponentials because the variable q appears in the coefficient as well as in the exponents. A plot of $\ln(M)$ versus $q^2\tau_2$ of equation 5-50 for different values of τ_2 is given in **Figure 12**.
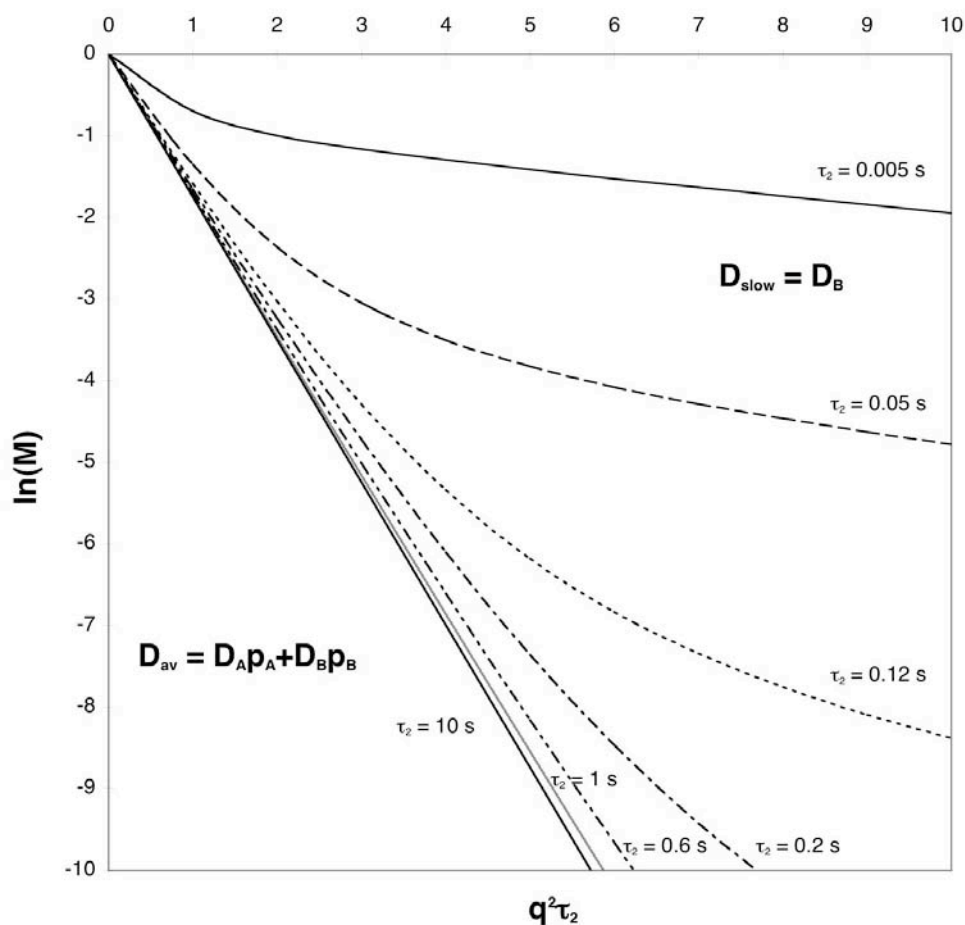
Figure 12: Effects of the echo amplitude $\ln(M)$ versus $q^2\tau_2$ for a two-site exchange calculated with equation 5-50 using $D_A = 2.0$; $D_B = 0.1$; $k_A = 10$; $M_{A0} = 0.4$ and $k_B = 66.6$; $M_{B0} = 0.6$.

The two site exchange was calculated using $D_A = 2.0$; $D_B = 0.1$; $k_A = 10$; $M_{A0} = 0.4$ and $k_B = 66.6$; $M_{B0} = 0.6$. The slow exchange limit is given in the upper curves for large values of $q^2\tau_2$, where $\tau_2 < 2/k = 0.12$ and $N < 1$. The dominating effect of these curves is the summation of two exponentials and thus, basically, the slope is associated with D_A and D_B. In the limit of large $q^2\tau_2$ values or short τ_2 storage times dominates D_{slow}, which corresponds to D_B, whereas the initial slope for small values of $q^2\tau_2$ or longer τ_2 storage times is the fast exchange limit which corresponds to a population averaged diffusion constant $D_{av} = p_A D_A + p_B D_B$. Therefore it is also possible to extrapolate the populations A and B, as the intercept, i.e. $q^2\tau_2 = 0$ value, of the line with slope D_{av} is taken to be $\ln(M_A + M_B)$, while the intercept of the slow exchange line extrapolated from large $q^2\tau_2$ values is equal to $\ln(M_A)$. The curve with the steepest slope, actually a straight line with slope D_{av}, represents the fast exchange limit, which can be obtained by setting $\tau_2 > 20/k$ so that $N > 10$.

Thus under favorable conditions it is possible to obtain a diffusion spectrum with two individual peaks in the slow exchange limit and similarly a diffusion spectrum with a single peak in the fast exchange limit by varying the diffusion storage time τ_2. The application of this theory for the analysis of protein / ligand interaction is called affinity NMR (Lin et al., 1997) and an example is given by Derrick et al. (Chen et al., 1998; Derrick et al., 2002).

5.3.5 Multiple Quantum Experiments

Large gains in sensitivity and resolution can be made through the use of pulse sequences which generate either homonuclear or heteronuclear multiple quantum transitions. In multiple quantum experiments, it is the effective sum of the gyromagnetic ratios, γ, of the nuclei involved in the coherence which is relevant to the attenuation. In fact, the effect of gradients is scaled up by n^2, where n is the coherence order, therefore homonuclear double quantum coherence is four times as sensitive to the effects of field gradients as single quantum coherence (Kay and Prestegard, 1986). In addition, for n coupled protons, the n-quantum transition is not subject to dipolar couplings, thus allowing an increase in the possible observation time owing to decreased relaxation. The attenuation of multiple quantum coherence requires a smaller gradient strength compared to the same degree of attenuation of single quantum coherence and thus introducing fewer eddy current effects. *Vice versa*, smaller diffusion coefficients can be distinguished using multiple-quantum coherence with the same gradient strength as for single quantum coherence, which is especially important for the application to macromolecules (Dingley et al., 1997). The use of double quantum coherence requires coupled spin systems with well-resolved one-quantum transitions which can be differentially excited to produce multi-quantum coherence. For the Stejskal and Tanner pulse sequence, in the case of free of free diffusion, the echo signal attenuation due to diffusion can be written as:

$$E(q,\Delta) = \exp\left[-f(\gamma)G^2\delta^2 D\left(\Delta - \frac{\delta}{3}\right)\right]$$
5-52

For normal single quantum coherence experiments as discussed above $f(\gamma)$ is given by:

$$f(\gamma) = \gamma^2$$
5-53

For homonuclear multiple quantum coherence experiments $f(\gamma)$ is given by:

$$f(\gamma) = (n\gamma)^2$$
5-54

For heteronuclear double quantum coherence with an *IS* spin system, where *I* is the observed nucleus $f(\gamma)$ is given by:

$$f(\gamma) = \left(\frac{\gamma_I + \gamma_S}{\gamma_S} \right)^2 \gamma_I \qquad\qquad 5\text{-}55$$

In **Figure 13** an example of a multiple quantum STE pulse sequence is presented (Kay and Prestegard, 1986).
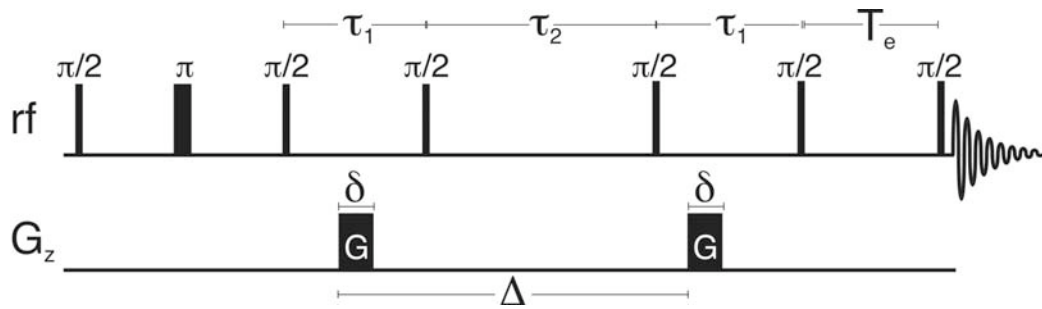
Figure 13: Multiple Quantum PFG sequence based on the stimulated echo experiment. The phase cycling can be found elsewhere (Kay and Prestegard, 1986).

5.3.6 Diffusion Ordered Spectroscopy: DOSY

As discussed in the previous chapters, the implementation of transport ordered NMR spectroscopy is possible because information about translational motion can be encoded in NMR data by the use of pulsed field gradient experiments. The principle idea of DOSY is analogous to conventional 2D NMR spectroscopy: The incrementation of an experimental variable that modulates the detected signal which can be transformed with respect to that variable to produce a "spectrum"; however, in this case related to molecular motion and thus related to overall molecular properties. Diffusion spectra can be obtained by incrementing the "gradient effect" which is reflected in the value of $q = f(\gamma)G\delta$ and in the separation of the gradient pulses Δ. Transformation of the signal amplitude with respect to q^2 yields the second dimension of a spectrum which correlates the chemical shift with its diffusion coefficient – a so-called DOSY spectrum (Johnson, 1994; Johnson, 1999).

The ability of DOSY to provide accurate distributions of diffusion coefficients for the construction of 2D and 3D DOSY displays depends on the inversion of data sets that consist of NMR spectra collected with predetermined values of $q^2\Delta'$, where Δ' is defined as $\Delta' = (\Delta + \delta\varepsilon)$ and ε depends on the shape of the gradient pulse. FT-PFG NMR experiments of the STE or BPP-STE types yield 2D data sets of the form,

$$S(q,v_m) = \sum_n A_n(v_m)\exp\left[-D_n q^2 \Delta'\right]$$

5-56

where $A_n(v_m)$ is the amplitude of the 1D NMR spectrum of the nth diffusing species when G is small but not zero, as (section 5.3.1) the echo amplitude will depend on the chemical shift for vanishing gradient strength, unless bipolar gradient pairs are used, and D_n is the associated diffusion coefficient. For the case that a polydisperse component contributes to the peak at frequency v_m, a continuum of values of D must be considered and the 1D data set describing the signal attenuation of this peak must then be described by

$$S(s) = \int_0^\infty a(\lambda)\exp(-\lambda s)d\lambda$$

5-57

where $\lambda = D$ and $s = q^2\Delta'$. Therefore the signal decay $S(s)$ is the Laplace transform of the Laplace spectrum of diffusion coefficients $a(\lambda)$. Considering a discrete system, consisting of a small set of decay constants λ_ι, $a(\lambda)$ is the weighted sum of delta functions and equation 5-56 is obtained.

However, unlike the Fourier transformation of an FID, yielding a unique NMR spectrum, the inverse Laplace transformation (ILT) of the decay function $S(s)$ is often not unique and a number of reasonable assumptions have to made, with the goal of

producing the most likely spectrum of diffusion coefficients. The problem is illustrated in **Figure 14**: at the top an FID is converted by Fourier transformation into a unique NMR spectrum, including line broadening due to exponential T_2 relaxation of the FID. At the bottom the PFG-NMR signal decay consists of two components with different diffusion coefficients and amplitude. For an ideal transformation like FT, the signal decay would yield the Laplace spectrum of delta functions, illustrated on the right side and the inverse transformation would exist. However, in fact there is no perfect and unique transformation and in the presence of noise it might be impossible to obtain any useful spectrum. Thus the dotted curves in the diffusion spectrum indicate an experimental error in an approximate transformation. However, many different software packages exist in literature, such as DISCRETE (Provencher, 1976), SPLMOD (Provencher and Vogel, 1983), CONTIN (Morris and Johnson, 1993) or MaxEnt (Delsuc and Malliavin, 1998), to deal with that problem and a review of available software is given by Johnson (Johnson, 1999).
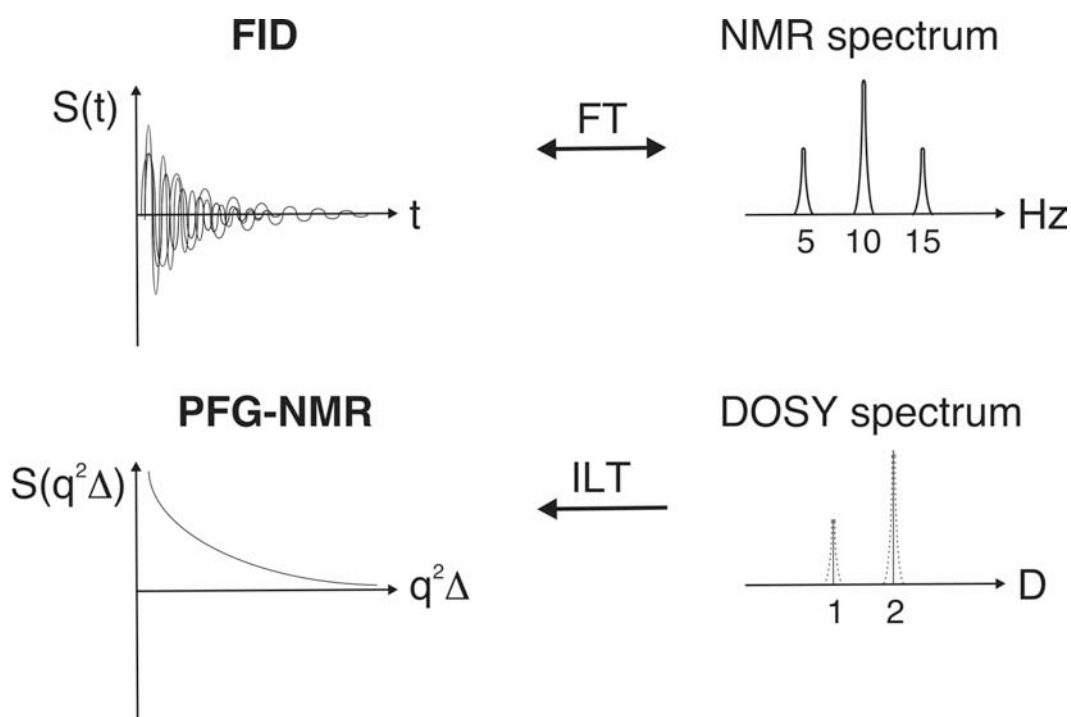
Figure 14: Illustration of the reversible Fourier transformation of an FID, producing a NMR spectrum, and the inverse Laplace transformation of a biexponential decay representing different diffusion coefficients. The dotted lines in the DOSY spectrum indicate experimental errors in using an approximate transformation.

The initial motivation for the development of 2D and 3D DOSY spectra was to obtain an additional dispersion of NMR peaks in order to avoid overlap in the analysis

of compound mixtures, spreading cross-peaks in a conventional 1D or 2D NMR spectrum according to the diffusion coefficient of the various species in the additional dimension. Therefore the third or second axis in a DOSY spectrum is not a chemical shift, but a diffusion dimension. The creation of 3D DOSY requires the design of a combined 2D NMR and PFG-NMR pulse sequence and the development of algorithms which group data points to cross-peaks and relate them versus their q^2-dependent data sets in the third dimension. Any 2D NMR experiment can be used in this combination and **Figure 15** illustrates a 3D COSY-DOSY (Wu et al., 1996). However, HMQC- (Bax et al., 1983) or HSQC-DOSY (Bodenhausen and Ruben, 1980), TOCSY-DOSY (Jerschow and Müller, 1996), and NOESY-DOSY (Gozansky and Gorenstein, 1996) have been reported in literature.
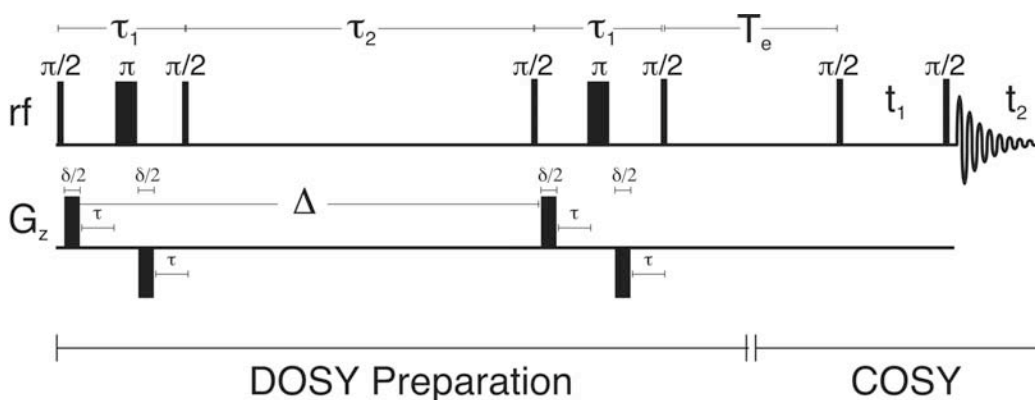
Figure 15: Pulse sequence for the 3D DOSY-COSY experiment. The phase cycling is given in (Wu et al., 1996).

5.3.7 Gradient Calibration

Prior to the determination of absolute diffusion coefficients, the gradient strength has to be determined quite accurately as the gradient is squared in calculating the diffusion coefficient (equation 5-36). There are several methods to calibrate the gradient strength, although it should be noted that relative diffusion coefficients between different species can be measured without any calibration.

5.3.7.1 *Theoretical Coil Calculation*

Theoretically the applied gradient strength can be calculated from the known dimensions, the geometry, the number of turns of wire in the coil and the applied current. This method gives an estimate of the gradient strength with an error of < 10%. Interactions with nearby metal in the probe and non-ideal gradient pulse generation are major problems in this method in order to determine a more accurate gradient

strength. The gradient strength which is delivered by the design of contemporary Bruker Biospin high-resolution probes is as follows:

- High resolution *Z*-gradient probe: 5.35 G/(cmA)
- *Z*-gradient of a high resolution *XYZ*-gradient probe: 6.50 G/(cmA)
- *X* and *Y* gradients of a high resolution *XYZ*-gradient probe: 5.00 G/(cmA)

5.3.7.2 *Standard Sample with Known Diffusion Coefficient*

The most simple, but nevertheless very accurate method of calibrating the gradient strength is to use a standard sample of known diffusion coefficient. Ideally, a reference compound should have a diffusion coefficient and T_2 relaxation rates that are not strongly temperature dependent. Usually one will use a water sample for the calibration, in practice a so-called "doped water" sample is best, which is 1% H_2O in D_2O with 0.1 g/L $GdCl_3$. Because the sample is practically D_2O whereas H_2O only serves as a tracer, the proton diffusion coefficient is that of D_2O at a given temperature. The temperature control and calibration is of importance and can be achieved by measuring a calibration curve, using methanol as standard sample. Diffusion coefficients of water at different temperature and with different concentration of D_2O are listed in literature (Holz et al., 2000). Other useful values are given in table 1, a comprehensive listing can be found in (Holz and Weingärtner, 1991).

Table 1: Reference compounds and their diffusion coefficient at 298 K for the calibration of the gradient strength

Compound	Diffusion Coefficient cm^2/s	Reference
H_2O	2.30×10^{-5}	(Mills, 1973)
H_2O in D_2O (trace)	1.902×10^{-5}	(Holz and Weingärtner, 1991)
H_2O in D_2O (10 mol%)	1.935×10^{-5}	(Holz and Weingärtner, 1991)
D_2O	1.872×10^{-5}	(Mills, 1973)
Alanine	7.3×10^{-6}	Bruker Almanac
Sucrose	2.9×10^{-6}	Bruker Almanac
Glucose	3.6×10^{-6}	Bruker Almanac

In addition, systematic investigations of isotope effects on water diffusion have yielded accurate values for the limiting self-diffusion coefficient of H_2O / D_2O mixtures (Weingärtner, 1984). From these data and others one can describe the self-diffusion coefficient of H_2O in H_2O / D_2O mixtures with the equation,

$$10^9 D = 2.30 - 0.4652 \cdot x_D + 0.0672 \cdot x_D^2 \qquad\qquad 5\text{-}58$$

where x_D is the mol fraction of the deuterons and D is given in m^2s^{-1}.

From the measured diffusion coefficient a gradient calibration constant (GCC) can be calculated to adjust the experimental determined values to the theoretically values by:

$$GCC_{new} = \sqrt{\frac{D_{measured}}{D_{Literature}}} \cdot GCC_{old} \qquad\qquad 5\text{-}59$$

This procedure can also be applied in the calibration of a three-axis gradient system in a similar way.

If the reference sample conditions (e.g. delays, pulse lengths, gradient strength etc.) are used in the subsequent experiment, this calibration procedure has the advantage of including all non-ideal gradient behavior.

5.3.7.3 *Shape Analysis of the Spin Echo*

It is possible to calculate the gradient strength using the echo shape from a sample of known geometry. The most commonly used sample geometry is a cylinder of length l and radius r (**Figure 16**), e.g., a well-defined sample in a Shigemi tube. A one-dimensional image of the sample can be obtained by the Hahn spin-echo experiment (Hahn, 1950) which consists of a read gradient of strength G during acquisition. In the absence of gradients there is no spatial dependence of the resonance frequency, however, in the presence of gradients there is. Therefore the observed spin-echo and its spectrum will reflect the gradient and the shape of the sample. For a gradient $G = G_x$ across the sample it can be calculated (Price, 1998) that the FID will have a characteristic Bessel function profile, whereas the FID acquired in the presence of a gradient $G = G_z$ along the sample has a sinc function profile. The Fourier transforms of both FIDs are more informative, they are rapidly oscillating functions with sharp frequency cutoffs in both cases. The power spectrum makes the cutoff easier to visualize. The width (Δv) of the spectrum in Hz is given by (**Figure 16**):

$$\text{For } G = G_x : \ \Delta v = \frac{\gamma \cdot G \cdot r}{2\pi}$$

$$5\text{-}60$$

$$\text{For } G = G_z : \ \Delta v = \frac{\gamma \cdot G \cdot l}{2\pi}$$

A detailed deviation of these equations, including the functions describing the FID profiles and their Fourier transformations, is given by Price et al. (Price, 1998) Experimentally, the FIDs are often much more truncated and therefore the oscillation artifacts in the transformed spectra are more pronounced. The higher the number of points used for the transformation, the sharper are the edges of the spectrum.

From equations 5-60 it is evident that even modest gradient pulses require a substantial receiver bandwidth to acquire the signal. In addition, if the gradient strength is increased, more scans are necessary to obtain a sufficient signal-to-noise ratio. The gradient strength can than be calculated by analyzing the shape of the respective FID (Murday, 1973; Price, 1998) or more conveniently by analyzing the Fourier transformed spectrum. Typically, this method is most useful in case where the gradient is along the cylinder axis G_z, since the shape of this image is ideally rectangular. The FID is recorded in the presence of a number of different gradient strengths and for calibration, the bandwidth Δv is plotted against the applied current. Ideally the final result will have an error of $< 5\%$. An advantage of this method is that the sample diffusion coefficient is not involved in the calibration, as long as the dimensions of the NMR tube holding the sample are accurately known. However, this method is only applicable to rather small gradients, since the gradient broadened spectrum rapidly exceeds the maximum bandwidth of the receiver.
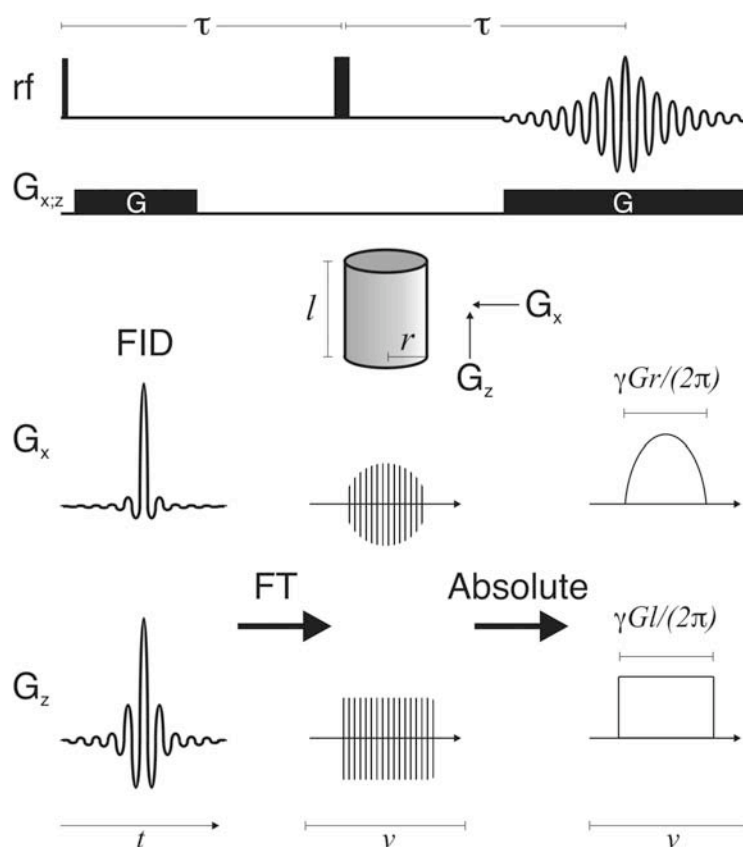
Figure 16: Schematic diagram of the cylindrical sample of length l and radius r used for the determination of the gradient strength G by a one-dimensional image of the sample using the Hahn spin-echo sequence. In the upper row a gradient G_x is aligned in the x direction of the sample, and in the lower row along the z direction.

5.4   Hydrodynamic Calculations

5.4.1   Types of Bead Modeling

The hydrodynamic behavior of macromolecules in solution can be calculated and simulated starting from the atom coordinates of a given molecule. The macromolecular properties which can be obtained from hydrodynamic calculations are translational diffusion coefficients, D_t, rotational diffusion coefficients, D_r, relaxation times, τ, the intrinsic viscosity, η, and the radius of gyration R_g. From one or more properties it is possible to determine the size and shape of proteins, their anisometry (axial ratio) and the degree of hydration. This classical approach was already described in section 5.1.

The problem of predicting the hydrodynamic properties of rigid macromolecules of arbitrarily complex shape was first studied by Bloomfield et al. (Bloomfield et al., 1967). They worked within the Kirkwood-Risenman theory of macromolecular hydrodynamics (Kirkwood, 1954) which had been applied to very simple models of identical elements (Riseman and Kirkwood, 1950) and devised procedures for calculating the properties for models composed of equal or unequal spherical elements, so-called beads. In general, a bead model is any representation of a particle as an array of spherical frictional elements. Individual Stokes-law friction coefficients are assigned to each element, and the hydrodynamic interaction between them is accounted for by means of the Oseen tensors. However, there are different strategies for building the hydrodynamic bead model.

The bead model, in strict sense, is a method in which the particle is represented by as few beads as possible, identical or different, and occupying approximately the volume of the particle. The array of beads should have an envelope that resembles the shape of the particle as closely as possible (**Figure 17**; **A**). A classical example of bead modeling is Bloomfield´s model for T2 bacteriophage (Bloomfield et al., 1967b).

As it is only the surface of a solid particle where hydrodynamic friction occurs, Filson and Bloomfield proposed the shell model (Filson and Bloomfield, 1967), in which the particle surface is represented by a shell-like assemblage of many small, identical frictional elements. Hydrodynamic calculations can be performed by varying the elements radius and the result can be extrapolated to an elements radius of zero and an infinite number of elements (**Figure 17**; **B**).

In an alternative modeling method, the volume occupied by the particle is filled by elements (beads) (**Figure 17**; **C**) which is the accurate procedure for predicting properties that depend specifically on the particles volume. Such is the case for the angular dependence of radiation (light or x-ray) scattering from the particle (Muller et

al., 1983). However, for simple hydrodynamic calculations this model is inefficient because it includes internal beads that do not contribute to friction. Thus with a decreasing elements radius the computer time grows dramatically due to the high number of beads needed. In the case where these innermost beads are simply removed (a bead is considered internal when it is completely surrounded by other beads) and the particles surface is represented in a rough manner, which becomes better by decreasing the elements radius, one speaks of a rough-shell model (**Figure 17**; **D**).
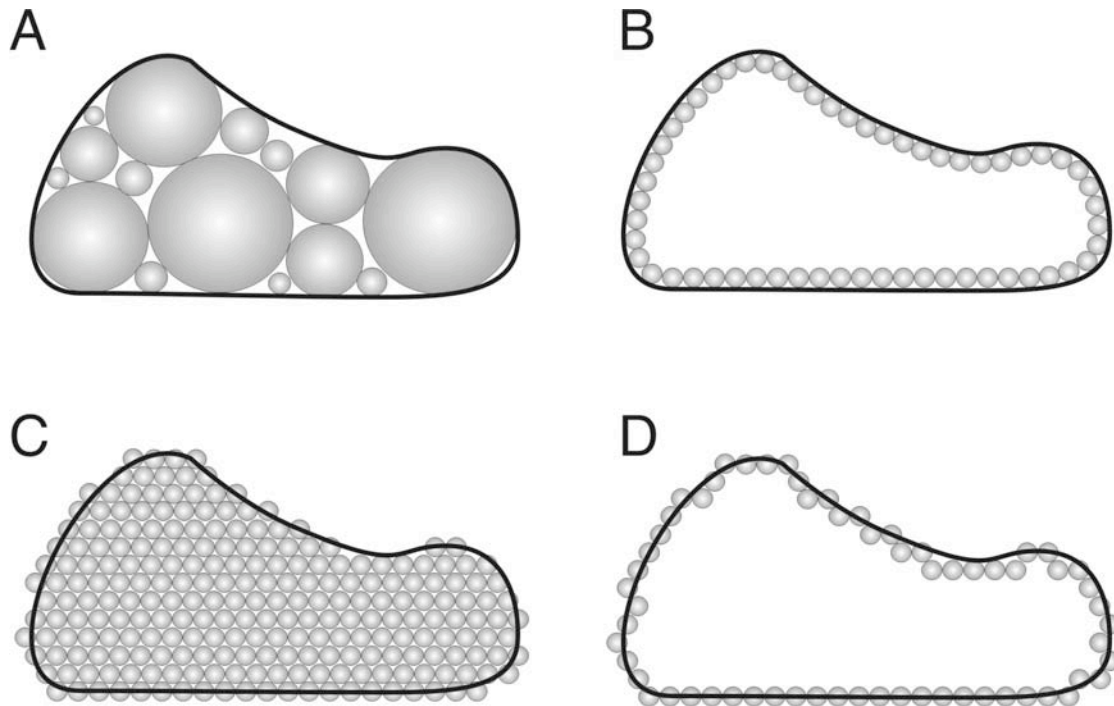
Figure 17 Two-dimensional analogies of various model types. (A) Bead model in strict sense; (B) Shell model; (C) Filling model; (D) Rough-shell model.

A review of these different modeling approaches and their advantages and disadvantages is given by García de la Torre et al. (García de la Torre et al., 2000a).

5.4.2 Rigid-Body Theory

For a particle of arbitrary shape, the hydrodynamic resistance is expressed by means of a 6 x 6 friction tensor, Ξ, and the Brownian diffusion is expressed similarly by a 6 x 6 diffusion matrix, $\mathbf{D}$. The friction forces must be compensated for by the averaged kinetic energy of the particle and thus according to the Einstein equation (equation 5-10), the diffusion tensor is inverse proportional to the friction tensor (García de la Torre, 1989):

$$\mathbf{D} = \frac{kT}{\Xi} \qquad\qquad 5\text{-}61$$

Both Ξ and $\mathbf{D}$ can be partitioned into 3 x 3 blocks, which correspond to translation (tt), rotation (rr) and a translation-rotation coupling (tr), so that

$$\mathbf{D} = \begin{pmatrix} \mathbf{D}_{tt} & \mathbf{D}_{tr}^{T} \\ \mathbf{D}_{tr} & \mathbf{D}_{rr} \end{pmatrix} = kT \begin{pmatrix} \Xi_{tt} & \Xi_{tr}^{T} \\ \Xi_{tr} & \Xi_{rr} \end{pmatrix}^{-1} \qquad\qquad 5\text{-}62$$

The superscript T indicates transposition. The degree of translation-rotation coupling is, however, rather small (Beloborodov et al., 1998), so that the translational and rotational diffusion coefficients and their friction coefficients are given by

$$D_t = \frac{1}{3} Tr(\mathbf{D}_{tt}) \text{ and } f_t = \frac{kT}{D_t} \qquad\qquad 5\text{-}63$$

$$D_r = \frac{1}{3} Tr(\mathbf{D}_{rr}) \text{ and } f_r = \frac{kT}{D_r} \qquad\qquad 5\text{-}64$$

where Tr is the trace of the tensor. The rotational relaxation times are calculated from the eigenvalues of the $\mathbf{D}_{rr}$ tensor and yield:

$$\tau_h = \frac{1}{6D_r} = \frac{1}{2Tr(\mathbf{D}_{rr})} = \frac{f_r}{6kT} \qquad\qquad 5\text{-}65$$

The theory of hydrodynamic properties of bead models provides a procedure to calculate the components of Ξ. A key concept in bead model hydrodynamics is the hydrodynamic interaction effect. The frictional force experienced by a bead depends not only on its relative velocity and its friction coefficient, but also on the frictional forces that act at all the other beads. From the Cartesian coordinates and radii of the N beads in the model, the 3 x 3 hydrodynamic interaction tensors between beads i and j, $\mathbf{T}_{ij}(i, j = 1, ..., N)$ are calculated. This tensor was originally formulated by Oseen as

$$\mathbf{T}_{ij} = \left(8\pi\eta_0 R_{ij}\right)^{-1}\left(\mathbf{I} + \mathbf{R}_{ij}\mathbf{R}_{ij}/\mathbf{R}_{ij}^2\right) \qquad\qquad 5\text{-}66$$

where $\mathbf{I}$ is the unit tensor and $\mathbf{R}_{ij}$ is the distance vector between elements i and j. This equation was later generalized for elements of different radii (García de la Torre and Bloomfield, 1977).

After calculating the tensors $\mathbf{T}_{ij}$ a $3N$ x $3N$ supermatrix $\mathbf{B}$ is composed of

$$\mathbf{B}_{ij} = \mathbf{T}_{ij} \text{ if } i \neq j$$

$$\mathbf{B}_{ij} = \left(\frac{1}{\varsigma_i} \right)\mathbf{I} \quad \text{where } \varsigma_i = 6\pi\eta_0\sigma_i \qquad \text{5-67}$$

where ζ_i is the Stokes law friction coefficient of bead i, with radius σ_i and η_0 being the viscosity of the solvent. The inverted supermatrix $\mathbf{C} = \mathbf{B}^{-1}$ gives in turn the components of Ξ as:

$$\Xi_{tt} = \sum_i \sum_j \mathbf{C}_{ij}$$

$$\Xi_{tr} = \sum_i \sum_j \mathbf{U}_i \cdot \mathbf{C}_{ij} \qquad \text{5-68}$$

$$\Xi_{rr} = \sum_i \sum_j \mathbf{U}_i \cdot \mathbf{C}_{ij} \cdot \mathbf{U}_j$$

where

$$\mathbf{U}_i = \begin{pmatrix} 0 & -z_i & y_i \\ z_i & 0 & -x_i \\ -y_i & x_i & 0 \end{pmatrix} \qquad \text{5-69}$$

The rotational friction calculated from equation 5-68 and the intrinsic viscosities are erroneous when applied to models in which one or a few spheres have a size close to the whole particle. Actually, for a single sphere, these equations give the erroneous results of $\Xi_{rr}{}^{uncorr} = 0$ and $\eta^{uncorr} = 0$ instead of the Einstein expressions. Therefore, a simple additive correction for the rotational friction tensor was developed – the so-called volume correction (García de la Torre and Rodes, 1983):

$$\Xi_{rr} = \Xi_{rr}^{uncorr} + 6\eta_0 V \mathbf{I} \qquad \text{5-70}$$

where $\mathbf{I}$ is the unitary tensor, η_0 is the solvent viscosity and V is the volume of the model, equal to

$$V = \frac{4}{3}\pi \sum_{i=1}^{N} \sigma_i^3 \qquad \text{5-71}$$

where σ_i are the individual bead radii.

A similar correction is possible for the intrinsic viscosity (García de la Torre et al., 1994):

$$\eta = \frac{5N_A V}{2M} + \eta^{uncorr} \qquad \text{5-72}$$

where V is again the total volume of the whole bead model, understood as the sum of the volumes of all the spheres.

6 Biochemical and Structural Studies on p53, p63 and Bcl-xL

6.1 Introduction

6.1.1 Overview of Apoptosis

Apoptosis is a key component in the development and maintenance of tissues within multicellular organisms, providing a tightly regulated and selective mechanism for the deletion of superfluous, infected, mutated or aged cells. It is involved in embryogenesis, metamorphosis, endocrine-dependent tissue atrophy, normal tissue turnover, and a variety of pathologic conditions resulting from its dysregulation (Ellis et al., 1991; Nicholson, 1996; Steller, 1995; Thompson, 1995). Apoptotic cells are characterized by a condensation of chromatin, reduction in nuclear size, DNA cleavage, shrinkage and breakdown of the cell into membrane-bound apoptotic bodies (Hacker, 2000; Wyllie, 1980). These bodies are subsequently phagocytosed by other cells.

In contrast, the process of necrosis is characterized by a swelling of cells and their organelles due to the disruption of the plasma membrane. The cell contents then leak out leading to inflammation and ultimately cell disintegration. Thus, normal apoptosis is a programmed and highly regulated physiological response in which cell death occurs without collateral damage to surrounding tissues (**Figure 18**).

A diverse group of signals induce apoptosis, including UV or γ-irradiation, oxidative damage, growth factor withdrawal, or the cytokines TNF-α and TGF-β. As tumor cells show a disturbed equilibrium between proliferation and apoptosis, conventional cancer therapies take advantage of this apoptotic mechanism by employing ionizing radiation or chemotherapeutic drugs to damage DNA and induce selective apoptosis of rapidly growing cells. However, killing of tumor cells is often incomplete, allowing tumor recurrence and progression toward more aggressive phenotypes.

Therefore an understanding of the molecular mechanisms by which cells undergo and induce apoptosis is an important goal for the development of new tumor therapies.
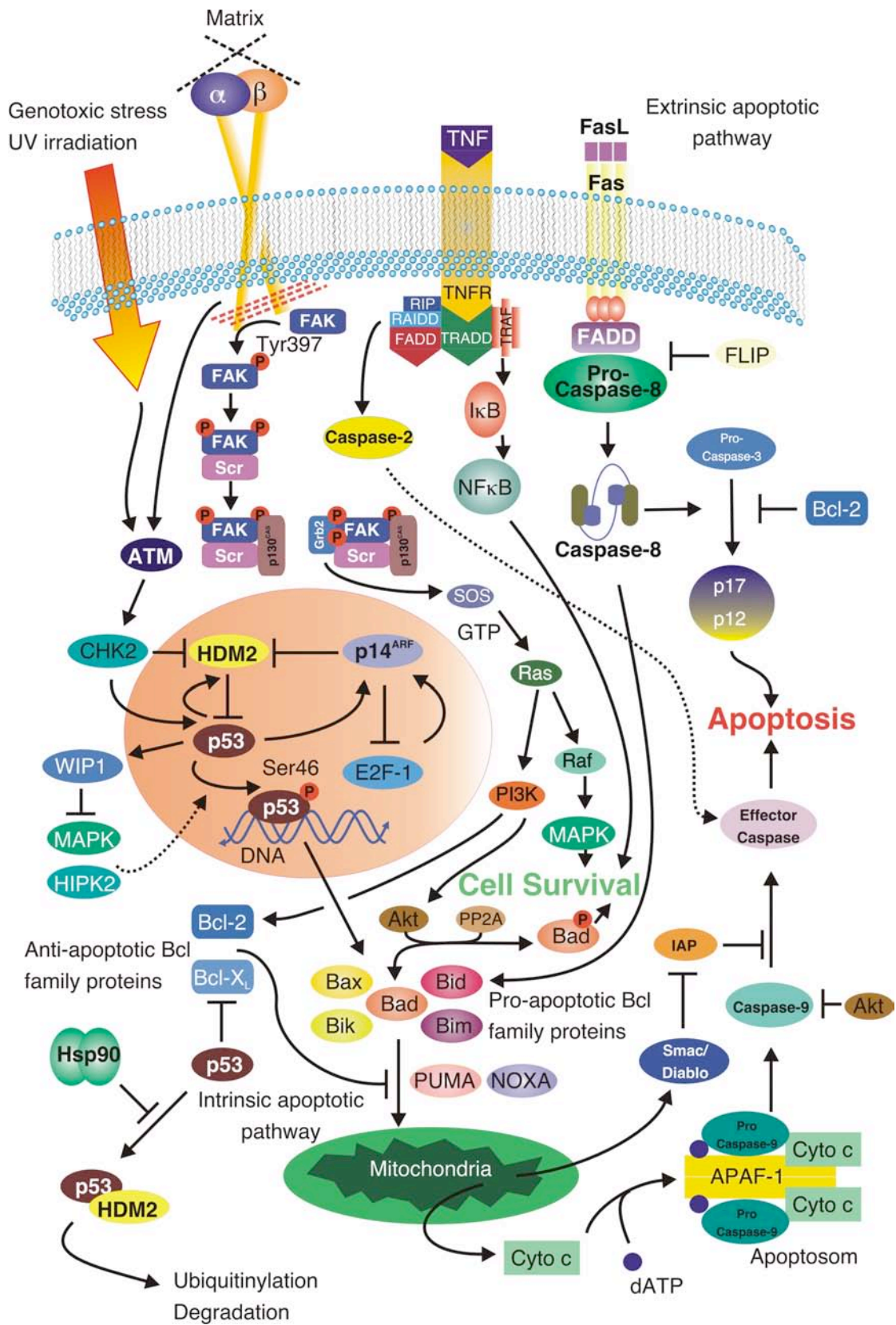
Figure 18: Schematic overview of selected signal pathways regulating apoptosis.

Apoptosis is regulated by two principle pathways (**Figure 18**). First, the intrinsic pathway emerges from the mitochondria as a result of radiation, redox damages from detoxification and drugs that cause direct DNA damage. The central role of mitochondria in the control of apoptosis has been firmly established (Ravagnan et al., 2002). Wang and co-workers demonstrated that the release of cytochrome *c* from the mitochondria into the cytosol by a membrane permeability transition pore complex results in the activation of caspases which are cystein proteases and the central regulators of apoptosis. This culminates in the formation of the large apoptosome protein complex, consisting of procaspase 9, APAF 1 and cytochrome *c*, and the activation of effector caspases (caspases 3, 6 and 7). Once these caspases are activated they cleave cytoskeletal and nuclear proteins and execute apoptosis (Los et al., 1999).

The intrinsic pathway overlaps with the extrinsic pathway in many regulatory as well as downstream effector molecules. The extrinsic pathway is activated by ligand binding to specific death receptors on the cell surface and has a central role in physiologically programmed cell death as well as immune system diseases. The prototypical receptor pair in the large tumor necrosis receptor superfamily is the Fas-FasL system (Varfolomeev and Ashkenazi, 2004). Death receptors possess an extracellular death domain (DD). Binding of the ligand to the receptor stimulates the oligomerization of the receptors through their death domains. The receptors then recruit and bind to other DD-containing proteins such as adaptor proteins, FADD and RAIDD. These adaptors then bind a proximal caspase forming a death inducing signaling complex and activate the caspase proteolytic cascade via clustering (Ashkenazi and Dixit, 1998; Schulze-Osthoff et al., 1998).

Apoptosis is both positively and negatively regulated. Numerous factors are involved in the induction of apoptosis and many other factors have been identified that prevent cell death. Anti-apoptotic ligands include growth factors and cytokines, many of which induce anti-apoptotic Bcl-2 family members. These Bcl-2 family members protect the integrity of the mitochondrial membrane, thus preventing cytochrome *c* release and caspase activation (Ravagnan et al., 2002). Apoptosis inhibitors include factors that inhibit caspases directly or prevent their activation. Akt, a serine/threonine protein kinase, is an important anti-apoptotic factor in a number of ways, e.g., it inhibits the pro-apoptotic Bcl-2 family member, Bad, and directly inhibits caspase 9. The TNF-α receptor has anti-apoptotic effects in addition to its pro-apoptotic effects, as it can activate the transcription factor NF-κB, which then induces the expression of IAP, an inhibitor of caspases 3, 7 and 9. Integrines are receptors that mediate attachment and spreading on extracellular matrix (ECM) proteins and transduce signals that regulate cell growth, survival and gene expression (Gottschalk and

Kessler, 2002; Ridley et al., 2003), which involves cascades of phosphorylation reactions catalyzed by intracellular phosphokinases (Berman et al., 2003). It was found that integrine aggregation into clusters not only induces focal adhesion assembly involving cytoskeletal proteins (DeMali et al., 2003; Hayashi et al., 2002), but also causes concentrating of phosphokinases in these structures (Vuori, 1998). In fact, FAK plays a key role in the transduction of integrine mediated signaling. Concentrating FAK in focal adhesions causes autophosphorylation at tyrosine 397. The phosphorylated Tyr397 binds to the SH2 domain of the protooncoprotein c-Src. Binding to FAK activates Src kinase which catalyzes phosphorylation of other tyrosine residues in FAK, followed by the binding of the adaptor proteins p130[Cas] and Grb2 to the FAK-Src complex. Grb2 activates the SOS enzyme which catalyzes guanine nucleotide exchange in Ras, resulting in the active Ras-GTP, which again triggers the MAP-kinase cascade, including sequential activation of the serine/threonine type kinases Raf, MEKK and Erk. The latter one is translocated into the nucleus where it phosphorylates and activates genes responsible for proliferation (Kopnin, 2000). Pathways of integrine-mediated proliferation and growth-factor regulated proliferation converge at the stage of Grb2-Ras. However, a lack in integrine signaling leads to activation of ATM / CHK2 kinases which phosphorylate p53 at serines15 and 20 (Hirao et al., 2000) and therefore block binding to MDM2, resulting in p53 stabilization by preventing MDM2-mediated degradation of p53 (Stommel et al., 1999). Additionally, increased levels of p14/p19[Arf] have been observed, inhibiting the action of MDM2 (Lewis et al., 2002). Increased p53 results in transactivation of a number of targets including genes that control cell growth, cell arrest, apoptosis or DNA repair (Hofseth et al., 2004).

Overall, apoptosis is a complex process involving numerous factors operating in multiple pathways that must be carefully regulated for the proper growth and development of an organism. Failure to properly execute apoptosis can lead to a number of disease states such as cancer, Parkinson´s disease and AIDS (Ghibelli et al., 2003; Genini et al., 2001; Roumier et al., 2003).

6.1.2 p53: Function, Structure and Family Members

6.1.2.1   p53 Function

The intense interest in p53 has generated up to now (August 2004) more than 32500 publications. This fascination with p53 stems from its contribution to tumor suppression, and the fact that loss of normal p53 function by mutation occurs in almost all cancers of both mice and men (Hollstein et al., 1991; Vousden, 2003; Vousden, 2002). The p53 protein is a transcription factor regulating many cellular processes, including cell cycle, DNA repair, apoptosis, angiogenesis, senescence, and thus acts as major tumor suppressor (Levine, 1997; May and May, 1999; Vogelstein et al., 2000; Vousden, 2003; Vousden, 2000). p53 induces growth arrest or cell death upon DNA damage or other genotoxic stress and prevents an accumulation of mutated genome (Rubbi and Milner, 2003). In addition, p53 can transcription-independently induce mitochondrial membrane permeabilization by complexation with the anti-apoptotic proteins Bcl-xL and Bcl-2 (Mihara and Moll, 2003) (**Figure 18**).

    The major mechanisms through which p53 function is controlled are regulation of p53 protein levels, control of the localization and modulation of the activity of p53 by several post-translational modifications (Appella and Anderson, 2001). p53 levels are kept low in most normally proliferating cells by rapid protein degradation. One of the key components regulating p53 stability is MDM2, a protein that functions as a ubiquitin ligase for p53, mediating ubiquitination of p53 and allowing it to be recognized and degradated by the proteasome (Ashcroft et al., 1999; Kubbutat et al., 1997; Lohrum et al., 2003) (**Figure 18**). MDM2-mediated p53 degradation depends on the interaction between the two proteins, where a small domain in the N-terminus of p53 directly contacts a deep hydrophobic cleft in the N-terminus of MDM2 (Kussie et al., 1996). This interaction can be impaired by phosphorylation of p53 within the MDM2 binding region which occurs in response to stress such as DNA damage, mediated at least in part by the kinases Chk1, Chk2, ATM and ATR that are activated by genotoxic damage (Appella and Anderson, 2001). MDM2 again is a transcriptional target of p53, and the importance of this feedback loop, in which p53 controls the expression of its own regulator was demonstrated by the generation of mice in which MDM2 is deleted (Luna et al., 1995). Nuclear localization of MDM2 and enhanced degradation of p53 is associated with MDM2 phosphorylation by the serine/threonine kinase Akt (Zhou et al., 2002). Similarly, phosphorylation in the C-terminus of p53 by protein kinase C enhances the ubiquitination and degradation of p53 in unstressed cells (Chernov et al., 2001), whereas a dephosphorylation of these sites is seen in

response to ionizing radiation and may thus contribute to the DNA damage-induced stabilization of p53 (Waterman et al., 1998). Furthermore the stability and cellular localization of p53 is modulated by the interaction with molecular chaperones. Chaperones play a key role in the recognition and folding of nascent polypeptide chains (Chapter 7) and maintain an active conformation of the substrate (Buchner, 1996). Thus mutant p53 are complexed by the Hsp90/Hsp70 chaperone system yielding a p53 stabilization (Stebbins et al., 1997).

Since one of the key function of p53 is the regulation of transcription, its localization to the nucleus plays an important role. Active transport of p53 towards the nucleus by dynein and the microtubule network has been described (Buey et al., 2004; Giannakakou et al., 2002; Giannakakou et al., 2000; O'Brate and Giannakakou, 2003). *Vice versa*, the p53 protein contains two nuclear export sequences, one in the C-terminal oligomerization domain (Stommel et al., 1999), and the other in the N-terminal MDM2 binding region (Zhang and Xiong, 2001). The ability of p53 to be exported is greatly enhanced by the action of MDM2 (Freedman and Levine, 1999), although export is not absolutely dependent on the presence of MDM2. Nuclear export is not only required for p53 degradation, but also for transcription-independent aspects of the apoptotic response (Marchenko et al., 2000). Mutations that abolish the trans-activating function of p53 or prevent its nuclear localization do not suppress its apoptogenic potential. In addition, p53 can promote cell death even in the presence of transcriptional or translational inhibitors. Mitochondria play a central role in apoptotic events through the release of pro-apoptotic factors such as cytochrome *c* and others and it has been shown recently that p53 can localize to the mitochondria and directly interact with anti-apoptotic Bcl-xL and Bcl-2 proteins, allowing permeabilization of the outer mitochondrial membrane, leading to the release of cytochrome *c* (Mihara and Moll, 2003).

In addition to p53 stability and localization its regulation is augmented by the modulation of the ability of p53 to bind to DNA and interact with components of the transcriptional machinery. A well-established model based on *in vitro* studies suggests that p53 can exist in two conformations that are latent or active for DNA binding. The C-terminal region of the p53 protein has been described as playing a key role in regulating p53´s DNA binding activity through an allosteric mechanism (Hupp and Lane, 1994); however, recent structural analysis of full-length and C-terminally truncated p53 proteins showed no evidence for changes in conformation when comparing latent or active p53 and therefore question the allosteric model (Ayed et al., 2001). Yet, the C-terminal region of p53 contains several covalent and non-covalent modifications (Jayaraman and Prives, 1999) which could modulate its DNA

binding affinity. Particularly interesting are phosphorylation (Lu et al., 2001), acetylation (Gu and Roeder, 1997; Gu et al., 1997) and sumoylation (Rodriguez et al., 1999).

The cellular response to p53 is dependent on many factors, such as cell type, cell environment and whether the cell has sustained oncogenetic alterations. The abilities of p53 to induce cell cycle arrest or apoptosis appear to be separable functions (Rowan et al., 1996), depending on which target genes it chooses to activate. p53 interacts with numerous proteins that enhance its transcriptional activity, in particular with transcriptional co-activators like ASPP and JMK, targeting p53 to induce apoptosis. In addition, phosphorylation of p53 on serine 46 is required to induce the expression of apoptotic genes, although the responsible kinase is not yet definitely identified. The regulation of p53 serine 46 phosphorylation is carried out by proteins which are themselves the product of p53-inducible genes, such as p53DINP1 which activates the phosphorylation at serine 46 (Okamura et al., 2001) and Wip1, which functions as a phosphatase to inhibit p53´s apoptotic function (Takekawa et al., 2000) (**Figure 19**).
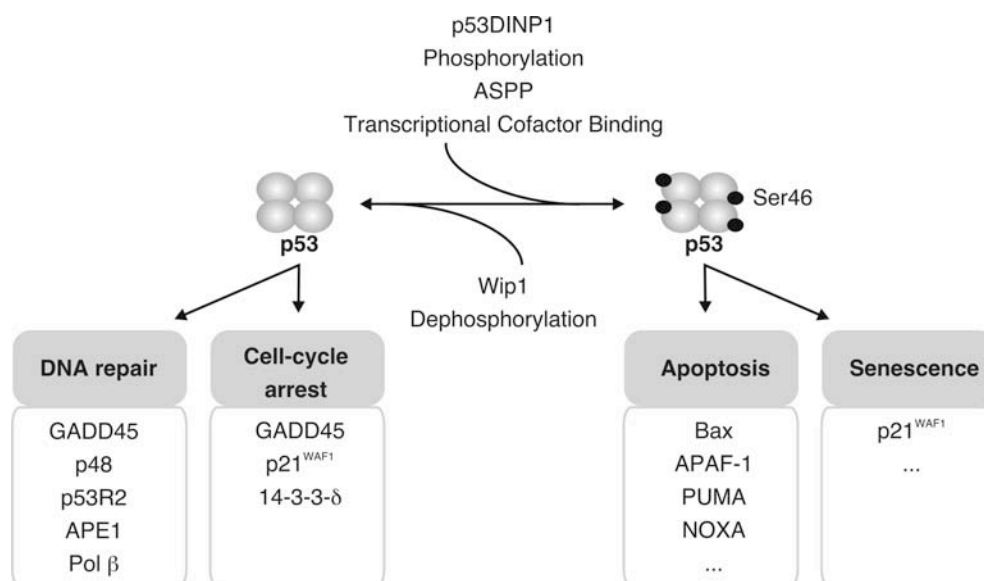
Figure 19: Downstream targets of p53. Following activation by post-translational modifications including phosphorylation, acetylation and others, p53 plays a key role in protection of cells from stress through transcriptional activation of genes involved in cell-cycle checkpoints, apoptosis, DNA repair or cellular senescence. Adapted from (Hofseth et al., 2004).

6.1.2.2   p53 Structure and Domain Organization

Human p53 (393 amino acids) consists of four functional domains (Arrowsmith and Morin, 1996). The N-terminal transactivation domain, a highly conserved DNA binding domain (residues 102-292) (Cho et al., 1994) which is most critical to its tumor-suppressing function (Hollstein et al., 1991); a tetramerization domain (residues 323-356) which forms D_2 symmetric dimers of dimers (Cho et al., 1994; Clore et al., 1995; Clore et al., 1994; Lee et al., 1994); finally a regulatory C-terminal region of about 30 residues (Wang and Prives, 1995) (**Figure 20**).

As a transcription factor, p53 possesses a transcription activation domain (TAD) which, together with the proline-rich domain, forms the N-terminal domain (NTD) (Fields and Jang, 1990; Raycroft et al., 1990) **Figure 20**. The transcription activation domain (aa 1-63) (Fields and Jang, 1990) consists of two contiguous transcriptional transactivation subdomains (Fields and Jang, 1990; Raycroft et al., 1990; Soussi and May, 1996). The adjacent proline-rich SH3-target subdomain (aa 62-91) contains five copies of the amino acid sequence *PXXP* which contributes to the apoptotic functions of p53 (Sakamuro et al., 1997; Venot et al., 1998; Walker and Levine, 1996). The transcription activation functions of p53 are modulated through binding of several target molecules in the TAD. The regulation of gene expression requires the binding of TATA-associated factors to p53 (Lu and Levine, 1995; Thut et al., 1995). Negative regulators of transcription such as MDM2 bind within the same site in the N-terminal domain (Böttger et al., 1997; Kussie et al., 1996; Uesugi and Verdine, 1999). Experiments using p53 peptides and MDM2-fragments revealed several key residues in the TAD (F19, L22, W23) which contribute to the binding of MDM2 (Böttger et al., 1996; Chen et al., 1993; Kussie et al., 1996; Lin et al., 1994; Picksley et al., 1994). The resulting interactions rely on van der Waals contacts and steric complementarities between the hydrophobic cleft of MDM2 and p53 (Chen et al., 1993; Kane et al., 2000; Kussie et al., 1996). A previous study on the structural organization of full length p53 suggested that the N-terminal domain of p53 contains unstructured regions in its native state (Bell et al., 2002).

Most of the mutations of p53 involved in cancer were found within the core DNA-binding domain, (Hollstein et al., 1991) most frequently at six hot-spots of mutation: R175, G245, R248, R249, R273 and R282 (Hainaut et al., 1997; Hollstein et al., 1994). An understanding of these mutations is provided by the crystal structure of the DNA-bound p53 core domain consisting of a four-stranded and a five-stranded antiparallel β sheet, a loop-sheet-helix (LSH) motif, comprising loop L1 (residues 113-123), a three-stranded β sheet and helix H2 (residues 278-286). The loop L2 (residues 164-194), which is interrupted by the short helix H1, and the loop L3

(residues 237-250) are stabilized by a single coordinated zinc atom (Cho et al., 1994; Zhao et al., 2001). The hot-spot residues R273 within the H2 helix of the LSH motif and R248 within the L3 loop contact directly the major and minor groove of bound DNA. The four remaining hot-spot mutations are involved in stabilizing the surrounding structure *via* a hydrogen bond network. Thus so far there are two major classes of mutations preventing DNA binding: (i) Mutations involved in direct DNA contact and (ii) mutations destabilizing the structural integrity of the DNA binding region (R249S, G245S) and/or causing a globally denatured p53 structure (R175H, C242S, V143A) – both will result in a loss of DNA binding affinity (Bullock and Fersht, 2001). Furthermore both classes of mutations can be distinguished by two polyclonal antibodies: first PAb1620, which binds preferentially to the p53 DBD wild-type conformation including solvent-exposed "DNA contact mutants" which do not alter its native conformation, and second PAb240, which binds specifically to non-natively folded "structural mutants" of p53 DBD (Milner, 1995).
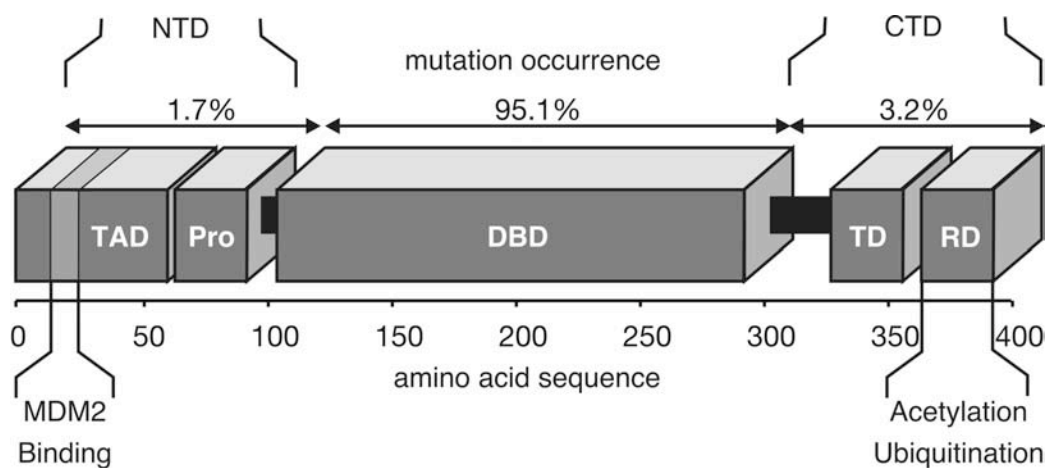
Figure 20: Domain organization of p53. The N-terminal domain (NTD) domain is natively unfolded and consists of a transactivation domain (TAD), interacting with components of the transcriptional machinery and including the MDM2 binding site and a SH2 binding region (Pro). Within the central DNA binding domain (DBD) most of the oncogenetic mutations occur: 95.1%. The C-terminal domain of p53 consists of an oligomerization domain (TD) and a regulatory domain (RD) for phosphorylation, acetylation, ubiquitination and sumoylation. In addition the nuclear localization and export sequences are located in the C-terminal domain. The mutation rate is shown above the sequence (Hollstein et al., 1994).

At present no structural information is known about full-length p53 and its tetrameric organization bound to DNA. However, in solution DNA binding of the p53 core domain is highly cooperative (Klein et al., 2001a; Klein et al., 2001b; McLure and Lee, 1998; McLure and Lee, 1999; Nagaich et al., 1999) as demonstrated by four

p53 DBDs binding to a 20mer DNA consensus sequence, and two p53 DBDs binding to a 12mer DNA recognition sequence, even when excess DNA is present in solution (Rippin et al., 2002). However, binding of p53 DBD to a pentameric single quarter-site (CON1x5) could not be detected, as confirmed by electrophoretic shift assays, FCS and NMR measurements (Klein et al., 2001a; Klein et al., 2001b). This cooperativity in DNA binding of p53, even in the absence of the tetramerization domain, implicates the existence of core-core interactions and therefore several reports discuss inter-domain contacts in p53 (Arrowsmith and Morin, 1996; Cho et al., 1994; Lebrun et al., 2001; Nagaich et al., 1999; Prives, 1994; Zhao et al., 2001) based on modeling of the individual structures of p53 DBD (Cho et al., 1994; Zhao et al., 2001) and the tetramerization domain (Clore et al., 1995; Lebrun et al., 2001; Lee et al., 1994). However, interactions observed in the crystal structures of the p53 DNA binding domains are most likely packing artifacts (Cho et al., 1994; Zhao et al., 2001).
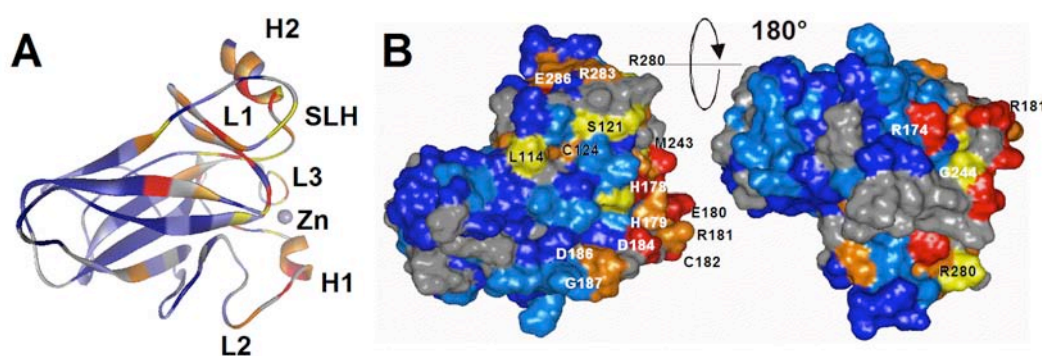
Figure 21: Chemical shift perturbation mapping of p53 DBD upon titration with CON2x5 oligonucleotide. **(a)** Ribbon representation of p53 DBD, loops, helices and the bound Zn are indicated. **(b)** Connolly surface representation in front and back view. Residues labeled in yellow are missing after complexation; residues in red are shifted by more than a linewidth; residues in orange and light blue are shifted by more than half a linewidth or less than half a linewidth, respectively. Residues in blue are not shifted upon complexation and gray residues have not been assigned. Adapted from (Klein et al., 2001b) and (Klein, 2002).

NMR spectroscopic titration experiments (Klein et al., 2001b; Rippin et al., 2002) of ^{15}N-labelled p53 DBD with CON2x5 oligonucleotide provided an indication for the existence of such a dimerization interface (**Figure 21**). The chemical shift perturbations of backbone ^{15}N,^{1}H chemical shifts of p53 DBD upon addition of DNA are localized near the helix H2, which is the binding interface for DNA. In addition chemical shift changes are particularly pronounced for the H1 helix, located near the zinc coordination site. Interestingly this second H1 perturbation site does not participate in DNA binding directly (Cho et al., 1994) and could possibly be involved

in protein-protein intermolecular interactions, forming the necessary dimerization interface in order to bind DNA cooperatively (Klein et al., 2001b; Rippin et al., 2002). In contrast, as NMR chemical shift changes may be caused by intermolecular contacts and/or induced conformational rearrangements as well (Dehner et al., 2003), these observed chemical shift changes within the H1 helix might be also due to a translated effect (e.g. *via* the bound zinc atom) from the DNA binding interface and not caused by protein-protein interactions as proposed by Rippin et al. (Klein et al., 2001b; Rippin et al., 2002).

6.1.2.3 *p53 Family Members: p63, p73*

Twenty years after the discovery of the p53 tumor suppressor gene, Kaghad and coworkers reported in 1997 their discovery of p73 (Kaghad et al., 1997), followed by the cloning of p63 (Yang et al., 1998), giving rise to the notion of a p53 family of genes. All members of the p53 family possess a modular architecture with an N-terminal transactivation domain, a 60 % homologous DNA-binding domain followed by a tetramerization domain and a regulatory C-terminal domain. On the basis of structural similarity it was expected that their function would be similar to p53, regarding its tumor suppression, induction of apoptosis and cell cycle control (Maisse et al., 2003).
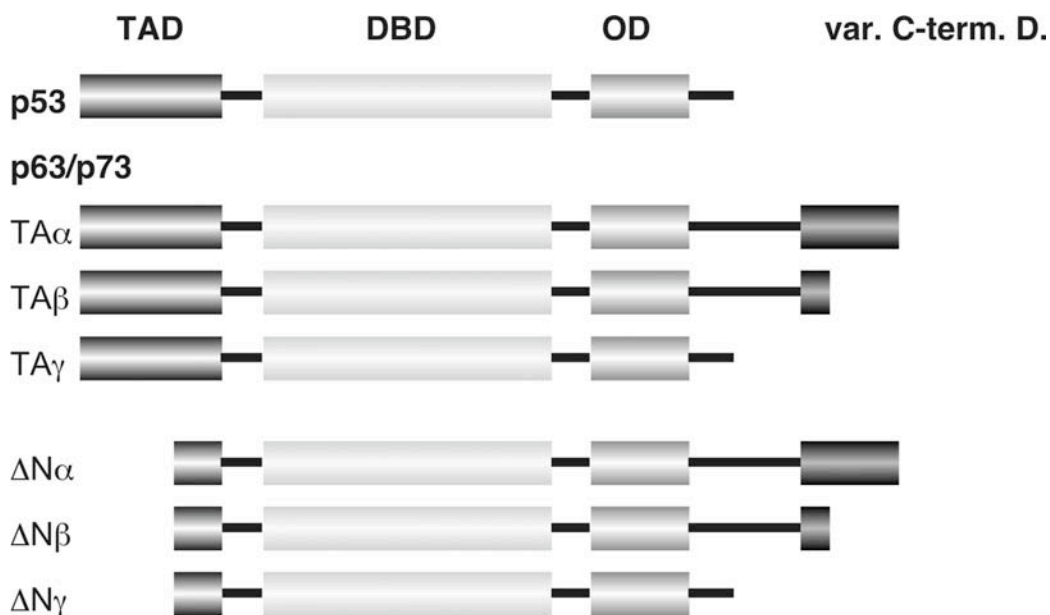
Figure 22: Domain organization of p53, p63 and p73. In contrast to p53, p63 and p73 exist in two different isoforms, the pro-apoptotic TAp63/p73 and the anti-apoptotic DNp63/p73. Each of the isoforms undergo alternative splicing resulting in different isotypes. TAD: transactivation domain; DBD: DNA binding domain; OD: oligomerization domain.

However, p53 has a single promoter with three conserved domains (TAD, DBD and OD) (**Figure 22**), whereas p63 and p73 each have two promotors, resulting in two different types of isoforms (Trink et al., 1998; Yang et al., 2002): The pro-apoptotic TAp73 / TAp63 which contain the N-terminal transactivation domain and the anti-apoptotic ΔNp73 / ΔNp63 which lack a part of the transactivation domain. In addition, both of the genes undergo alternative mRNA splicing at the C-terminal end, giving rise to three isotypes each (Fillippovich et al., 2001; Kaghad et al., 1997; Yang et al., 1998) (**Figure 22**). Several isotypes of p63 and p73 have a conserved C-terminal extension of about 100 residues which is not present in p53. The structure of this region has been determined (Chi et al., 1999; Wang et al., 2001) and the α forms of each of the proteins contain sterile α motifs (SAM domain) which might be a protein-protein interaction module with a regulatory function (Schultz et al., 1997).
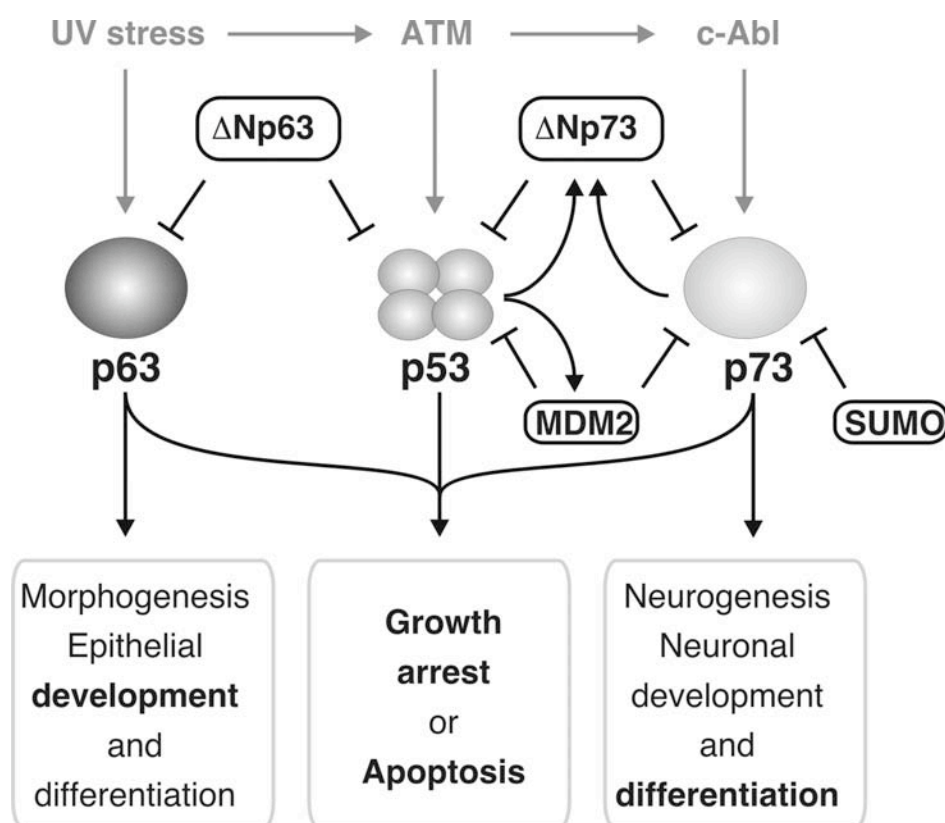
Figure 23: Schematic p53 family members pathway. Besides specific developmental and physiological functions, p63 and p73 interplay with p53 to achieve growth arrest and apoptotic functions. In addition two negative feedback loops controlling p53 and p73 by MDM2 and ΔNp73 keep cell death under tight control. Adapted from (Bénard et al., 2003) and (Maisse et al., 2003).

Recently two studies have indicated that first, TAp73 directly activates the transcription of ΔNp73 by binding to the two p73-specific target elements located on the distal promoter P2 (Nakagawa et al., 2002) and second, p53 induces ΔNp73 both on the mRNA and protein levels, as a result of a direct activation of the P2 promoter (Kartasheva et al., 2002). The ΔNp73α isoform associates with TAp73α/β and p53, as assessed by immunoprecipitation assay, and inhibits their pro-apoptotic transactivation activities.

The negative feedback loop of TAp73 and p53 by their ΔNp73 target provides a novel autoregulatory system modulating cell survival and death (Nakagawa et al., 2003). Another remarkable distinctive property of the p53 homologs concerns their degradation by MDM2. In contrast to the short-lived p53 protein which is regulated by MDM2-mediated ubiquitination and degradation by the proteasome, the p73α and β proteins bind to MDM2 through their N-terminal domain, but this interaction leads to inactivation of transcription and apoptosis and does not result in p73 degradation by the proteasome (Balint et al., 1999; Lu et al., 1999). So far, p73 ubiquitination has not been demonstrated, but a p73α modified by covalent linking with SUMO-1 (small ubiquitin-like modifier) was found to be more rapidly degradated by the proteasome than the unmodified p73 (Minty et al., 2000). In addition it was found that MDM2 does not bind to p63, revealing another difference between p53, p73 and p63 (Dohn et al., 2001). Therefore one can distinguish two negative feedback loops controlling p53 and TAp73, namely the MDM2 and ΔNp73 loops, keeping the cell death trigger under tight control (**Figure 23**).

TAp63/p73 proteins overexpressed in human cells also bind to p53 DNA target sequences, transactivate p53-responsive genes, and thereby induce cell cycle arrest, differentiation and apoptosis in a p53-like manner (Kaghad et al., 1997; Yang et al., 1998). However, transcriptional activity alters with p63/p73 splice variants, and in contrast to p53 null-mice, p63/p73 null-mice do not develop any spontaneous tumors. Yet a recent study showed that in response to various stresses (drug, γ-irradiation), p53 requires p73, as well as p63, to activate promoters of apoptotic target genes such as Bax or Noxa (Flores et al., 2002), supporting a crucial role for the homologues in p53-mediated apoptosis.

6.1.3 Bcl-2 Family Members, Structure and Function

The proteins of the Bcl-2 family (B-cell lymphoma 2) are important regulators of programmed cell death (**Figure 18**). To date, over 25 Bcl-2 family members have been identified (Cory and Adams, 2002; Reed, 2000). These can be divided into two major classes: those that inhibit apoptosis and those that promote apoptosis. Homeostasis is maintained by controlling the relative amount of active pro- and anti-apoptotic family members along with tissue-specific patterns of expression. The pro-survival class of Bcl-2 family members has been divided into two subclasses based on the presence of one or more "Bcl-2 homology" (BH) regions (Adams and Cory, 1998). Four of these regions (BH1-4) have been identified and each Bcl-2 member contains at least one of them (**Figure 24**).
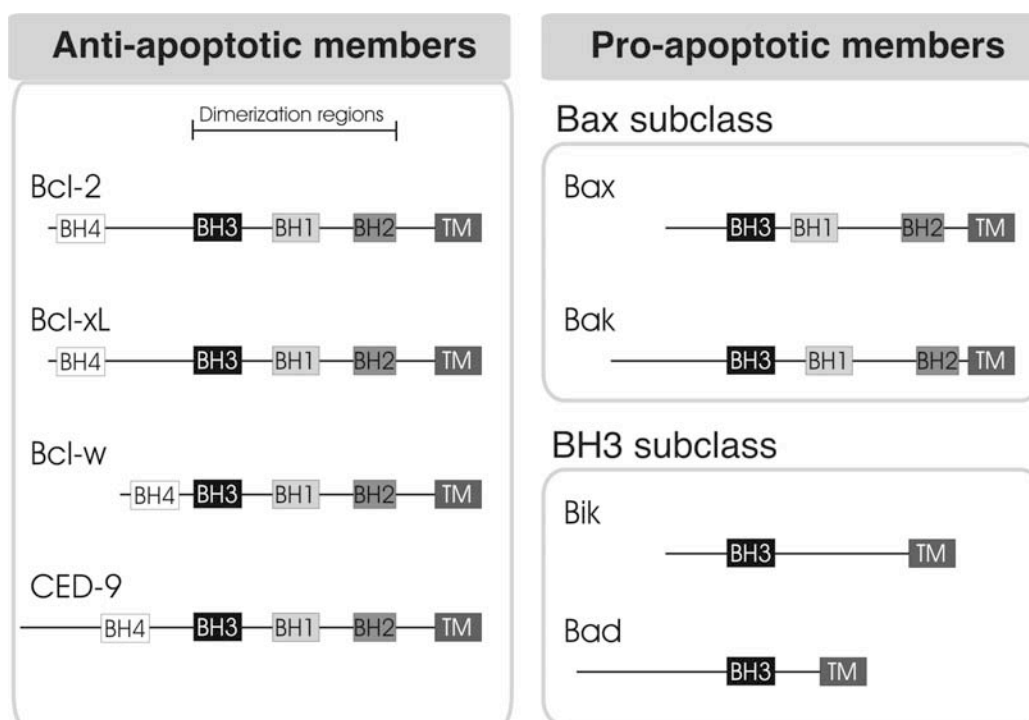
Figure 24: Domain organization of Bcl-2 family members. Indicated are Bcl homology regions (BH) and the transmembrane region (TM) of pro- and anti-apoptotic Bcl-2 members.

Several members of the anti-apoptotic subclass, namely Bcl-2, Bcl-xL, Bcl-w and Ced-9 protein from *C. elegans*, possess all four BH regions. For the pro-apoptotic proteins, members of the Bax subclass possess sequence homology for the BH1, BH2 and BH3 regions while members of the BH3 subclass have strong sequence homology only in the BH3 region (**Figure 24**). Mutagenesis studies indicate that the BH1, BH2

and BH3 regions strongly influence homo and hetero dimerization of these proteins (Adams and Cory, 1998). Furthermore, pro-apoptotic family members that contain BH1 and BH2 regions, such as Bax or Bak, can promote apoptosis through their interactions with the mitochondrial membrane; as only the BH3 region is responsible for mediating the interaction with anti-apoptotic family members and thus for promoting apoptosis, the interaction with the mitochondrial membrane is an independent activity (Chittenden et al., 1995).

Peptides derived from the BH3 regions of pro-apoptotic Bcl-2 family members can bind to anti-apoptotic family members such as Bcl-xL and modulate Bcl-2 regulated apoptotic pathways in living cells. The carboxy-terminal hydrophobic domain (**Figure 24**) found in many Bcl-2 family members is responsible for membrane localization (Green and Reed, 1998), while the patterns of membrane localization differ between anti- and pro-apoptotic proteins. It has been shown that Bcl-2 resides on the cytoplasmatic face of the outer mitochondrial membrane. This membrane anchoring may play a key role in modulating and regulating the release of cytochrome *c* from the intermembrane space which is the rate-limiting step in the initiation of apoptosis and is inhibited by Bcl-2 and Bcl-xL. In contrast, the pro-apoptotic family members are found in the cytosol and only upon activation they are localized to the mitochondrial membrane (Wolter et al., 1997). Either Bax or Bak is required for mitochondrial membrane permeabilization resulting in the induction of apoptosis (Wei et al., 2001). The precise mechanism of membrane permeabilization is still unclear (Kroemer and Reed, 2000), but it probably involves a variety of different mitochondrial proteins and is often accompanied by a conformational change of Bax or Bak, together with their full insertion into the mitochondrial membranes as homo-oligomerized multimers, resulting in the formation of large protein-permeable pores (Kroemer, 2003). The BH3-only proteins cannot induce apoptosis in the absence of Bax or Bak (Cory and Adams, 2002) and therefore must act upstream in the pathway. The eight or more mammalian BH3 proteins, such as Bid, Bad, Noxa or Puma, are widely expressed and presumably allow a more refined control over cell death by binding their anti-apoptotic relatives and blocking their protective interactions with Bax or Bcl-xL. In addition, Bcl-2 family members have been recently identified as cytoplasmic targets of p53 by Moll and colleagues (Mihara and Moll, 2003). p53 binding to anti-apoptotic Bcl-2 and Bcl-xL allows the p53 protein to interact directly with the mitochondria and promote membrane permeabilization. This is likely to occur through disrupting the interaction of Bcl-xL or Bcl-2 with pro-apoptotic family members and thus inhibiting their protective function. This is corroborated by the observation that recombinant p53 can induce the oligomerization of Bak and the

release of cytochrome *c* when added to purified mouse liver mitochondria in a reaction which is inhibited by an excess of Bcl-xL (Mihara and Moll, 2003). In a recent study of George and colleagues (Leu et al., 2004) they report that Bak might also be a principle target of p53. The interaction of p53 with Bak is suggested to liberate Bak from its interaction with the mitochondrial anti-apoptotic Bcl-2 protein. Molecular modeling and site-directed mutagenesis indicate that the interaction with Bcl-xL involves the central conserved DNA binding domain (Mihara and Moll, 2003); others report that this interaction relies on the p53 polyproline (PP) domain (residues 62-91). However, deletion mutant of p53, compromising the first 102 amino acids, and therefore lacking the DNA binding domain - is reported not to interact with Bcl-xL, but to trigger apoptosis through Bax.

Despite the sequence diversity among the Bcl-2 family members and the diversity of function, they have a remarkably similar fold. This fold consists of two central, predominantly hydrophobic α-helices surrounded by six or seven amphipathic α-helices (Muchmore et al., 1996). The overall topology of the Bcl-2 proteins is similar to that observed for the membrane translocation domain of the bacterial toxins such as diphtheria toxin, leading to experiments which showed that Bcl-xL and Bcl-2 can form pores in artificial membranes (Petros et al., 2004b). A predominantly hydrophobic groove is present on the surface of the anti-apoptotic family members. This groove is the binding site for peptides mimicking the BH3 region of various pro-apoptotic family members such as Bax and Bak and it forms the molecular basis for hetero-dimerization between members of the Bcl-2 family (Sattler et al., 1997).

6.2   Mutational Study on the Dimerization Interface of p53 DBD

6.2.1   Results

6.2.1.1   p53 DBD Dimerization Mutants

The H1 helix of p53 DBD contains several highly conserved solvent-exposed residues (**Figure 25** and **Figure 26**), which could be responsible for protein-protein interactions: H178, E180, R181, C182.
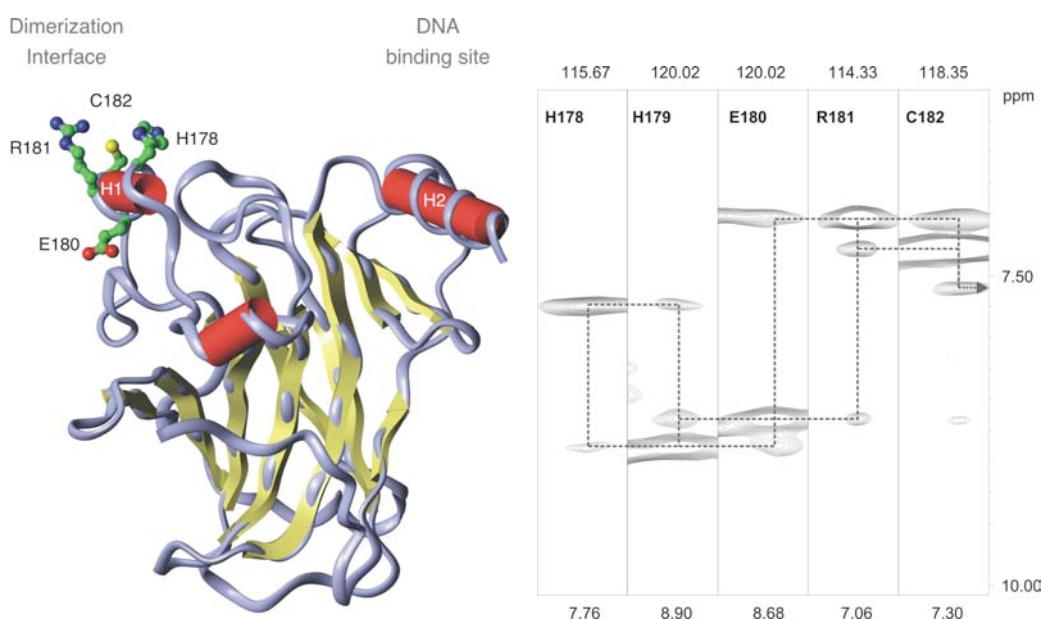
Figure 25: Left side: Ribbon diagram of p53 DBD. The solvent-exposed residues H178, E180, R181 and C182 within the H1 helix are shown as ball and sticks. The following p53 dimerization mutants were introduced by single-site mutagenesis: H178A, R181A, C182A, E180R, R181E, as well as one double site mutation: E180R/R181E. Right side: The helical geometry of the H1 helix in solution is supported by strong sequential HN-HN NOE signals observed in a 3D HNH NOESY spectrum.

The possible significance of these residues was studied by site-directed mutagenesis and the p53 DBD mutant ability to bind cooperatively to p53 consensus DNA via electrophoretic mobility shift assays and NMR spectroscopic diffusion measurements. The helical geometry of this designated H1 helix dimerization interface could be confirmed by strong sequential HN-HN NOE signals in a 3D HNH NOESY spectrum using p53 DBD assignment of Wong et al. (**Figure 25**). The following "dimerization mutations" were introduced by site-directed mutagenesis: H178A, R181A, C182A, E180R, R181E, as well as one double-site mutation: E180R/R181E. The mutant p53 DBD cDNA was introduced into the NdeI/XhoI site

of a modified pQE40 (Quiagen) expression vector (**Figure 27**) of the wild-type p53 DBD and mutant p53 DBD proteins were expressed in ^{15}N-labeled M9 minimal medium at 37 °C as inclusion bodies and refolded and purified (**Figure 29**) as described in Materials and Methods and in (Klein et al., 2004).
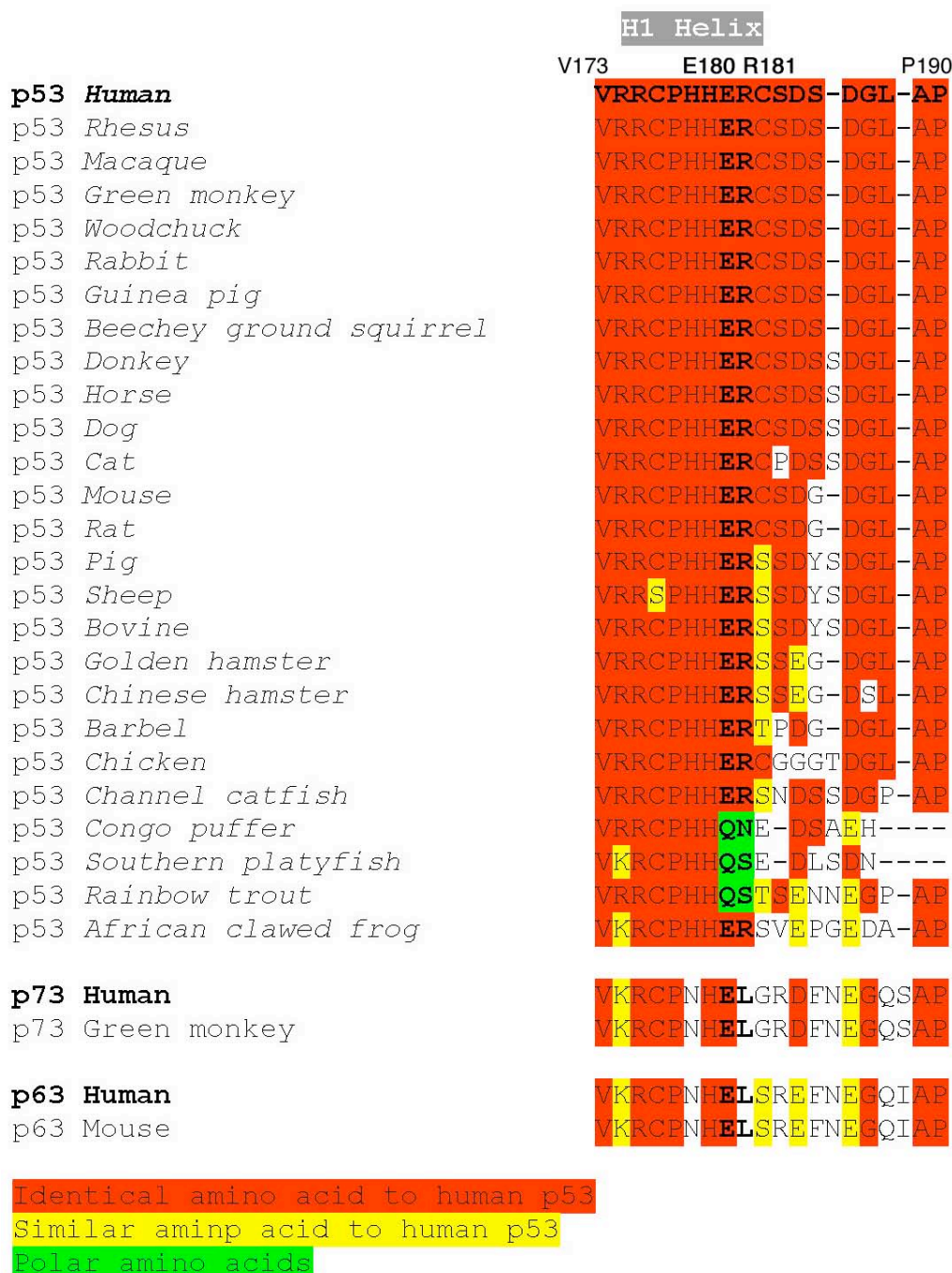
Figure 26: Primary structure alignment of the H1 helix region of p53 DBD and the homologs p63 and p73 DBDs. Sequence numbering for human p53 is indicated. Identical residues compared to human p53 are shown in red. Similar residues are given in yellow and polar residues are color coded in green.
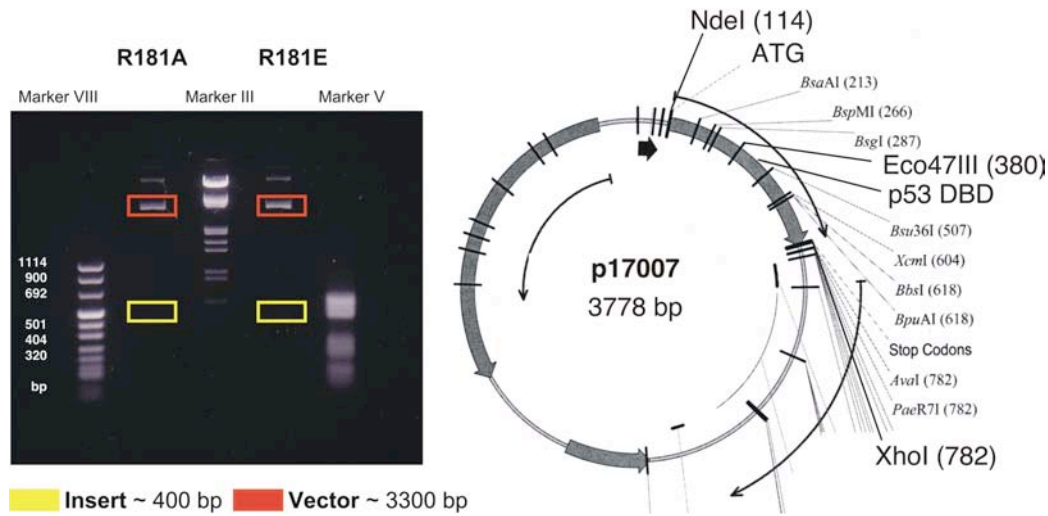
Figure 27: Mutant p53 cDNA was cloned into the NdeI/XhoI or Bsu36I restriction sites of a wild-type p53 DBD expression vector. Left side: DNA gel for the case of R181A and R181E mutation after restriction with NdeI/XhoI. Right side: Illustration of the of the expression vector used.
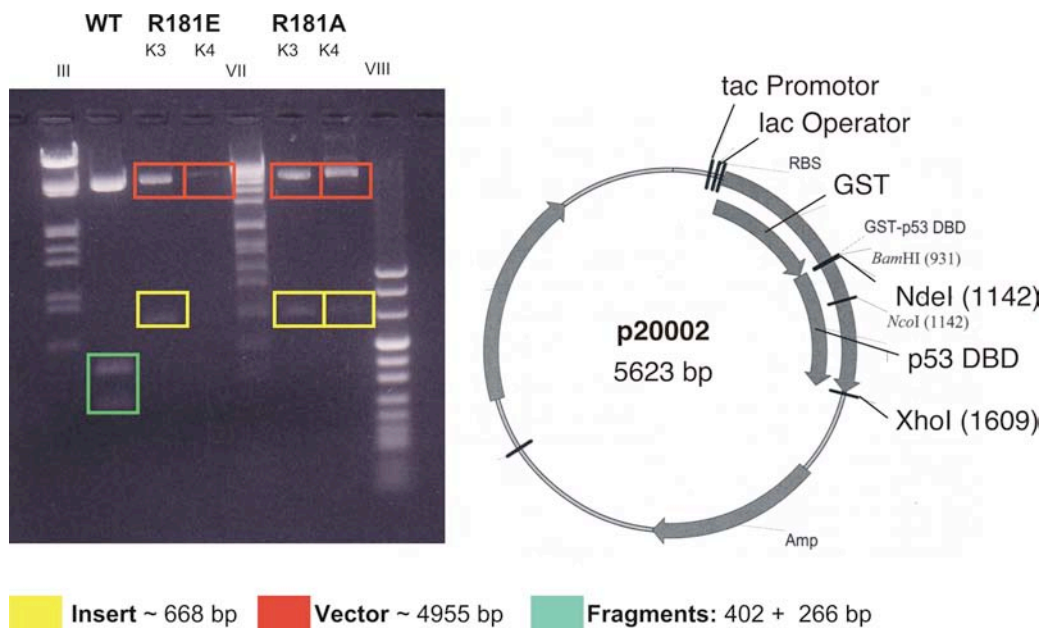
Figure 28: Mutant p53 cDNA was cloned into the NdeI/XhoI restriction sites of a wiled-type GST-p53 DBD fusion expression vector. Left side: DNA gel for the case of R181A and R181E mutation after restriction with NdeI/XhoI and Eco47III. Since the mutations R181E and R181A destroy the Eco47II site only two fragments (red and yellow) are seen upon digestion. Right side: Illustration of the of the GST-fusion protein expression vector used.

Furthermore three Ala mutations H178A, R181A, C182A and the R181E mutation were introduced into a GST-fusion plasmid yielding GST–mutant p53 DBD fusion proteins (**Figure 28**). Since the GST domain acts as an artificial dimerization domain, these constructs are supposed to enhance the cooperative DNA binding affinity as already studied for p63 DBD and GST–p63 DBD (Klein et al., 2001a). GST-fusion proteins were expressed as soluble proteins and purified by affinity chromatography and a final size exclusion step as described by Klein et al. (Klein et al., 2001a).
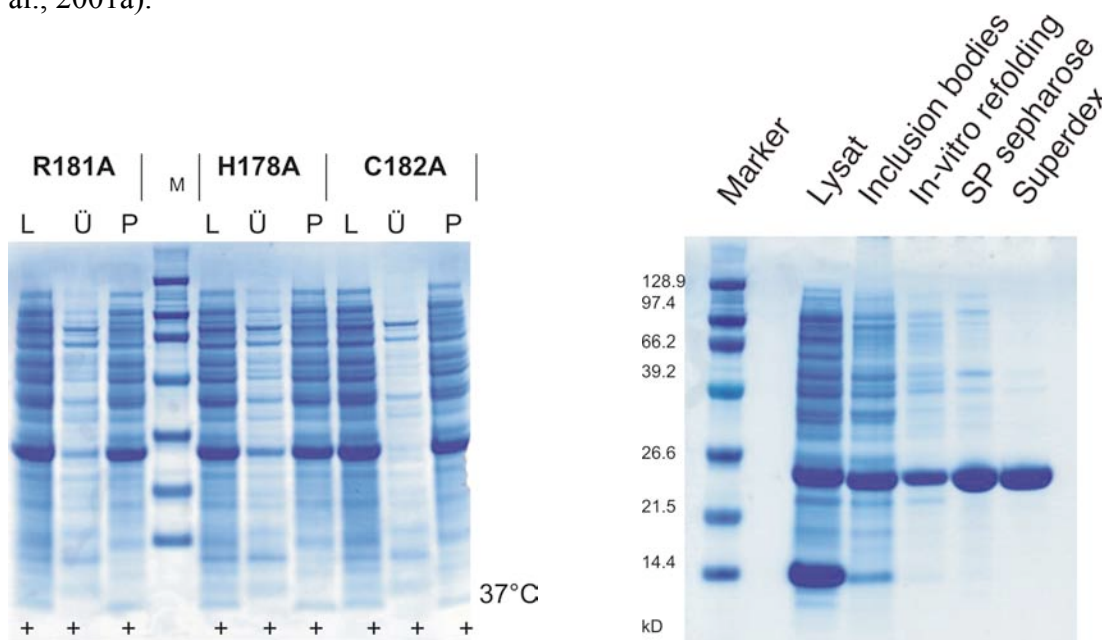
Figure 29: Left side, expression analysis of p53 DBD R181A, H178A and C182A mutants. L: Lysat, Ü: Soluble fraction, P: pellet, +: IPTG induction. All p53 DBD were expressed as inclusion bodies (pellet) and *in vitro* refolded and purified. **Right side**: Refolding of the p53 DBD H178A mutant shown are aliquots of the full lysat, after inclusion body preparation, after *in vitro* refolding and after each purification step.

6.2.1.1.1 p53 DBD Dimerization Mutants are Natively Folded

As solvent-exposed residues and their side chains do not have an impact on the structural integrity of p53 DBD all H1 helix dimerization mutants should be natively folded, which can be revealed by NMR spectroscopy. **Figure 30** shows an overlay of the ^{15}N HSQC spectra of all six discussed mutants and wild-type p53 DBD (Wong et al., 1999b). Major chemical shift differences can only be observed for signals of residues within or nearby the H1 helix due to different sequential amino acid residues. Residues further away are only slightly affected upon these mutations or not affected at all, allowing the conclusion that all dimerization mutants discussed here are natively folded.
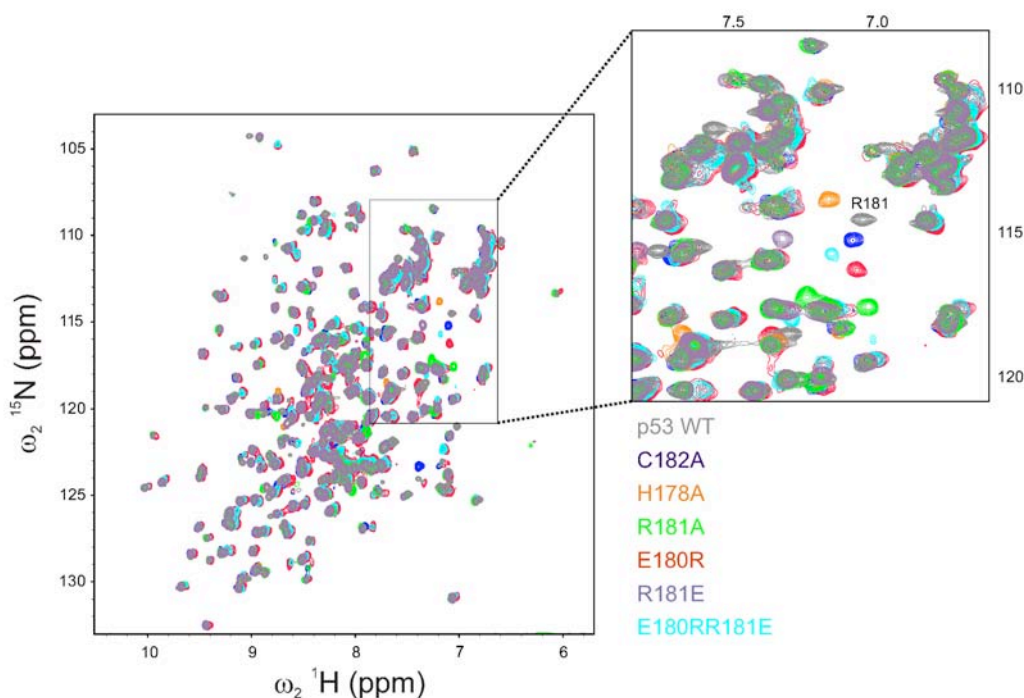
Figure 30: Superposition of the ^{15}N HSQC spectra of p53 DBD wild-type (grey) and the six mutated p53 DBDs. The enlarged section shows residue R181 within the H1 helix, which is perturbed due to different sequential amino acids. The overall signal dispersions in the spectra of the dimerization mutants are similar to the wild-type spectrum, leading to the conclusion that all dimerization mutants are natively folded.

Addition of a 0.5 M equivalent of a decameric consensus DNA oligonucleotide (CON2x5) to the [U-^{15}N]-labeled p53 DBD dimerization mutants resulted in shift changes and a strong line broadening (data not shown) in the protein ^{15}N, ^{1}H correlation spectrum which, is due to slow exchange processes in the micro- to millisecond range as has been observed for the p53 DBD wild-type DNA complex (Klein et al., 2001b; Rippin et al., 2002). Addition of DNase II to the p53 DBD dimerization mutants complex restored the original spectrum of the respective mutant, excluding protein degradation. All this indicates a "binding" of the CON2x5 oligonucleotide to all p53 DBD dimerization mutants. However, whether this binding is specific and cooperative or rather unspecific cannot be deduced from this ^{15}N HSQC titration experiments, since the primary source for the observed line broadening is slow chemical or conformational exchange and not due to size-dependent relaxation losses (Klein et al., 2001b; Rippin et al., 2002).

6.2.1.1.2 p53–DNA Complex Diffusion studied by NMR Spectroscopy

However, the translational diffusion coefficient of a molecular species is proportional to its "effective molecular weight and shape" (Cantor and Schimmel, 1980) and is therefore sensitive to overall molecular properties, but not to rather local intramolecular spin-spin interactions measured by classical relaxation NMR experiments, yielding correlation times which can be quite different for different nuclei in the same molecule. Thus measuring the diffusion rate is an independent way to study intermolecular interactions (Dehner et al., 2003; Derrick et al., 2002; Dingley et al., 1995). Therefore the hydrodynamic properties of p53 DBD dimerization mutants and their DNA binding were analyzed by pulsed field gradient diffusion experiments (Price, 1997b). Addition of CON2x5 oligonucleotide to p53 DBD wild-type causes a reduction of 27.1 % in the diffusion coefficient of p53 DBD (Table 2 and **Figure 31**). This is due to a cooperative binding of two p53 DBDs to one decameric half site consensus oligonucleotide.

Table 2: Diffusion coefficients of p53 wt, p63 wt and p53 DBD dimerization mutants free and bound to CON2x5 oligonucleotide in H_2O/D_2O at 289 K.

Sequence	D free [$m^2/s\ 10^{-10}$]	exp. error [$m^2/s\ 10^{-12}$]	D with CON2x5 [$m^2/s\ 10^{-10}$]	exp. error [$m^2/s\ 10^{-12}$]	% reduction	error
p53 wt	1.03	±3.04	0.75	±2.72	27.1	±0.4
p63 wt	0.96	±1.942	0.76	±2.32	21.6	±0.8
p53 H178A	1.00	±1.99	0.87	±4.26	13.4	±2.4
p53 R181A	1.03	±1.75	0.88	±4.22	14.9	±2.6
p53 C182A	0.99	±2.26	0.81	±4.06	18.3	±2.1
p53 E180R	1.04	±4.23	0.87	±2.71	15.8	±0.8
p53 R181E	0.97	±1.2	0.80	±3.00	17.2	±1.8
p53E180RR181E	1.11	±5.93	0.85	±2.74	22.6	±1.7

The measured value is in good agreement with hydrodynamic calculations using the shell model of HYDRONMR (García de la Torre et al., 2000a) and a dimeric p53 DBD–DNA model complex as described by Klein et al. (Klein et al., 2001b) which results in a theoretical reduction of the diffusion coefficient of about 33%. The monomeric p53 DBD-DNA complex (PDB-code: 1TSR; chain B including the DNA) was also used for hydrodynamic calculations yielding a reduction of 18% upon DNA binding compared to free p53 DBD. Thus these two theoretical values represent the range expected for an equilibrium of monomeric / unspecific and fully cooperative DNA binding. Deviations from theoretical and experimental data reflect an averaging of higher and – most probably – lower oligomeric states. **Figure 31** illustrates the

reduction of the diffusion coefficient upon addition of 0.6 equivalents CON2x5 half-site oligonucleotide to achieve a stoichiometric 1:2 = DNA:p53 DBD ratio of wild-type DBDs of p53 and p63 and the p53 DBD dimerization mutants. As already indicated by ^{15}N HSQC titration all mutants bind to DNA, resulting in a reduction of at least 13%. NMR experiments were done without any unspecific competitor DNA and therefore it cannot be concluded whether this overall reduction is due to an unspecific or a partially cooperative DNA binding. However, considering the experimental errors two classes for p53 can be distinguished: p53 DBD wild-type and the p53 DBD E180R/R181E double site mutation have a significant higher population of oligomeric states upon DNA binding than all other p53 DBD dimerization mutants (**Figure 31**). Therefore it can be concluded that p53 DBD wild-type and the double site mutation E180R/R181E have a similar tendency to bind DNA cooperatively, whereas for the single site mutations H178A, R181A, C182A and E180R, R181E this tendency is less pronounced or due to unspecific binding. This would indicate a crucial role of these residues for the dimerization interface.
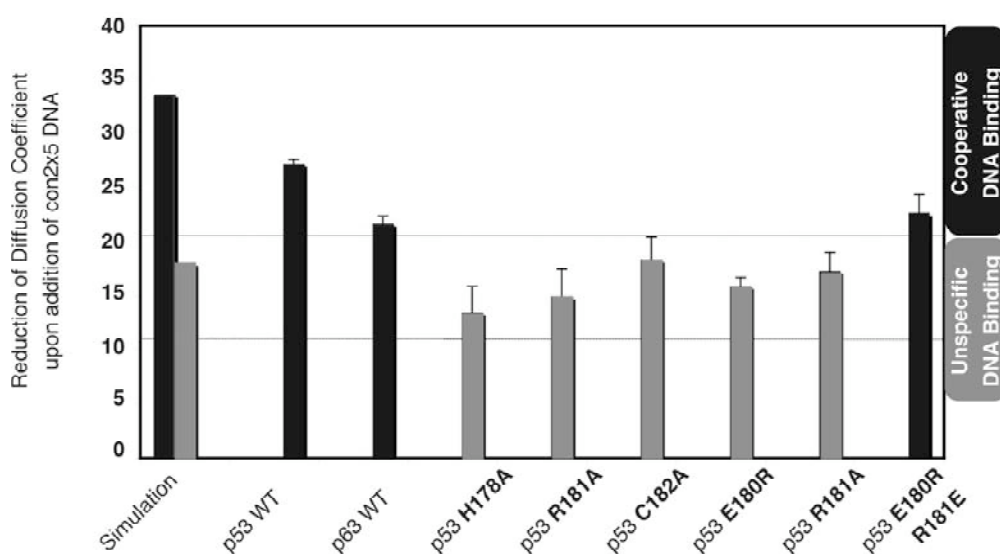
Figure 31: Reduction of the diffusion coefficients of p53, p63 DBD and the p53 dimerization mutants upon complexation with consensus DNA. Diffusion coefficients were measured by pulsed-field gradient NMR experiments in the absence and presence of DNA. Hydrodynamic simulations (García de la Torre et al., 2000a) using a cooperative p53 DBD : DNA model complex as proposed by Klein et al. (Klein et al., 2001b) yield a theoretical reduction of 33 % while a single site binding of DNA (PDB code: 1TSR, chain B, including DNA) results in 18 %. All dimerization mutants bind to DNA; however, unspecific and partially specific cooperative DNA binding cannot be distinguished without competitor DNA.

6.2.1.1.3 DNA Binding Behavior of p53 Dimerization Mutants

To clarify the question of specific and unspecific DNA binding of these dimerization mutants, electrophoretic mobility shift assays were performed. After incubation with fluorescence labeled double stranded consensus site oligonucleotide (CON4x5) in the presence of unspecific and unlabelled competitor DNA, p53 DBD wild-type dimerizes and binds specifically to labeled consensus DNA (**Figure 32**, lane 1).
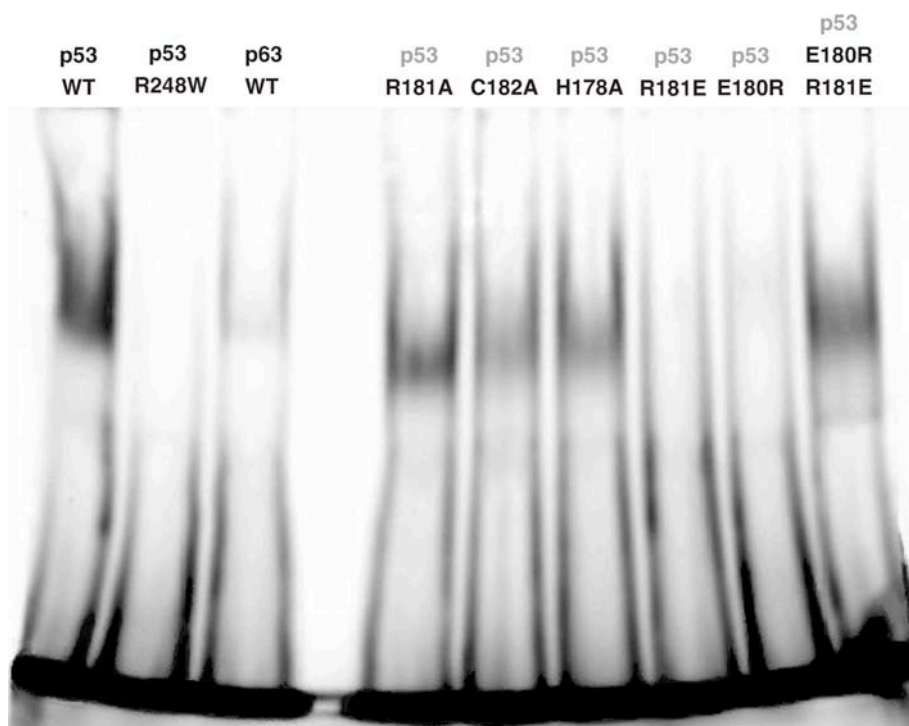
Figure 32: Electrophoretic mobility shift assays of wild-type p53 DBD, p53 DBD R248W, p63 DBD wild-type and p53 DBD dimerization mutants in the presence of unspecific unlabeled pBluescript II SK$^+$ competitor DNA. Specific, cooperative DNA binding occurs for wild-type p53 DBD and the p53 DBD E180R/R181E double mutant. Reduced DNA binding affinity is observed for the almandine dimerization mutants as well as for p63 wild-type, whereas for p53 DBD E180R and for p53 DBD R181E no DNA binding is observed.

As a negative control the p53 DBD mutant R248W has been analyzed which is a major hot-spot residue belonging to the class of direct DNA contact mutations (Bullock and Fersht, 2001). Consequently we do not observe any DNA binding affinity under the same conditions (**Figure 32**, lane2). p63 DBD was not able to bind significantly to labeled consensus DNA, whereas an artificial dimerization of p63 DBD by using the GST–p63 DBD fusion protein yields again a DNA binding affinity similar to p53 DBD (**Figure 34**, lane2) (Klein et al., 2001a). The three following lanes (**Figure 32**, lane 4-6) show that the alanine mutations of solvent

exposed residues H178A, R181A and C182A have a reduced specific DNA binding affinity compared to p53 DBD wild-type. While the single site mutations E180R and R181E, in which two Glu and two Arg residues, respectively, are sequential in sequence, do not show any DNA binding (**Figure 32**, lanes 7,8). A switch in position of these two residues, i.e. the double site mutation E180R/R181E, restores a DNA binding affinity nearly similar to p53 DBD wild-type (**Figure 32**, lane 9). As a cross-check whether two identically charged sequential residues in mutations E180R and R181E might have an impact on the structural integrity of the H1 helix and thereby prevent DNA binding, each 100 ng E180R and R181E were co-incubated with consensus DNA and 200 ng competitor DNA which fully restored specific DNA binding affinity (**Figure 33**).

Figure 33: A 1 : 1 mixture of p53 DBD R181E and E180R restores the DNA binding affinity to the level of wild-type p53 DBD.

Furthermore electrophoretic mobility shift assays were performed under the same conditions, but using a selection of GST-mutant p53 DBD fusion proteins: the three Ala mutations H178A, R181A, C182A as well as R181E, in which two negatively charged residues (E180, R181E) are sequential. The GST domain of these mutants serves as an artificial dimerization site – similar to the tetramerization domain of full-length p53 wild-type and thus enhances cooperativity and therefore specific DNA binding. As a positive control lanes 1 & 2 in **Figure 34** contain GST–p53 DBD and GST–p63 DBD which bind both in similar affinity to consensus DNA, whereas free p63 DBD without the GST domain lacks this cooperativity (**Figure 32**, lane 2) (Klein et al., 2001a). Analogous to p63 DBD the three Ala mutations of p53 DBD exhibit enhanced cooperativity in DNA binding with the dimeric GST-fusion domain and show an affinity which is comparable to p53 DBD wild-type. The GST-R181E mutant, however, does not show any specific DNA binding, thus the induced cooperative effect of this artificial GST dimerization domain is not strong enough to overcome the repulsive charged-charged interactions which would occur in the designated dimerization interface.

Figure 34: Electrophoretic mobility shift assays for wild-type p53 DBD and GST-fusion proteins. The GST domain serves as an artificial dimerization site which enhances the cooperativity in DNA binding of p63 wild-type and the alanine dimerization mutants of p53 DBD. For the GST–p53 DBD R181E mutant the repulsive charge-charge interactions within the dimerization interface overcome the cooperative effect of the GST domain.

6.2.1.2 Discussion

Several electrophoretic mobility shift assay studies have shown that p53 DBD binds cooperatively to a decameric half site consensus DNA sequence (CON2x5) and with higher affinity and cooperativity to a dodecameric two half-site consensus DNA sequence (Balagurumoorthy et al., 1995; Bullock et al., 2000; McLure and Lee, 1998; Wang et al., 1995b). However, binding of p53 DBD to a pentameric single quarter-site (CON1x5) could not be detected, as confirmed by electrophoretic shift assays, FCS and NMR measurements (Klein et al., 2001a; Klein et al., 2001b). In contrast to p53 DBD, the homologous isolated p63 DBD fails to bind consensus DNA cooperatively as studied by electrophoretic mobility shift assays using GST-mediated p63 DBD dimers, which again bind to the consensus DNA sequence (Klein et al., 2001a). Both tumor supressor proteins p53 and p63 contain a tetramerization domain which forms dimers of dimers (Clore et al., 1995; Jeffrey et al., 1995; Lee et al., 1994), thus both proteins build up a homotetramer which is the predominant form in solution and which binds specifically to DNA (Friedman et al., 1993). Accordingly an additional dimer-dimer interface within p53 DBD, but not present in p63 DBD, stabilizes the cooperative DNA binding independent of the oligomerization domain of full-length p53 (McLure and Lee, 1998).

At present no structural information is known about full-length p53 and its tetrameric organization bound to DNA, yet several reports discuss inter-domain contacts in p53 (Arrowsmith and Morin, 1996; Cho et al., 1994; Lebrun et al., 2001; Nagaich et al., 1999; Prives, 1994; Zhao et al., 2001) based on modeling of the individual structures of p53 DBD (Cho et al., 1994; Zhao et al., 2001) and the tetramerization domain (Clore et al., 1995; Jeffrey et al., 1995; Lee et al., 1994). NMR spectroscopic titration experiments (Klein et al., 2001b; Rippin et al., 2002) of ^{15}N-labelled p53 DBD with CON2x5 provided an indication for the existence of such a dimerization interface. The chemical shift perturbations of backbone ^{15}N,^{1}H chemical

shifts of p53 DBD upon addition of DNA are localized near the helix H2, which is the binding interface for DNA. In addition chemical shift changes are particularly pronounced for the H1 helix, located near the zinc coordination site. Interestingly this second H1 perturbation site does not participate in DNA binding directly (Cho et al., 1994) and could possibly be involved in protein-protein intermolecular interactions, forming the necessary dimerization interface in order to bind DNA cooperatively (Klein et al., 2001b; Rippin et al., 2002).

However, as NMR chemical shift changes may be caused by intermolecular contacts and/or induced conformational rearrangements (Dehner et al., 2003) as well, these observed chemical shift changes within the H1 helix might be due to a translated effect (e.g. *via* the bound zinc atom) from the DNA binding interface and not caused by protein-protein interactions as proposed by Rippin et al. (Klein et al., 2001b; Rippin et al., 2002) This second possibility cannot be ruled out on the basis of NMR data only. In addition none of the crystal structures published so far of the p53 core domain (Cho et al., 1994; Zhao et al., 2001) contain the proposed dimerization interface, but show most probably crystal artifacts not compatible with a cooperative DNA binding as it occurs in the native p53-DNA complex. Yet no direct experimental proof has been presented for the participation of the H1 helix in protein-protein interactions upon cooperative binding of DNA.

To study the potential role of this H1 helix region solvent-exposed residues were mutated which might be responsible for direct protein-protein interactions within the H1 helix dimerization interface in question; and analyzed their ability to bind consensus DNA cooperatively by NMR spectroscopy and electrophoretic mobility shift assays. **Figure 25** shows these residues whereby two different classes of mutations were introduced: (i) Alanine mutations of residues H178, R181 and C182 and (ii) mutations which yield a reversion of polarity of the respective side chain: E180R and R181E. In addition one sequential switch in amino acid position was done with a double site mutation E180R/R181E. Besides the structural important residues coordinating the zinc atom, e.g., H179, (Cho et al., 1994) even these solvent-exposed residues are highly conserved and mostly identical through different species which is illustrated by the sequence alignment of this H1 helix region in **Figure 26**. Nevertheless these solvent-exposed residues do not have a substantial impact on structural features of a single p53 core domain as all dimerization mutants are natively folded, which can be concluded by the ^{15}N HSQC spectra of all six p53 mutants differing only for sequential residues and neighboring residues with respect to the introduced mutation (**Figure 30**). All other signals are only slightly affected or identical to the p53 DBD wild-type spectrum. The results of ^{15}N HSQC titration of

[15]N-labelled dimerization mutants with CON2x5 oligonucleotide and the PFG diffusion experiments show that unspecific binding takes place for all mutants, including E180R and R181E, due to a fully functional DNA binding site. Yet significantly higher oligomeric states are populated for p53 DBD wild-type and the double-site mutation E180R/R181E, indicating that E180R/R181E binds similar to p53 DBD wild-type and thus cooperatively to DNA.
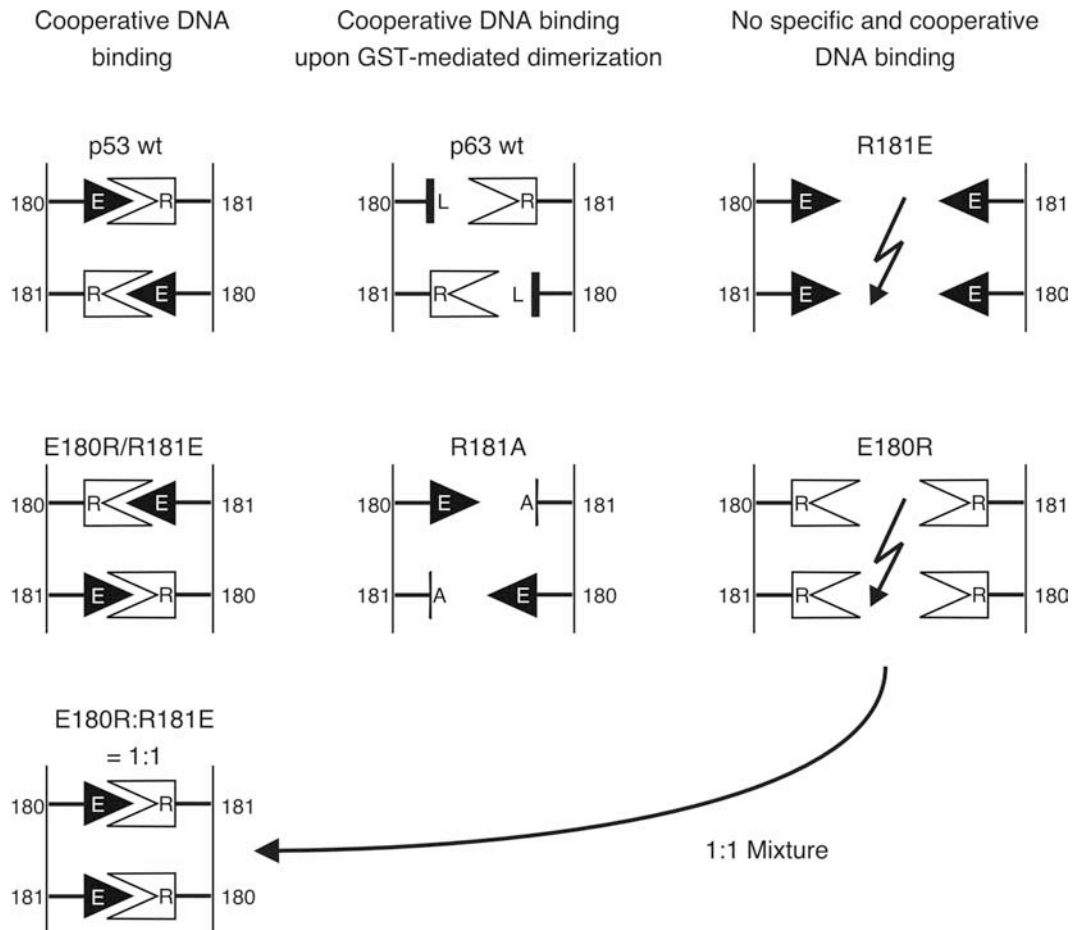
Figure 35: Schematic representation of observed dimerization patterns. Cooperative DNA binding is achieved by p53 DBD wild-type, the double site mutation E180R/R181E and a 1 : 1 mixture of p53 DBD E180R and R181E. Cooperative DNA binding can be enhanced by GST-mediated dimerization for p63 DBD wild-type and alanine dimerization mutants of p53 DBD. Strong repulsive charge-charge interactions prevent a cooperative DNA binding of p53 DBD E180R and R181E mutants.

This result was corroborated by electrophoretic mobility shift assays where both p53 DBD wild-type and the E180R/R181E mutations bind in the presence of competitor DNA specifically and cooperatively to fluorescence labeled consensus DNA. In contrast, to the single-site mutations E180R and R181E, which both display

two identical-charged sequential residues within the designated dimerization interface, do not show any specific binding of consensus DNA (**Figure 32**, lane 7 & 8) This can be attributed to a lack in cooperativity resulting from repulsive charged-charged interactions; this is clear evidence for the necessary cooperativity for a selective binding of DNA and in addition localizes the cooperative dimerization interface to residues E180 and R181 in the H1 helix of p53 DBD (**Figure 35**).

These repulsive charged-charged interactions (**Figure 35**) are indeed strong enough to overcome the cooperative effect of an artificial GST-dimerized p53 DBD R181E fusion protein which is not able to bind consensus DNA selectively and cooperatively (**Figure 34**). From this can be concluded that there is no other dimerization interface within the p53 DBD which could replace this E180–R181 intermolecular interface. Similar to the double site mutation E180R/R181E, where these two residues are switched in sequence (**Figure 33**), a molar 1 : 1 mixture of E181R : R181E single mutation is again able to bind selective consensus DNA cooperatively by heterodimerization of each mutant.

The three alanine mutations H178A, R181A and C182A, however, do not actively prevent a possible dimerization upon binding of DNA, which demonstrates (i) residual cooperative DNA binding and (ii) this cooperative DNA binding can be enhanced by the GST-mediated dimerized p53 DBD (**Figure 34**). This GST-mediated enhancement of cooperative DNA binding was already observed for the p63 DBD (Klein et al., 2001a). It was deduced that conformational differences within the H1 helix might be responsible for the different dimerization behavior.

However the backbone NMR chemical shifts of p63 DBD have been assigned (section 6.5) (Furrer et al., 2003) and it was found that all secondary structural elements in the isolated DBD of p63 are analogous to p53 DBD, including the H1 helix also. Considering the sequence alignment (**Figure 26**) the highly conserved/identical amino acid E180 is replaced by a leucine residue. Thus it is likely that the aliphatic leucine is not able to build up an intermolecular salt bridge, which would account for the previously observed lack in selective and cooperative DNA binding of free p63 DBD (Klein et al., 2001b).

The results support the idea that the proposed additional dimerization interface of p53 DBD resulting in cooperativity and selectivity of DNA binding consists mainly of two intermolecular Glu180–Arg181 salt bridges from each monomer to the other as presented in **Figure 36**. This salt bridge is in agreement with a C_2 symmetric model complex as proposed by Lebrun and Klein (Klein et al., 2001b; Lebrun et al., 2001) and rationalizes the different DNA binding behavior of p53 DBD and p63 DBD.
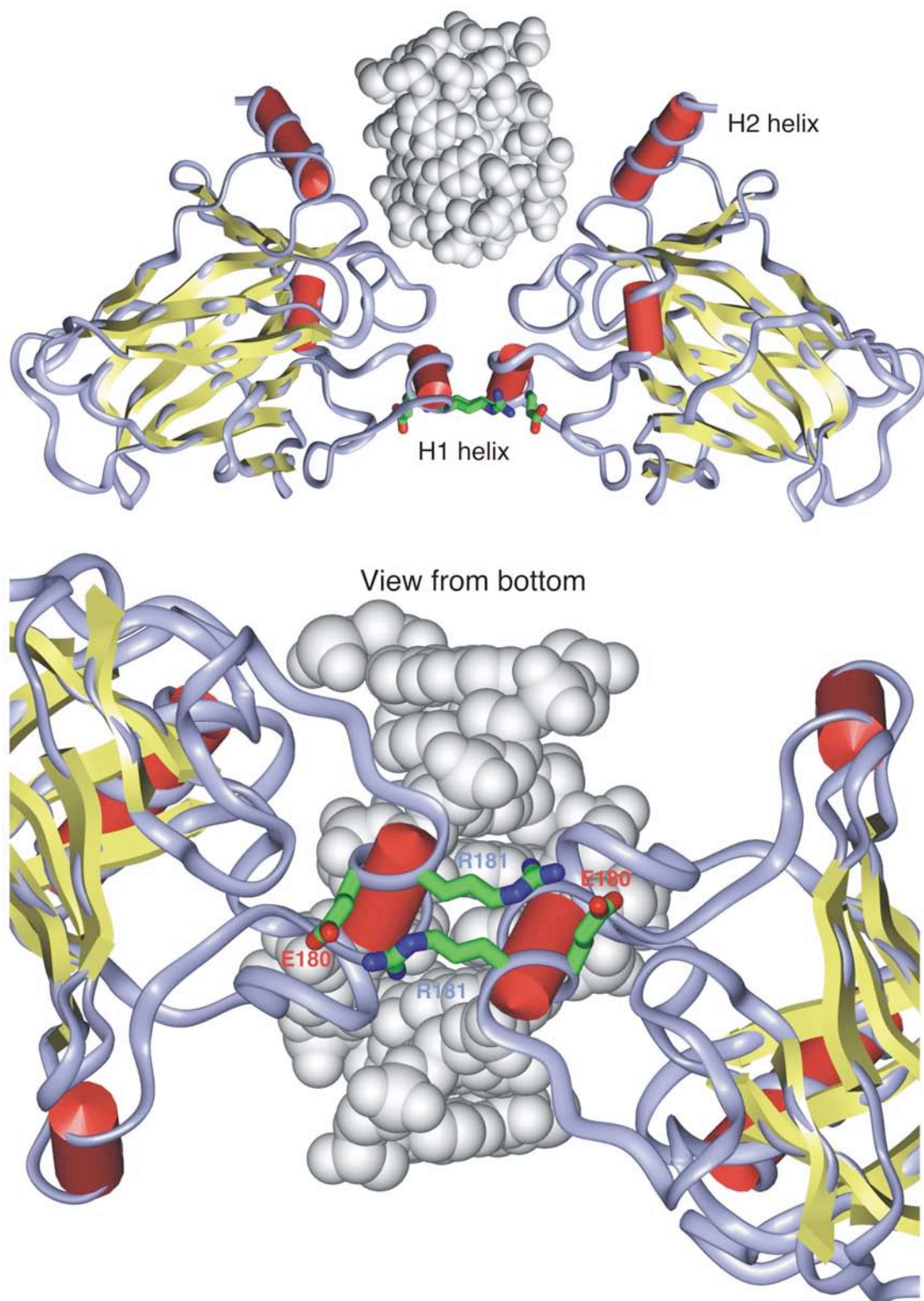
Figure 36: C$_2$ symmetric model complex for the identified dimerization interface of p53 DBD upon cooperative DNA binding. The dimerization interface is stabilized by a double intermolecular salt bridge between the E180 and R181 residues.

Furthermore the essential role of the identified H1 helix dimerization interface for a proper p53 function is demonstrated by the germline p53 E180K mutation which is associated with the Li-Fraumeni syndrome and a lost transcriptional activation of Bax and Pig3 (Campomenosi et al., 2001; Olivier et al., 2002). The lost p53 activity of this germline H1 helix mutation can be explained on a molecular level, displaying sequential equally charged residues, which lack a selective and cooperative DNA binding by abolishing the formation of the dimerization interface, due to repulsive charge-charge interactions. This kind of oncogenic mutation cannot be assigned to any of the two major p53 mutation classes (Bullock and Fersht, 2001), as these solvent-exposed mutations neither alter the structural integrity of p53, nor show direct contact to bound DNA. Therefore a new class of p53 mutations is postulated which lack p53 activity due to a hindered cooperativity of DNA binding.

6.3   The N-terminal Domain of p53 is Natively Unfolded

6.3.1   Results

6.3.1.1   The N-terminal Domain of p53

To study the structure and stability of the N-terminal part of p53 (aa 1-93), the respective construct was expressed in *E. coli* and purified it to homogeneity. The identity of the protein was confirmed by westernblot. ESI-TOF mass spectrometry of the purified protein gave a value of 11 733.8 Da. This corresponds very well to the theoretically calculated molecular mass of 11 733.0 Da (Dawson et al., 2003).

6.3.1.2   NMR Spectroscopic Analysis of Np53

To gain further insight into the conformation of Np53, we analyzed its structure at pH 7.5 and 298 K by NMR spectroscopy.
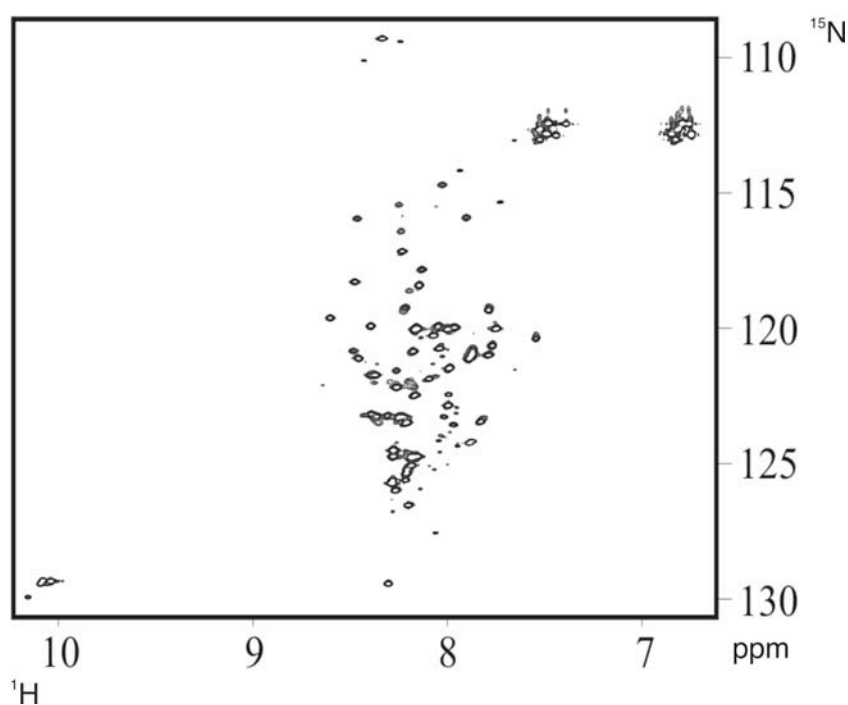
Figure 37: ^{15}N HSQC spectrum of ^{15}N-labeled Np53. The ^{1}H-^{15}N HSQC spectrum of the N-terminal domain of human p53 (1.2 mM) was determined at 298 K and pH 7.5 in 90% H_2O / 10% D_2O at 750 MHz. Adapted from (Dawson et al., 2003).

A small proton resonance dispersion in a spectral range of 7.5 ppm to 8.7 ppm is observed in the ^{15}N HSQC spectrum, characteristic for a highly unfolded protein. In addition, the seven NH_2-side chain signals of asparagine and glutamine residues

accumulate in their characteristic random coil region of 7.59 ppm / 6.88 ppm. The same was observed for the side chain signals of the three tryptophanes of Np53 which appear at 10.2 ppm. Taken together, the spectrum shows on the level of amino acids that residues 1-93 of p53 are mostly unstructured.

6.3.1.3 *PFG Diffusion Experiments and Hydrodynamic Calculations*

To corroborate the hydrodynamic properties of Np53 pulsed field gradient diffusion measurements were performed and the data were compared to theoretical hydrodynamic calculations using the bead model of HYDRONMR (García de la Torre et al., 2000b) and a regularized random-coil structure which was generated by XPLOR (Brünger, 1992). The diffusion coefficient of Np53 was calculated from 23 non-exchangeable signal decays which were averaged and fitted using the equation of Stejskal and Tanner (Stejskal and Tanner, 1965). The experimental diffusion coefficient was $6.457 \cdot 10^{-11} +/- 5.17 \cdot 10^{-13}$ $m^2 s^{-1}$. This value is in good agreement with the calculated one using HYDRONMR $D_{thr} = 7.426 \cdot 10^{-11}$ $m^2 s^{-1}$.
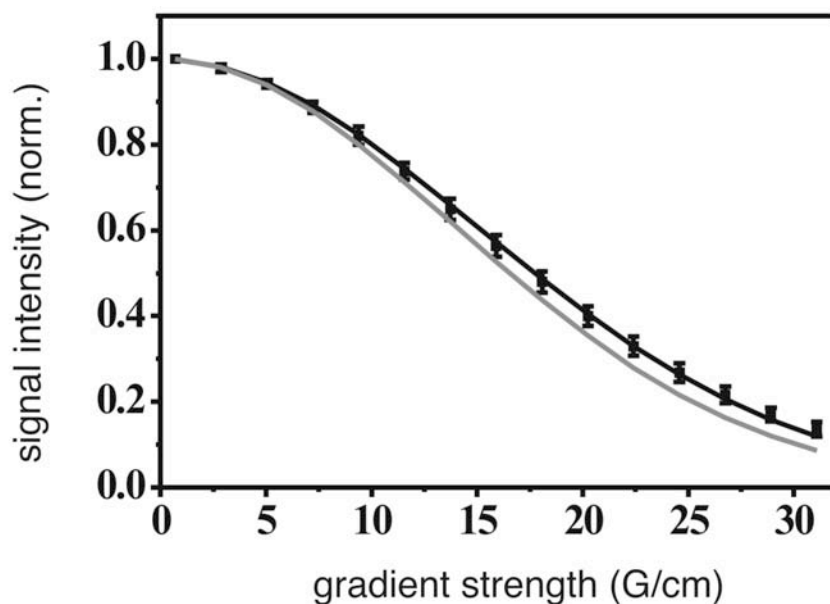
Figure 38: Pulsed field gradient diffusion experiment of Np53. The squares represent experimental values with increasing gradient strength. Error bars are the result of an average of 23 convergent signal decays of non-exchangeable protons. The nonlinear curve fitting using Stejskal and Tanners equation (Stejskal and Tanner, 1965) is shown as a black line. The grey line represents the expected signal decay for a regularized extended model structure of Np53 using the theoretical diffusion coefficient calculated by HYDRONMR. Adapted from (Dawson et al., 2003).

The diffusion coefficient is about two times smaller than the one of a globular folded protein of the same size. This is due to an increased hydrodynamic radius, typical for a globular folded protein of about 20 kDa. Thus both the hydrodynamic calculation and the NMR diffusion experiments support the idea of an unfolded state of Np53 under physiological conditions.

6.3.1.4 ^{15}N HSQC Titration of Np53 with MDM2

A series of ^{15}N HSQC titration spectra was recorded of ^{15}N-labeled Np53 with an increasing molar excess of unlabeled MDM2. However, no detectable signal shifting is observed during titration up to an eightfold molar excess of MDM2, leading to the conclusion that no global structural rearrangements or no global gain in secondary structure of Np53 is induced upon binding to MDM2.

6.3.2 Discussion

The N-terminal domain of p53 seems to play an essential role in the regulation of the p53 network. However, the structure and precise function of this domain is still not known. The suggestion that segments of the N-terminal part of p53 could be unfolded in the native state has important implications for the functional mechanism of p53 (Bell et al., 2002).

The structural analyses of the entire N-terminal part including the transcription activation domain and the proline-rich SH3-target domain demonstrates that the N-terminal part of p53 (aa 1-93) shows canonical features of intrinsically unstructured proteins. ^{15}N ^{1}H HSQC NMR spectra as well as far-UV CD spectroscopy demonstrate that Np53 lacks extensive contributions of ordered secondary structure (Dawson et al., 2003). Near-UV CD and fluorescence emission spectra of Np53 confirm a high main chain flexibility in the domain and a complete absence of tertiary structure (Dawson et al., 2003). The hydrodynamic dimensions of Np53 are typical for a protein of low compactness and an extended conformation under physiological conditions. The molecular mass obtained by ultracentrifugation corresponds well with the theoretical mass of an Np53 monomer. Interestingly, the values for the apparent molecular mass obtained by analytical gelfiltration are approximately a factor of two higher than the calculated ones from sequence. In addition, the diffusion coefficient obtained by NMR spectroscopy is about two times smaller than the one expected for a globular folded protein of the same size. Both characteristics are in line with the concept of an unfolded conformation of the N-terminal part of p53 under physiological conditions. This is in good agreement with the findings of Bell et al. (Bell et al., 2002) demonstrating that the N-terminal part of full-length p53 contains large unstructured

regions. Thus, an interaction between the unfolded N-terminal part and other domains of p53 cannot be excluded.
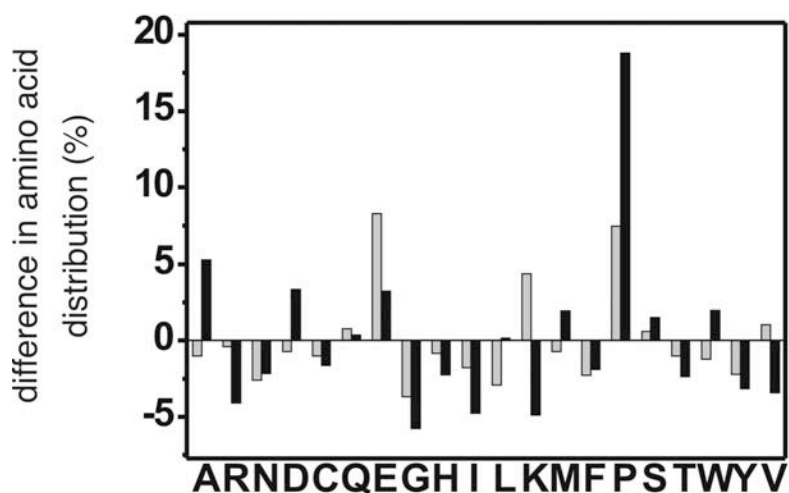
Figure 39: Amino acid distribution of natively unfolded proteins and Np53. Comparison of the amino acid composition of intrinsically unfolded proteins (grey bars) and Np53 (black bars) compared to the average amino acid composition of globular proteins from the PDB (Tompa, 2002). Amino acids are represented by the single letter code. The proportional difference of the frequency of individual amino acids is indicated. Adapted from (Dawson et al., 2003).

The depletion of order-promoting amino acids like proline as well as the enrichment of disorder-favoring amino acids like tyrosine, phenylalanine, cysteine and isoleucine in the sequence of Np53 seems to be a reason for the hydrodynamic properties of Np53 and the lack of ordered secondary and tertiary structure. This result is based on an amino acid sequence comparison of Np53 with average folded proteins from the Swissprot database (**Figure 39**). Furthermore, Np53 is predicted to be natively unfolded by a correlative index based on mean hydrophobicity versus mean net charge values (**Figure 40**). At the level of primary structure, Np53 demonstrates the typical amino acid composition for intrinsically unfolded proteins (Dunker et al., 2001). Generally, the low content of hydrophobic amino acid residues and their flanking by numerous acidic residues inhibits the formation of a hydrophobic core (Dyson and Wright, 2002; Tompa, 2002) and disfavors the formation of rigid secondary structure elements resulting in an extended conformation due to electrostatic repulsion (Uversky, 2002). The high content of prolines, especially in the SH3-binding domain, might facilitate the formation of a more open conformation, the lefthanded polyproline II (PPII) helix (Adzhubei and Sternberg, 1993; Williamson, 1994). The formation of such a motif is postulated for the interaction of SH3-domains

within the proline-rich subdomain of p53 (aa 63-93) based upon the recurrent *PXXP*-binding motif of SH3-domains and the high content of the hydrophobic amino acid alanine in that region (Kay et al., 2000; Mayer, 2001). The overall content of prolines and alanines accounts for 74% of the amino acids in this domain.
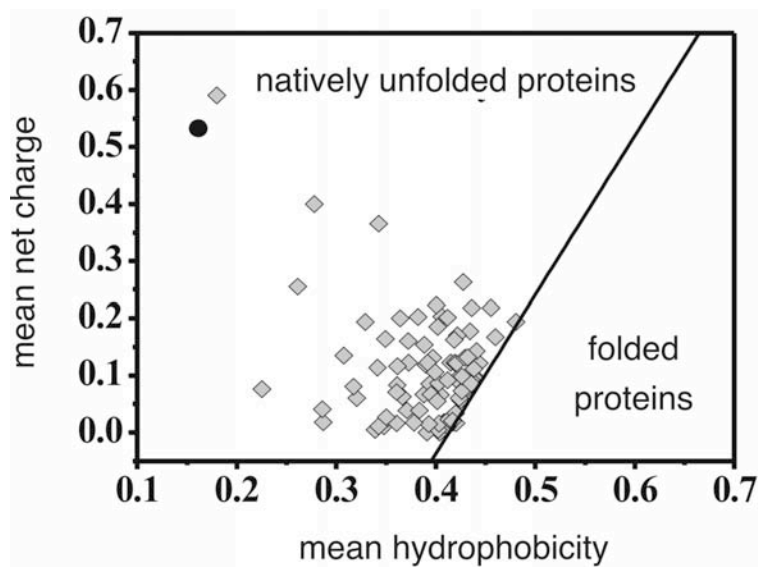
Figure 40: Charge-hydrophobicity phase space for intrinsically unfolded proteins and Np53. The diagram monitors correlates the mean hydrophobicity $\langle H \rangle$ and the mean net charge $\langle R \rangle$ for a set of 90 natively unfolded proteins ($\Diamond$) as summarized elsewhere (Uversky, 2002) and Np53 (•). The solid line represents the border between natively unfolded and native proteins (equation: $\langle R \rangle = 2.785\langle H \rangle - 1.151$) (Tompa, 2002). Adapted from (Dawson et al., 2003).

The large hydrodynamic dimensions and the intrinsic disorder make Np53 a good target for the initial molecular collision and permits multiple approach orientations in the binding process thus facilitating association (Dunker et al., 2001; Pontius, 1993). Many natively unfolded proteins (Dunker et al., 2001; Dunker and Obradovic, 2001; Dyson and Wright, 2002; Wright and Dyson, 1999), and among them isolated acidic transcription activation domains (Dahlman-Wright et al., 1995; Donaldson and Capone, 1992) demonstrate the induction of secondary structure elements upon binding to target proteins. This concept seems to hold true for Np53 and MDM2. The complexation could be described as a local disorder-to-order transition (Dunker et al., 2001; Kriwacki et al., 1996; Tompa, 2002) suggesting that the initial flexible, highly specific conformation of low binding affinity switches to a conformation of higher binding affinity in complex (Dunker et al., 2001). However, induced global structural changes upon MDM2 binding within Np53 can be ruled out

due to a series of ^{1}H ^{15}N HSQC titration experiments which show no detectable signal shifting upon binding of unlabelled MDM2 to ^{15}N Np53 up to an eightfold excess.

Taken together, the results directly demonstrate that the entire N-terminal region of p53 is natively unfolded and that this is its functional state. Furthermore the interaction of human MDM2 with Np53 or p53 shows that unstructured and folded parts of p53 function in a synergetic manner. In a more general view, the structural feature of being natively unfolded under physiological conditions seems to be in good agreement with the observation of intrinsic structural disorder for a variety of transcription activation domains (Triezenberg, 1995; Wright and Dyson, 1999).

6.4   Mapping the Binding Sites of Bcl-xL / Bcl-2 and the p53 DBD

6.4.1   Results and Discussion

6.4.1.1   NMR Chemical Shift Mapping Identifies a Novel Binding Interface of p53 DBD and Bcl-xL

To map the p53 surface residues affected by Bcl-xL, ^{1}H, ^{15}N HSQC spectra of ^{15}N labeled p53 DBD were acquired when one of the three types of the Bcl-xL proteins, Bcl-xL, Bcl-xLΔT, or Bcl-xLΔLT was titrated in. Titration of p53 DBD with full-length Bcl-xL protein resulted in disappearance of most of the signals in the ^{1}H,^{15}N HSQC spectrum of p53 DBD, which provided the first NMR evidence for an actual interaction event occurring between p53 DBD and Bcl-xL. The disappearance of signals may be attributed to the formation of a large molecular weight oligomeric complexes of p53 DBD (25kDa) and full-length Bcl-xL (26kDa), which may also be involved in a conformational exchange broadening. The full-length Bcl-xL contains the putative transmembrane domain, which is exposed in the absence of the membrane in the NMR sample. To rule out the possibility that the hydrophobic transmembrane domain is the case of the artificial oligomerization of Bcl-xL and p53, the experiments were repeated with Bcl-xL without the C-terminal transmembrane region. The ^{1}H,^{15}N HSQC spectra of p53 DBD with Bcl-xLΔT (lacks the transmembrane domain), and with Bcl-xLΔLT (lacks transmembrane domain and the flexible loop) showed induced chemical shifts changes, which is an evidence that p53 and Bcl-xL is forming a hetero oligomer at the rate sub-ms or faster (fast exchange on the NMR chemical shift time scale), instead of loss of signals seen in case of full-length Bcl-xL. Therefore, it can be concluded that there is an intrinsic ability for p53 to oligomerize with Bcl-xL, and further NMR studies were conducted using Bcl-xLΔLT since it gives the simplest HSQC spectra. Importantly, this protein still exhibits anti-apoptotic functions and is routinely applied in biochemical and structural studies on Bcl-xL (Muchmore et al., 1996; Petros et al., 2004a; Sattler et al., 1997).

Titration of Bcl-xLΔLT to ^{15}N-p53 DBD did not result in large overall chemical shift perturbations, suggesting that binding of Bcl-xL does not induce major conformational rearrangements in p53 DBD. As a result, chemical shift changes in the p53 DBD/Bcl-xL complex were determined by the minimum deviation between each position of the free and the complexed signal in the HSQC spectra (Dehner et al., 2003) (**Figure 41**).
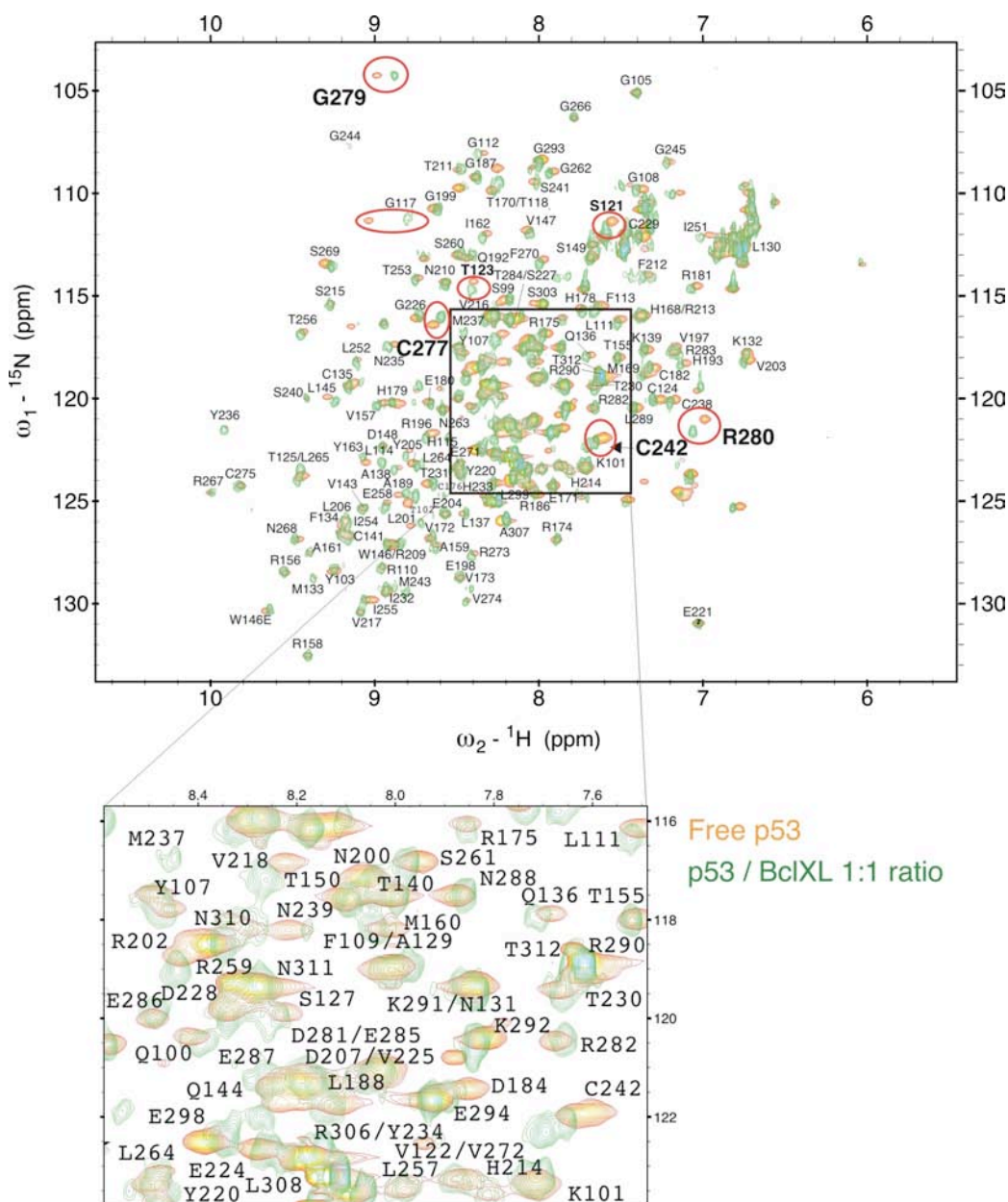
Figure 41: Overlay of the ^{1}H, ^{15}N HSQC spectra of free p53 DBD (orange) and p53 DBD bound to unlabelled Bcl-xLΔLT (green) at near equimolar ratio (1:1.1). The sequential resonance assignment of free p53 DBD has been published and could be transferred onto our spectra (Wong et al., 1999b).

Figure 42 illustrates the observed chemical shift perturbations using a weighted averaged chemical shift change of ^{1}H and ^{15}N resonances in the free and complexed HSQC spectra. Significant chemical shift perturbations (larger than 0.4 in the relative scale) occur for residues Arg-280, Gly-279, Cys-277, Cys-242 and Cys-176, as well as for several residues in the flexible loop region Phe-113 – Cys-124 such as Ser-121, Thr-123, Gly-117, His-115 und Leu-114. These residues are color coded according to their solvent accessibility which has to be above 50% for side-chain or backbone

atoms in order to be considered in the docking calculations to be an so-called active residue. Residue R287 has been additionally used as active residue in the calculations, since it is a direct surface neighbor of G279 and R280, solvent accessible and with a relative chemical shift perturbation of 0.36 nearly fulfils the requirement of 0.4. The secondary structure of p53 DBD is given below in red (helix) and yellow (sheet) bars.
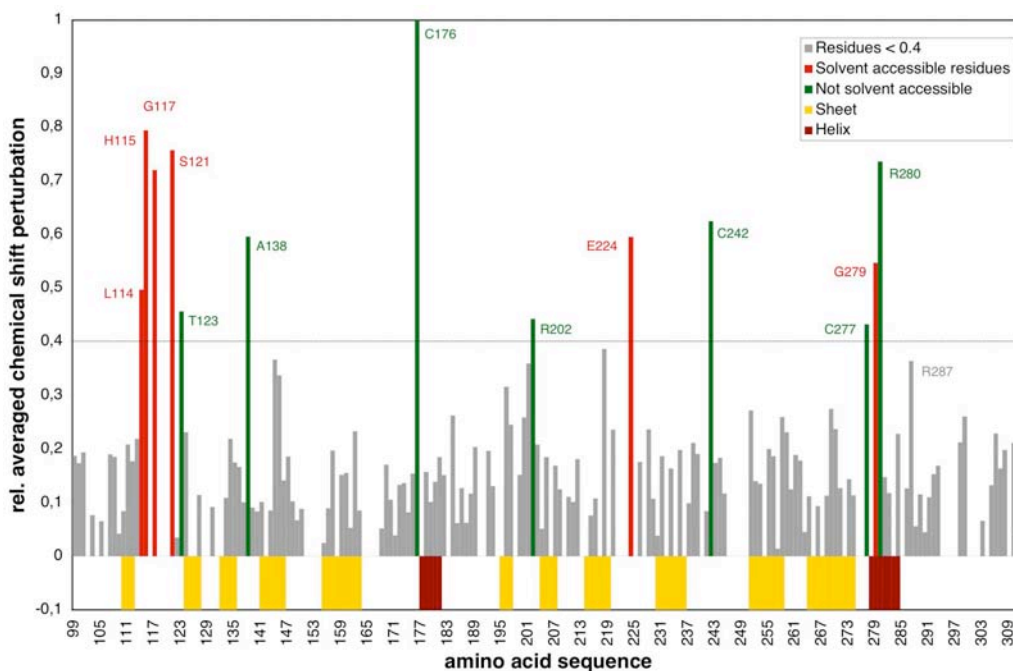
Figure 42: Average chemical shift perturbation of ^{1}H and ^{15}N chemical shifts of p53 DBD given by $\Delta_{av} = [(\Delta\delta^2_{NH} + \Delta\delta^2_N/25)/2]^{1/2}$ against residue number upon titration with a 1.1-fold excess of Bcl-xLΔLT. Residues with a relative chemical shift perturbation larger than 0.40 and a solvent accessibility of side chain or backbone atoms above 50% are shown in red and those with relative chemical shift perturbations larger than 0.40 and a solvent accessibility smaller than 50% are shown in green. Residues which are not significantly shifted are colored in gray. The secondary structure is given below as red (helix) and yellow (sheet) bars.

6.4.1.2   NMR Spectroscopy Identifies the Binding Interface of p53 DBD and Bcl-2

Since Bcl-xL and Bcl-2 share high structural and functional homology, a p53/Bcl-2 complex could also be expected. Indeed Mihara et al. showed using immunoprecipitation that p53 not only interacts with Bcl-xL but also forms complexes with the anti-apoptotic protein Bcl-2 (Mihara and Moll, 2003). In fact, upon titration of unlabeled Bcl-2 to ^{15}N labeled p53 DBD, induced chemical shift changes in the ^{15}N HSQC spectra of p53 DBD are observed (**Figure 43**).
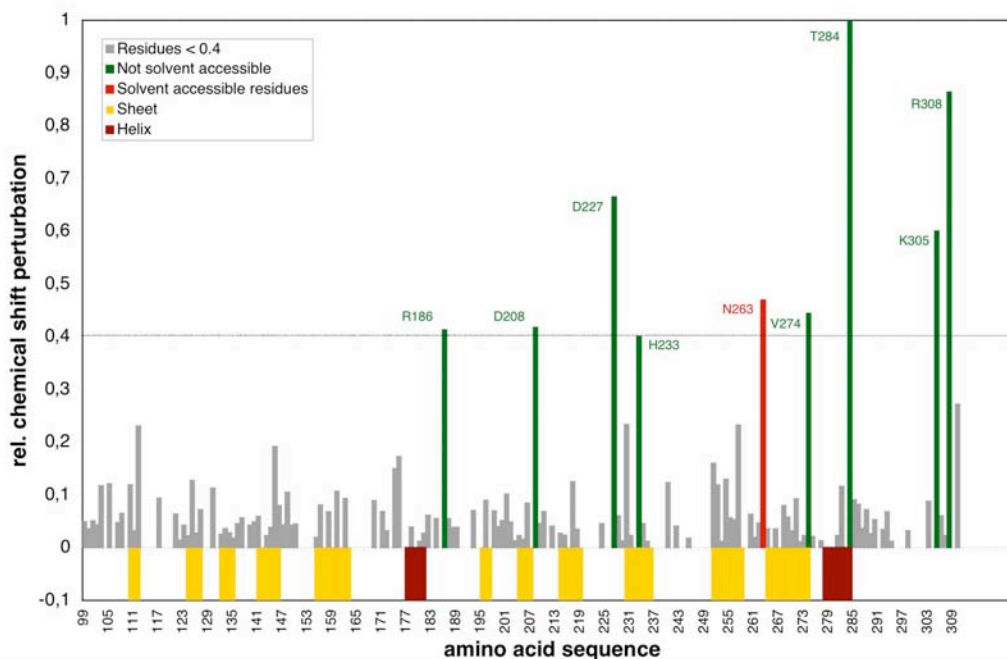
Figure 43: Average chemical shift perturbation of ^1H and ^{15}N chemical shifts of p53 DBD given by $\Delta_{av}=[(\Delta\delta^2_{NH}+\Delta\delta^2_N/25)/2]^{1/2}$ against residue number upon titration with a 1.1-fold excess of Bcl-2. Residues with a relative chemical shift perturbation larger than 0.40 and a solvent accessibility of side chain or backbone atoms above 50% are shown in red and those with relative chemical shift perturbations larger than 0.40 and a solvent accessibility smaller than 50% are shown in green. Residues which are not significantly shifted are colored in gray. The secondary structure is given below as red (helix) and yellow (sheet) bars.

The area on p53 affected by Bcl-2 is – however less pronounced – similar but not identical to the one by Bcl-xL and close to the DNA binding site of p53. As for Bcl-xL, titration of Bcl-2 to ^{15}N-p53 DBD did not result in large global chemical shift perturbations, suggesting that binding of Bcl-2 does not induce major conformational rearrangements of p53 DBD. However, the signals corresponding to the interaction site of p53 have disappeared instead of shifted as in Bcl-xL suggesting that the p53/Bcl-2 oligomer formation is in the intermediate exchange on the NMR chemical shift time scale (the exchange rate is expected to be in ms). p53 residues Gln-136 and Ala-138 (between S2' and S23), Ala-161 and Tyr-163 (S4), Arg-175 (L2), His-179 (H1), Ile-195 (S5), Asn-236 (S8), Met-237, Asn-239, and Gly-244 (Joerger et al., 2004). Residues which have disappeared upon complexation are localized at the DNA-contact interface of p53 DBD. In contrast to Bcl-xL-induced residue shifts on p53, Bcl-2 did not induce observable shifts on residues Leu-114, His-115, Gly-117, Ser-121, Arg-202 and Glu-224.

The binding of p53 may also modulate the anti-apoptotic function of Bcl-2 and Bcl-xL by changing its affinity to the pro-apoptotic BH3 domain-only Bcl-2 proteins

such as Bim and Bid. If the affinity of Bim to Bcl-2/Bcl-xL is decreased by p53, the released Bim can induce apoptosis through Bax/Bak pathway. Conversely, Bim or Bid may be able to weaken the interaction between p53 and Bcl-2, or p53 and Bcl-xL. To test this hypothesis, the 21mer Bid BH3 peptide was titrated into the p53/Bcl-2 complex in the NMR HSQC experiment. At as low as 1 : 0.5 ration of Bcl-2 to the Bid peptide, the p53 signals in the ^{15}N HSQC spectra started to be restored to the state of free p53, suggesting that the Bid peptide can promote the dissociation of p53 from Bcl-2. Similar findings were reported for the p53/Bcl-xL complex, where the 25-mer Bad BH3 peptide (K_d 0.6nM to Bcl-xL) inhibited the association of p53 to ^{13}C labeled Bcl-xL monitored by ^{13}C HSQC. This is a rather unexpected result from the structural point of view since the p53 binding site and the peptide binding site (the BH3 binding pocket) are almost at the opposite side of Bcl-xL nevertheless, a subtle global structural changes in Bcl-xL caused by the Bad peptide binding prohibits p53 to bind to the Bcl-xL/Bad complex.
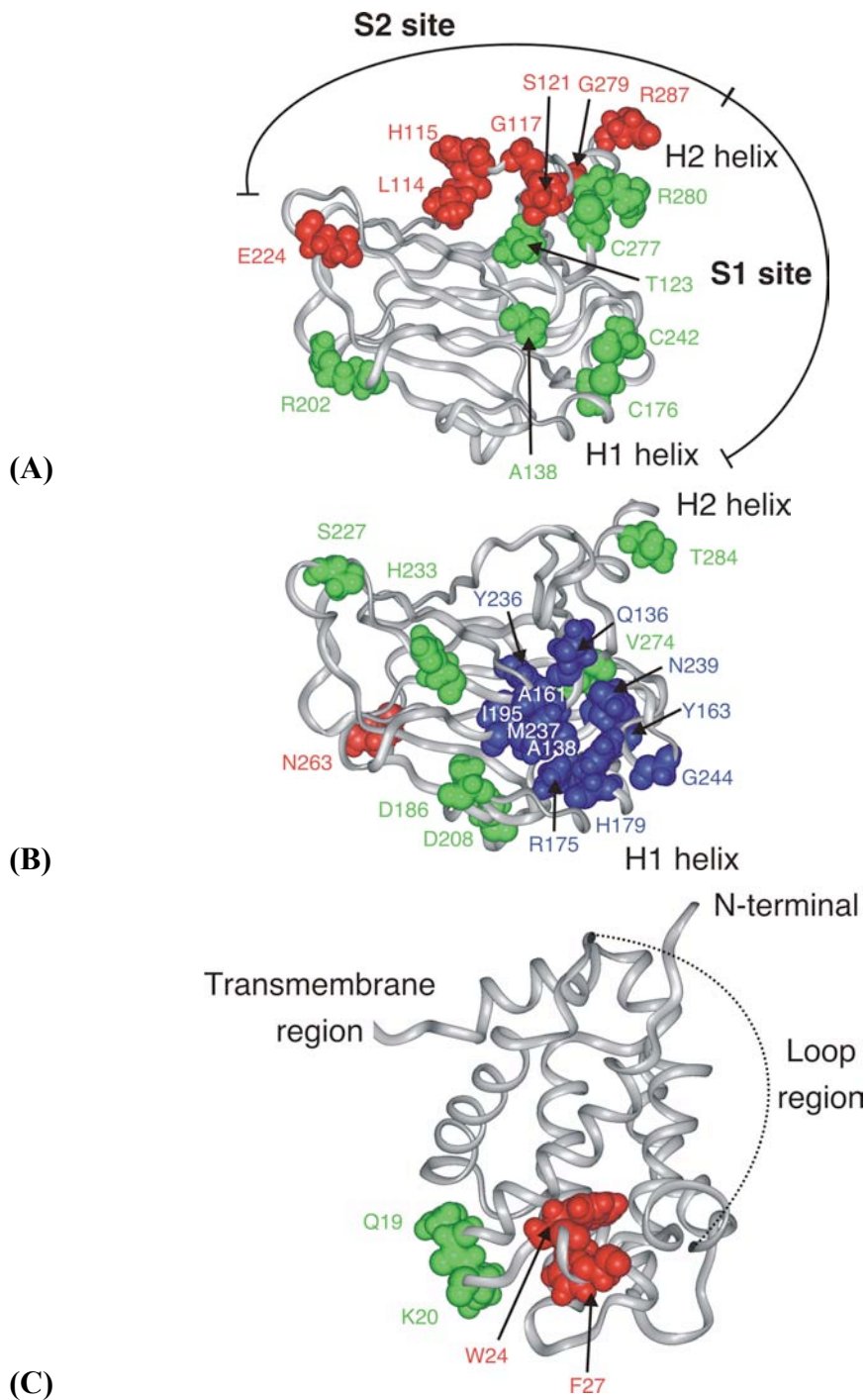
Figure 44: p53 DBD residues that are perturbed upon titration of Bcl-xLΔLT **(A)** and Bcl-2 **(B)** are mapped onto the crystal structure of (p53 DBD, PDB-Code 1TSR) The color coding corresponding to figure 2. Residues which disappeared upon titration with Bcl-2 **(B)** are given in blue. In figure 3(A) the binding sites S1 and S2 are indicated additionally. **(C)** Residues which are perturbed for Bcl-xL upon titration with p53 DBD.

6.4.1.3   A Model for the p53 DBD-Bcl-xL Complex

Based on the experimental NMR data, significantly shifted residues in the HSQC spectra of p53 DBD and loop-deleted Bcl-xLΔLT upon complexation were introduced as ambiguous interactions restraints in a calculation of an NMR-based complex-model using HADDCOK (Dominguez et al., 2003). Docking calculations were started from the monomeric structures for p53 DBD (PDB code 1TSR) and Bcl-xL, Bcl-xLΔLT (PDB code 1LXL and 1BXL, respectively). For p53 DBD 7 residues (Leu-114, His-115, Gly-117, Ser121, Glu-224, Arg-280, Glu-287) were defined as active, and 12 additional residues as surface neighbors (passive residues). For Bcl-xL, two active (Trp-24 and Phe-27) and six passive residues were defined (Table 3) **Figure 45** shows in the upper part the energetically best cluster of ten complex-models after refinement in a "water-box" (Table 4).

Table 3: List of active and passive residues used for the definition of ambiguous interaction restraints (AIRs) and flexible / fully flexible segments

p53 DBD	*Active residues[a]*	L114, H115, G117, S121, E224, R280, E287
	Passive residues[b]	S116, K120, V122, P128, E221, P222, P223, V225, S227, T231, R283, N288, L289
	Flexible interface	G112-A129; P219-H233; P278-L289
	Fully flexible segments	none
Bcl-xL	*Active residues[a]*	W24, F27
	Passive residues[b]	S23, S25, Q26, F27, K157, E158
	Flexible interface	Q19-E31; V155-Q160
	Fully flexible segments	G21-P82; G196-E211

[a] All solvent accessible residues which are significantly shifted in the HSQC spectra are defined as „active".

[b] All solvent accessible residues which are surface neighbors of active residues are defined as „passive".
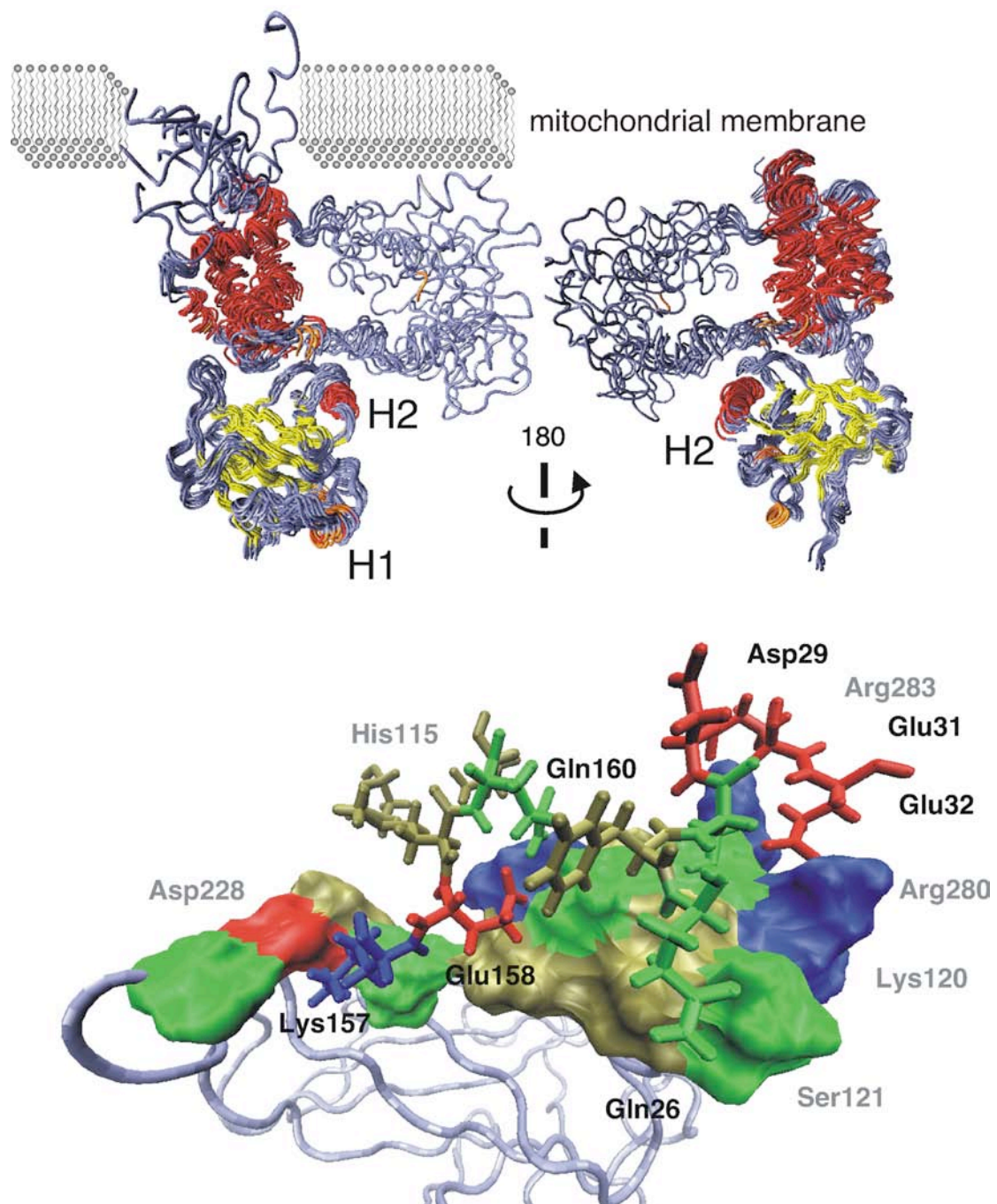
Figure 45: Ribbon ensemble of 10 energetically best complex structures of loop-deleted Bcl-xLΔLT bound to p53 DBD at the S2 surface, complex structure calculations was done based on HSQC chemical shift changes using HADDOCK (Dominguez et al., 2003). At the bottom a surface representation (residue labels in gray) of the p53 DBD-Bcl-xL interface S2; Bcl-xL residues are given as "ball and sticks" diagram labeled in black: Positive charged residues are colored blue, negative charged residues are colored in red. Green residues are polar.

Table 4: Structural statistics of the ten best water-refined Bcl-xL-p53 DBD model structures

Backbone RMSD (Å) with respect to mean	
All backbone (including flexible loop regions)	2.49 ± 2.46
Backbone p53 DBD	1.21 ± 0.37
Backbone Bcl-xL	3.73 ± 2.94
Flexible interface backbone	1.45 ± 0.65
Number of ambiguous interactions restraints (AIRs)	
From p53 DBD	7
From Bcl-xL	2
Total number of AIRs	9
Protein-protein intermolecular energies	
E(vdW) (kcal mol^{-1})	-35.50 ± 7.81
E(elec) (kcal mol^{-1})	-575.42 ± 67.96
Proteins flexible interface energies	
E(vdW) (kcal mol^{-1})	-395.57 ± 11.09
E(elec) (kcal mol^{-1})	-3961.62 ± 51.95
Buried surface area (Å^2)	1359.01 ± 145.88
RMSD from idealized geometry	
Bonds (Å)	$3.2*10^{-03} \pm 2.8*10^{-5}$
Angles (deg)	0.41 ± 0.004
Ramachandran analysis	
Residues in most favored regions (%)	82.8
Residues in additional allowed regions (%)	14.0
Residues in generously allowed regions (%)	1.1
Residues in disallowed regions (%)	2.2

Based on the ten energetically best structures after flexible docking with HADDOCK 1.2 followed by refinement in explicit water.
[a] Definition of flexible interface see Table 1
[b] Non-bonded energies were calculated with the OPLS parameters using a cut-off distance of 8.5 Å.
[c] The buried surface area was calculated with CNS using a 1.4 Å radius water probe.

In the case of full-length Bcl-xL, these loop regions are defined as fully flexible throughout the calculations. Using stepwise refinement as described in Methods, complex formation according to the experimental shift data and stabilization of the complex by additional attractive interactions can be modeled. The long loop region (residues 21 – 82) of Bcl-xL has a predominant orientation towards the H2 helix of p53 which is due to attractive interactions of negatively charged residues Aps-29, Glu-31 and Glu-32 of Bcl-xL, which are not part of the deleted long flexible loop in Bcl-xLΔLT, with positively charged residues Arg-283, Arg-280 and Lys-120 of p53 DBD (**Figure 45**).

To corroborate that the calculated complex structures are not biased by the long flexible loop region 44 - 82 of Bcl-xL in terms of binding interface rigid-body

complex structures were generated using the loop-deleted structure 1BXL including the same interactions restraints. As stabilizing interactions of the flexible loop are restricted to the residues Asp-29, Glu-31 and Glu-32 the resulting complex structures are identical in terms of binding interface and in directionality of this loop. Thus in Bcl-xLΔLT, the loop shortening does not induce a significant tilt of these residues compared to the configuration they have in the full-length protein. This result is in agreement with NMR chemical shift titration experiments which yield no difference in shift perturbations of p53 DBD using the loop-deleted or the full-length Bcl-xL construct.

6.4.1.4 *Model of the p53/Bcl-xL Complex in the Context of the Mitochondrial Membrane*

The data are consistent with a recent report by Petros et al. which provided a first limited determination of chemical shift perturbation of ^{15}N labeled p53 DBD upon addition of Bcl-xL (Petros et al., 2004a). The chemical shift changes on p53 observed in the Petros et al. report are Arg-280, Cys-277, Ser-241, Cys-38, Cys-182 and Val-173, although they are rather small, not exceeding half a line width. The data confirm and extend this observation, since residues Arg-280 and Cys-277 are identically perturbed or in sequential neighborhood (e.g. our shifted residue Cys-242 is close to Petros Cys-238 and Ser-241). Perturbations observed in the spectra here presented are significantly pronounced and are supplemented by sequential residues of strongly shifted signals. More importantly, in addition and in contrast to Petros, significant changes for residues Leu-114 to Thr-123 from the p53 DBD loop region are observed. Concerning the contact sites on Bcl-xL, significantly shifted residues of Bcl-xLΔLT (Gln-19, Lys-20, Trp-24, Val-155 and Ser-164) in our ^{15}N-HSQC spectra are in general agreement with ^{13}C-HSQC Bcl-xLΔLT/p53 DBD data of Petros et al. (Petros et al., 2004a).

Taken together, this identifies a new unique binding interface (called S2). The molecular modeling that used the NMR data as restraint localized this second surface on the β-strand scaffolding of p53, at 90 degrees to the DNA and dimerization contact surface. However, this result needs to be put in context with previously published contextual model of Bcl-xL binding to the DNA contact surface of p53 DBD (which is called S1) (Mihara and Moll, 2003). The "S1"–model was generated using mutational analysis plus contextual restrains implemented in the Global Range Molecular Matching program (Vakser et al., 1999) and was experimentally validated by HSQC NMR results of Petros et al.

Bcl-2 is a very close structural homologue of Bcl-xL, in fact their tertiary structures are superimposable (residual mean squares deviation of 1.40A for 468 atoms involved). Our NMR data identify the binding site for Bcl-2 on the DNA contact surface S1 of p53 DBD (**Figure 43**).

Assuming exclusive binding of Bcl-xL to the S2 surface, one might predict that Bcl-xL is unable to displace p53 from it cognate DNA sequence. In fact, electrophoretic mobility shift assays show that a substantial excess of Bcl-xL is needed to compete against DNA binding (**Figure 46**) which would suggest that DNA binding and Bcl-xL binding sites are not identical.
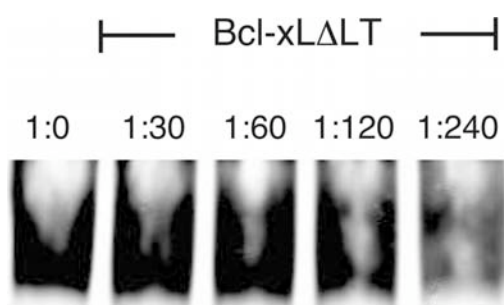
Figure 46: Inhibition of p53 DBD DNA binding activity in an electrophoretic mobility shift assay (EMSA) by competition with Bcl-xLΔLT. 4 µM fluorescence labeled consensus DNA was mixed with 8 µM p53 DBD and incubated at 4°C for 20 min. Subsequently a molar excess of 30, 60, 120 and 240 of Bcl-xLΔLT was added to the mixture and DNA binding was quantified by EMSA.

Integrating all available structural and biological data from this and our previous studies and that of Petros et al (Petros et al., 2004a), the following unifying trimeric model is proposed (**Figure 47**): Because of the ~90° relative orientation of S1 and S2 interaction sites, p53 can simultaneously interact with two molecules of anti-apoptotic Bcl-xL proteins. In this model, the p53 interface on Bcl-xL is the solvent accessible charged surface contributed by positions 17-24, 113-117 and 155-158 of Bcl-xL. Moreover, C-termini of both Bcl-xL remain sterically available to anchor in the outer mitochondrial membrane.
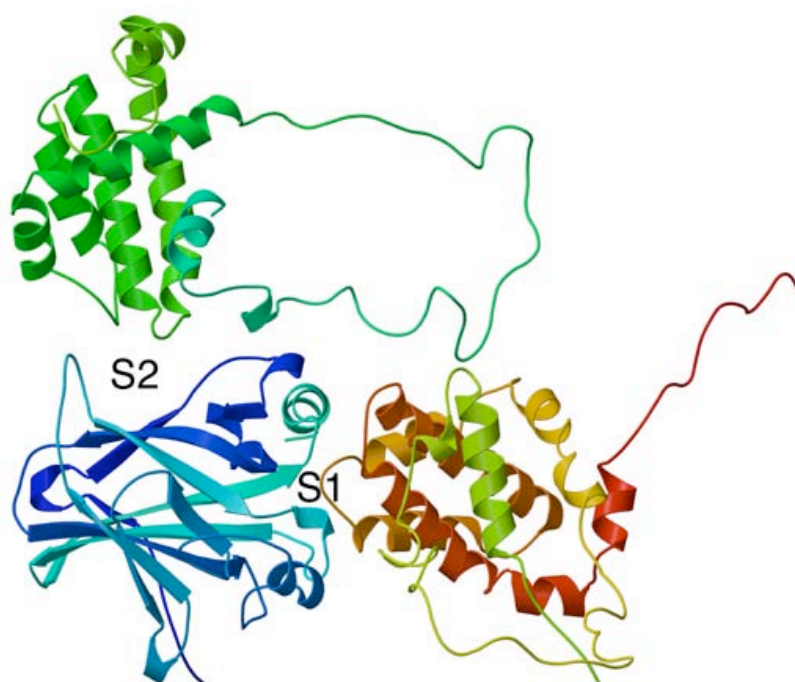
Figure 47: Unifying trimeric model of the p53/Bcl-xL complex using data from this study, Petros et al. (Petros et al., 2004a) and Mihara et al. (Mihara and Moll, 2003): Because of the ~90° relative orientation of S1 and S2 interaction sites, p53 (blue colors) can simultaneously interact with two molecules of Bcl-xL (green, S2 and orange, S1). C-termini of both Bcl-xL molecules remain sterically available to anchor in the outer mitochondrial membrane. The Figure was generated using Molscript (Kraulis, 1991) and Raster3D (Merritt and Bacon, 1997).

In summary, the study identifies a novel interaction surface S2 for antiapoptotic Bcl-xL on p53 DBD. This spectroscopic evidence, in conjunction with *i*) endogenous population of Bcl-xL/p53 in 4:1 molar ratio on stressed mitochondria; *ii*) displacement of cognate DNA from p53 DBD by Bcl-xL; *iii*) previously identified binding site (Petros et al., 2004a) by mutational and docking studies, and *iv*) evidence that p53 can bind Bcl-2 via S1 together provide a strong rationale for an oligomeric structural model of the p53/Bcl-xL complex. Since the function of p53 is to liberate the proapototic Bcl-2 family proteins from pre-existing inhibitory interactions with anti-apoptotic Bcl-2 members such as Bak, Bax and Bid (Perfettini et al., 2004) and reference therein), the ability of one p53 molecule to neutralize two anti-apoptotic molecules increases the overall efficacy of this step.

6.5   Sequential Backbone Assignment of p63 DBD

6.5.1   Results and Discussion

Triple labeled [75%-^{2}H,U-^{13}C,^{15}N], double labeled [U-^{13}C,^{15}N], and [U-^{15}N]-p63 DBD for the sequential resonance assignment were expressed and purified as described in Materials and Methods and by Klein et al. (Klein et al., 2001a). From 2L M9 minimal medium, 130 mg double labeled p63 DBD could be yielded. SDS gel electrophoresis after size exclusion chromatography shows however that a small fraction of p63 DBD is in a dimer-monomer equilibrium (**Figure 48**).
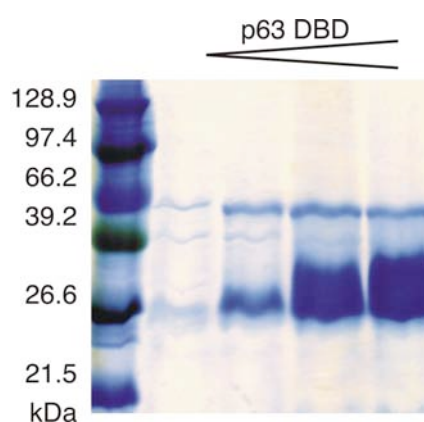
Figure 48: SDS-PAGE of [U-^{13}C,^{15}N]-p63 DBD after size-exclusion chromatography in increasing concentrations. The small band at approximately 50 kDa indicates a possible dimerization of p63 DBD.

6.5.1.1   NMR Spectroscopy

All NMR spectra were acquired at 303 K on Avance spectrometers (Bruker, Karlsruhe) operating at nominal ^{1}H frequencies of 600, 750 and 900 MHz, equipped with triple (^{1}H, ^{13}C, ^{15}N) and quadruple (^{1}H, ^{13}C, ^{15}N, ^{31}P) probes including triple axis pulse field gradients and lock switch units for ^{2}H decoupling. The following 3D triple resonance experiments were carried out with gradient selection and sensitivity enhancement: [U-^{15}N]-labeled sample; 2D ^{1}H,^{15}N-HSQC, 3D HNHA, 3D HNHB, 3D ^{15}N-edited TOCSY-HSQC (50 ms mixing time), 3D ^{15}N-edited NOESY-HSQC (80 ms mixing time) and 3D ^{15}N,^{15}Nedited HSQC-NOESY-HSQC (100 ms mixing time). [U-^{15}N, ^{13}C, 75% ^{2}H] labeled sample (with ^{2}H decoupling): 3D HNCO, 3D TROSY-HNCA, 3D TROSY-HN(CA)CO, 3D TROSY-HN(CO)CACB, 3D TROSY-HNCACB. All the experiments were processed and analyzed using the XWinNMR and Aurelia software (Bruker, Karlsruhe), respectively. The sequence specific resonance assignments were obtained with the help of our automatic assignment

program (Leutner et al., 1998). The backbone assignments could be confirmed through the observation of sequential NH_i-NH_{i+1} and $H\alpha_t$-NH_{i+1} interproton NOEs. Chemical shifts were indirectly referenced via the Ξ ratios (Wishart et al., 1995a; Wishart et al., 1995b).
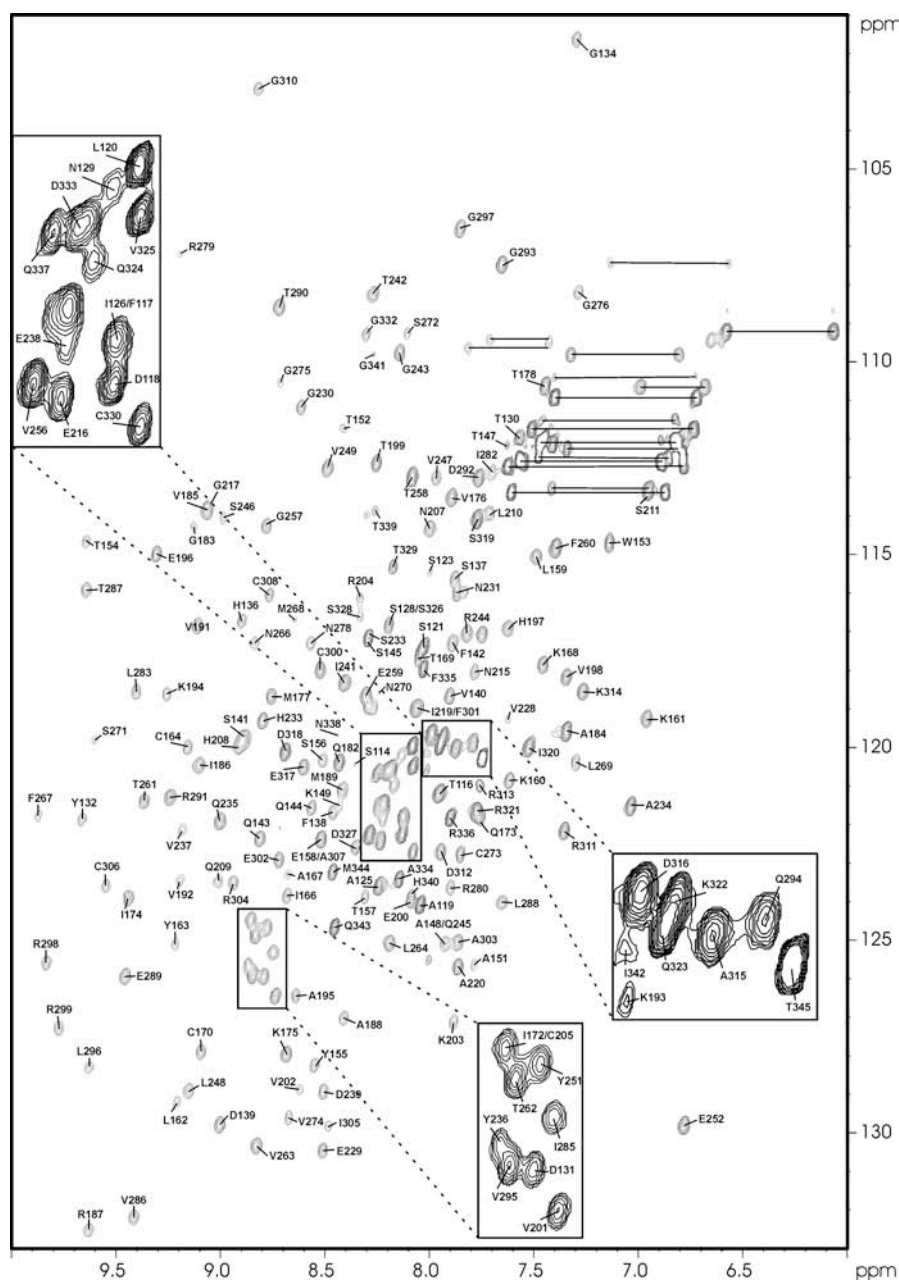
Figure 49: $^1H,^{15}N$ HSQC spectrum with three expanded views of ^{15}N, ^{13}C-labelled p63 in 90% H_2O, 10% D_2O at pH = 6.8, recorded on a 900 MHz Bruker spectrometer at 303 K. The peaks are labeled according to their original position in the complete p63 sequence (113–345). Sidechain amide proton resonances are connected with horizontal lines.

6.5.1.2   Extend of Assignment and Secondary Structure

The 2D ^{1}H,^{15}N HSQC spectrum of the p63 DBD (**Figure 49**) displays a good dispersion of the proton and nitrogen resonances. From the abovementioned triple resonance experiments, an almost complete backbone assignment (94% of the 214 non-Pro residues) could be achieved. Definitive assignments have not been obtained for residues Gly113, Ser114 and the short segment His224-Arg227, whereas Ser115, Arg212, Ser232, Tyr265, Met277, Ile284 and Asn331 could only be sequentially assigned. Overall, the backbone chemical shifts of the p63 DBD were found to be very similar to that of the p53 DBD for most sequence positions (Wong et al., 1999b). In combination with the high sequence homology, this is consistent with a similar global fold for both proteins. Overall, the secondary structure elements revealed by both chemical shifts and interproton NOEs of the p63 DBD are essentially identical to those found previously for p53, which is also consistent with a p53-like fold.
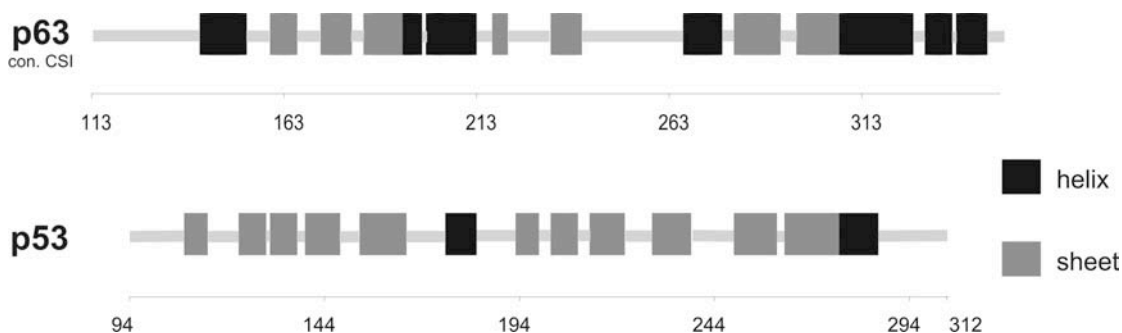
Figure 50: Secondary structural elements according to the consensus chemical shift index (CSI) of Hα, Cα, Cβ and CO of p63 DBD. Secondary structure of p53 DBD is given according to the crystal structure (Cho et al., 1994).

The chemical shifts for backbone resonances of p63 DBD have been deposited in the BioMagRes-Bank (http://www.bmrb.wisc.edu/) under the accession number BMRB-5700 (Furrer et al., 2003).

7 Studies on the Molecular Chaperones Hsp90 and Hsp12

7.1 Introduction

7.1.1 Protein Folding and Molecular Chaperones

Protein folding generates a particular three-dimensional structure from linear, one-dimensional polypeptide chain with a particular sequence of amino acid residues. However, most globular folded proteins are only marginally stable and slight changes in pH or temperature can convert a solution of biologically active proteins in their native state to a biologically inactive denatured state. The energy difference between these two states under physiological conditions is rather small, about 5-15 kcal/mol, which is comparable to the energy contribution of a single hydrogen bond in the order of 2-5 kcal/mol (Branden and Tooze, 1998). The low stability of the native state over the denatured state is biologically important, as living cells need active, globular folded proteins in correct quantities at appropriate times, and proteins in cells usually have a rapid turnover between protein synthesis and degradation. Furthermore, the functional activities of many proteins depend upon large conformational changes triggered by ligand binding, which would be inconsistent with a rigidly stabilized structure. Investigations of protein folding began in the 1960s with experiments of Christian Anfinsen and co-workers on the *in vitro* folding of ribonuclease A (Anfinsen et al., 1961). Ribonuclease A was denatured by incubation with 8 M urea and a reducing agent (Kauzmann, 1959), resulting in a loss of biological activity. When the denaturant and the reducing agent were removed by dialysis in Anfinsen´s experiment, the enzyme was found to slowly regain its activity and therefore obviously had refolded *in vitro* (Anfinsen, 1973). This observation showed that the three-dimensional structure of this protein is encoded in its amino acid sequence, and that no other factors are required for protein folding which is an autonomous and, under proper conditions, spontaneous process.

Intuitively one might imagine that all proteins search through all possible conformations in a random fashion until they are frozen at the lowest energy in the conformation of the native state. However, the biophysicist Cyrus Levinthal showed in 1968 by a simple calculation that this is not possible. Assuming that each peptide group has only three possible conformations in the Ramachandran diagram and that it converts one conformation into another in the shortest possible time of one picosecond

(10^{-12} seconds). A polypeptide chain of 150 residues would then have $3^{150} = 10^{68}$ possible conformations. To search all these conformations would require 10^{48} years which is far beyond the actual folding time of 0.1 to 1000 seconds. Therefore the folding process must be directed in some way through a kinetic pathway of unstable intermediates (Fersht, 1995) and consequently the observed natively folded conformation is possibly not the one with the lowest free energy but rather the most stable conformation kinetically accessible.
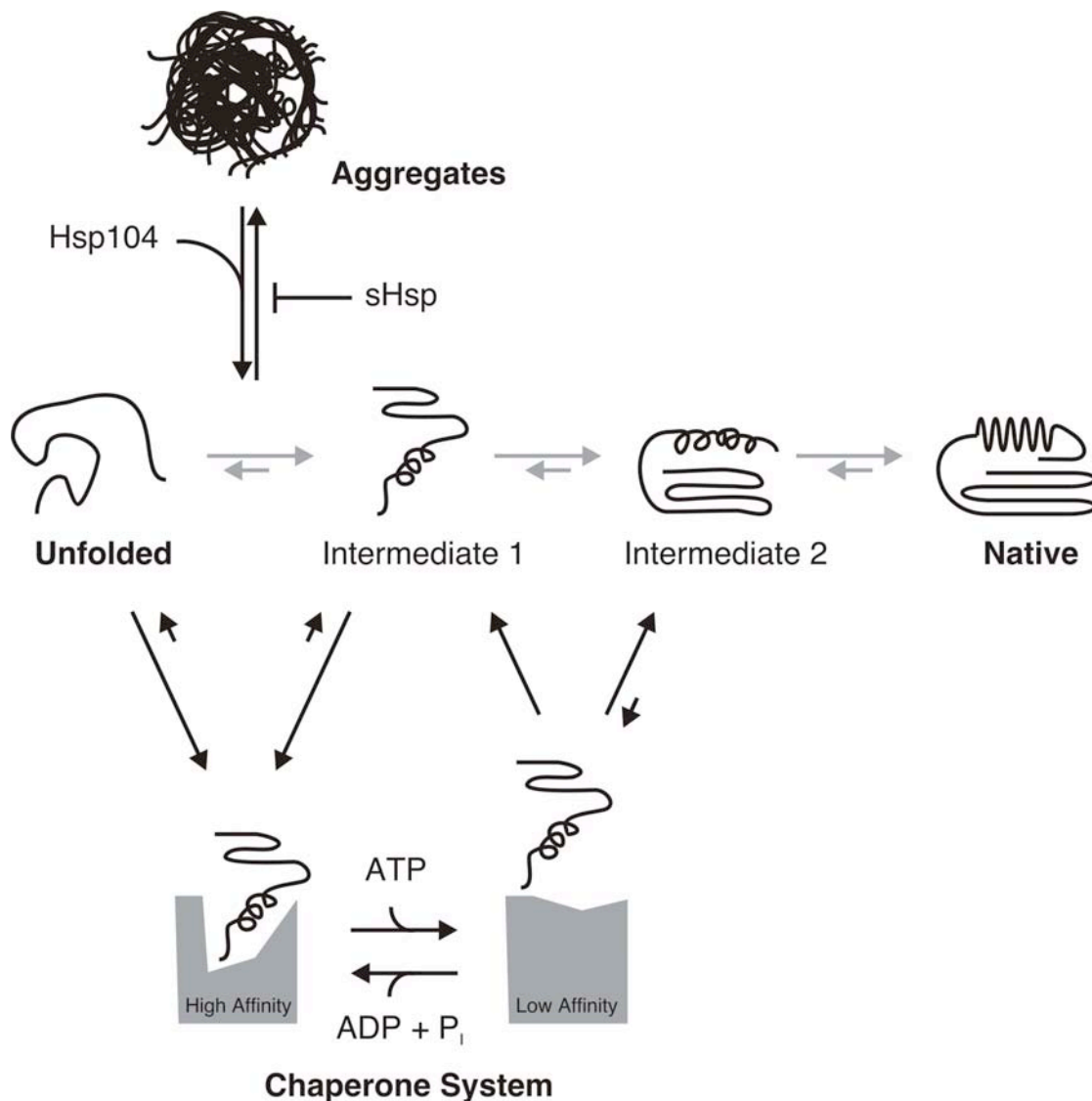
Figure 51: Chaperone-assisted protein folding. Protein biosynthesis and cellular stress result in unfolded polypeptide chains which fold via several intermediates to their native functional state. Intermediates which expose hydrophobic surfaces might be subject to aggregation processes. Molecular chaperones compete against this aggregation by binding to these species. ATP-mediated conformational changes trigger the release of the bound polypeptide chain.

Therefore it is important for living cells to prevent intermediate stages which block the further folding process. The most common obstacles to correct folding are (1) aggregation of these intermediates through exposed hydrophobic groups (prevented by molecular chaperones), (2) formation of incorrect disulfide bonds (corrected by the DsbA,B,C system) and (3) isomerization of proline residues (catalyzed by peptidyl-prolyl-cis/trans-isomerases). To circumvent these problems cells developed molecular chaperones, a special set of proteins that assist the folding process by preventing aggregation (Kiefhaber et al., 1991; Schwarz et al., 1996) and promoting a productive folding in a complex ATP-dependent manner (Buchner and Kiefhaber, 1990; Hartl, 1996). Although protein synthesis is the major source of unfolded polypeptide chains, molecular chaperones are found in all compartments of a cell where conformational rearrangements of proteins occur. In addition, at non-physiological high temperatures or in the presence of other stress-inducing factors, the possible loss of protein function, due to protein unfolding, is counteracted by producing an increasing amount of specific heat-shock proteins, which prevent an accumulation of protein aggregates (**Figure 51**). Several of these heat-shock proteins are found to be molecular chaperones.

7.1.2 Classes of Molecular Chaperones

Heat shock proteins can be divided into several major families or classes, according to their molecular weight and sequence homologies: Hsp100, Hsp90, Hsp70, Hsp60, Hsp40 and the family of small heat-shock proteins (Fink, 1999). Proteins from the same class are often structurally and functionally related, while there are hardly any homologies between chaperones from different classes. Nevertheless, they all share a common set of functional features, as there are (1) binding to proteins with exposed hydrophobic surfaces, (2) induction of conformational changes in the target proteins and (3) a controlled release of the bound polypeptide chain (Walter and Buchner, 2002). In the following sections the different classes of molecular chaperones are briefly presented. As most of the results in this chapter refer to Hsp90, a more detailed discussion is given for this family.

7.1.2.1 Hsp100 Family

The members of the Hsp100 family perform a diverse set of functions, including proteolysis. They are highly conserved, present in all organisms and contain an ATP and a polypeptide binding site. Hsp104 and ClpA (ClpB in *E. coli*) form six-membered rings; however, their diameter is much smaller than in GroEL, making it unlikely that the Hsp100 functions analogously to Hsp60. Hsp104 may act in concert with Hsp70 and DnaJ homologs to increase the yields of renatured protein (Glover et al., 1998). In addition, Hsp104 has been observed to solubilize aggregated proteins both *in vivo* and *in vitro* (Lee et al., 2004; Parsell et al., 1994; Shorter and Lindquist, 2004). Another feature of Hsp104 is its role in triggering a prion-like disorder in yeast, involving the extrachromosomal element PSI+ (Debburman et al., 1997; Narayanan et al., 2003; Reif et al., 2004).

7.1.2.2 Hsp60 Family

Many of the Hsp60 chaperones are known as chaperonins, like GroEL (cpn60), and TCP-1 are barrel-shaped oligomeric protein complexes with a large central cavity in which non-native proteins can bind (Saibil and Ranson, 2002). The term chaperonin was originally proposed by Ellis to refer to non-heat-induced Hsp60 (Ellis, 1990). GroEL is probably the most studied of all molecular chaperones; in combination with its co-chaperonin GroES (cpn10) and ATP it facilitates protein folding by preventing aggregation and in addition also allowing partially folding in an environment conducive to stabilizing the native fold (Chen et al., 2001; Lilie and Buchner, 1995). GroEL and its homologs are found in prokaryotes, chloroplasts, and mitochondria, whereas TCP-1 and its homologs are found in the eukaryotic cytosol. Members of the

Hsp60 family are also involved in the assembly of large multiprotein complexes such as Rubisco (Cheng et al., 1989; Viitanen et al., 1990) and in the thermophilic archaea (Heller et al., 2004; Horwich and Saibil, 1998). The structure of the *E.coli* chaperonin GroEL has been solved by X-ray crystallography (Boisvert et al., 1996; Xu et al., 1997) (**Figure 52**) and electron microscopy (Saibil, 1996) and consists of 14 identical subunits (each 57 kDa) in two stacked heptameric rings, each containing a central cavity with a diameter of 45 Å. This cavity is large enough to accommodate proteins of 40-50 kDa. Each domain consists of three subunits, the equatorial, the intermediate, and the apical. The latter, forming the entrance of the central cavity, undergoes major conformational changes on binding of ATP and the co-chaperonin GroES (Heller et al., 2004; Saibil et al., 2002), leading to substantial changes in the hydrophobic nature of the cavity. The co-chaperone GroES is a dome-shaped ring-structure with a diameter of 75 Å (Hunt et al., 1994), consisting of seven subunits (each 10 kDa). Peptide binding is mediated by a so-called mobile loop of GroES (Landry et al., 1993; Richardson et al., 2001) and is in addition dependent on nucleotides bound to the equatorial domain of the GroEL ring.
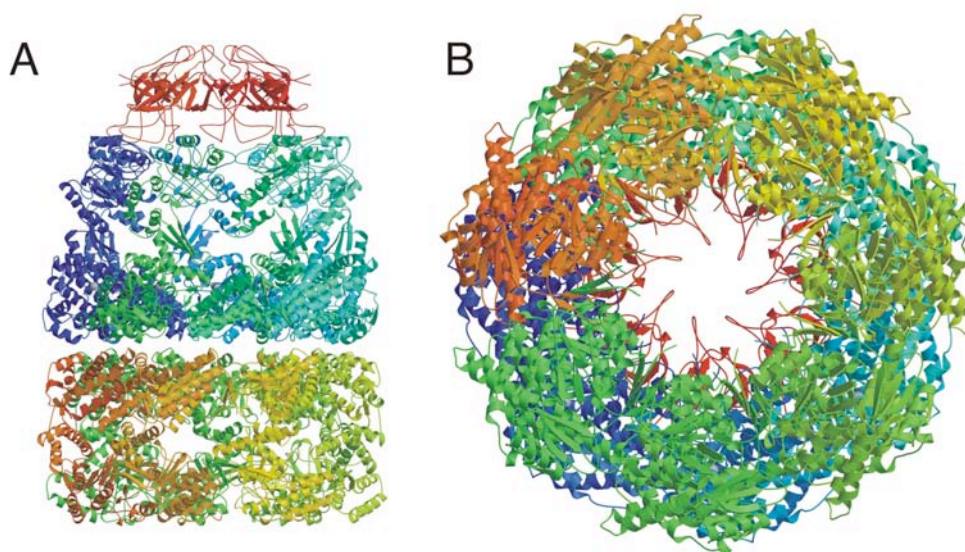
Figure 52: Crystal structure of the asymmetric GroEL/GroES chaperonin complex (pdb-entry: 1AON) (Xu et al., 1997). (A) Front view of the complex. In red is shown the co-chaperonin GroES; GroEL is composed of two rings, each consisting of seven subunits. The *cis* ring (blue) has bound seven ATP and is associated with GroES, resulting in major structural changes of this GroEL ring. Hydrolysis of ATP induces second conformational rearrangements, which allows the *trans* ring (yellow) to bind polypeptide. Bound ATP to the *trans* ring induces the release of polypeptide in the *cis* ring. (B) View from the bottom. The figures were generated with Molscript (Kraulis, 1991) and Raster3D (Merritt and Bacon, 1997)

The TCP-1 is a hetero oligomeric 970 kDa complex containing several structurally related subunits of 52-65 kDa. These are assembled into a ring complex that resembles the GroEL double ring. In contrast, to GroEL, the TCP-1 ring complex appears to function independently of a small co-chaperonin protein such as GroES. However, it has been shown that TCP-1 complexes are involved in the folding of very few proteins in the eukaryotic cytosol (Frydman et al., 1992; Kubota et al., 1994).

7.1.2.3 Hsp70 Family

The Hsp70 family is very large, with most organisms having multiple members; many eukaryotes have at least a dozen and more different Hsp70 proteins, occurring in a variety of cellular compartments. For example, the yeast *S. cerevisiae* produces 14 different versions of Hsp70 (Craig et al., 1999). The most extensively studied member of the Hsp70 family is DnaK from *E. coli*. It is involved in many cellular processes, including protein folding and degradation of unstable proteins by binding short hydrophobic segments in partially folded polypeptides (Fink, 1998; Frydman et al., 1999; Hartl, 1996; Hartl et al., 1994). Hsp70 chaperones are composed of two major functional domains. The N-terminal, highly conserved ATPase domain binds and hydrolyzes ATP, whereas the C-terminal domain is required for polypeptide binding; both act in a cooperative manner for target protein folding. Crystallographic structures of the bovine ATPase domain, the DnaK peptide-binding domain complexed with a peptide substrate and the human Hsp70 ATPase domain have been determined (Flaherty et al., 1990; Sriram et al., 1997; Zhu et al., 1996). The ATPase domain is structurally similar to actin and hexokinase, comprised of two subdomains separated by a deep cleft within which the MgATP and MgADP bind (Flaherty et al., 1991). The structure of the peptide binding domain consists of a β-sandwich subdomain followed by α-helices. The peptide is bound to DnaK in an extended conformation through a channel defined by the loops of the β-sandwich. Only five residues of the substrate make significant contacts with Hsp70, which might explain the observed specificity for short hydrophobic peptides. The stability of the Hsp70/polypeptide complex is increased by the hydrolysis of ATP.

However, kinetic studies indicate that Hsp70 alone is not able to compete against fast aggregation processes in the order of seconds, as the ATP hydrolysis is too slow. The efficiency is enhanced by the co-chaperones Hsp40 and GrpE (**Figure 53**). In the presence of Hsp40, ATP hydrolysis is accelerated, thus forming the more stable Hsp70/ADP/polypeptide ("closed") complex. GrpE decreases the affinity of Hsp70 for nucleotides and therefore facilitates nucleotide exchange (Langer et al., 1992; Schroder et al., 1993) (**Figure 53**).
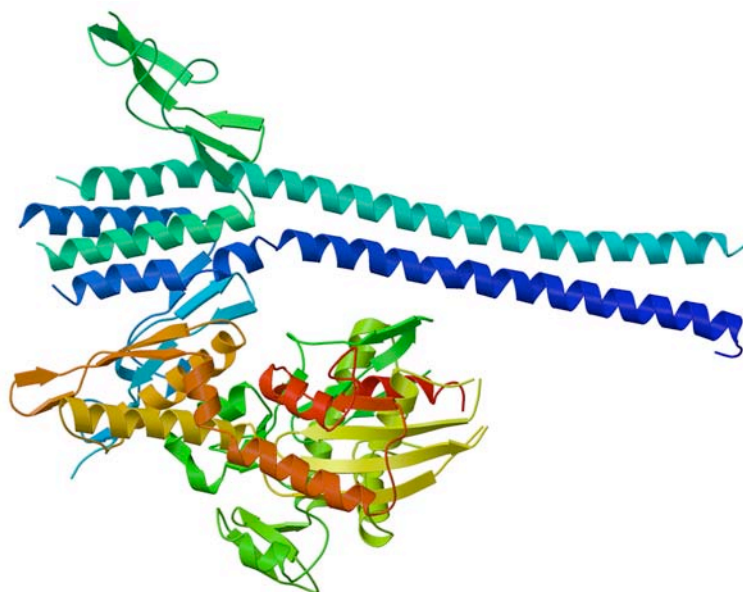
Figure 53: Crystal structure of the nucleotide exchange factor GrpE (blue and green), bound to the ATPase domain of the molecular chaperone DnaK (pdb-entry: 1DKG). The nucleotide is bound in the cleft between the two subdomains of the ATPase domain (Harrison et al., 1997). The figure was generated using Molscript (Kraulis, 1991) and Raster3D (Merritt and Bacon, 1997)

7.1.2.4   Hsp40 Family

The Hsp40 or DnaJ (from *E. coli*) family consists of over 100 members and is defined by the presence of a highly conserved J domain of about 78 residues (Caplan et al., 1993). Mutational analysis revealed that this domain is essential for the interaction between Hsp40 and Hsp70. Much variability is seen in the non-J domains of members of this family. The most important features of Hsp40 are its binding to peptides and its stimulation of ATP hydrolysis of Hsp70 (Cyr et al., 1994). Nuclear magnetic resonance has been used to determine the three-dimensional structure of the J domain in DnaJ from *E. coli* and humans (Hill et al., 1995; Qian et al., 1996; Szyperski et al., 1994). The structure is dominated by two long helices, with a hydrophobic core of highly conserved sided chains. A current model of Hsp40 and Hsp70 cooperativity assumes that a polypeptide substrate first binds to Hsp40 (Schroder et al., 1993). The Hsp40/substrate complex than associates with Hsp70/ATP, followed by a substrate transfer to the open cleft of Hsp70 which is locked by Hsp40-stimulated ATP hydrolysis. The functional cycle of Hsp70/Hsp40 is completed by the GrpE-mediated (Liberek et al., 1991) exchange of ADP for ATP and the dissociation of the complex.

7.1.2.5 Small Heat Shock Proteins

The small heat shock protein (sHsp) family consists of 12 to 43 kDa proteins which form oligomeric complexes, mainly of 12 to 42 subunits (**Figure 54**). These proteins have been found in almost all organisms studied so far. In contrast to the other classes, they show a larger heterogeneity in sequence and size (Haslbeck et al., 2004; Haslbeck and Buchner, 2002; Jakob and Buchner, 1994; Jakob et al., 1993). They all have in common a conserved C-terminal domain, the α-crystallin domain, which refers to the most prominent member of the family, the eye-lens protein α-crystallin, its major role is being the binding of denatured proteins and preventing their aggregation which would result in cataracts (Dejong et al., 1993). Compared to the molecular chaperones, sHsps have a higher binding capacity. They are able to bind large amounts of non-natively folded proteins, up to one target protein per subunit of the oligomeric sHsp complex (Jakob and Buchner, 1994). Upon substrate binding sHsps form, in a highly cooperative fashion, large, globular shaped complexes (Haslbeck et al., 1999). *In vitro* studies on Hsp26 from yeast showed that at temperatures above 40 °C, the well-defined oligomeric complex dissociates reversibly into stable dimers which expose binding sites for non-native proteins (Haslbeck et al., 1999). The resulting Hsp26/substrate complex shows an organization which is completely different from the original Hsp26 complex. In contrast to other molecular chaperones no active release mechanism has been found so far; furthermore the release of substrate from these sHsp complexes is not spontaneous.

Figure 54: Biologically active unit of the archaeal sHsp16.5 as determined by X-ray crystallography (Kim et al., 1998). The figure was generated using Molscript (Kraulis, 1991) and Raster3D (Merritt and Bacon, 1997).
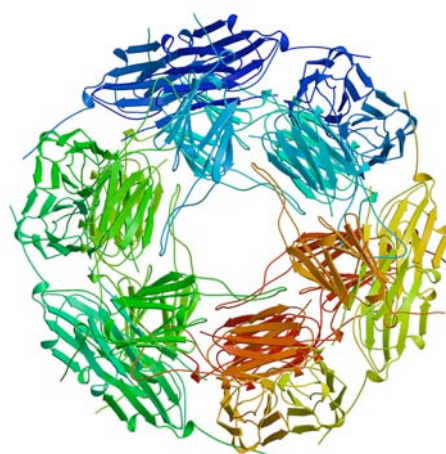
However, it has been demonstrated that bound enzyme can be shifted back to its native state by adding a ligand which stabilizes its functional conformation (Ehrnsperger et al., 1997). In addition, in some organisms the expression of sHsp and Hsp70 is genetically linked (Michelini and Flynn, 1999). These findings imply that sHsps bind non-native proteins under stress conditions where large quantities of

unfolded proteins occur, and thereby prevent their aggregation, making a subsequent refolding by Hsp70 or other ATP-dependent chaperones possible (Kampinga et al., 1994; Kim et al., 2003).

The three-dimensional structure of an archaeal sHsp (Hsp16.5) has been studied by X-ray crystallography (Kim et al., 1998), showing a hollow sphere with openings to the inside and an external diameter of 120 Å, consisting of 12 identical dimer subunits. The C-terminal domain of each monomer is predominantly a β-sheet (**Figure 54**), whereas the N-terminal domain could not be resolved in detail.

7.1.3 Hsp90 Family

Members of the Hsp90 family are highly conserved, essential proteins found in all organisms from bacteria to humans. Examples include the cytosolic form in eukaryotes, the ER form Grp94, and the *E. coli* homolog HtpG. The Hsp90 system is a chaperone complex which is far more complex than both GroEL/GroES and Hsp70, as it includes the Hsp70 system, at least in parts of the chaperone cycle. Furthermore it includes a large number of cofactors. In contrast to other chaperone systems, a growing number of client proteins have been identified which depend on Hsp90 in order to reach their native and functional state (Richter and Buchner, 2001). The common structural feature of client proteins is not yet known; however, Hsp90 has several specific interactions, for example with cytoskeleton elements, signal transduction proteins and protein kinases (Bose et al., 1996; Buchner, 1999; Jakob and Buchner, 1994; Yahara, 1998; Young et al., 2001). Therefore Hsp90 is an important key component in the regulation of the cell cycle, revealing an additional level of regulation and consequently constituting an interesting target for therapeutic intervention (Buchner, 1999). For example, *in vivo* screens for *src* inhibitors led to the selection of the ansamycin Geldanamycin. However, subsequent analysis showed that this potential *src* inhibitor binds in fact to Hsp90 with high affinity and specificity, leading to Hsp90 inactivation and in turn to decreased levels of active *src* kinase (Whitesell et al., 1994).

7.1.3.1.1 *Hsp90 Domain Organization and Structural Properties*

Hsp90 consists of two highly conserved domains which are connected by a charged linker region. This linker region has a variable length for different eukaryotic species, whereas prokaryotic Hsp90 family members such as *E. coli* HtpG miss this linker region at all (Lindquist and Craig, 1988). Hsp90 is functional as a homodimeric protein with a dimerization subdomain localized at the very C-terminal end of the C-terminal domain with a dissociation constant of about 60 nM (Harris et al., 2004; Richter et al., 2001). The N-terminal domain of Hsp90 (residues 1-215) binds and hydrolyses ATP and it has been shown that the hydrolysis of ATP by the N-terminal domain of Hsp90 is necessary to perform its chaperone task *in vivo*, because mutant Hsp90 proteins that do not hydrolyze ATP do not support the functions of Hsp90 essential for viability (Obermann et al., 1998; Panaretou et al., 1998; Prodromou et al., 1997).
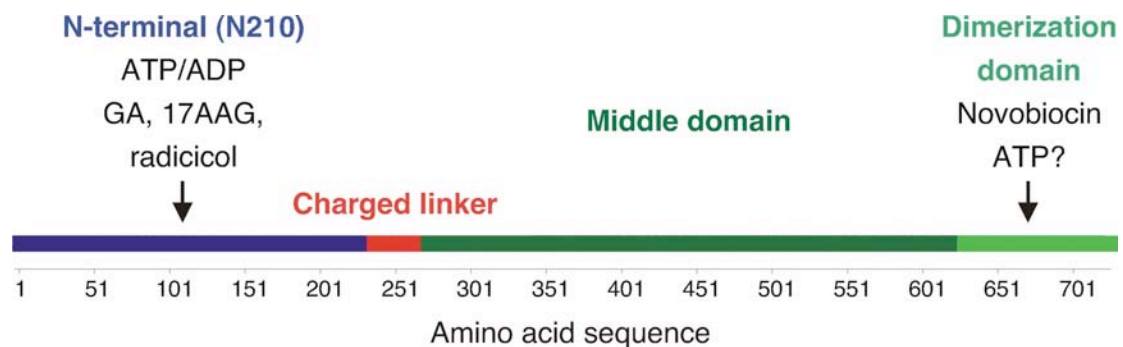
Figure 55: Domain organization of Hsp90 in yeast. The N-terminal ATP binding domain is shown in blue. A charged linker (red) separates the N-terminal from the C-terminal domain (green). At the very end of the C-terminal domain the dimerization site of Hsp90 is localized. The ATP binding domain also binds the competitive inhibitors Geldanamycin (GA) and its analogs 17AAG and Radicicol.

Recent studies indicate that ATP binding to the N-terminal domain leads to a transient dimerization of the N-terminal domains, inducing major conformational changes, followed by the stimulation of the ATPase activity (Prodromou et al., 2000; Richter et al., 2001). This N-terminal dimerization is achieved by a "strand swapping" mechanism, which includes the first 24 amino acids of the N-terminal domain (Richter et al., 2002). These ATP-induced conformational changes might be needed for the specific interactions with different cofactors and partner proteins (Walter and Buchner, 2002).
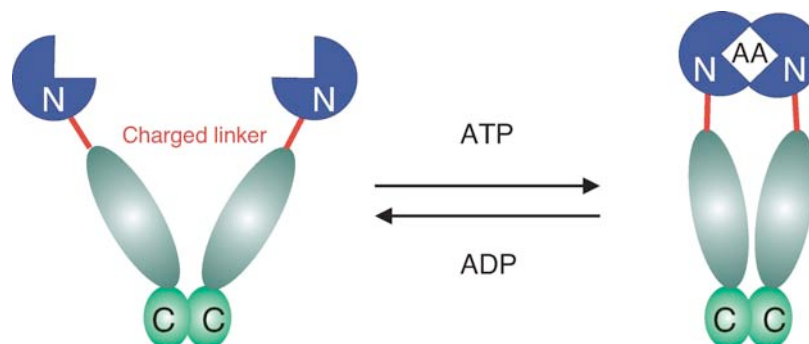
Figure 56: ATP binding to the N-terminal domain induces its transient dimerization. Major conformational changes might be necessary during the ATPase cycle in order to bind to different cofactors and partner proteins. *A* indicates bound ATP.

Up to now, the X-ray crystallographic structures of the N-terminal nucleotide-binding domain from yeast and human Hsp90 in complex with ADP, ATP, Radicicol and Geldanamycin are known (Prodromou et al., 1997; Roe et al., 1999; Stebbins et

al., 1997). These structures identified Hsp90 as a member of the GHKL (Gyrase, Hsp90, Kinase, MutL) superfamily of proteins (Bergerat et al., 1997), whose nucleotide binding sites share a common fold (Dutta and Inouye, 2000) (**Figure 57)**. Studies on gyrase and MutL also indicated that the nucleotide binding domains dimerize in response to ATP binding.
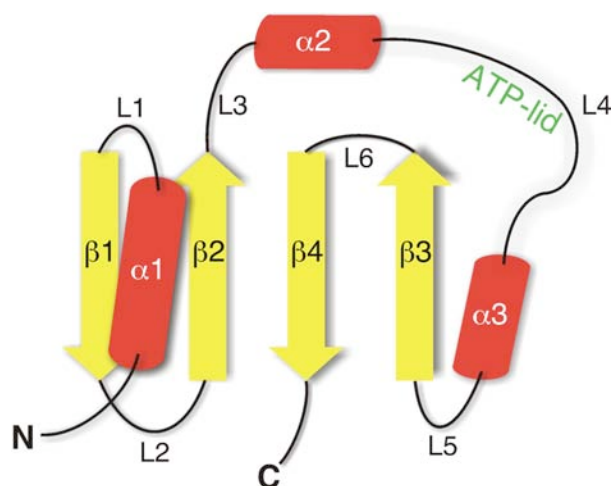
Figure 57: Schematic representation of the core elements of the GHKL ATP-binding fold (Bergerat) (Bergerat et al., 1997) as deduced from the structures of the ATP-binding domains of EnvZ, CheA, DNA gyrase B, Hsp90 and MutL. Three helices form a layer over a four-stranded antiparallel β sheet. The most unique feature characterizing this fold is the long flexible ATP-lid (L4). Hsp90 has two additional helices (α´and α´´) within this L4 loop between helices H2 and H3. High mobility of this ATP-lid has been indicated of the solved structures of all the member families of the GHKL superfamily (Dutta and Inouye, 2000).

The three-dimensional structures of the N-terminal domain of Hsp90 (**Figure 58**) has nine helices and an antiparallel β sheet of eight strands that together fold into an α/β sandwich. One face of the β sheet is hydrophobic and packs against a layer of five helices. A second layer of helices is localized at the periphery of the sandwich. At the center of the "helical face" of the α/β sandwich, a wide opening extending into the hydrophobic core of the structure forms a pronounced pocket of about 15 Å depth.

The pocket has the β sheet as its base and at its side three helices and a loop, containing residues which are highly conserved throughout species (Stebbins et al., 1997). All ligands have been shown to bind into this pocket; for ATP and ADP, the nucleotides adopt a unique kinked conformation which has not been observed for any other type of ATP binding protein. In this conformation, the γ-phosphate points to the outside of the protein and is the only part of the nucleotide which is solvent-accessible. Unexpectedly, in crystal structures of the N-terminal domains, ligand

binding did not result in detectable conformational changes (Prodromou et al., 1997; Roe et al., 1999; Stebbins et al., 1997).

Figure 58: Three-dimensional structure of the N-terminal of Hsp90 (pdb-entry: 1A4H). The domain consists of an α/β sandwich with a central 15 Å deep nucleotide binding pocket with the β sheet as its base. The competitive inhibitor Geldanamycin is shown as CPK model. The figure was generated using Molscript (Kraulis, 1991) and Raster3D (Merritt and Bacon, 1997).

Furthermore the three-dimensional structures of the middle domain of Hsp90 from yeast (residue 273-560) (Meyer et al., 2003) and the C-terminal domain of HtpG from *E. coli* (residue 511-624) have been solved (Harris et al., 2004). The crystal structure of the middle segment of yeast Hsp90 reveals considerable evolutionary divergence from the equivalent regions of other GHKL protein family members such as MutL and GyrB, including an additional domain of new fold. The middle domain of Hsp90 has been identified as the binding site for the co-chaperones p50 (cdc37) and Aha1. These results suggest possible mechanisms by which p50 inhibits and Aha1 stimulates Hsp90s ATPase activity (Meyer et al., 2004; Roe et al., 2004). The C-terminal domain of HtpG folds to an α/β sandwich, containing five helices and a small three-stranded β sheet. The C-terminal helices H4 and H5 interact with their equivalent counterparts from a second molecule around a 2-fold symmetry axes to form the dimer via a four-helix bundle. The helix-helix interface is predominantly hydrophobic and fringed by a few charged residues (Harris et al., 2004).

7.1.3.1.2 Role and Function of Hsp90

Hsp90 is highly abundant, comprising up to 1-2 % of the total cellular proteins (Buchner, 1999). As Hsp90 is involved in the regulation of ligand binding to steroid receptors and also influences the phosphorylation status of many key signal transduction proteins such as c-Raf-1, Akt or ErB2, as well as cell cycle checkpoint control proteins such as Polo-1 and other mitotic kinases, it has a major impact on all the pathways that regulate cellular outcome, including cell growth, division, differentiation and apoptosis (Sreedhar and Csermely, 2004; Buchner, 1999; De Carcer et al., 2001; Isaacs et al., 2003; Maloney and Workman, 2002) (**Figure 59**). Furthermore recent studies revealed that Hsp90 plays a key role in development and evolution, by acting as a buffer against phenotypic mutations which can be effectively kept functionally hidden by Hsp90 (Queitsch et al., 2002).
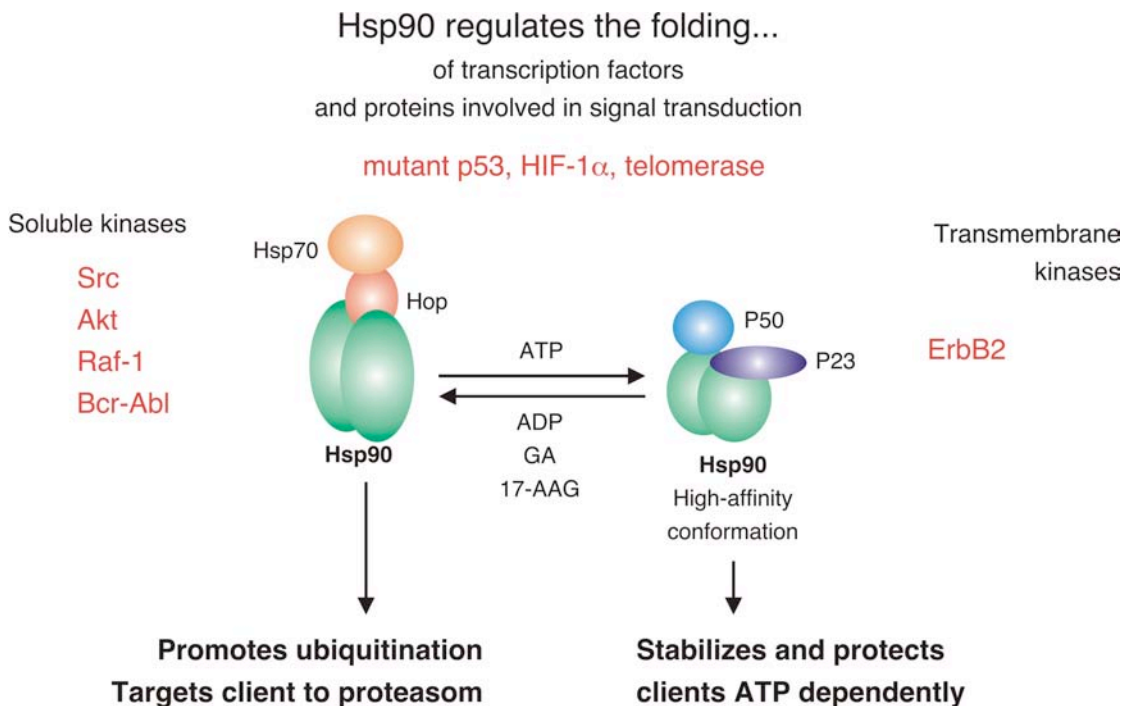
Figure 59: Hsp90 – depending on a number of cofactors – regulates the folding of several key components in signal transduction, cell cycle control and apoptosis.

The activity of Hsp90 is regulated positively and negatively by various co-chaperones and partner proteins. These include the Hsp70 system and Hop/p60/Sti1 which bring the Hsp90 and Hsp70 system together and function as an ATPase inhibitor of Hsp90 upon binding (Walter and Buchner, 2002). Cdc37/p50, Sba1/p23 are other partner proteins and co-chaperones. In addition, the recently discovered Aha1 functions as an activator of Hsp90 ATPase activity (Meyer et al., 2004;

Panaretou et al., 2002). Further Hsp90 cofactors belong to the class of peptidyl-prolyl isomerases (PPIases) (Walter and Buchner, 2002).

For the regulation of the conformation, client proteins have to pass through three complexes during a ATPase chaperone cycle (**Figure 60**), which differ in the composition of cofactors. Thereby also Hsp90 undergoes large conformational changes involving regions C-terminal of the ATP-binding site (Grenert et al., 1997; Weikl et al., 2000) which are also required for an efficient proceeding of the ATPase reaction. **Figure 60** illustrates the Hsp90-assisted hormone uptake of a steroid hormone receptor (SHR). First, a non-hormone-binding conformation of the SHR is captured by the Hsp70 system, which then binds via Hop/Sti1 to the Hsp90 dimer. ATP hydrolysis by Hsp70 results in a substrate transfer from Hsp70 to Hsp90, forming the intermediate complex. Hsp70/Hop are replaced by peptidyl-prolyl isomerase and the co-chaperone p23 upon binding of ATP to Hsp90, forming the mature complex. The receptor switches to its active conformation and upon hormone binding the SHR is released (Walter and Buchner, 2002; Pratt and Toft, 2003).
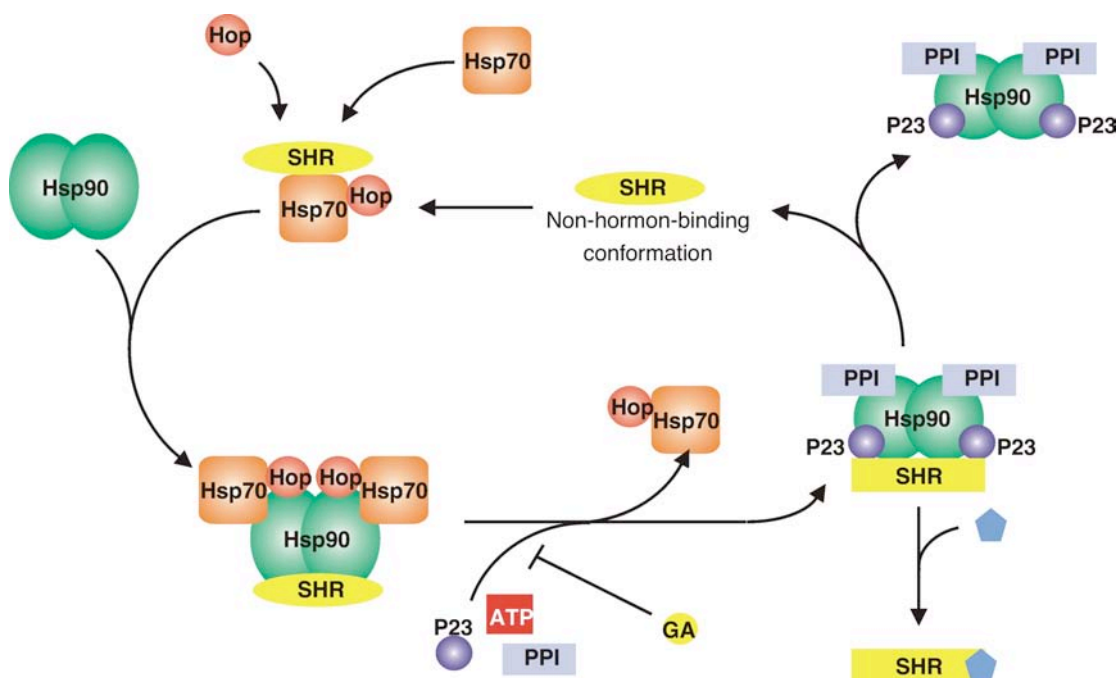
Figure 60: Hsp90-assisted steroid hormone uptake. Hsp70 captures an inactive conformation of the SHR, followed by Hop mediated interaction with Hsp90. ATP hydrolysis of Hsp70 results in the substrate transfer from Hsp70 to Hsp90. Hsp70 and Hop are replaced by p23 and PPI upon ATP binding to Hsp90. Upon binding of the hormone ligand the SHR is released from the complex. Adapted from (Walter and Buchner, 2002).

As it has been shown for steroid receptors, also p53 shuttles between the cytoplasm and the nucleus. And like unliganded steroid receptors (Pratt and Toft, 2003), some cytoplasmic p53 mutants retained in the cytoplasm were found to be heterocomplexed with Hsp90. These p53-Hsp90 complexes are formed by the same Hsp90/Hsp70-based chaperone system that assembles steroid receptor complexes (King et al., 2001)s. One effect of Hsp90 complexation is the stabilization and protection of client proteins from degradation by the ubiquitin-proteasome pathway. This has been shown for p53, where its binding to Hsp90 inhibits MDM2-mediated degradation (**Figure 18**) (Peng et al., 2001). Another effect is the Hsp90-mediated transport to the nucleus. It is known that p53 tracks along microtubules by cytoplasmic dynein "motors" to the nucleus (Gee et al., 1997; Vallee and Gee, 1998). In a recent study it could be demonstrated that Hsp90 is responsible for the linkage between the p53 "cargo" and the immunophilin-dynein complex and that prevention of this link *in vivo* inhibits the nuclear transport of p53 (Galigniana et al., 2004; Pratt et al., 2004).

7.1.4 Heat Shock Proteins as Pharmalogical Targets in Apoptosis Modulation

Heat shock proteins such as Hsp70, Hsp27 and Hsp90, which can inhibit apoptosis by direct physical interaction with apoptotic molecules, are overexpressed in several tumor cells (Jolly and Morimoto, 2000). Hsp70 is highly expressed in human breast tumors and is needed for their survival (Nylandsted et al., 2002), and Hsp90 was reported in prostata carcinomas (Akalin et al., 2001). Heat shock proteins can bind to procaspases and inhibit their activation (Beere and Green, 2001), they also can block several caspase-independent pathways of apoptosis, which makes their inhibition an efficient tool in inducing a relatively tumor-cell-specific apoptosis. *Vice versa*, key pro- and antiapoptotic processes also regulate the synthesis of heat shock proteins, by down-regulating the respective transcription factor, HSF-1 and by apoptosis-induced proteolysis of HSF-1 (Sreedhar and Csermely, 2004). Moreover, tumors undergo facilated evolution due to the increased proliferation and selection pressure, and the overexpression of heat shock proteins may help the accumulation of hidden mutations in tumors (Fares et al., 2002; Rutherford and Lindquist, 1998), which can help their further progression to more aggressive types of metastatic cells. The induction of Hsp70 by hyperthermia and anticancer drugs was shown to be more effective in chemoresistant tumors.

Various heat shock protein inhibitors for Hsp60 and Hsp70 are known; however, because of the specific ATP-binding site of Hsp90 (Bergerat et al., 1997), targeting of Hsp90 became a central attraction in Hsp-related tumor inhibition. The most important Hsp90 inhibitors are Geldanamycin, its less toxic analogs, 17-allylamino-17-demethoxy-Geldanamycin (17-AAG) (Schulte and Neckers, 1998), Radicicol and the more stable oxime derivatives (Soga et al., 1998), which have a higher affinity for Hsp90 than Geldanamycin (Roe et al., 1999). New Geldanamycin analogous and a third class of inhibitors, the purine scaffold inhibitors were developed (Hargreaves et al., 2003). When Hsp90 becomes activated, it forms a large complex with several co-chaperones in tumor cells, whereas in normal cells a latent uncomplexed Hsp90 is found (Kamal et al., 2003).

In a recent report it could be shown that the Geldanamycin-derivative, 17-AGG, binds to the tumor-specific, complexed form of Hsp90 with a 100-fold higher affinity that the latent form in normal cells (Kamal et al., 2003). This specific accumulation in tumor cells helps to explain why Hsp90 inhibitors are generally not as toxic to patients as one would expect from the pleiotropic roles of Hsp90 inhibited by them.

Table 5: Pharmalogical modifiers of Hsp action (Sreedhar and Csermely, 2004).

Drug	Affected Hsp
Hsp inhibitors	
Geldanamycin and 17-AGG	Hsp90
Radicicol	Hsp90
Cisplatin	Hsp90
Novobiocin	Hsp90
Deoxyspergualine	Hsp70, Hsp90
MKT-077	Hsp70
Mizobirin	Hsp60
Hsp inducers	
Amphetamine	all Hsp
Carbenoxolone	all Hsp
Geldanamycin and 17-AGG	all Hsp
Proteasome inhibitors	all Hsp
Stannous chloride	all Hsp
p38 kinase inhibitors	Hsp27
Geranyl-geranyl-acetone	Hsp70
Hsp co-inducers	
Aspirin	all Hsp
Bimoclomol	all Hsp

Hsp90 inhibition induces apoptosis of various tumor cells and leads to a defect in a number of proliferative signals, including the Akt-dependent pathway (Sreedhar and Csermely, 2004). In addition, it has been shown that inhibition of Hsp90 was successful in reducing chemoresistant tumors with poor prognosis (Munster et al., 2001). Many other drugs, widely used in chemotherapeutic agents, such as cisplatin (Itoh et al., 1999), taxol (Byrd et al., 1999) or novobiocin (Marcu et al., 2000) were shown to interact with Hsp90.

Although the very first Hsp90 inhibitor, Geldanamycin, showed clear antitumor effects, it encountered difficulties in clinical trials due to its high hepatoxicity (Supko et al., 1995). 17-AAG possesses all the Hsp90-related characteristics of Geldanamycin, but, with lower toxicity and could enter Phase I clinical trials (Neckers, 2002; Neckers and Lee, 2003).

7.2   Chemical Shift Perturbation Study of the N-terminal Domain of Hsp90 upon ADP, AMP-PNP, Geldanamycin and Radicicol

7.2.1   Results

7.2.1.1   Sequential Backbone Assignment of the N-terminal Domain

To analyze the consequences of ligand binding to the N-terminal domain of Hsp90 initially the ^{1}H, ^{13}C and ^{15}N backbone resonances of the free [70%-^{2}H, U-^{13}C, ^{15}N]-labeled N-terminal domain of Hsp90, residue 1-210 (Nhsp90), have been assigned using a set of triple resonance experiments (see Materials and Methods).
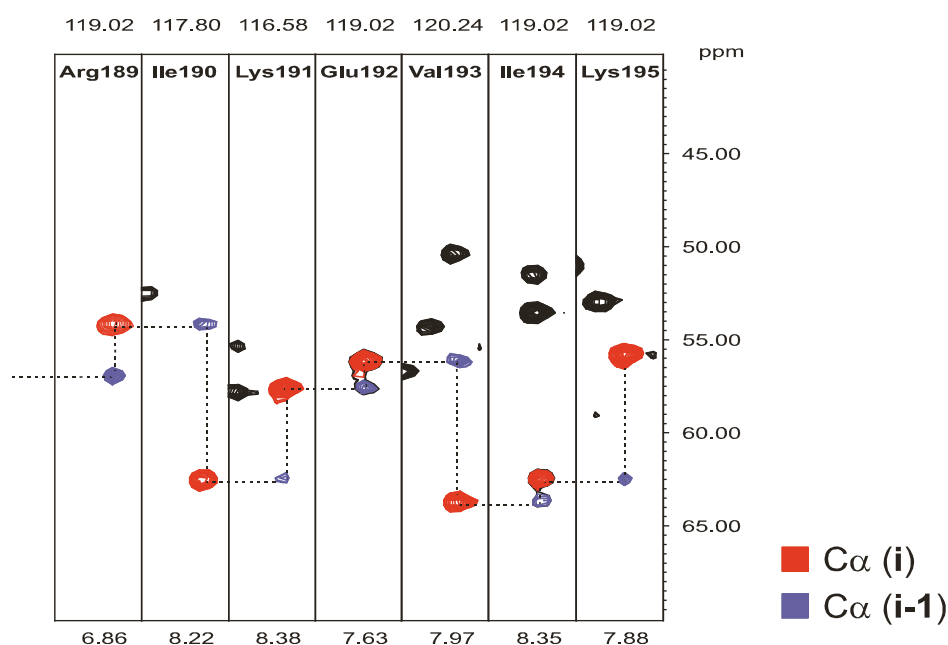
Figure 61: Strip plot representation of the 3D HNCA experiments for the sequential assignment of the N-terminal domain of Hsp90. Signals in red belong to the Cα resonance of the same residue, signals in blue belong to the Cα resonance of the preceding amino acid.

All assignments have been confirmed by a recently published backbone signal assignment of a Hsp90 construct comprising amino acids 1 to 207 (Salek et al., 2002). The secondary structure of Nhsp90 in solution is indicated by the consensus chemical shift index of Cα, Cβ and CO chemical shifts (Wishart et al., 1992). With the exception of the loop region 97-101 the secondary structure in solution is identical to that in the crystal (**Figure 62**) (Prodromou et al., 1997).
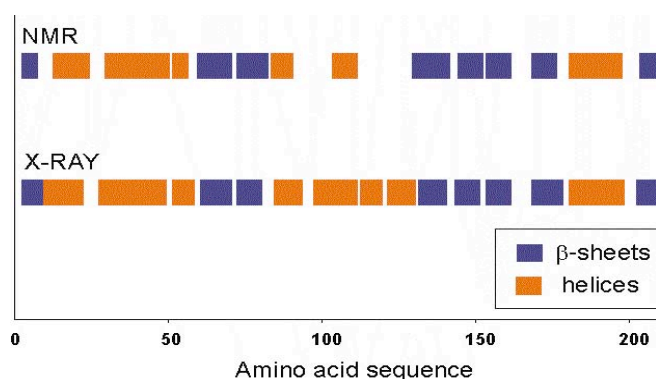
Figure 62: Comparison of the secondary structures of Nhsp90 in solution, indicated by the consensus chemical shift index (Wishart et al., 1992), compared to the crystal structure (Prodromou et al., 1997).

This provided the basis for analyzing the interaction of ATP, ADP and the competitive inhibitors Geldanamycin and Radicicol with Nhsp90. Furthermore R_1, R_2 und $\{^1H\}^{15}N$-hetero NOE relaxation measurements of Nhsp90 reveal a ms time-scale dynamic around the "ATP-lid" region 85-110, recognizable from reduced R_2 relaxation times for surrounding residues.
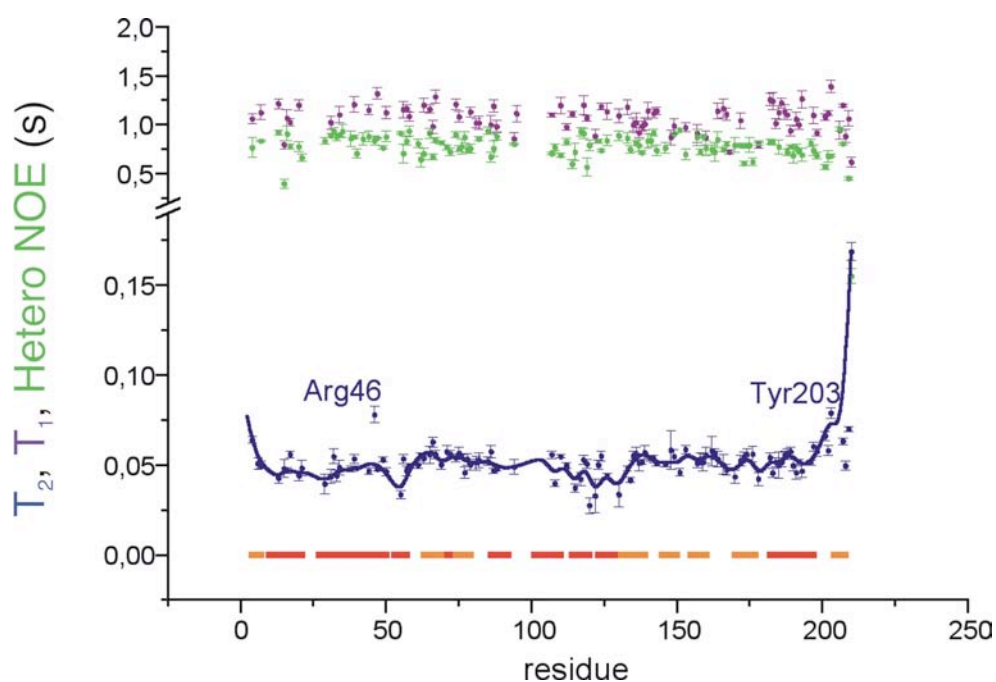
Figure 63: T_1, T_2 und $\{^1H\}^{15}N$-Hetero NOE relaxation measurements of Nhsp90 at 750 MHz. Secondary structure of Nhsp90 is indicated by yellow (β sheet) and red (helix) bars.

7.2.1.2   Titration with AMP-PNP, ADP, Geldanamycin and Radicicol

The ^{1}H,^{15}N-correlation spectrum of a protein and its specific pattern can be regarded as a fingerprint of its structure. Changes in resonance frequencies of individual nuclei are due to a different electronic and/or conformational environment. Perturbations of ^{15}N and H^N chemical shifts of a protein upon complexation with a ligand are a qualitative tool for mapping residues involved in binding sites and/or identifying conformational rearrangements (Gemmecker et al., 1997; Shuker et al., 1996). However, there is no quantitative correlation between the size of the induced shift and the strength of binding or the conformational rearrangement. In addition, complete disappearance of peaks can occur upon complexation, and this has to be taken into account when analyzing the data. Since these effects can extend beyond the binding site, a comparison of the chemical shifts of all cross peaks in the presence and absence of ligands is required to correctly define the area of the protein directly involved in binding and those only indirectly perturbed due to conformational rearrangements.

Figure 64: Superposition of the ^{1}H-^{15}N HSQC spectra of free Nhsp90 (red contours) and Nhsp90/ADP complex (blue contours). Cross peaks are labeled at their position in the free Nhsp90 (red). Both samples contained approximately 550 μM Hsp90 in 40 mM phosphate buffer, pH 7.5, in 90% H$_2$O/10% D$_2$O. Spectra were recorded at 298 K.

In **Figure 64** a superposition of the ^{15}N-fHSQC (Mori et al., 1995) of free ^{15}N-Nhsp90 (red contours) and ADP bound ^{15}N-Nhsp90 (blue contours) is shown. The

titration of Nhsp90 with ADP (but also with AMP-PNP, Radicicol and Geldanamycin; data not shown) caused significant shifts in several crosspeaks in the HSQC spectrum, while the large majority of peaks were rather slightly affected. Due to the strong binding constants of the nucleotides and the inhibitors, the complexes are long-lived on the NMR chemical shift time scale ($\tau > 10$ ms), which resulted in a second signal set, instead of a successive signal shifting during the titration experiments. Thus, it is not possible to trace the signals from the free state to the complexed state as is feasible for binders of lower affinity. A classical assignment would have required a set of triple resonance experiments and triple labeled Nhsp90 for each ligand complex. Due to the low sample stability, a different strategy was used (Lüttgen et al., 2002), where chemical shift perturbations of the Nhsp90 complexes were determined by the *minimum deviation* between each position of the free and complexed peak in the HSQC spectra (Lüttgen et al., 2002). Using the disappearance of a signal and by identifying the next neighbor the minimal induced shift due to complexation of each residue was determined.

To prevent chemical shift changes in the ^{1}H-^{15}N correlation spectra due to fast hydrolysis of ATP to ADP the non-hydrolysable AMP-PNP was used for the perturbation experiments. In **Figure 65**, changes in chemical shifts are exhibited using the normalized weighted chemical shift average (Grzesiek et al., 1996) Δ_{av} between the free Nhsp90 and its complex with AMP-PNP, ADP, Radicicol and Geldanamycin. Titration of all four ligands to ^{15}N-labelled Hsp90 caused significant chemical shift perturbations and disappearance of individual resonances in the ^{1}H,-^{15}N-fHSQC spectra, while the chemical shifts of the remaining signals were slightly affected or unaffected at all.

Figure 65: Average chemical shift perturbation of ^{1}H and ^{15}N chemical shifts of Nhsp90 given by $\Delta_{av} = [(\Delta\delta^2_{NH} + \Delta\delta^2_{N}/25)/2]^{1/2}$ [ppm] *versus* residue number upon titration with AMP-PNP; ADP; Radicicol and Geldanamycin. Negative gray bars indicate amino acids which could not be unambiguously assigned in the ligand complex. The secondary structure is given by yellow bars indicating a β-strand and red bars indicating a helix.
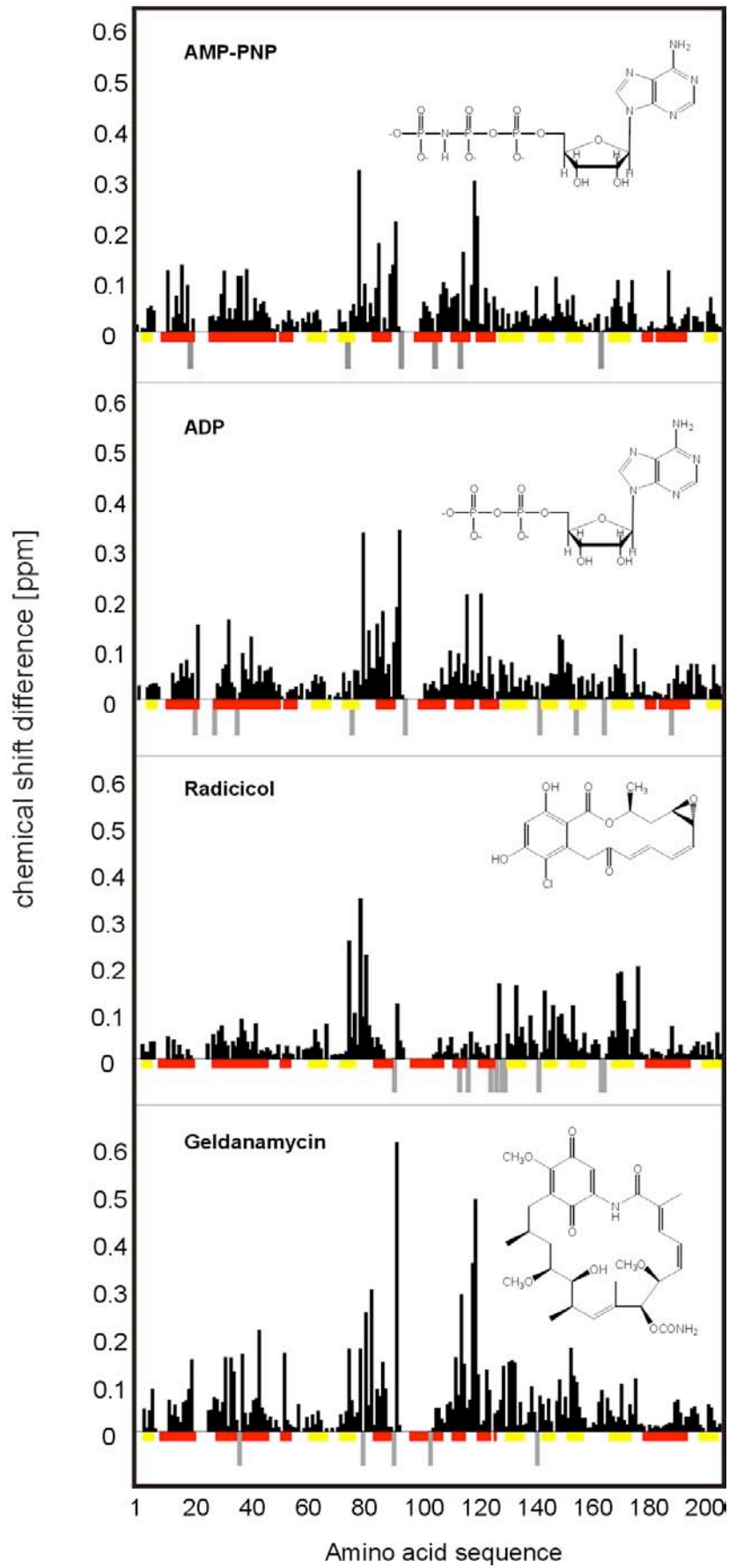
The results for the AMP-PNP ligand are depicted in the **Figure 65**. Three defined regions show severe chemical shift changes in the spectra. The first is localized in the so-called binding pocket of Hsp90 (**Figure 66**), which, according to the crystal structure determined for the Hsp90/ATP complex, is the main interaction surface of the protein (Prodromou et al., 1997). The largest chemical shift perturbations can be found for residues Gly81, Gly83, Asn92, Leu93, Gly94, Ile117, Gly118, Gly121, Val122 and Gly123 and the peaks of Ile77 and Ile96 which could not be followed upon complexation. The second region perturbed due to AMP-PNP binding is the very N-terminal part encompassing the first α-helix (Ala10-Thr22) and the second α-helix (Glu28-Leu50), which surround the central binding pocket.
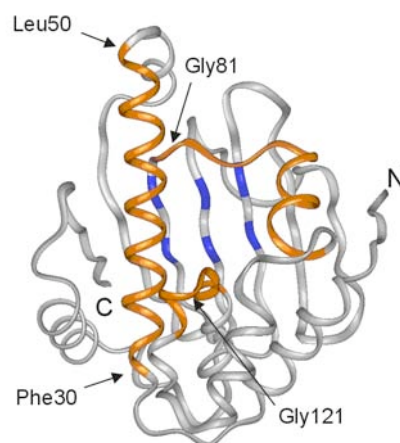
Figure 66: Ribbon representation of the binding pocket of Hsp90. Residues in orange represent the helices 28-50, and 85-94 and the loops 117-124 and 81-85. Residues in blue are 77, 79, 136, 138, 171 and 173 in the base building β-sheet (Prodromou et al., 1997).

In these helices, Ala12, Leu15, Ser17, Ile20, Arg32, Glu33, Ala38, Ser29, Ala41 and Lys44 show significant shift changes, whereas the signal for Asn21 could not be followed. The third region is localized in the β-sheets forming the C-terminal part (150-210) of Nhsp90 and the base of the binding pocket (residues Ile77, Asp79, Val136, Ser138, Thr171 and Ile173; (**Figure 66**). In particular, residues Glu144, Asn151, Ser155, Ile172, Leu173, Lys178 and Lys191 show significant shift perturbations, whereas the signal for Ile167 completely disappears.

The results for the ADP-Nhsp90 complex are presented in **Figure 65**. Despite of localized differences, the overall chemical shift perturbation pattern is similar to that for the AMP-PNP complex described above which is expected, given the very similar chemical structure of the nucleotides. The largest chemical shift changes due to complexation are localized in the binding pocket and in the surrounding N-terminal α-

helices (Ala10-Thr22, Glu28-Leu50) and C-terminal β-sheets (Arg133-Lys139, Tyr146-Pro150, Ser155-Leu160 and Gly170-Leu177). The signals for residues Asn21, Glu28, Ser36 in the first α-helix and Glu144, Thr157 in the C-terminal part could not be followed upon ligand binding.

For the Radicicol-Nhsp90 complex the results are shown in **Figure 65**. The overall chemical shift perturbation map is different from that described above for AMP-PNP and ADP, which indicates that Radicicol binding leads to different effects within the ATP binding domain of Hsp90. While some residues, namely Ile77, Gly81, Ile82, Gly83, Asn92 and Gly93, show strong chemical shift perturbations, the overall binding pocket is less affected upon Radicicol binding compared to AMP-PNP and ADP. In addition, the shifts changes observed within the two surrounding α-helices (Ala10-Thr22, Glu28-Leu50) remain rather weak. In contrast, the residues belonging to the loop region Ser126-Asp132 and the four β-sheets Arg133-Lys139, Tyr146-Pro150, Ser155-Leu160 and Gly170-Leu177 forming the base of the binding pocket are more affected.

Among the four discussed ligands, the overall strongest chemical shift perturbations were induced by Geldanamycin (**Figure 65**). Within the binding pocket the shift changes are strong, especially the signals of residues Gly94, Gly121 and Val122 are extremely affected. In addition the signals of Ile82 and Asn92 could not be followed, which is not the case for AMP-PNP, ADP and Radicicol binding. Similar to AMP-PNP and ADP complexation, the shift differences for the residues within the two surrounding α-helices (Ala10-Thr22, Glu28-Leu50) are strongly affected and the signal for Ala39 is missing at all. In contrast, the residues in the β-sheet belonging to the base of the binding pocket (Arg133-Lys139, Tyr146-Pro150, Ser155-Leu160 and Gly170-Leu177) are similarly perturbed as upon Radicicol binding.

7.2.2 Discussion

The binding of ATP to the N-terminal domain of Hsp90 marks the beginning of the ATPase-cycle which leads to the hydrolysis of the nucleotide via a coordinated series of conformational changes (Weikl et al., 2000). These changes involve as a critical transient state a conformation in which the N-terminal domains dimerize (Maruya et al., 1999; Prodromou et al., 2000; Richter and Buchner, 2001). In this state, it is speculated that at least a part of the N-terminal α-helix is swapped from one N-terminal domain to the other (Richter et al., 2002). Furthermore, the ATP molecule becomes trapped inside the protein, possibly by interactions of the N-terminal with the central domain (Weikl et al., 2000). These conformational changes require a ligand-specific behavior of the ATP binding domain which cannot be explained on the basis

of the crystal structures in the complexed state because no differences in the conformation compared to the free state were observed (Prodromou et al., 1997; Roe et al., 1999).

The NMR data aim to explore the ligand binding site and additional conformational effects of the N-terminal domain of Hsp90 due to AMP-PNP, ADP, Radicicol and Geldanamycin binding. Chemical shift perturbations of ^{15}N are a qualitative tool to detect changes in the electronic environment of specific nuclei which could result either from a direct ligand interaction or from a conformational rearrangement around the observed nuclei. Mapping these sites on the three dimensional structure of the N-terminal domain determined by X-ray crystallography (**Figure 66**) provides the structural basis for the described chemical shift perturbations mapping. Significant shift deviations of signals belonging to residues which are not coinciding with the binding site can be interpreted as conformational flexibility induced by ligand binding (**Figure 67**).
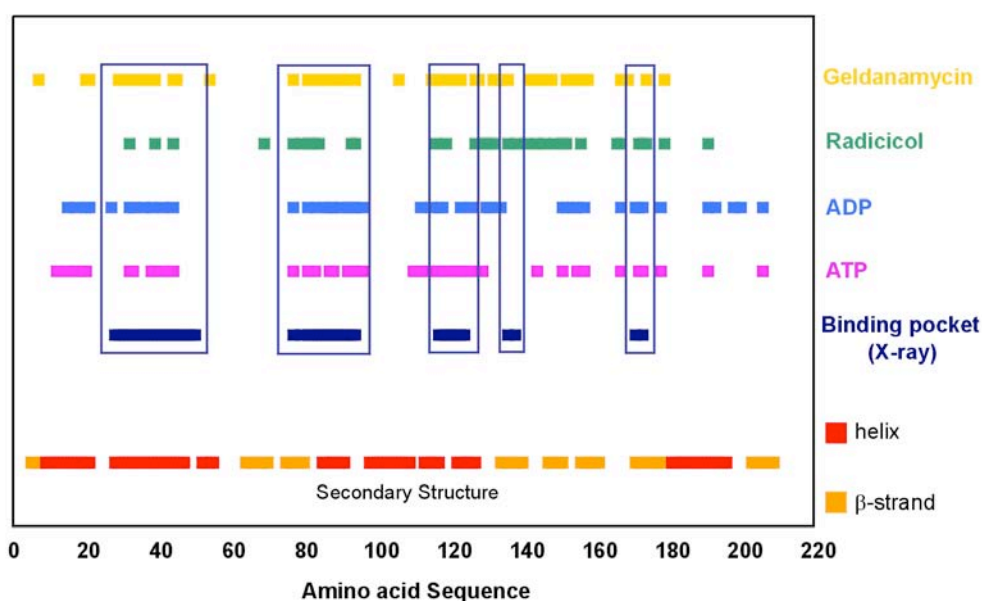
Figure 67: Comparative representation of relative chemical shift perturbations (normalized by $\Delta_{av}/\Delta_{max}=1.0$ for each ligand) larger than $\Delta_{av} > 0.2$ for AMP-PNP, ADP and Radicicol and $\Delta_{av} > 0.11$ for Geldanamycin upon ligand binding *versus* residue number. Chemical shift perturbations which are within the binding pocket are indicated by a box.

Even though all four ligands are known to bind to the same site of the protein in competition with each other, the effects on the N-terminal domain of Hsp90 are different. The front and back views of Nhsp90 displayed in **Figure 68** represent a colorcoding of amino acids significantly affected upon AMP-PNP, ADP, Radicicol

and Geldanamycin binding. As expected, the strongest induced chemical shift changes for all four ligand complexes occur within and around the binding pocket. In particular the loop 81-85, the helix 85-94 and the loop 117-124 are most strongly affected as they are in direct contact with the ligands. In addition, it is likely that these flexible loops experience a conformational rearrangement and thus experience stronger chemical shift changes upon ligand binding. Located just between the β2 strand and the so-called "ATP-lid" region (residues 85-110), residues Gly81, Val82 and Gly83 are significantly perturbed upon binding of each ligand. The backbone amide of residue Gly83 had been shown to be involved in water-bridged hydrogen bonds with each ligand (Roe et al., 1999). These residues belong to the "ATP-lid", which is a part of the nucleotide binding motif common within the GHKL superfamily (Dutta and Inouye, 2000). At the end of helix α' of this "ATP-lid", the signals of residues Asn92, Val93 and Gly94 show stronger chemical shift perturbations, especially for the titration with AMP-PNP and ADP. In particular, the sidechain carbonyl of Asn92 had been shown to make direct contacts with the O2′ of the ribose sugar of ATP and ADP (Roe et al., 1999). In contrast, Radicicol and Geldanamycin complexes do not display strong chemical shift deviations for these residues (except for Gly94 for Geldanamycin). This is in agreement with the crystal structure, where both inhibitors are not involved in direct contacts with Asn92, Val93 or Gly94 (Roe et al., 1999). The L4 loop (residues 95-102) (Dutta and Inouye, 2000; Young et al., 2001) of this ATP-lid region remains not visible in the NMR spectra at all and could not even be assigned in the free Nhsp90 protein, indicating a millisecond-timescale flexibility which is corroborated by R_1/R_2 relaxation measurements of Nhsp90 which exhibit reduced R_2 values around and within this "ATP-lid" region. Taken together, the results corroborate that this loop region is subject to conformational rearrangements upon AMP-PNP, ADP and Geldanamycin binding. Another ligand-specific perturbation can be observed for residues Gly121, Val122 and Gly123, which are strongly affected upon AMP-PNP, ADP and Geldanamycin binding only. **Figure 69** illustrates a ribbon representation of this region, in which the localization and the orientation of ADP, Radicicol and Geldanamycin are shown. Regarding the conformation and the smaller size of ADP, it is likely that the additional γ-phosphate group of bound ATP is involved in water-bridged contacts with these residues, in particular with the carbonyl group of Gly121 and the amide proton of Gly123. These direct interactions are reproduced by Geldanamycin, with HN of Gly123 strongly bonding to the macrocycle (Roe et al., 1999), whereas the smaller Radicicol ligand is directed away from this loop region and therefore exhibits weaker direct interactions with these three residues.
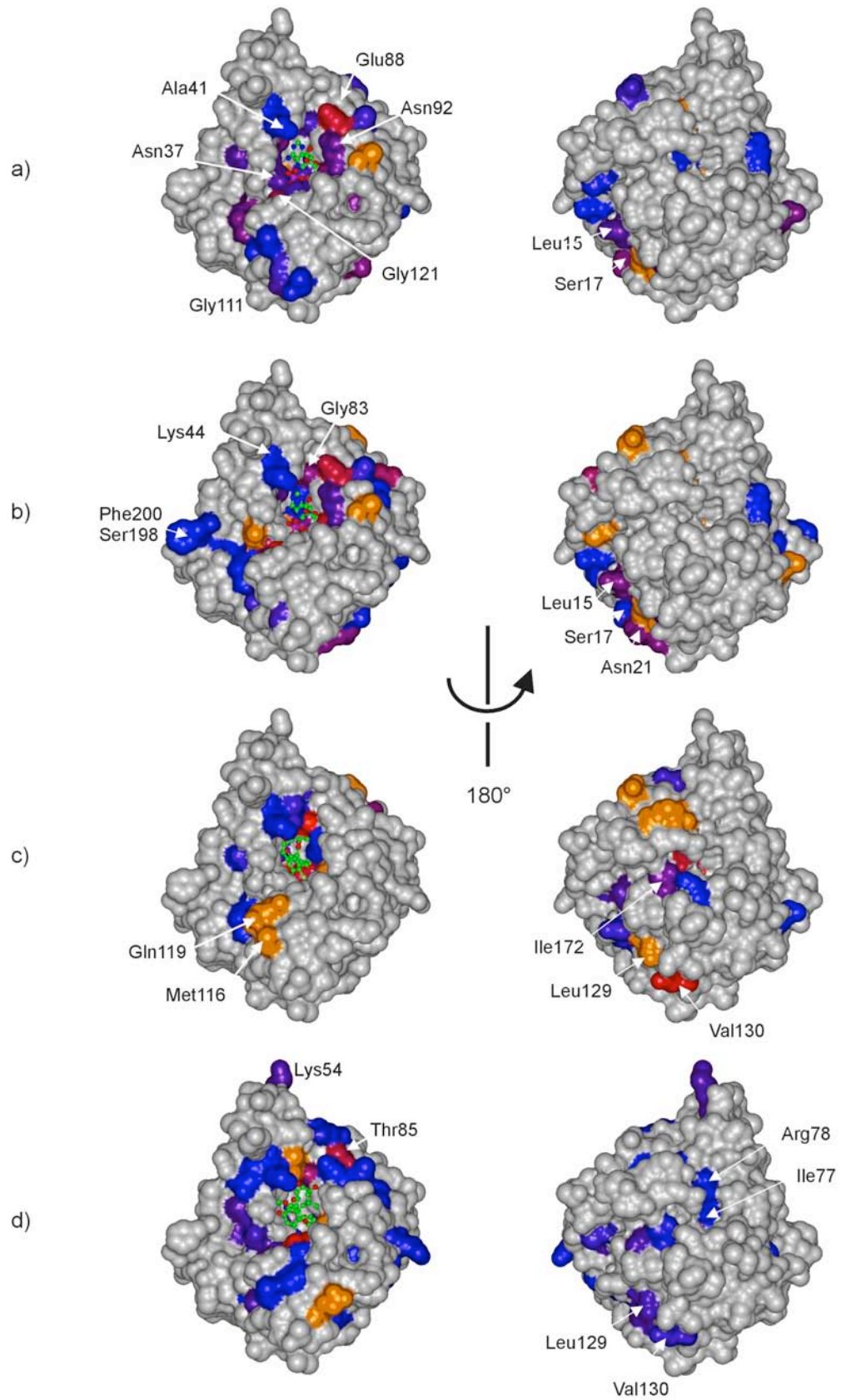
Figure 68: Residues affected by chemical shift perturbation are mapped onto the crystal structure of Hsp90 using a Connolly surface with a probe radius of 1 Å. The relative orientation of the protein is identical to the ribbon diagram in **Figure 66**. The residues are colored according to the following scheme: Residues with a relative chemical shift perturbation (normalized by $\Delta_{av}/\Delta_{max}=1.0$ for each ligand) smaller than twice the average over all (0.11 in the case of Geldanamycin and 0.20 for AMP-PNP, ADP and Radicicol) are not significantly shifted and color coded in gray. Residues with a large relative chemical shift perturbation of 0.60 are given in red. Residues with relative chemical shift perturbations between 0.20 and 0.60 are given from blue to red. Residues which are missing in the complexed spectrum or which could not be unambiguously assigned are given in orange (negative gray bars in **Figure 65**). Residues G94, G81, G123 and V122 are within the binding pocket and therefore buried by the solid surface. (a) Titration with AMP-PNP; (b) with ADP; (c) with Radicicol; and (d) with Geldanamycin.

Several residues belonging to the base of the binding pocket (residues 138–178) are significantly affected upon each ligand complexation (**Figure 68**). Especially residues Val136, Ser138, Thr171 and Ile173 are particularly affected upon Radicicol complexation. Due to its smaller size, it seems to insert more deeply into the binding pocket which is in agreement with the crystal structure of the Radicicol-complexed N-terminal domain (Roe et al., 1999). Residues Ile77 and Asp79 are also part of the binding pocket´s base. The interaction of the ATP/ADP N6 exocyclic amino group with the carboxyl side chain of Asp79 has been shown to be critical for the function of Hsp90 *in vivo* (Obermann et al., 1998; Panaretou et al., 1998). Mutation of Asp79 to Asn is sufficient to abolish ATP-binding. Our results show that the backbone amide group of Asp79 is perturbed by this interaction with AMP-PNP, ADP, and with Radicicol. Even though binding of Geldanamycin resembles the binding of nucleotides (Roe et al., 1999), as it has been observed that very similar residues are involved in the binding reaction, the chemical shift perturbation of Asp79 backbone amide upon Geldanamycin binding is not pronounced.

The long helix α2 (Glu28-Leu50) flanking the binding pocket is also affected upon binding of AMP-PNP, ADP and Geldanamycin. This helix in particular contains residues such as Glu33, which are critical for the catalysis reaction. Therefore, it is likely that residues in this helix form direct contacts with the bound nucleotides. Mutation of Glu33 to Ala reduces the catalytic efficiency of full-length Hsp90 to undetectable levels, but still allows efficient binding of nucleotides (Grenert et al., 1997; Panaretou et al., 1998). The distinct perturbation effect of AMP-PNP, ADP and Geldanamycin on this helix again highlights the similarity between Geldanamycin binding and nucleotide binding. In contrast the effect of Radicicol on this helix is

much less pronounced, which confirms that Radicicol penetrates more deeply into the binding pocket.
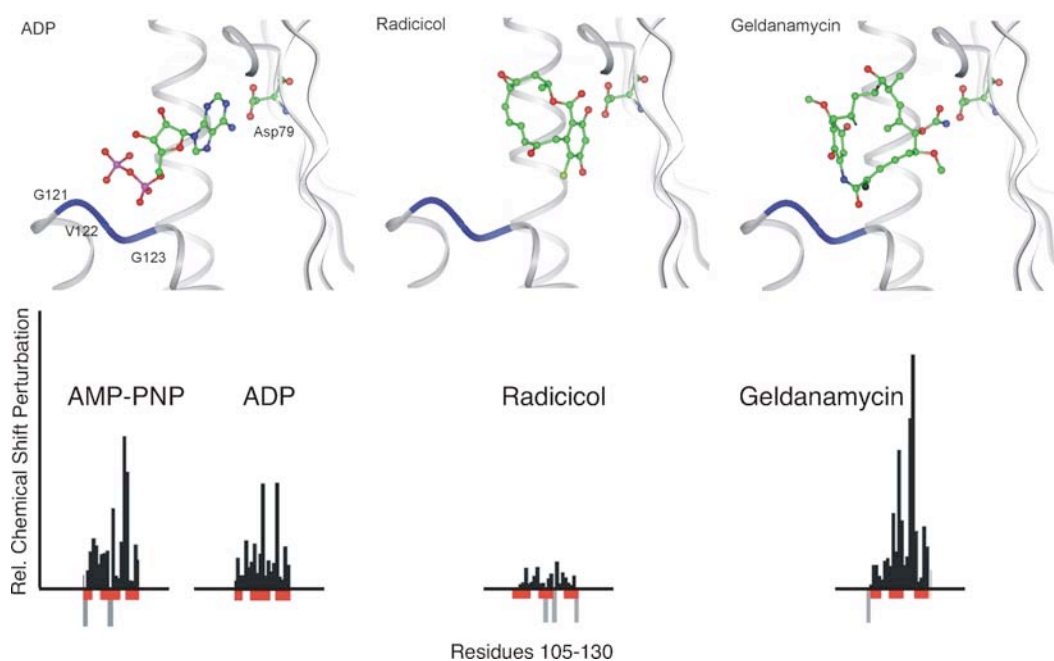
Figure 69: Localization of ADP, Radicicol, and Geldanamycin within the binding pocket with respect to the loop 117-124 according to the crystal structures viewed perpendicular to **Figure 66**. Ribbon representation in blue is given for residues Gly121, Val122 and Gly123. Additionally residue Asp79 is displayed in the β-sheet for orientation. In the lower panel the relative chemical shift perturbation of this loop region is given according to **Figure 65**.

Another interesting structural element is the first helix α1 (Ala10-Thr22) of the protein. Although the chemical shift deviations are not pronounced, this helix merits attention, as it has been suspected to form a flexible structure, which may be involved in a "strand swapping" reaction between the two N-terminal domains during the ATP-hydrolysis reaction (Richter et al., 2002). Specific chemical shift perturbations could be evidenced for residues localized in this first α-helix (Ile12, Leu15, Ser17, Ile19 and Ile20) upon AMP-PMP, ADP and Geldanamycin binding. The crystal structure (Prodromou et al., 1997) of the domain suggests that these residues are involved in conformational rearrangements together with the loop region 90-103 which is also strongly affected upon AMP-PNP, ADP and Geldanamycin binding (but not Radicicol). As the deletion of the first 24 amino acids does not affect nucleotide binding to the N-terminal domain (Richter et al., 2002), a direct involvement of these residues can be ruled out. Thus, it is likely that the observed chemical shift deviations

of these residues are the result of a different chemical environment and therefore a ligand-induced conformational change.

The large degree of similarity in the pattern of chemical shift changes of AMP-PNP and ADP binding suggests that they lead to similar – although not identical – effects on the structure of the domain. Clear differences in chemical shift perturbations between AMP-PNP and ADP can only be observed for Gly121, Val122 and Gly123 which may be explained by the presence or absence of a water-bridged hydrogen bond. This observation may point to additional effects of the other domains of Hsp90, which have been suspected to make contact with the exposed γ-phosphate residue of the ATP (Weikl et al., 2000).

The differences in chemical shift perturbations upon ligand binding add to our understanding of conformational effects induced by AMP-PNP, ADP and the competitive inhibitors in the N-terminal domain of Hsp90. Ligand-specific internal dynamic may be transferred to the C-terminal domain of Hsp90 and thereby controls its functionality. Taken together, our results imply that binding of ATP to the N-terminal domain of Hsp90 affects the conformation in a specific way. In the light of biochemical data (Prodromou et al., 2000; Richter et al., 2001) it is reasonable to assume that these changes are necessary for subsequent domain interactions in the Hsp90 molecule, linking ATP hydrolysis to a coordinated sequence of conformational changes required for assisting protein folding.

7.3   NMR Spectroscopic Studies of Unfolded and SDS-Micelle Folded Hsp12

7.3.1 Results and Discussion

7.3.1.1 Introduction

Because of its low molecular weight and the overexpression during heat shock, Hsp12 was classified as a member of the small heat shock protein family in yeast (Varela et al., 1995); (Praekelt and Meacock, 1990). A sequence alignment with other sHsps in *S. cerevisiae* such as Hsp26 or Hsp42 reveals a low overall homology between those sHsps and Hsp12 in general and the homology to the conserved α-crystallin domain is low. Interestingly, an analysis of the Hsp12 sequence using different protein databases revealed no significant homology to any other known polypeptide sequence.

   To clarify the membership of Hsp12 to the group of the small heat shock protein family, the secondary structure of this polypeptide was further investigated by NMR spectroscopic methods. As described in section 7.1.2.5, most of the known members of the sHsp family tend to form large oligomeric complexes. However, even at high concentrations of Hsp12 (25 µM) and glutaraldeyde (40 mM) as a crosslinking agent, a detectable Hsp12 oligomerization was not observed. The equilibrium sedimentation analysis of Hsp12 resulted in a molecular mass of 12 kDa, which is consistent with the monomeric protein size of Hsp12 (Fischer, 2003).

   Since Hsp12 showed no significant structure in aqueous solutions by CD spectra, the effect of different solvents and conditions on the conformation of Hsp12 was tested. The protein has a tendency to adopt an α-helical structure in the presence of different alcohols such as methanol, propanol or TFE. Here, the highest structural changes were achieved by the addition of 70 % TFE, a helix-supporting solvent (Jasanoff and Fersht, 1994). Under this condition, the deconvolution of the CD spectrum suggests the presence of approximately 34 % α-helical conformation. Also in presence of SDS, the CD spectrum of Hsp12 changed significantly. The addition of uncharged CHAPS micelles had no influence on the structure of Hsp12 (Fischer, 2003). These results lead to the assumption that Hsp12 potentially interacts with anionic charged membrane components *in vivo*.

Figure 70: ^{15}N HSQC spectra of Hsp12 at 310 K. (a) 1.2 mM in sodium phosphate buffer pH 7.5, 90% H_2O / 10% D_2O at 600 MHz. (b) 1.2 mM in sodium phosphate buffer pH 7.5 + 300 mM SDS micelles, 90% H_2O / 10% D_2O at 600 MHz.
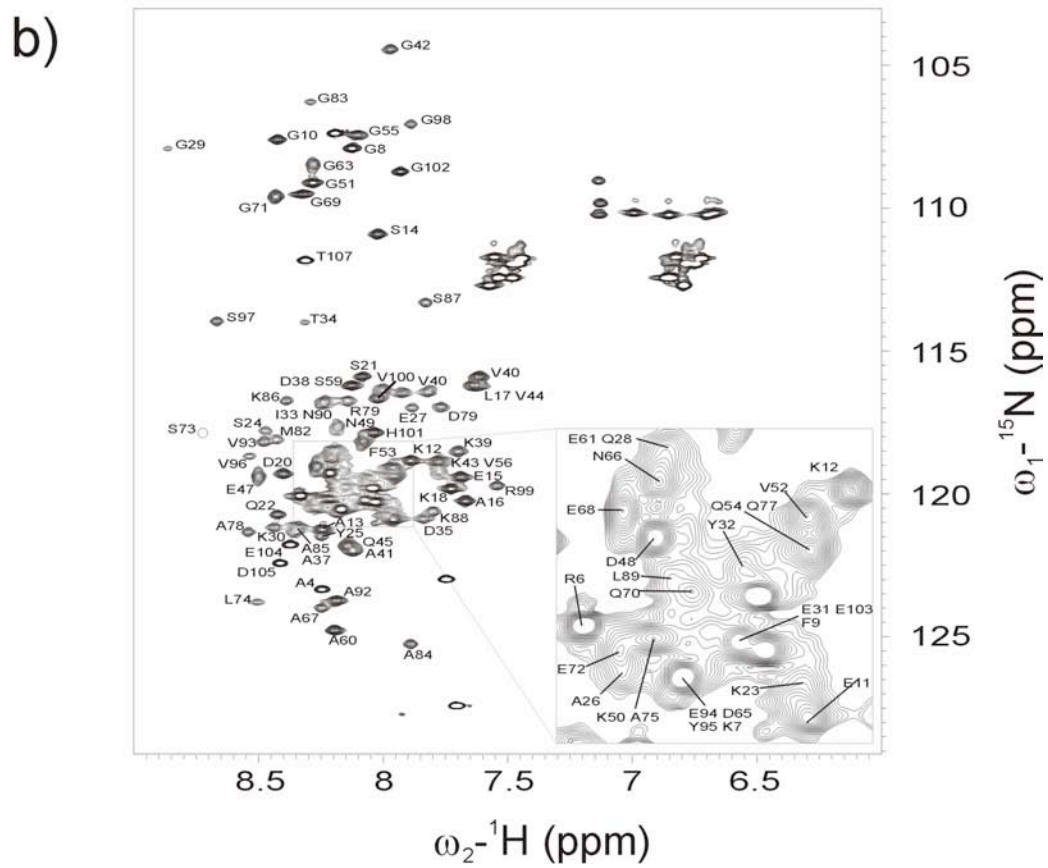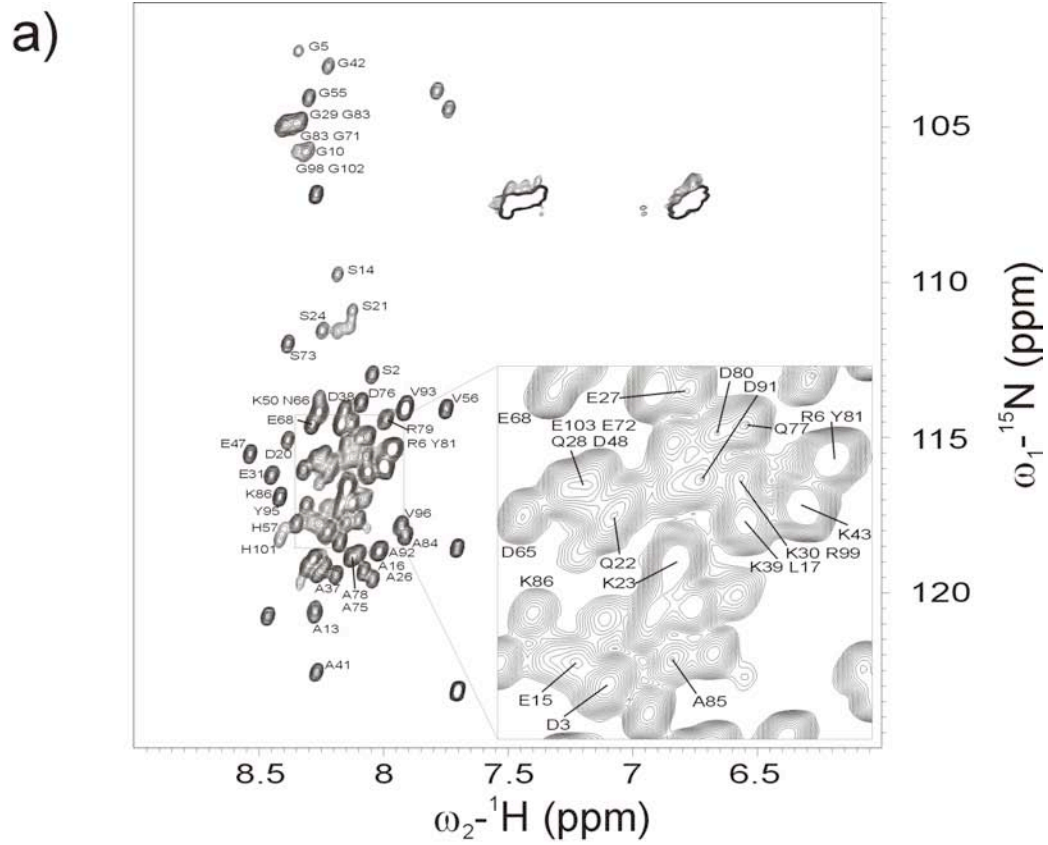
7.3.1.2 Sequential Backbone Assignment of SDS-folded and Unfolded Hsp12

To gain further insight into structural properties of Hsp12 protein (residues 1- 109) initial titration of Hsp12 with d^{25}-SDS was done recording a set of ^{15}N-HSQC spectra (see Material and Methods). **Figure 70** (a) displays the ^{15}N-HSQC spectrum of Hsp12 in sodium phosphate buffer pH 7.5 without any SDS. The small amide proton resonance dispersion in a spectral range of 7.7 ppm up to 8.7 ppm and the accumulation of NH$_2$-sidechain signals at their random coil regions of 7.5 and 6.8 ppm support the idea of an highly unfolded protein.

Titration of Hsp12 with SDS at 20 mM, 50 mM, 100 mM, 150 mM up to a concentration of 300 mM changed the signal pattern of the ^{15}N-HSQC spectrum significantly, resulting mainly in a broadening of the signal dispersion in the proton dimension ranging from 7.5 ppm to 8.9 ppm. This is most obvious comparing the glycine residues (ω_1 = 105-110 ppm) and the NH$_2$-side chain signals in **Figure 70** (b) (with 300 mM SDS) and **Figure 70** (a). Thus the titration of Hsp12 with SDS suggests that the unfolded Hsp12 becomes at least partially structured under SDS micelle conditions.

Despite the rather small signal dispersion and strongly overlapping signals, 96 of the 106 non-proline residues (90.5 %) of Hsp12 protein in 300 mM SDS micelles could be assigned using a set of triple resonance experiments (see Materials and Methods). Unique assignments are obtained for HN, N, Cα, Cβ and partially for Hα chemical shifts except for the first three and last two residues as well as for residues H57, D58, K62, D80, D91 (**Figure 70** b). Hsp12 without any SDS could be assigned only partially, due to high signal overlap even in the triple resonance experiments (see Materials and Methods). Thus 63 of the 106 non-proline residues (59.4 %) could be assigned on the basis of typical chemical shift combinations of sequential amino acids (**Figure 70** a).

7.3.1.3 Secondary Structure of Hsp12

Consensus chemical shift values of Cα, Cβ, CO and partially Hα were used to determine secondary structural elements in SDS-folded Hsp12 and unfolded Hsp12 (**Figure 71**) (Wishart et al., 1992). Random coil shift values were referenced in both cases to those published by Wüthrich et al. (Wüthrich, 1986) The chemical shift index for Hsp12 in SDS micelles is given in **Figure 71** as orange bars, indicating a long C-terminal helix H3 ranging from residue L74 to V96 and two smaller helices at the N-terminus ranging from residue E11 – S14 (H1) and Y25 – K39 (H2), which are interrupted by a proline residue at sequence position 19. Interestingly helix H2 and helix H3 form amphiphilic helices displaying their hydrophobic and hydrophilic

residues to only one side of a helical wheel (**Figure 73**). In contrast the consensus chemical shift index for Hsp12 without SDS shows a clear random coil structure over the entire sequence.

7.3.1.4   *Hydrogen Exchange Rates of Unfolded Hsp12*

Hydrogen exchange rates of amid protons are strongly reduced if they are involved in hydrogen bonds of secondary structural elements. Therefore rapid amid-water exchange rates were measured using the NewMEXICO experiment (Gemmecker et al., 1993; Koide et al., 1995) and mixing times of 40, 80 and 160 ms for each, the SDS-folded Hsp12 and the unstructured Hsp12. Signal intensities of the MEXICO-HSQC spectra compared to a standard HSQC spectrum are dependent on mixing time and exchange rate as described in Material and Methods.

For the SDS-folded Hsp12 all three mixing times could be used in a fitting procedure to calculate the amide exchange rates which are given in **Figure 71** as blue bars. Within the helices (orange bars) the exchange rates are about 1.0 Hz and in average two times slower than in regions between the helices, especially around residue 20, 21, 22 and in the region between residue 50 and 73 (also there are a few signals missing due to signal overlap in the HSQC spectrum). Thus the measured exchange rates and their pattern corroborate the secondary structural elements indicated by the chemical shift index.

The unfolded Hsp12 (without SDS micelles) showed the full intensity of the New MEXICO HSQC spectrum already after 80 ms – thus indicating a very fast proton exchange (Koide et al., 1995). Therefore only the 40 ms New MEXICO experiment could be used for calculating exchange rates. These are plotted in **Figure 71** as red squares for the non-overlapping signals. All measured exchange rates are in between 5 and 30 Hz with an average of about 14 Hz. This average is in perfect agreement with theoretical calculated exchange rates (gray dots in **Figure 71**) for a random coil structure of this specific sequence – taking into account pH, temperature and salt concentration (Bai et al., 1993). Thus Hsp12 without SDS micelles contains no secondary structural elements and behaves in terms of hydrogen exchange like an unstructured polypeptide sequence.
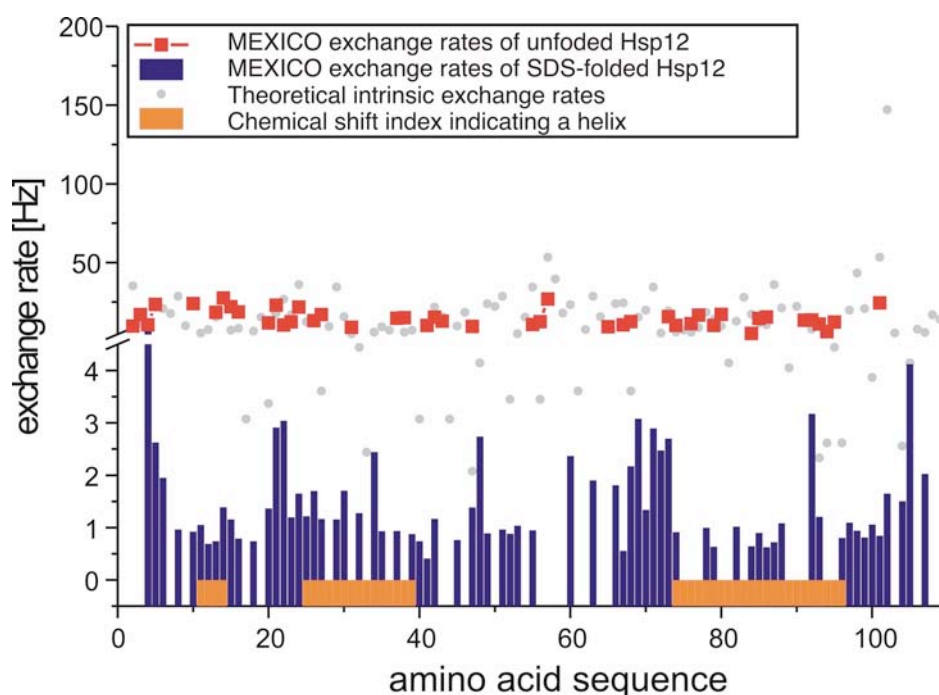
Figure 71: Fast amide exchange rates (blue bars) of SDS-micelles folded Hsp12 as determined by 40 ms, 80 ms and 160 ms NewMEXICO experiments (Koide et al., 1995) against amino acid sequence. Orange bars represent the consensus chemical shift index indicating an α helix. Fast amide exchange rates (red squares) of unfolded Hsp12 as determined by a 40 ms NewMEXICO experiment against amino acid sequence. Grey dots are theoretical calculated hydrogen exchange rates for a random coil polypeptide of this specific sequence taking into account pH, temperature and salt conditions (Bai et al., 1993).

7.3.1.5   *PFG Diffusion Measurements of Unfolded Hsp12*

Spin-echo diffusion measurements of unstructured Hsp12 at 298 K yield a diffusion coefficient of $1.0066 \times 10^{-10} \pm 4 \times 10^{-13}$ m^{2}s^{-1} (**Figure 72**). Using the equation of Cantor and Schimmel (Cantor and Schimmel, 1980) and a Perrin factor of $F = 1$ (representing a spherical shape) one calculates an apparent molecular weight of approximately 34 kDa for Hsp12 which is three times larger than its actual weight of 11.7 kDa. For this molecular weight the dimensionless Perrin factor yields a value of 1.4. F is related to the shape of the molecule and can be calculated for ellipsoids in which two of the semiaxes are identical; it is defined by the following equation:

$$F = \frac{f}{f_{sphere}} = \frac{\sqrt{p^2 - 1}}{p^{2/3} \arctan\left(\sqrt{p^2 - 1}\right)} \qquad \text{5-73}$$

where $p = a/b$, and a and b are the long and short semiaxes of the ellipsoid. For the unstructured Hsp12 p yields a value of 9.3 which is in good agreement with a more or less extended conformation of Hsp12. The regularized random coil structure

of Hsp12 generated by X-PLOR (Brünger, 1992), used for hydrodynamic calculations, exhibits a diameter of approximately 180 Å *versus* 19Å. The diffusion coefficient using the bead model of HYDRONMR (García de la Torre et al., 2000b) yields a value of $D_{HydroNMR}$=0.7216 x 10^{-10} m^2 s^{-1}, of same magnitude but 28% smaller than the experimental value, which is probably due to a single model structure used in the hydrodynamic calculations instead of a conformational ensemble.
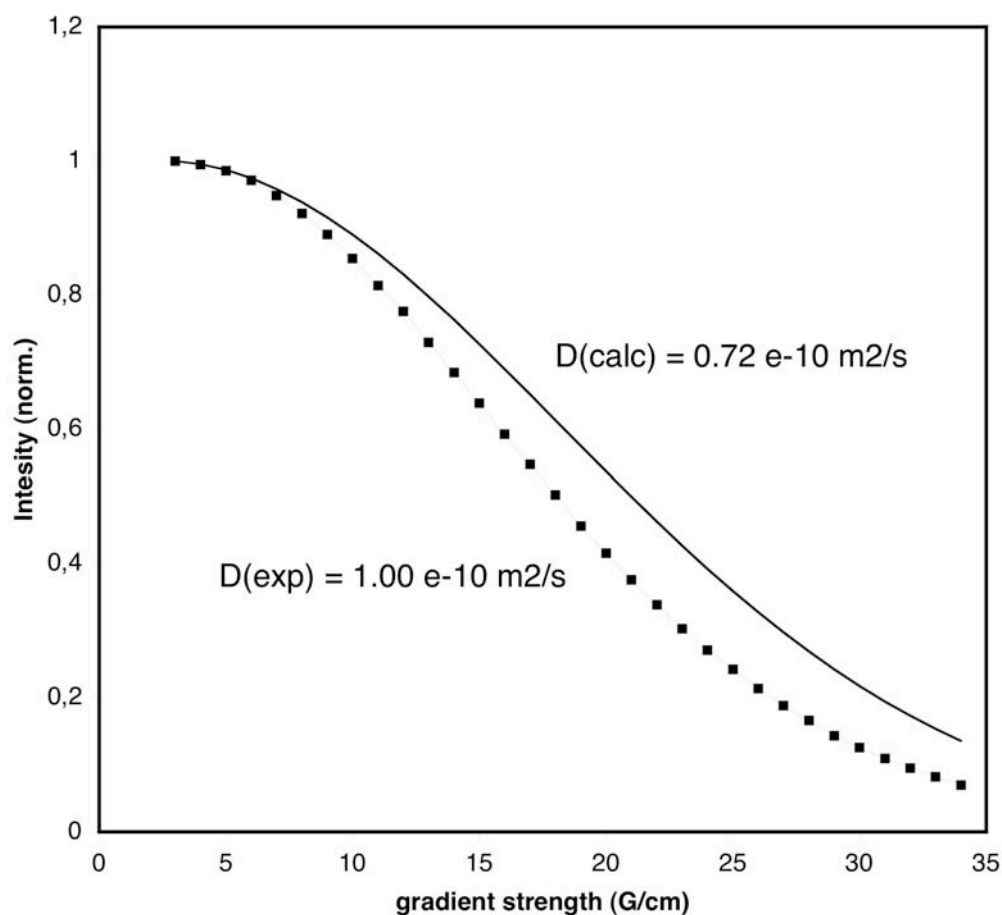
Figure 72: Pulsed field gradient diffusion experiment of unfolded Hsp12. Squares represent averaged experimental values of 40 convergent non-exchangeable signal decays with increasing gradient strength. Non-linear least square regression using the equation of Stejskal and Tanner (Stejskal and Tanner, 1965) yields the diffusion coefficient. The thin black line represents the signal decay for a regularized extended model structure of Hsp12 using the theoretical diffusion coefficient calculated by HYDRONMR (García de la Torre et al., 2000b).

7.3.1.6   Spin Label Experiments

Paramagnetic broadening experiments yield information about the position of Hsp12 in the SDS micelle (**Figure 75**). Therefore the spin label 5-doxyl-stearic acid, which inserts into the SDS membrane, as well as Mn^{2+} ions were used to induce selective broadening of resonances of amino acids close to the paramagnetic probes. 5-doxyl-stearic acid broadens resonances close to the micelle surface whereas Mn^{2+} affects resonances outside the SDS micelle. **Figure 74** shows the effect of both paramagnetic agents on the signal intensities in a ^{15}N HSQC spectrum. 5-doxyl-stearic acid affects amino acids located in helical regions of the protein as indicated by orange bars. Mn^{2+} has an opposite effect. Basically residues located outside the assumed helices are affected.
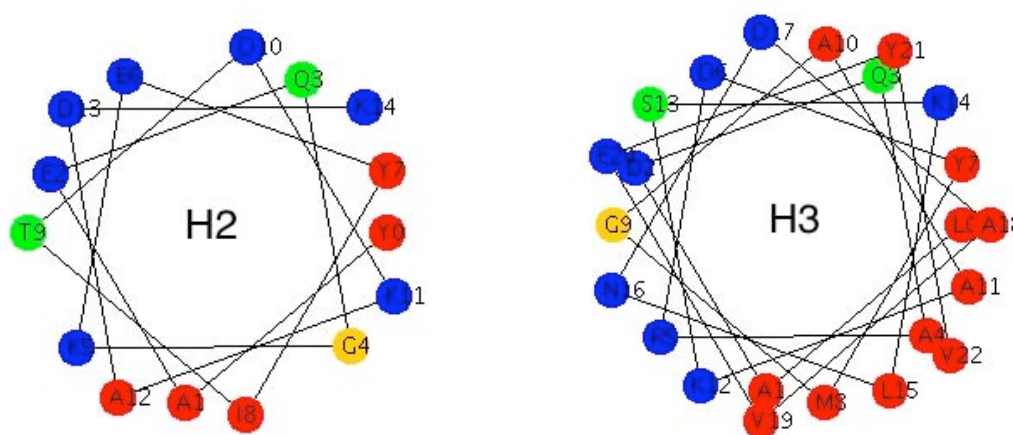
Figure 73: Helical wheel representation of helix 2 and helix 3 as indicated by the chemical shift index. Polar residues are labeled in green, unpolar residues are shown in red. Positively charged residues are labeled in blue and glycine is given in yellow. Helix 2 and helix 3 clearly display amphiphilic helices.

From these experiments it can be concluded that Hsp12 "swims" in the SDS membrane, where all hydrophilic and charged residues of the amphiphilic helices interact with the charged head groups of SDS, while lipophilic residues are located within the SDS membrane, interacting with the hydrophobic SDS tails (**Figure 75**).
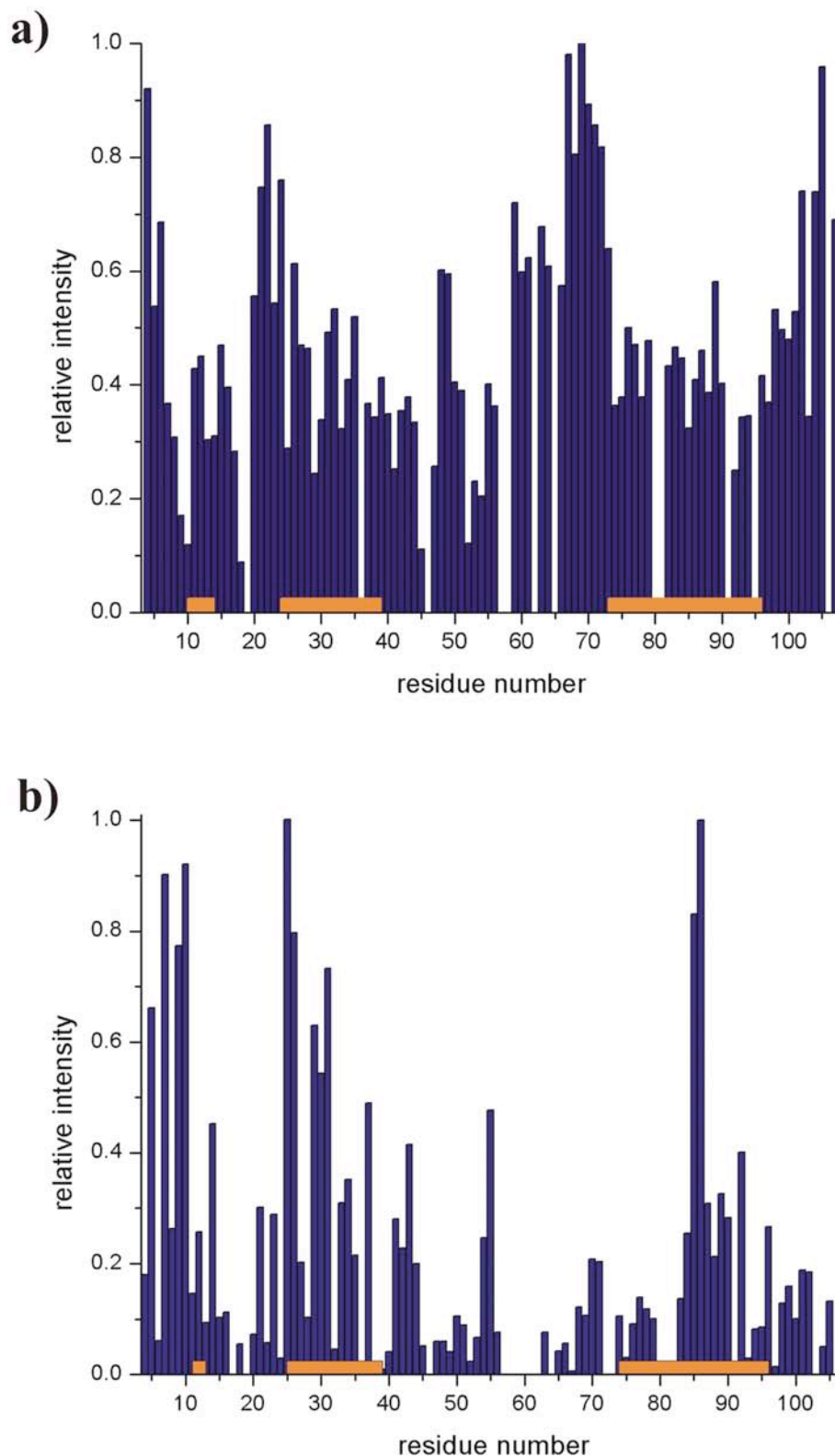
Figure 74: Relative signal intensities of ^{15}N HSQC peaks of Hsp12 in 300 mM SDS after addition of (a) 5 mM 5-doxyl-stearic acid and (b) 1 mM MnCl$_2$ referenced to a ^{15}N HSQC without a paramagnetic agent (blue). Orange bars represent helical regions of the protein.
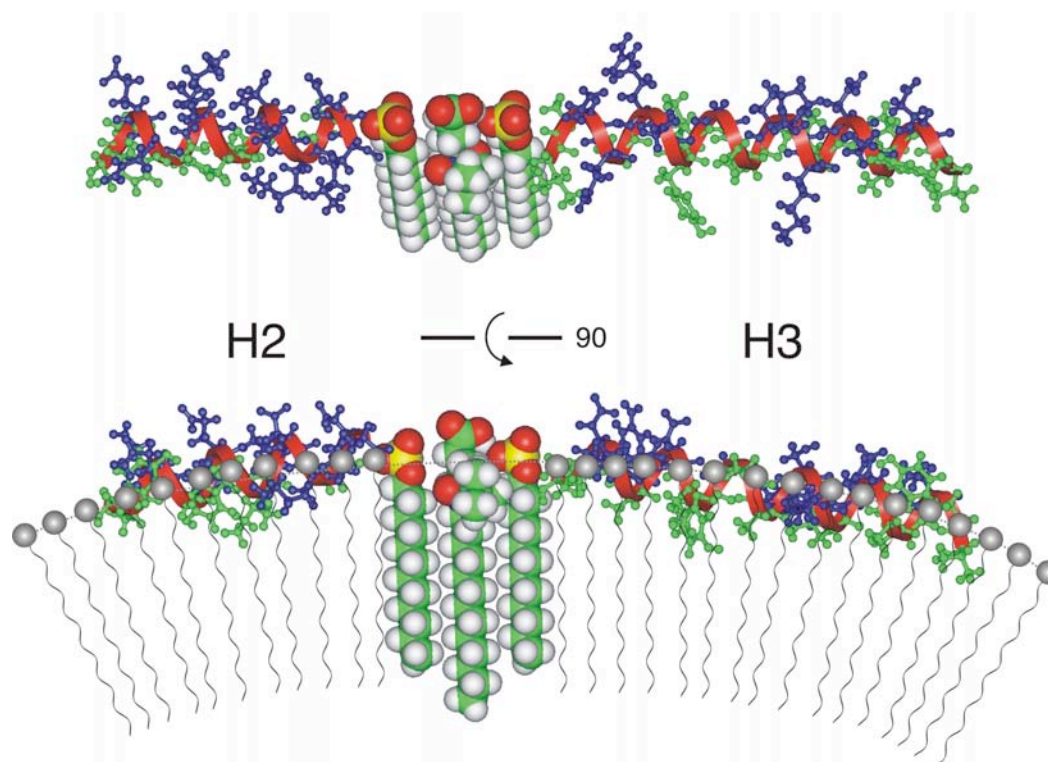
Figure 75: Model of the Hsp12 structure in SDS micelles. Helix 1 and 2 display charged residues to the outside of the SDS micelles, interacting with the charged head group of SDS, while unpolar residues are directed to the inside of SDS micelle establishing hydrophobic interactions.

The physiological role of this SDS-induced secondary-structure gain is still elusive, as it is known that proteins tending to build up an amphiphilic helix gain secondary structure upon addition of SDS (Parker and Song, 1992). However, the model suggests that Hsp12 is possibly localized at the cell membrane of *S. cerevisiae*. This is corroborated by fluorescence microscopy of *S. cerevisiae* cells expressing GFP-Hsp12 fusion proteins (Fischer, 2003). Moreover, it has been shown that Hsp12-depleted cells growing under increased temperatures exhibit a diffuse actin cytoskeleton (Haslbeck, 2001). Thus Hsp12 might be involved in an anchoring of actin during periods of growth or other stress stimuli. The localization of two further heat shock proteins, Hsp30 (Seymour and Piper, 1999) and Hsp17 (Tsvetkova et al., 2002), has been identified and both could be localized in the plasma membrane, regulating the membrane stability and integrity. Weinreb and coworkers (Weinreb et al., 1996) have observed that for a prominent member of the young group of natively unfolded proteins, α-synuclein, the addition of SDS leads to the formation of α-helical structure and suggest a model where parts of the protein interact with the membrane cytoplasmatic surface.

8 Material and Methods

8.1 General Materials and Methods

8.1.1 Chemicals

All chemicals used were of analytical grade and obtained from commercial suppliers: Roche Molecular Biochemicals, Mannheim; Merck Eurolab, Darmstadt; Sigma Aldrich, Irvine, UK; Amersham Pharmacia Biotech, Freiburg; Invitrogen, Karlsruhe; Quiagen, Hilden; Biozym, Oldendorf; Biorad, München; Millipore, Bedford, CT, USA. DNA oligonucleotides were purchased from MWG-Biotech AG, Ebersberg, Germany and TIB Molbiol. Berlin, Germany $^{15}NH_4Cl$ and $^{13}C_6$ glucose were obtained from Spectra Stable Isotopes, Columbia, MD, USA.

8.1.1.1 Vectors and DNA Oligonucleotides

The expression vectors p17007 (wild-type p53 DBD, residues 94-312, pQE40) under control of a T5 promotor and p20002 (GST-wild-type p53 DBD, pGEX-4T) under control of a *tac* promotor are a kind gift of Dr. Silke Hansen and Dr. Christian Klein (Roche Diagnostics GmbH, Penzberg). DNA oligonucleotides for cloning, sequencing and binding studies are specified in Table 6, Table 7 and Table 10.

Table 6: Sequencing primer for the expression vector pQE40 and pGEX.

Name	Sequence
Mia-1 for	5´-ATTTATTTGCTTTGTGAGCGG-3´
PQ40 rev	5´-CATTACTGGATCTATCAACAGG-3´
pGEX for	5´-GTATATAGCATGGCCTTTGC-3´
pGEX rev	5´-CATGTGTCAGAGGTTTTCAC-3´

Table 7: p53 consensus oligonucleotides (Hupp et al., 1992; Pavletich et al., 1993).

Name	Sequence
PG for	5´-AGCTTAGGCATGTCTAGGCATGTCTA-3´
PG rev	5´-AGCTTAGACATGCCTAGACATGCCTA-3´
CON1x5A	5´-GGAGGCACC-3´
CON1x5B	5´-GGTGTCTCC-3´
CON2x5	5´-CCTAGACATGCCTAAT-3´
CON4x5	5´-CCTAGACATGCCTAGACATGCCTAAT-3´

8.1.1.2 Bacteria Strains

The following *E. coli* bacteria strains have been used for cloning and protein expression:

Table 8: *E. coli* bacteria strains used.

E. coli	**genotype**	**reference**
BL21	*E. coli* B F⁻ *ompT hsdS(r⁻$_B$, m⁻$_B$) dcm⁺ gal*	(Grodberg and Dunn, 1988; Sambrook and Russell, 2001)
HB101	*E. coli* K12 x *E. coli* B hybrid F⁻ *supE44 hsdS20(r⁻$_B$, m⁻$_B$) recA13 ara14 proA2 lacY1 galK2 rpsL20 (Str^r) xyl-5 mtl-1 mcrB thi-1 leuB6 glnV44l*	(Bolivar and Backman, 1979; Boyer and Roulland-Dussoix, 1969)
UT5600	*E. coli* K12 F⁻ *ara14 proC14 leuB6 azi-6 lacY1 tsx67 entA403 trpE38 secA6 rfbD1 rpsL109 xyl-5 mtl-1 thi-1 (ompT-fepC)266*	(Grodberg and Dunn, 1988)

8.1.1.3 Culture media

All media were prepared according to Sambrook and Russell (2002), 20 minutes autoclaved at 121 °C and 2 bar pressure, sterilized or sterile filtered.

Table 9: Culture media for protein expression.

LB medium	10 g/L Bactotrypton 5 g/L Bactoyeast extract 5 g/L NaCl
M9 minimal medium	7.5 g/L Na_2HPO_4 2.5 g/L KH_2PO_4 0.24 g/L MgSO4 2 g/L NH_4Cl (or $^{15}NH_4Cl$) 20 mL/L 50% (w/v) glucose (or $^{13}C_6$ glucose) 4 mL/L glycerol 100 μL/L trace elements according to Maass 10 mL/L MEM vitamins

8.1.1.4 Buffer solutions

Brij buffer	6% (v/v) Brij (pH 7.0), 1.5 M NaCl 60 mM EDTA
Solubilization buffer	100 mM TRIS/HCl (pH 7.5), 6 M GdnCl/HCl 100 mM DTT
SDS gel solution 12.5%	0.375 M TRIS/HCl (pH 8.8) 12.5% acrylamide, 0.3% bisacrylamide 0.1% (w/v) SDS + 0.015% (w/v) APS, 0.01% (v/v) TEMED
SDS gel solution 3%	0.125 M TRIS/HCl (pH 6.8) 3% acrylamide, 0.1% bisacrylamide 0.1% (w/v) SDS + 0.03% (w/v) APS, 0.02% (v/v) TEMED
10x TG running buffer	250 mM TRIS/HCl (pH 8.5), 1.92 M glycerol
10x TG-SDS running buffer	250 mM TRIS/HCl (pH 8.5), 1.92 M glycerol 1% (w/v) SDS
Coomassie staining sol.	30% (v/v) ethanol, 10% (v/v) conc. acetic acid, 1% (w/v) Coomassie Brilliant Blue R-250
Coomassie bleaching sol.	30% (v/v) ethanol, 10% (v/v) conc. acetic acid
2x DNA binding buffer	40 mM HEPES (pH 8.0), 50 mM KCl, 10 mM $MgCl_2$ 20% (v/v) glycerol, 5mM DTT, 0.1% (v/v) Triton X100, 1 mg/mL BSA
Native 4% gel solution	30 mM TRIS (pH 8.4), 30 mM boric acid, 4% acrylamide, 0.15% bisacrylamide, 0.1% (v/v) Triton X100, 1mM EDTA, + 0.1% (w/v) APS, 0.1% (v/v) TEMED
10x DNA sample buffer	4% (w/v) brom phenol blue, 50% (v/v) glycerol
10x TAE running buffer	400 mM TRIS/acetat (pH 8.0), 10 mM EDTA
TBS buffer	50 mM TRIS/HCl (pH 7.4) 150 mM NaCl
TE buffer	10 mM TRIS/HCl (pH 8.0) 1 mM EDTA
10x PBS buffer	0.1 M Na_2HPO_4, 0.01 M KH_2PO_4 (10x pH 7.0; 1x pH 7.4) 1.37 M NaCl, 27 mM KCl
10x TBE buffer	890 mM TRIS (pH 8.4), 890 mM boric acid, 20 mM EDTA

8.1.2 General Methods

8.1.2.1 Conservation of E. coli Strains

E. coli strains were grown at 37 °C in LB medium supplemented with corresponding antibiotics. Cultures were inoculated by a single colony of an LB plate or from a glycerol culture. The determination of cell density was done by measuring the optical density at 595 nm, while an $OD_{595} = 1.00$ equaling a cell density of about 10^9 cells/mL. For long-term conservation 0.5 mL of an over-night culture were added to 0.5 mL glycerol, flash-frozen and stored at –80 °C.

8.1.2.2 Polymerase Chain Reaction

For the amplification of DNA fragments the polymerase chain reaction (PCR) was used. A typical preparation of 100 μL contains 1-10 ng template cDNA, each 1 μM oligonucleotide primer, 0.2 mM dNTP PCR nucleotide mix and 2.5-5 U Pwo DNA polymerase in Pwo PCR buffer. PCR amplification was achieved on a Perkin Elmer thermocycler using the following program:

Denaturation	2 min, 93 °C
Addition of polymerase	
Denaturation	30 sec, 94 °C
Hybridization	30 sec, 58-63 °C
Elongation	1 min, 72 °C (cycle)
Elongation	10 min 72 °C

8.1.2.3 Site-Directed Mutagenesis

Site-directed mutagenesis was performed using the QuikChange Site-directed Mutagenesis Kit (Stratagene, La Jolla, CA, USA) according to the specifications. Mutagenic primer must contain the desired mutation and anneal to the same sequence on opposite strands of the plasmid. Primers should be between 25 and 45 bases in length, with a melting temperature T_M of > 78 °C. The following equation has been used to estimate the T_M of primers,

$$T_M = 81.5 + 0.41(\%GC) - 675/N - \%mismatch \qquad \text{8-1}$$

where N is the primer length in bases. The minimum GC content should be 40% and the desired mutation is supposed to be in the middle of the primer Table 10. A typical sample reaction contains 5 μL 10x reaction buffer, 5-50 ng template dsDNA, 125 ng oligonucleotide forward primer and 125 ng oligonucleotide reverse primer, 1 μL dNTP mix in a total volume of 50 μL ddH$_2$O. The reaction is started by adding 1 μL *PfuTurbo* DNA polymerase (2.5 U/μL) in a thermocycler:

1. Denaturation	30 sec, 95 °C
Denaturation	30 sec, 95 °C
Hybridization	1 min, 55 °C
Elongation	1 min/kb of plasmid length, 68 °C (cycle 16)

For digestion of parental (nonmutated) DNA, 1 µL *DpnI* restriction enzyme was added to the amplification reaction and incubated for 1h at 37 °C. 1 µL of the *DpnI*-treated DNA was transformed into XL1-Blue supercompetent cells by mixing, incubation on ice for 30 min followed by a 45 sec heat pulse at 42 °C and another 2 min on ice. After addition of 0.9 mL LB medium and incubation / shaking (225-250 rpm) at 37 °C, transformed cells were plated on LB-ampicillin agar plates. Single colonies were analyzed by plasmid isolation and sequencing.

8.1.2.4 Restriction Analysis

For the verification of restriction sites and for the preparation of sequence specific DNA fragments during cloning, 200-500 ng plasmid DNA were treated with 5-10 U restriction endonuclease under recommended buffer and temperature conditions for 1 h. DNA fragments were analyzed by gel electrophoresis.

8.1.2.5 Agarose Gel Electrophoresis

The analytical and preparative separation of DNA fragments according to their molecular weight was done by electrophoresis using 1% (w/v) agarose gels (0.5-10 kb). 1g agarose was dissolved in 100 mL TAE buffer boiled up in a microwave and after cooling to about 60 °C supplemented with 50 mg ethidiumbromide. DNA samples were supplemented with 10x DNA sample buffer and separated by electrophoresis under constant voltage (50-100 V). DNA bands were identified by their fluorescence at 254 nm.

8.1.2.6 Isolation of DNA Fragments from Agarose Gels

Single DNA fragments after restriction digestion and gel electrophoresis in low melting SeaPlaque agarose gels are recovered by the QIAquick Gel Extraction Kit (Quiagen, Hilden) according to the specifications.

8.1.2.7 Ligation

Ligation of isolated DNA fragments from restriction digestion was achieved by T4 DNA-ligase using the Rapid DNA Ligation Kit (Roche Molecular Biochemicals, Mannheim) according to the specifications. A typical digestion of 200 ng vector DNA was mixed with a five times molar excess of insert DNA and 15 min. at 20 °C ligated. Ligation products were transformed into competent *E. coli* cells.

8.1.2.8 *Transformation of* **E.coli**

For the transformation of recombinant DNA, 100 μL competent *E. coli* cells were chilled on ice and supplemented with 0.2-0.4 μg DNA from a ligation reaction or 0.01-0.1 μg plasmid DNA and incubated for 30 min on ice. Subsequently the cell were heat shocked for 90 sec at 42 °C in a water bath and again incubated on ice for another 5 min. After addition of 900 μL LB medium the transformation reaction is incubated for 1h at 37 °C and subsequently plated onto LB-agarplates containing the corresponding antibiotics. For analysis, plasmid DNA was isolated from 5-10 single colonies and subjected to restriction digestion and gel electrophoresis.

8.1.2.9 *Isolation of Plasmid DNA from* **E. coli**

Plasmid DNA for further experiments such as PCR, cloning, restriction analysis and sequence analysis were isolated using the QIAprep Spin Miniprep Kit (Quiagen, Hilden) according to the specifications. 1.5 mL of an over-night culture were subjected to an alkaline lyses, cellular RNA was digested by RNase A addition and plasmid DNA was bound to a silica matrix under high-salt conditions. Elution of plasmid DNA with concentrations of 100-200 ng/μL was done with 50 μL low-salt buffer.

8.1.2.10 DNA Sequencing

The sequence of all plasmid constructs were analyzed by the chain-terminating method (Sanger et al., 1977) by insertion of fluorescence labeled didesoxynucleotides using a Big Dye Terminator Cycle Sequencing Kit (Perkin-Elmer) according to the specifications. A typical reaction volume of 20 mL contained 500 ng plasmid DNA supplemented with 5 pmol sequencing primers and 4 mL sequencing mix. The sequencing reaction was done on an GeneAmp 2400 Thermocycler (Perkin Elmer) using the following program:

Denaturation	10 sec, 94 °C
Hybridization	15 sec, 55 °C
Elongation	4 min, 60 °C (cycle)

Free nucleotides were removed by the QIAquick DyeEx Kit (Quiagen, Hilden) according to the specifications. Electrophoretic separation and fluorescence detection was done using a capillarelectrophoresis system (ABI Prism 310; Perkin Elmer)

8.1.2.11 Expression Analysis

For the analysis and optimization of expression conditions, each 5 mL LB medium was inoculated 1:100 with an over-night culture using different parameters such as induction, IPTG concentration, temperature induction time. Bacteria pellets were

subsequently spinned down (500 rpm, 10 min.) and suspended in 250 μL 50 mM TRIS (pH 7.5), 50 mM EDTA and lysed using a supersonic Sonifier Cell Disruptor B15 (Branson). Soluble proteins were separated from the pellet by centrifugation (1200 rpm, 10 min.) and the later one was again suspended in 250 μL 50 mM TRIS (pH 7.5), 50 mM EDTA. Each 10 μL of the soluble and resuspended insoluble fraction were subjected to an SDS-PAGE and analyzed.

8.1.2.12 Purification of Inclusion Bodies

For the preparation of inclusion bodies followed by *in vitro* refolding, 100 ng *E. coli* in 500 mL 100 mM TRIS/HCl (pH 7.0), 1 mM MgSO$_4$ at 4 °C were homogenized using a Ultraturrax T25 Basic (IKA) supplemented with 300 ng lysozyme and 500 U benzonase. After incubation at room temperature for 20 min the cell suspension was digested in an APV-Gaulin Lab 60-15 RPF high pressure press and subsequently incubated at room temperature for another 30 min. The lyses was diluted 2:1 with Brij buffer and incubated for another 30 min at room temperature; the insoluble fraction was separated by centrifugation (8000 rpm, 20 min). The inclusion bodies were washed twice using an Ultraturrax in 100 mL 100 mM TRIS/HCl (pH 6.5), 20 mM EDTA and stored at –20 °C.

8.1.2.13 In Vitro *Refolding*

Isolated and washed inclusion bodies were solubilized in 6 M GdnCl, 100 mM TRIS (pH 7.5), 100 mM DTT. The *in vitro* folding is done at 4° - 10 °C in steps of 3-4 pulses, each 200 μg/mL solubilized inclusion bodies over 24 h in 4 L of the following buffer: 0.1 M TRIS (pH 8.0), 0.5 M GdnCl, 0.5 M L-arginine, 20 mM ZnCl$_2$, 5 mM DTT, 1mM benzamidine. After *in vitro* folding in 4 L, the volume has to be concentrated to 1/20 by ultrafiltration using a Provario Pall Filtron and subsequently dialyzed against 50 mM potassium phosphate buffer (pH 6.6), 50 mM KCl, 5mM DTT. Not successfully folded protein precipitates and is separated by centrifugation (13000 rpm, 20 min).

8.2   Mutational Study on the Dimerization Interface of p53 DBD

8.2.1   Cloning, Expression and Purification of p53 Dimerization Mutants

Residues 94-312 of human p53 coding for the wild-type p53 DBD (Bullock et al., 2000; Cho et al., 1994; Wong et al., 1999a) were amplified from plasmid pT7.7Hup53 (Midgley et al., 1992) by polymerase chain reaction and cloned into a modified pQE40 vector (Quiagen). Single and double mutations were introduced by Quick-Change Site-directed Mutagenesis (Stratagene) according to the specifications (see section 6.2.1.2.3). Gene-specific oligonucleotide primers were synthesized as given in Table 10 by MWG Biotech AG or metabion.

Table 10: Forward and backward primer for the site-directed mutagenesis of p53 DBD dimerization mutants.

Mutant	Forward and Backward Sequence
H178A	5´-GGCGCTGCCCCGCCCATGAGCGCTGCTCAGATAGCG-3´ 5´-CGCTATCTGAGCAGCGCTCATGGGCGGGGCAGCGCC-3´
E180R	5´-CTGCCCCCACCATAGGCGCTGCTCAGATAGC-3´ 5´-GCTATCTGAGCAGCGCCTATGGTGGGGGCAG-3´
E180R/R181E	5´-GCTGCCCCCACCATAGGGAATGCTCAGATAGCG-3´ 5´-CGCTATCTGAGCATTCCCTATGGTGGGGGCAGC-3´
R181A	5´-GCCCCCACCATGAGGCCTGCTCAGATAGC-3´ 5´-GCTATCTGAGCAGGCCTCATGGTGGGGGC-3´
R181E	5´-GGCGCTGCCCCCACCATGAGGAATGCTCAGATAGC-3´ 5´-GCTATCTGAGCATTCCTCATGGTGGGGGCAGCGCC-3´
C182A	5´-GCCCCCACCATGAGCGCGCCTCAGATAGCGATGG-3´ 5´-CCATCGCTATCTGAGGCGCGCTCATGGTGGGGGC-3´

The mutant p53 DBD cDNA was PCR-amplified, sequenced (Sequencing primer are given in Table 6) using the Big Dye Terminator Sequencing Kit (Perkin Elmer) and introduced into the NdeI/XhoI site of a modified pQE40 (Quiagen) expression vector. The mutant p53 DBD expression vectors were identical to the wild-type vectors except for specific single and double site nucleotide substitutions.

p53 DBD wild-type and p53 DBD mutants were expressed in *Escherichia coli,* co-transfected with pUBS520 at 37 °C in LB medium as inclusion bodies, refolded *in vitro* and purified as described elsewhere (Klein et al., 2004) (see section 6.2.1.2.12 – 13). For the preparation of uniformly ^{15}N-labeled p53 DBDs, bacteria were grown at 37 °C in M9 minimal medium containing antibiotics, minerals and vitamins supplemented with 2 g/L ^{15}NH$_4$Cl as sole nitrogen source. The polymerase chain reaction product was subcloned into a pGEX-4T-1 vector (Amersham Pharmacia Biotech). The resulting recombinant expression vector pGEX-4T(GST-p53

DBD) codes for the corresponding GST-p53 DBD (mutant) fusion protein including a Gly-Ser-Gly linker that remains at the N-terminus after digestion of the fusion protein with thrombin. All vector constructs were confirmed by sequencing. Fusion proteins were expressed in *Escherichia coli* strains HB101 and UT5600, which were grown at 20 °C in Luria broth medium, and soluble protein was purified as described in (Klein et al., 2004). All proteins were concentrated using 5K Ultrafree 4 centrifugal filter devices (Millipore), dialyzed against 50 mM potassium phosphate, pH 6.8, 50 mM KCl and 5 mM DTT, flash-frozen and stored at −80 °C.

8.2.2 Analytical Procedures

Protein concentration was measured spectrophotometrically according to the method of Bradford (Bradford, 1976) or using an extinction coefficient of $\varepsilon_{280\ nm}$ = 15.930 M^{-1} cm^{-1} for the p53 DBD and 14.650 M^{-1} cm^{-1} for p63 DBD, calculated according to the method of Edelhoch (Edelhoch, 1967). SDS-polyacrylamide gel electrophoresis was performed with 12.5% gels.

8.2.3 Electrophoretic Mobility Shift Assay (EMSA)

DNA binding was examined via electrophoretic mobility shift assay (EMSA) as described (Hupp et al., 1992). For each lane 200 ng of p53 DBD wild-type, p63 DBD wild-type or mutant p53 DBD as indicated were incubated on ice for 15 min in 10 µl DNA binding buffer (40 mM HEPES (pH 8.0), 50 mM KCl, 10 mM $MgCl_2$, 0.1% Triton X-100, 1 mg/mL bovine serum albumin, 5 mM DTT, 15% glycerol) with a 1.1 µM solution of fluorescence labeled double-stranded PG consensus-site oligonucleotide (5'-IRDye700-AGCTT AGACA TGCCT AGACA TGCCTA-3' and 3'−ATCTG TACGG ATCTG TACGG ATTCGA-5') in the presence of 200 ng unspecific unlabeled pBluescript II SK$^+$ competitor DNA (Stratagene) in 10 µL DNA binding buffer. DNA complexes were separated from unbound oligonucleotides on native 4% polyacrylamide gels; the running buffer consisted of 30 mM Tris-HCl (pH 7.5), 30 mM boric acid and 1 mM EDTA with 0.01% Triton X-100. and quantified with an Odyssey Imager (LI-COR).

8.2.4 NMR Spectroscopy

NMR investigations were carried out on a Bruker DMX700 spectrometer equipped with a triple channel (^1H, ^{13}C, ^{15}N) inverse probe. Water suppression was achieved by employing heteronuclear or homonuclear WATERGATE gradient echoes (Piotto et al., 1992). Standard sample conditions were 200 – 800 µM ^{15}N-labeled protein in 50 mM potassium phosphate, pH 6.8, 50 mM KCl and 5 mM DTT. Standard

temperature was 298 K. DNA oligonucleotides containing one 10-mer p53 consensus half site, 16-meric CON2x5 (5´-CCT <u>AGACA</u> <u>TGCCT</u> AAT-3´) were annealed with complementary oligonucleotides, diluted into the NMR buffer, and titrated to the NMR sample. A 1.2 M excess of consensus quarter sites relative to the p53 DBD was used to achieve a stoichiometric 1 : 2 = dsCON2x5 : p53 DBD binding. Spin-echo diffusion measurements were performed on *apo* p53 DBD wild-type and mutants and on their DNA complexes using a standard stimulated echo pulse train with sine-shaped bipolar diffusion-encoding gradients, one z-spoil gradient and a WATERGATE water suppression scheme. 64 ^{1}H spectra were recorded using a gradient ramp ranging from 1.07 to 50.80 G/cm and stored as a pseudo-2D experiment. The dephasing and refocusing gradient length *LD* was set to 4 ms, and the diffusion delay *BD* was 120 ms. The evaluation of the data was carried out using the T_1/T_2 relaxation menu of XWin-NMR 3.5. Convergent non-exchangeable signal decays between 4.0 ppm and 0 ppm were averaged and a nonlinear least-squares regression onto the signal decay using Origin Version 5.0 yielded the translational diffusion coefficient.

8.2.5 *Hydrodynamic Calculations*

Hydrodynamic calculations were performed with HYDRONMR Version 5a (García de la Torre et al., 2000b) using the published crystal structure of the p53 DBD (pdb-ID: 1TSR, chain B) with and without DNA and a dimeric p53 DBD-DNA complex as proposed by Klein et al. (Klein et al., 2001b) to build up the bead model.

8.3 NMR Spectroscopic Analysis of the N-terminal Domain of p53

8.3.1 Cloning, Expression and Purification of Np53 and MDM2

Cloning, expression and purification of Np53 and MDM2 was done in the group of Prof. J. Buchner, Garching and is described in (Dawson et al., 2003). For NMR experiments, ^{15}N Np53 was expressed and purified as described, except that bacterial growth was performed in M9 medium containing ^{15}NH$_4$Cl (Spectra Gases). Samples used for NMR experiments were concentrated using 5 K Ultrafree 4 centrifugal filter devices (Millipore) to a final concentration of 1.2 mM in 20 mM sodium phosphate pH 7.5, 300 mM sodium chloride and supplemented with 0.01 (v/v) sodium azide.

8.3.2 NMR Experiments

All spectra were acquired at 298 K on a 750 MHz Avance Bruker spectrometer equipped with a four channels probe and triple axis gradients. For the ^{1}H-^{15}N HSQC spectrum a total of 1024 complex points in t_2 and 512 t_1 increments were acquired. The spectral width used was 8865.2 Hz for ^{1}H and 2057.6 Hz for ^{15}N. Water suppression was carried out using the WATERGATE sequence (Piotto et al., 1992). NMR data were processed using the Bruker program package XWin-NMR Version 3.1 and Aurelia. Zero-filling, gaussian (t_2) and 90° shifted sine-bell apodisation (t_1) were applied prior to Fourier transformation, and subsequent baseline corrections were carried out in both dimensions. Titration experiments were performed using a series of ^{1}H-^{15}N HSQC spectra of ^{15}N Np53 up to an eightfold excess of unlabelled MDM2. Spin-echo diffusion measurements were performed at 298 K using a standard stimulated echo pulse train with bipolar diffusion gradients, one z-spoil gradient and a WATERGATE water suppression schema (Piotto et al., 1992). 16 ^{1}H spectra were recorded using sine shaped gradients, a gradient ramp between 0.7 and 33.2 G/cm, 32 scans, a sweep width of 8865.2 Hz and a digital resolution of 8k real data points and stored as a pseudo-2D experiment. The dephasing and refocusing gradient length *LD* was set to 4 ms, and the diffusion delay *BD* was 300 ms. The evaluation of the data were carried out using the T_1/T_2 relaxation menu of XWin NMR 3.1 with the provided fitting function for variable gradient strength. 23 convergent non-exchangeable signal decays between 3.5 ppm and 0 ppm were averaged and a nonlinear curve fitting procedure using Origin 5.0 was performed. Hydrodynamic calculations were performed using HYDRONMR Version 5a (García de la Torre et al., 2000b) and a regularized random model structure of Np53 generated by XPLOR Version 3.851 (Brünger, 1992).

8.4   Mapping the Binding Sites of Bcl-xL / Bcl-2 and the p53 DBD

8.4.1   Cloning, Expression and Purification of p53 DBD and Bcl-xL

Residues 94 – 312 of human p53 coding for the wild-type p53 DNA binding domain (DBD) cloned into a modified pQE40 vector (Qiagen) were expressed in *Escherichia coli* BL21(DE3) co-transfected with pUBS520 as described (Klein et al., 2001a; Klein et al., 2004). Unlabeled and uniformly ^{15}N-labeled p53 DBD proteins were prepared as previously described (Klein et al., 2001a; Klein et al., 2004).

Full-length human Bcl-xL cloned into pGEX-2T (Amersham Bioscience, Inc.), was expressed as GST-Bcl-xL fusion protein in E. coli as described (Chittenden et al., 1995; Zhou et al., 2000) and purified via GSH-Sepharose (Amersham Bioscience, Inc.). The GST-tag was cleaved off by over-night Thrombin cleavage at 4 °C and free Bcl-xL was recovered after adsorption of free GST and uncleaved GST-Bcl-xL on GSH-Sepharose. For the NMR studies, a more soluble version of Bcl-xL was constructed by removing the putative C-terminal trans-membrane domain, Bcl-xLΔT (containing Bcl-xL residues 1-213). The Bcl-xL gene was subcloned from pcDNA-Bcl-xL (a gift from RJ, Biochemistry Section, Surgical Neurology Branch, National Institute of Neurological Disorders and Stroke, National Institutes of Health, Bethesda, MD 20892, USA) into the pET30 overexpression system, which contains an N-terminal His$_6$-tag (Novagen, Darmstadt, Germany), and transformed into the *Escherichia coli* BL21(DE3) cells (Nogaven). The ^{15}N labeled protein was expressed and purified as previously described (Petros et al., 2001). Briefly, Ni-NTA (Novagen) affinity chromatography, His-tag removal by Thrombin digestion, ion-exchange chromatography with a HiLoad Q-FF (Amersham Bioscience, Inc.), and size-exclusion chromatography with a 16/70 Superdex G75 column (Amersham Bioscience, Inc.) were used. The p53 and Bcl-xLΔT samples were finally dialyzed against 25 mM Na phosphate (pH 7.2), 150 mM KCl, and 5 mM DTT for the NMR studies.

In addition, another Bcl-xL deletion mutant lacking both a large flexible loop between helix 1 and 2, and the C-terminal putative transmembrane domain, Bcl-xLΔLT (containing Bcl-xL residues 1-43, 83-209) was constructed to simplify ^{15}N HSQC spectra as follows (Sattler et al., 1997): point mutation E43A was generated by site directed mutagenesis on the wild type template, resulting in an additional NcoI site. Digestion with NcoI, followed by re-ligation results in deletion of residues 44-82. The C-terminus of this construct was then deleted by PCR, using an antisense primer spanning residues 203-209, followed by a His$_6$-tag and subsequently cloned into a

modified pQE40 vector via NdeI/XhoI restriction sites. The anti-apoptotic potential of Bcl-xLΔLT is not affected by this deletion (Sattler et al., 1997). Unlabeled and ^{15}N labeled Bcl-xLΔLT was expressed in *E. coli* UT5600 co-transfected with pUBS520. The protein was purified by affinity chromatography on a Zn-NTA column (Roche Molecular Biochemicals). Final purification was achieved by size exclusion chromatography on a High Load 26/60 Superdex 75 column (Amersham Bioscience, Inc). p53 DBD and Bcl-xLΔLT samples were dialyzed into an uniform buffer (50 mM potassium phosphate (pH 6.8), 50 mM KCl, 5 mM DTT) and both samples were concentrated to a final concentration of 250 mM.

8.4.2 Cloning, Expression and Purification of Bcl-2

Cloning, protein expression and purification of Bcl-2 constructs were performed by York Tomita, Lombardi Cancer Center, Georgetown University Medical Center, Washington, DC as follows:

Several entries of Bcl-2 genes are deposited in GenBank and they differ by only a few residues. Two isoforms were described in the recent publication of the Bcl-2 structures, isoform 1 (Bcl-2 (1)) with Ala at position 96 and Gly at 110 and isoform 2 with Thr at 96 and Arg at 110 (Petros et al., 2001). The isoform 2 was used for our study since this isoform has higher affinity to the Bak and Bad peptides in the FP assay than the isoform 1. Bcl-2 was sub-cloned into pET28b plasmid (Novagen) and a large flexible loop of Bcl-2 was replaced with a shortened loop of Bcl-xL at the equivalent position (between the helixes 1 and 2) and the putative transmembrane helix was removed to increase the protein solubility and stability without alternating its native biological functions (Petros et al., 2001). The protein was expressed and purified as previously described (Petros et al., 2001).

8.4.3 NMR Spectroscopy

The NMR spectra for ^{15}N p53 DBD and unlabeled Bcl-xLΔLT were acquired at 300 K on a DMX Bruker spectrometer (700 MHz ^{1}H frequency) equipped with a triple-channel probe and z-gradients. All experiments were processed and analyzed by XWin-NMR 3.5 (Bruker Biospin) and Sparky Version 3.106. The titration experiments were performed by titrating a molar 1:1.1-fold excess of Bcl-xLΔLT into 350 µM samples of uniformly ^{15}N-labeled p53 DBD in 50 mM potassium phosphate buffer (pH 6.8), 50 mM KCl, 5 mM DTT at 300 K. For the ^{1}H,^{15}N HSQC spectra a total of 1024 complex points in t_2 with 128 t_1 increments were acquired, with 32 scans for each increment. NMR data were processed with the Bruker program package XWin-NMR Version 3.5 and analyzed with the program Sparky Version 3.106

(Goddard and Kneller; Kneller and Kuntz, 1993). Zero-filling, gaussian (t_2) and 90° shifted sine-bell apodisation (t_1) were applied prior to Fourier transformations, and subsequent baseline corrections were performed in both dimensions. Prior to titration of Bcl-xLΔLT, a single reference ^{1}H,^{15}N HSQC of the free p53 DBD sample was recorded. Backbone assignments of ^{1}H, ^{15}N chemical shifts of p53 DBD were taken from the published assignment (Wong et al., 1999b) and could be transferred onto the measured spectra. Chemical shift perturbations of the p53 DBD-Bcl-xLΔLT complexes were determined from the minimum deviation between each position of the free and the complexed peak in the ^{1}H,^{15}N HSQC spectra (Dehner et al., 2003). For analysis of the chemical shift perturbations of ^{1}H and ^{15}N backbone resonances, a weighted average chemical shift change given by $\Delta_{av} = [(\Delta\delta^2_{NH} + \Delta\delta^2_N/25)/2]^{1/2}$ used was calculated and normalized by Δ_{av}/Δ_{max}, where Δ_{max} is the maximum observed weighted shift difference (Grzesiek et al., 1996).

NMR spectra for ^{15}N p53 DBD with unlabeled Bcl-xLΔT or unlabeled Bcl-2, and ^{15}N Bcl-xLΔLT with unlabeled p53 DBD were acquired at 293 K in the sample buffer (25 mM Na Phosphate (pH 7.2), 150 mM KCl, and 5 mM DTT) on DMX Bruker spectrometers (500 and 750 MHz ^{1}H frequency) equipped with a triple-resonance, (xy)z-gradient probe. All experiments were processed and analyzed by use of nmrPipe and nmrDraw (Delaglio et al., 1995). Approximately 200 µM of the ^{15}N labeled protein was titrated with 0 - 200 µM of the unlabeled protein.

8.4.4 Modelling and Chemical Shift Based Protein-Protein Docking

Structural coordinates of the DNA binding domain of p53 (pdb entry 1TSR) and Bcl-xL (pdb entries 1BXL and 1LXL) were taken from the RCSB Protein Data Bank. Docking was performed using the Python scripts of HADDOCK 1.2 (Dominguez et al., 2003). Ambiguous interaction restraints (AIRs) for the subsequent structure calculations are defined by significant shift perturbations (> 0.4) in the ^{15}N HSQC spectra of p53 DBD and Bcl-xL upon titration of a 1.1 molar excess of unlabeled Bcl-xLΔLT and p53 DBD, respectively. In addition so-called active residues have to be solvent accessible, which was calculated using NACCESS (Hubbard and Thornton, 1993). Only these residues which show a backbone or side-chain solvent accessibility above 50 % were considered in the definition of active and passive residues. Whereas passive residues are surface neighbors of active residues and were determined visually using VMD (Humphrey et al., 1996). Interface residues are active and passive residues taken together plus one or two sequential residues (Table 3). The loop region 29 – 82 and the C-terminal region 196 – 211 in Bcl-xL were defined as fully flexible segments throughout the calculation.

200 rigid-body structures were generated and for each starting conformation, ten rigid-body trials were performed. Only the best solutions in terms of intermolecular energy were kept, resulting in 2000 total rigid-body trials. The best 60 solutions according to van der Waals, electrostatic and AIRs energy terms were subjected to a semi-flexible simulated annealing refinement (4000 steps from 2000 to 50 K with 4 fs time steps; side-chains are allowed to move) and a third refinement (1000 steps from 500 to 50 K with 2 fs time steps) in which side-chains and backbone in the interface are allowed to move. Fifteen of the best solutions in terms of total energy were further refined in a 8 Å shell of TIP3P water molecules (Dominguez et al., 2003). Due to the long flexible loop in Bcl-xL the solutions were clustered manually and sorted by total energies; the ten lowest-energy structures were further analyzed (Table 4). As NMR titration experiments were performed with the loop-deleted construct Bcl-xLΔLT we also generated 200 rigid-body complex structures using pdb entry 1BXL as a starting structure which does not contain this loop regions in order to prove that calculated full-length Bcl-xL complex structures are not biased by this loop in terms of binding sites

8.4.5 Electrophoretic Mobility Shift Assay

DNA binding was examined via electrophoretic mobility shift assay (EMSA) as described (Klein et al., 2001a). For each lane, 100 ng of p53 DBD protein was incubated with 0, 50, 100, 200, 400 and 800 ng of full length Bcl-xL or Bcl-xLΔLT protein in 15 mL DNA binding buffer (15 mM Tris, 50 mM KCl, 5 mM DTT, pH 7.2) on ice for 15 min. Separately, 12 ng of fluorescence-labeled double-stranded PG13 consensus-site oligonucleotide (sense 5'-IRDye700-GGAACATGTTCC-3') was dissolved in 30 mL of binding buffer in the presence of 200 ng unspecific competitor DNA (pBluescript, Stratagene) and 5 mL aliquots were added to each p53 tube to incubate for another 15 min on ice. Each sample was mixed with 5 mL of 75% glycerol and then p53 DBD-DNA complexes were separated from unbound oligonucleotides on native 8% polyacrylamide gels and quantified with an Odyssey Imager (LI-COR).

8.5   Sequential Backbone Assignment of p63 DBD

8.5.1   Expression and Purification of p63 DBD for NMR Studies

A modified pQ40 expression vector p20020 (C. Klein, Roche Diagnostics) (Klein et al., 2001a), codes for human p63 DBD residues 114-349 without tags, including an additional N-terminal glycine residue. Unlabeled and double-labeled [U-^{13}C,^{15}N]-p63 DBD were expressed in *E. coli* BL21 cells which were cotransfected with pUBS520 (Brinkmann et al., 1989). Cells were grown in LB medium and M9 minimal medium (using ^{13}C$_6$-glucose and [^{15}N]-NH$_4$Cl), respectively, at 37 °C supplemented with ampicillin (100 g/mL) and kanamycin (50 g/mL) to an absorbance of OD$_{595}$ = 0.5–0.8 before overnight induction at 37 °C with 1 mM isopropyl-β-D-thiogalactopyranoside. After induction, cells were harvested by centrifugation; resuspended in 50 mM Tris (pH 6.8), 5 mM DTT, 1 mM benzamidine, and Complete protease inhibitor mixture (EDTA-free; Roche Molecular Biochemicals) and disrupted by high-pressure dispersion using an APV Gaulin Lab 40 homogenisator. For purification of the p63 DBD, soluble lysat was loaded onto an SP-Sepharose Fast Flow cation-exchange column (Amersham Pharmacia Biotech) and eluted with a linear KCl gradient (0–0.5 M). Final purification was achieved by preparative size-exclusion chromatography on a Superdex 75 HiLoad 26/60 column (Amersham Pharmacia Biotech) in 50 mM Tris (pH 7.0), 150 mM KCl, and 5 mM DTT. NMR samples were dialyzed against 50 mM potassium phosphate (pH 6.8), 50 mM KCl and 5 mM DTT, supplemented with 5% (v/v) D$_2$O, shock frozen and stored at –80 °C.

8.6   Chemical Shift Perturbation Study of Hsp90 upon Ligand Binding

8.6.1   Protein Purification and Sample Preparation

In collaboration with J. Buchner the N-terminal domain of Hsp90 (Nhsp90), consisting of the amino acids 1 to 210, was purified from the *E. coli* strain BL21 (DE3) carrying the plasmid pET11a-Nhsp90 (Scheibel et al., 1998). The bacteria were grown in M9 medium containing ^{15}N-labeled NH$_4$Cl (Cambridge Isotope Laboratories, Andover, USA) as the sole nitrogen source. For preparation of ^{13}C-labeled protein, ^{13}C$_6$-Glucose (Cambridge Isotope Laboratories, Andover, USA) was used as sole carbon source. Bacteria were grown to an OD$_{600}$ of about 0.5. Protein induction was then started with the addition of 1.5 mM IPTG and continued over night at 30 °C. Protein purification was achieved as described previously (Scheibel et al.,

1998). Purified protein was concentrated and dialyzed against 40 mM potassium phosphate, pH 7.5, which was the buffer used for the NMR-experiments.

The ^{2}H, ^{13}C, ^{15}N-labeled protein has been purified according to the same procedure, except that the bacterial growth was performed in 1 L LB until a OD$_{600}$ of about 1.5 was obtained. The cells were spun down and resuspended in M9 medium containing ^{15}NH$_4$Cl, ^{13}C$_6$-glucose and 70% D$_2$O (Cambridge Isotope Laboratories, Andover, USA). Bacterial growth was continued at 37°C until the OD$_{600}$ had doubled once and 1.5 mM IPTG was added thereafter. Protein expression was performed at 30°C over night.

Samples for the NMR experiments were concentrated to about 550 μM Nhsp90. Geldanamycin was a kind gift of the Experimental Drug Division (NIH, Bethesda, USA). Radicicol was obtained from Sigma, AMP-PNP and ADP from Roche Applied Sciences (Mannheim, Germany).

8.6.2 NMR Spectroscopy

8.6.2.1 Sequential Backbone Assignment

For the sequential assignment of the N-terminal domain of Hsp90, a uniformly ^{15}N, ^{13}C, ^{2}H (70%)-labeled sample in 40 mM phosphate buffer (pH = 7.5) in 90% H$_2$O / 10% D$_2$O with a concentration of 800 μM Nhsp90 was used. All NMR spectra were acquired at 303 °K on a 800 MHz Bruker Avance spectrometer equipped with a four-channel probe and triple axis gradients. The assignments of ^{1}H, ^{15}N, ^{13}CO, ^{13}Cα and ^{13}Cβ chemical shifts were determined by a series of TROSY-type triple resonance experiments with ^{2}H decoupling: HNCO, HNCA, HN(CO)CA, HN(CA)CO and a HN(CO)CACB (Salzmann et al., 1998; Salzmann et al., 1999). All the experiments were processed and analyzed using XWin-NMR 3.1 and Aurelia 3.5. Sequence specific resonance assignments were obtained with the assignment program PASTA (Leutner et al., 1998). The obtained backbone assignment independently confirms the recently published assignment (Salek et al., 2002).

The titration experiments were performed with uniformly ^{15}N-labeled Nhsp90 using four 600 μL samples (550 μM protein, 40 mM potassium phosphate buffer, pH 7.5, 10% ^{2}H$_2$O), at 298 K on a 750 MHz Bruker Avance spectrometer equipped with a four-channel probe and triple axis gradients. The ^{1}H and ^{15}N assignment was taken from the complete backbone resonance assignments deposited in the BioMagResBank with the accession number 5355 (Salek et al., 2002) and could be completely transferred onto our ^{1}H-^{15}N HSQC spectra which exhibit only slight chemical shift changes for the amide resonances, due to different sample preparation strategies. The

^{1}H-^{15}N HSQC spectra were obtained using the fast-HSQC method (Mori et al., 1995), in order to obtain a suitable signal to noise ratio for the water exchangeable amide protons and good water suppression which was carried out using the WATERGATE sequence (Piotto et al., 1992; Sklenar et al., 1993). A total of 2048 complex points in t_2 with 512 t_1 increments were acquired with 16 scans for each increment. The spectral width used was 12.818 ppm for ^{1}H and 39.15 ppm for ^{15}N. The NMR data were processed using the Bruker program package XWin-NMR Version 3.1 and Sparky Version 3.106 (Goddard and Kneller; Kneller and Kuntz, 1993). Zero-filling, gaussian (t_2) and 90° shifted sine-bell apodisation (t_1) were applied prior to Fourier transformations, and subsequent baseline corrections were performed in both dimensions.

8.6.2.2   *Titration Experiments*

The titration experiments were carried out using the nonhydrolysable AMP-PNP (Adenylyl-imidodiphosphate) instead of ATP. For AMP-PNP and ADP a 50 mM aqueous solution was prepared in 40 mM KP buffer (pH 7.5) and 100 mM Mg^{2+}. The ligands were added to a 550 µM solution of ^{15}N-labeled Nhsp90, and a series of ^{15}N-fHSQC spectra were recorded at various ligand concentrations in the range of $0 - 2.26$ mM in the case of AMP-PNP ($0 - 96\%$ bound complex; K_d(AMP-PNP) ~ 70 µM) and $0 - 4.64$ mM for ADP respectively ($0 - 99\%$ bound complex; K_d (ADP) ~ 10 µM) (Richter et al., 2002). The competitive inhibitors Radicicol and Geldanamycin were dissolved to a 60 mM solution in d^6-DMSO each. Prior to titration of the inhibitors, a single reference ^{1}H-^{15}N-fHSQC was recorded of the free Nhsp90 sample to which 1% d$_6$-DMSO was added. A series of ^{15}N-fHSQC spectra were recorded afterwards using increasing concentrations of Radicicol ($0 - 0.8$ mM; K_d(Radicicol) ~ 0.9 nM) and Geldanamycin ($0 - 0.6$ mM; K_d(Geldanamycin) ~ 1.2 µM). Due to the binding constants of AMP-PNP, ADP and the inhibitors ($K_d < 100$µM) the complexes were long-lived on the NMR chemical shift time scale ($\tau > 10$ ms). Accordingly, a second signal set for the ligand-complexed Nhsp90 appeared during the titration. Chemical shift perturbations of the Nhsp90 complexes were determined by the minimum deviation between each position of the free and complexed peak in the HSQC spectra (Lüttgen et al., 2002). For the analysis of the chemical shift perturbations of ^{1}H and ^{15}N backbone resonances a weighted average chemical shift change was calculated and normalized by $\Delta_{av}/\Delta_{max} = 1.0$, where Δ_{max} is the maximum observed weighted shift difference (Grzesiek et al., 1996).

8.7 NMR spectroscopic Studies of Unfolded and SDS-Folded Hsp12

8.7.1 Sample Preparation

Hsp12, consisting of the amino acids 1 to 109, was purified from the *E. coli* strain BL21 DE3. The bacteria were grown in M9 medium (minimal growth medium) containing ^{15}N-labeled NH_4Cl (Cambridge Isotope Laboratories, Andover, MA, USA) as the sole nitrogen source. For preparation of ^{13}C-labeled protein, $^{13}C_6$-glucose (Cambridge Isotope Laboratories, Andover, MA, USA) was used as sole carbon source. Samples for the NMR-experiments were concentrated to about 1.2 mM and dialyzed against 10 mM sodium phosphate, pH 7.5, which was the buffer used for the NMR-experiments.

8.7.2 Titration Experiments

Titration experiments were carried out using perdeuterated d^{25}-SDS (Cambridge Isotope Laboratories, Andover, USA) added to a 1.2 mM solution of ^{15}N-labeled Hsp12. Four ^{15}N-HSQC spectra were recorded at SDS concentrations of 20, 50, 150 and 300 mM on a 600 MHz Bruker Avance spectrometer (Karlsruhe, Germany) at 310 K. A total of 1024 complex points in t2 and 256 t1 increments were acquired. The spectral width used was 12.8581 ppm for ^1H and 25.0536 ppm for ^{15}N. Water suppression was carried out using the WATERGATE sequence (Piotto et al., 1992).

8.7.3 Sequential Assignments

For the sequential assignment of the SDS-micelle-folded Hsp12, a uniformly ^{15}N, ^{13}C labeled sample in 40 mM phosphate buffer (pH = 7.5) and 300 mM d^{25}-SDS in 90% H_2O / 10% D_2O with a concentration of 1 mM Hsp12 was used. NMR spectra were acquired at 310 K on a 750 MHz Bruker Avance spectrometer (Karlsruhe, Germany) equipped with a four-channel probe and triple axis gradients. The assignments of ^1H, ^{15}N, ^{13}CO, $^{13}C\alpha$ and $^{13}C\beta$ chemical shifts were determined using a set of triple resonance experiments: HNCO, HNCA, HN(CA)CO, HNCACB and a CBCA(CO)NH. For the sidechain assignments 3D CC(CO)NH and 3D H(CCCO)NH TOCSY experiments were performed. The backbone assignments of unfolded Hsp12 could be achieved partially, using the following set of triple resonance experiments: HNCO, HN(CA)CO, HNCACB and a CBCA(CO)NH. Identification of secondary structural elements on the basis of ^{13}C and Hα chemical shifts (chemical shift index) was calculated using the program CSI Version 2.0 (Wishart et al., 1992) which was referenced to random coil shift values according to Wüthrich et al. (Wüthrich, 1986).

8.7.4 Fast Water Exchange

Fast water exchange rates of amid protons was measured by New MEXICO (Koide et al., 1995) experiments at 310 K with mixing times of 40, 80 and 160 ms each for the SDS-micelle folded Hsp12 and unfolded Hsp12. Peak intensities were referenced to a standard HSQC pulse train without sensitivity enhancement. Exchange rates were calculated using the equation $I(mix) = I_0\left(1 - e^{-k_{ex}\tau_{mix}}\right)$, where $I(mix)$ is the peak intensity for a given mixing time τ_{mix}, I_0 the reference peak intensity and k_{ex} the exchange rate given in s^{-1}. Temperature dependent random coil hydrogen exchange rates were theoretically calculated using sequence specific correction factors and low salt conditions as described in Y. Bai et al. (Bai et al., 1993)

8.7.5 Diffusion Measurements

Spin-echo diffusion measurements were performed at 298 K on the unfolded Hsp12 without SDS micelles using a standard stimulated echo pulse train with bipolar diffusion gradients, one z-spoil gradient and a WATERGATE water suppression schema (Piotto et al., 1992). 32 ^{1}H spectra were recorded using sine shaped gradients, a gradient ramp between 0.7 and 33.2 G/cm, 32 scans, a sweep width of 8865.2 Hz and a digital resolution of 8k real data points and stored as a pseudo-2D experiment. The dephasing and refocusing gradient length LD was set to 4 ms, and the diffusion delay BD was 220 ms. The evaluation of the data were carried out using the T_1/T_2 relaxation menu of XWin-NMR 3.5. 40 convergent non-exchangeable signal decays between 4.0 ppm and 0 ppm were averaged and a nonlinear least-squares regression onto the signal decay using Origin Version 5.0 yields the translational diffusion coefficient. The apparent molecular weight, M, of the diffusing species can be calculated from the diffusion coefficient using the following equation (Cantor and Schimmel, 1980),

$$M = \left(\frac{kT}{6\pi\eta FD}\right)^3 \left(\frac{4\pi N_A}{3[v_2 + \delta_1 v_1]}\right) \qquad\qquad 8\text{-}2$$

where k is the Boltzmann constant (JK^{-1}), T the temperature which is 298 K, η is the viscosity of the solution which was taken to be that of water at 298 K (8.909 x 10^{-4} kg m^{-1} s^{-1}), D the translational diffusion coefficient determined by the spin echo diffusion experiment (1.0066 x 10^{-10} m^2 s^{-1}), N_A is Avogadro's number (mol^{-1}), v_2 is the partial specific volume of the molecule (0.73 x 10^{-6} m^3 kg^{-1}), δ_1 is the fractional amount of water bound to the molecule (0.34 g(H$_2$O)/g(protein)) corresponding to a protein hydration shell which is one water molecule thick. v_1 is the partial specific volume of water (m^3 kg^{-1}). For calculating the apparent molecular weight of Hsp12 the

dimensionless Perrin factor F was set to $F = 1$ which represents a hard sphere. For calculating F the molecular weight was set to 11.7 kDa. The Perrin factor is related to the shape of the molecule and one can calculate the relative dimensions of an diffusing ellipsoid (Cantor and Schimmel, 1980).

Hydrodynamic calculations were performed using HYDRONMR Version 5a (García de la Torre et al., 2000b) and a regularized random coil model structure of Hsp12 generated by X-PLOR Version 3.851 (Brünger, 1992).

All experiments were processed and analyzed using XWin-NMR 3.5, Aurelia 3.5 and Sparky 3.106 (Kneller and Kuntz, 1993). Sequence specific resonance assignments were obtained with the help of our assignment program PASTA (Leutner et al., 1998).

8.7.6 Paramagnetic Broadening Experiments

Spinlabel titration was done using a 600μM Hsp12 sample in 300 mM d_{25}-SDS, 10 mM sodium phosphate pH 7.5. A total SDS micelle aggregation number of 60 was assumed which corresponds to a micelle concentration of 5 mM. A 5-doxyl- stearic acid solution in d_4-methanol was added up to a concentration of 5 mM. This corresponds to a spin-label/micelle ratio of 1. Furthermore a sample containing 1 mM $MnCl_2$ was prepared. The $MnCl_2$ was dissolved in H_2O before added to the sample. Both experiments were measured at pH 7.5 and 310 K.

9   Appendix

9.1   Sequential Backbone Assignment of p63 DBD

The chemical shifts for backbone resonances of p63 DBD have been deposited in the BioMagRes-Bank (http://www.bmrb.wisc.edu/) under the accession number BMRB-5700 and can be found there.

9.2   Sequential Backbone Assignment of the N-terminal of Hsp90

The obtained backbone assignment independently confirms the recently published assignment (Salek et al., 2002).

Table 11: Chemical shift backbone resonances of Nhsp90 in ppm.

Residue	N	NH	CO	CA	CB
Met 1	-	-	176.8	55.1	32.3
Ala	125.0	8.50	178.0	52.3	18.4
Ser			171.1	55.2	61.5
Glu	123.8	8.45	171.9	52.6	31.2
Thr	117.9	8.02	170.1	58.9	67.0
Phe	124.5	8.51	-	53.0	-
Glu	-	-	-	-	-
Phe	-	-	-	-	-
Gln	-	-	-	-	-
Ala	-	-	-	-	-
Glu 11	-	-	-	-	-
Ile	-	-	-	-	-
Thr	-	-	-	-	-
Gln	-	-	176.0	56.0	25.0
Leu	122.0	7.86	176.0	55.5	37.6
Met	116.8	8.43	174.8	57.8	29.8
Ser	111.6	7.72	174.5	58.6	-
Leu	-	-	-	-	-
Ile	-	-	-	-	-
Ile	-	-	-	-	-
Asn 21	-	-	-	-	-
Thr	-	-	-	-	-
Val	-	-	-	-	-
Tyr	-	-	-	-	-
Ser	-	-	-	-	-
Asn	-	-	-	-	-
Lys	-	-	-	-	-
Glu	-	-	-	-	-
Ile	-	-	-	-	-
Phe	-	-	-	-	-

Residue	N	NH	CO	CA	CB
Leu 31	119.5	7.97	174.2	54.2	-
Arg	121.5	7.90	174.4	52.9	31.3
Glu	128.2	9.00	171.8	52.4	30.1
Leu	115.4	8.13	171.7	54.9	37.1
Ile	122.1	8.36	175.1	62.8	33.2
Ser	116.9	8.15	174.8	59.1	-
Asn	118.9	7.91	175.5	53.0	34.8
Ala	124.1	7.73	176.1	51.8	14.8
Ser	111.8	8.44	174.2	58.8	-
Asp	119.1	8.12	175.8	54.6	37.3
Ala 41	122.2	7.72	179.5	52.3	-
Leu	123.7	8.20	175.8	54.8	37.7
Asp	120.0	8.80	176.8	54.5	36.6
Lys	116.5	7.87	178.1	57.3	30.1
Ile	117.8	7.44	173.8	57.1	35.3
Arg	127.3	8.57	177.2	57.2	26.6
Tyr	117.8	8.55	177.1	58.2	34.7
Lys	119.8	7.84	176.5	56.3	-
Ser	112.7	8.15	172.5	57.3	-
Leu	-	-	-	-	-
Ser 51	-	-	-	-	-
Asp	-	-	-	-	-
Pro	-	-	176.9	62.0	28.6
Lys	117.7	7.98	177.0	55.7	27.7
Gln	115.8	7.91	174.6	54.3	24.3
Leu	112.9	7.14	176.8	52.1	39.2
Glu	116.1	7.37	174.5	56.3	26.2
Thr	105.1	6.97	173.3	59.4	65.8
Glu	114.3	7.13	169.9	52.4	-
Pro	-	-	173.7	61.8	29.3
Asp 61	116.9	8.51	172.9	50.8	39.1
Leu	122.4	8.23	172.2	50.9	37.2
Phe	119.3	7.44	-	53.4	38.7
Ile	117.9	8.08	171.9	57.7	36.7
Arg	128.1	10.08	172.6	51.5	31.5
Ile	130.0	9.50	171.6	57.5	36.6
Thr	122.8	9.16	179.1	56.2	-
Pro	-	-	-	-	-
Lys	-	-	-	-	-
Pro	-	-	176.9	63.0	28.6
Glu 71	117.8	9.33	175.1	56.2	25.0
Gln	115.0	7.21	172.0	52.5	27.2
Lys	114.6	7.81	171.3	55.3	-
Val	-	-	-	-	-
Leu	-	-	-	-	-
Glu	-	-	-	-	-
Ile	-	-	-	-	-
Arg	-	-	-	-	-

Residue	N	NH	CO	CA	CB
Asp	-	-	-	-	-
Ser	115.9	9.07	171.6	51.5	58.8
Gly 81	109.4	9.84	169.9	41.6	-
Ile	115.5	6.80	171.6	59.9	37.3
Gly	105.7	7.61	169.7	40.9	-
Met	117.4	8.07	173.1	51.6	33.7
Thr	113.1	8.94	171.1	57.6	67.6
Lys	120.2	8.76	175.4	53.7	34.1
Ala	115.8	8.20	172.3	51.6	-
Glu	123.3	8.08	172.7	54.3	33.2
Leu	121.4	7.68	-	52.6	39.6
Ile	119.5	8.41	175.8	53.4	31.7
Asn 91	118.5	8.59	174.4	54.3	37.6
Asn	113.4	8.36	174.7	50.4	-
Leu	-	-	-	-	-
Gly	105.3	7.64	172.5	43.5	-
Thr	-	-	-	-	-
Ile	-	-	-	-	-
Ala	-	-	-	-	-
Lys	-	-	-	-	-
Ser	-	-	-	-	-
Gly	-	-	-	-	-
Thr 101	-	-	-	-	-
Lys	-	-	-	-	-
Ala	-	-	-	-	-
Phe	-	-	-	-	-
Met	-	-	-	-	-
Glu	-	-	-	-	-
Ala	-	-	-	-	-
Leu	-	-	-	-	38.0
Ser	115.2	7.75		58.3	59.7
Ala	121.8	7.33	175.1	48.8	-
Gly 111	105.7	7.61	172.4	42.5	-
Ala	122.6	7.95	172.8	49.3	16.1
Asp	117.6	7.92	-	50.5	-
Val	-	-	-	-	-
Ser	-	-	-	-	-
Met	122.5	7.55	175.0	55.2	-
Ile	117.8	7.42	173.9	57.7	-
Gly	113.7	8.32	171.9	44.8	-
Gln	119.8	7..98	174.3	54.2	24.7
Phe	115.1	7.30	-	55.0	-
Gly 121	-	-	-	-	-
Val	-	-	-	-	28.0
Gly	107.9	8.78	173.0	44.7	-
Phe	123.5	8.98	175.9	58.4	-
Tyr	-	-	-	-	-
Ser	-	-	-	-	-

Residue	N	NH	CO	CA	CB
Leu	-	-	171.3	55.8	42.3
Phe	115.6	9.11	-	57.3	-
Leu	121.4	7.30	176.5	54.5	40.0
Val	103.3	6.84	170.4	57.4	30.3
Ala 131	124.2	7.68	172.8	48.0	18.8
Asp	117.0	8.20	169.5	51.3	39.1
Arg	114.5	7.49	180.4	52.0	30.0
Val	121.2	8.67	171.0	55.7	-
Gln	122.7	8.81	171.8	51.0	-
Val	125.0	10.39	171.9	58.4	-
Ile	-	-	-	-	-
Ser	-	-	-	-	-
Lys	-	-	-	-	-
Ser	-	-	-	-	-
Asn 141	-	-	-	-	-
Asp	-	-	-	-	-
Asp	-	-	-	-	-
Glu	-	-	-	-	-
Gln	-	-	-	-	-
Tyr	-	-	-	-	-
Ile	-	-	-	-	-
Trp	-	-	-	-	-
Glu	-	-	-	-	-
Ser	-	-	-	-	-
Asn 151	-	-	-	-	35.5
Ala	117.0	8.54	174.1	50.6	13.4
Gly	105.9	8.05	172.8	42.3	-
Gly	105.4	8.34	-	43.5	-
Ser	114.3	7.91	-	54.0	63.7
Phe	118.6	8.70	170.4	52.3	37.9
Thr	109.6	8.50	-	56.2	69.7
Val	120.2	9.06	173.9	58.8	32.0
Thr	124.4	9.33	171.1	58.6	68.9
Leu	130.2	8.61	174.4	54.0	38.2
Asp 161	127.5	8.51	174.4	51.7	39.3
Glu	127.9	8.77	173.9	52.3	27.8
Val	114.1	8.57	173.6	59.7	31.6
Asn	120.9	9.84	173.6	51.2	36.2
Glu	119.9	8.74	173.1	53.7	26.2
Arg	120.8	8.56	175.3	51.9	27.5
Ile	122.4	8.47	-	57.4	-
Gly	-	-	-	-	-
Arg	-	-	-	-	27.8
Gly	115.6	9.26	169.4	40.8	-
Thr 171	115.5	7.77	-	58.8	-
Ile	124.4	9.95	171.9	58.4	
Leu	129.8	9.60	-	-	-
Arg	-	-	-	-	-

Residue	N	NH	CO	CA	CB
Leu	-	-	-	-	-
Phe	-	-	-	-	-
Leu	-	-	-	-	-
Lys	-	-	-	-	26.0
Asp	115.9	7.11	170.8	55.8	40.5
Asp	125.9	8.42	-	50.1	36.4
Gln 181	119.2	7.94	173.1	51.0	24.5
Leu	114.7	7.66	177.3	53.4	35.8
Glu	120.4	8.63	174.1	55.3	25.1
Tyr	113.8	6.64	169.3	57.4	33.9
Leu	110.5	7.27	174.4	51.0	39.0
Glu	117.3	7.41	174.3	52.5	26.9
Glu	126.0	8.93	174.8	57.5	26.4
Lys	115.8	8.80	176.4	56.9	28.7
Arg	119.0	6.85	175.6	54.2	26.4
Ile	117.8	8.20	175.7	175.7	34.6
Lys 191	116.6	8.35	176.8	57.6	29.0
Glu	118.9	7.62	176.4	56.1	26.2
Val	120.3	7.95	176.3	63.8	27.9
Ile	119.0	8.35	175.9	62.4	34.4
Lys	119.0	7.87	175.6	55.8	28.6
Arg	115.5	7.49	175.8	55.5	27.5
His	112.8	7.60	174.6	54.4	30.3
Ser	114.5	8.21	174.5	55.5	-
Glu	120.8	7.93	174.4	55.6	26.1
Phe	114.1	7.94	173.1	54.0	35.0
Val 201	121.8	7.14	173.7	60.0	29.1
Ala	129.1	8.89	173.7	49.9	15.4
Tyr	116.2	6.60	169.6	52.8	-
Pro	-	-	172.7	60.3	29.0
Ile	120.8	7.98	174.0	57.3	35.7
Gln	127.4	9.24	171.8	51.1	26.5
Leu	127.0	8.68	173.6	50.9	39.3
Val	128.9	8.74	172.1	59.5	28.8
Val	122.4	8.10	173.1	58.0	30.2
Thr	122.6	7.88	176.7	60.4	-

9.3   Sequential Backbone Assignment of SDS-micelle Folded Hsp12

Table 12: Chemical shift backbone resonances of SDS-micelle folded Hsp12 in ppm

Residue	N	HN	CO	CA	CB	HA
Met 1	-	-	-	-	-	-
Ser 2	-	-	-	-	-	-
Asp 3	-	-	173.24	51.88	38.6	-
Ala 4	123.43	8.28	175.51	50.11	16.44	4.66
Gly 5	107.53	8.24	171.52	42.75		4
Arg 6	120.38	8.37	174.02	53.71	27.66	4.37
Lys 7	120.78	8.22	174.45	54.23	29.96	4.35
Gly 8	107.93	8.17	172.3	43.08		4.01
Phe 9	120.17	8.11	174.3	57.29	36.58	4.44
Gly 10	107.73	8.47	172.85	44.14		3.67
Glu 11	120.99	8.05	175.87	56.22	27.08	4.17
Lys 12	118.95	7.96	175.94	55.69	29.39	4.14
Ala 13	121.39	8.26	175.74	51.98	15.58	4.06
Ser 14	111.2	8.06	173.55	58.47	60.45	4.65
Glu 15	119.76	7.76	174.88	55.29	27.08	4.65
Ala 16	120.58	7.76	175.35	51.04	16.74	4.28
Leu 17	116.3	7.68	173.71	52.25	39.74	4.14
Lys 18	120.17	7.8	172.19	51.71	29.71	4.62
Pro 19	-	-	174.38	-	29.1	4.4
Asp 20	119.15	8.44	174.02	51.7	38.3	4.49
Ser 21	115.89	8.11	172.26	56.35	61.02	4.45
Gln 22	120.58	8.49	173.36	53.96	26.22	4.41
Lys 23	120.58	8	173.59	53.43	30.82	4.49
Ser 24	117.32	8.45	173.09	55.29	61.05	4.39
Tyr 25	121.6	8.26	175.2	58.21	34.85	4.51
Ala 26	120.78	8.29	176.45	52.77	15.58	4.1
Glu 27	117.11	7.95	176.6	56.75	26.8	4.07
Gln 28	118.54	8.23	176.6	56.22	26.51	4.21
Gly 29	107.93	8.86	171.87	44.8		3.94
Lys 30	121.19	8.46	176.37	57.68	29.39	3.73
Glu 31	119.76	8.12	175.55	56.75	26.54	4.05
Tyr 32	119.56	8.09	175.47		36.16	
Ile 33	116.7	8.3	174.92	61.26	35.15	4.41
Thr 34	114.05	8.31	173.98	63.65	65.92	-
Asp 35	120.99	7.91	175.33	54.36	38.88	4.54
Lys 36	-	7.72	175.39	-	28.82	-
Ala 37	121.39	8.35	176.21	52.65	15.58	4.05
Asp 38	116.3	8.08	175.74	53.96	38.01	4.46
Lys 39	118.54	7.78	175.98	55.55	29.69	4.19
Val 40	-	-	174.1	-	29.39	3.97
Ala 41	122.41	8.14	176.52	51.84	15.58	4.17
Gly 42	104.88	8.08	172.34	43.21		3.99
Lys 43	118.95	7.86	174.06	53.96	30.54	4.4
Val 44	-	7.74	172.42	-	29.67	-

Residue	N	HN	CO	CA	CB	HA
Gln 45	122.01	8.21	171.25	50.91	26.22	4.19
Pro 46	-	-	174.69	-	29.39	-
Glu 47	119.36	8.54	173.87	54.62	27.37	4.26
Asp 48	119.15	8.19	173.24	51.84	38.3	4.26
Asn 49	117.72	8.23	172.38	50.91	36.3	-
Lys 50	120.17	8.16	174.38	54.1	30.25	4.37
Gly 51	109.16	8.33	172.62	43.07		4.09
Val 52	-	7.99	173.79	-	29.1	-
Phe 53	118.13	8.09	173.87	55.95	35.74	4.65
Gln 54	119.36	8.02	174.57	54.76	26.22	4.2
Gly 55	107.73	8.15	172.66	43.43		4.02
Val 56	-	-	-	-	-	-
His 57	-	-	-	-	-	-
Asp 58	-	-	174.49	-	38.3	-
Ser 59	116.3	8.18	172.46	57.01	61.02	4.4
Ala 60	125.07	8.24	175.59	50.77	16.15	4.33
Glu 61	118.33	8.15	174.41	54.49	27.09	4.27
Lys 62	-	-	174.84	-	29.96	-
Gly 63	108.75	8.35	171.8	42.97		-.-
Lys 64	120.38	8.07	174.02	53.96	30.26	4
Asp 65	120.58	8.35	173.59	51.97	38.38	4.34
Asn 66	118.74	8.28	172.62	50.64	36.15	-
Ala 67	124.04	8.26	175.31	50.24	16.44	4.23
Glu 68	119.15	8.33	174.65	54.23	27.37	4.33
Gly 69	109.57	8.36	171.76	42.81		4.04
Gln 70	119.56	8.25	173.91	53.3	26.8	4.45
Gly 71	109.77	8.48	171.37	42.81		4.01
Glu 72	120.38	8.3	174.02	53.83	27.66	4.46
Ser 73	117.72	8.75	172.81	55.27	61.89	4.47
Leu 74	124.25	8.56	175.82	55.15	38.88	4.27
Ala 75	120.17	8.19	176.41	52.52	15.58	4.06
Asp 76	117.11	7.81	175.86	54.36	37.73	4.46
Gln 77	119.36	8.03	175.43	55.69	26.51	4.21
Ala 78	121.6	8.55	176.37	52.37	15.58	4.21
Arg 79	116.91	8.16	-	56.88	27.38	4.06
Asp 80	-	-	176.29	-	36.31	-
Tyr 81	120.17	8.17	175.23	58.08	35.42	-
Met 82	118.13	8.43	175.59	55.95	29.67	4.29
Gly 83	106.51	8.35	174.14	44.53		3.93
Ala 84	125.27	7.94	177.58	51.97	15.58	4.07
Ala 85	52.5	4.07			15.58	
Lys 86	116.91	8.4	175.86	57.41	29.38	3.93
Ser 87	113.44	7.89	173.87	58.87	60.16	4.35
Lys 88	120.78	7.87	175.94	55.02	29.11	-
Leu 89	119.76	8.23	175.59	55.42	38.88	4.13
Asn 90	116.91	8.26	175.2	54.36	36.01	3.86
Asp 91	-	-	176.21	-	37.18	-
Ala 92	123.84	8.3	176.37	52.77	15.56	-

Residue	N	HN	CO	CA	CB	HA
Val 93	-	-	176.17	-	-	-
Glu 94	120.38	8.22	176.72	57.02	26.58	-
Tyr 95	120.58	8.24	175.78	58.88	35.72	-
Val 96	-	-	175.16	-	29.1	3.32
Ser 97	114.26	8.69	174.26	59.01	60.45	4.08
Gly 98	107.32	7.95	172.97	43.74		3.99
Arg 99	119.76	7.63	175.27	54.36	27.08	4.23
Val 100	-	8.2	173.79	-	29.38	-
His 101	117.32	8.1	172.81	53.03	26.51	4.82
Gly 102	108.95	8.02	171.6	42.94		4.05
Glu 103	119.97	8.09	173.87	53.71	27.66	-
Glu 104	121.8	8.4	173.2	53.69	27.66	4.34
Asp 105	122.41	8.41	173.2	48.92	38.7	4.31
Pro 106	-	-	175	-	29.4	-
Thr 107	111.81	8.39	172.26	60.07	66.5	4.32
Lys 108	-	-	-	-	-	-
Lys 109	-	-	-	-	-	-

9.4   Sequential Backbone Assignment of Unfolded Hsp12

Table 13: Chemical shift backbone resonances of unfolded Hsp12 in ppm

Residue	N	HN	CO	CA	CB
Met 1	-	-	173.38	-	35.84
Ser 2	117.83	8.06	171.42	59.03	67.01
Asp 3	122.82	-	173.41	51.54	38.59
Ala 4	124.56	8.34	175.68	50.24	16.13
Gly 5	107.43	8.35	171.58	42.62	
Arg 6	120.27	7.99	173.77	53.3	30.18
Lys 7	-	-	-	-	-
Gly 8	-	-	-	-	
Phe 9	-	-	173.69	-	36.86
Gly 10	110.59	8.35	171.42	42.48	
Glu 11	-	-	-	-	-
Lys 12	-	-	171.85	-	61.02
Ala 13	125.57	8.29	175.25	49.96	16.31
Ser 14	114.67	8.18	172.12	55.83	60.9
Glu 15	122.62	8.27	173.45	53.69	27.51
Ala 16	124.15	8.09	174.59	49.66	16.36
Leu 17	121.5	8.05	173.55	52.25	39.45
Lys 18	-	-	-	-	-
Pro 19	-	-	174.16	-	29.23
Asp 20	119.97	8.39	173.96	51.68	38.16
Ser 21	115.79	8.14	172.05	56.15	60.89
Gln 22	121.39	8.27	173.34	53.26	26.36
Lys 23	121.8	8.08	173.73	53.55	30.25
Ser 24	116.4	8.2	171.69	55.42	61.03
Tyr 25	-	-	173.06	-	35.74

Residue	N	HN	CO	CA	CB
Ala 26	124.45	8.06	175.02	49.81	16.43
Glu 27	119.46	8.14	173.92	53.83	27.37
Gln 28	120.78	8.22	174.55	55.14	27.23
Gly 29	109.67	8.34	171.46	42.62	
Lys 30	120.48	8.08	173.73	53.4	30.22
Glu 31	121.09	8.46	173.28	54.85	27.23
Tyr 32	-	-	-	-	-
Ile 33	-	-	-	-	-
Thr 34	-	-	-	-	-
Asp 35	-	-	-	-	-
Lys 36	-	-	173.73	-	29.96
Ala 37	124.35	8.2	174.82	49.95	16.3
Asp 38	119.05	8.17	173.65	51.68	38.22
Lys 39	121.09	8.07	173.96	53.46	30.07
Val 40	-	-	173.26	-	29.82
Ala 41	127.41	8.27	175.41	49.81	16.31
Gly 42	107.93	8.23	171.15	42.33	
Lys 43	120.78	8.01	173.75	53.26	29.92
Val 44	-	-	-	-	-
Gln 45	-	-	-	-	-
Pro 46	-	-	174.31	-	29.24
Glu 47	120.38	8.54	173.57	53.81	27.39
Asp 48	120.99	8.23	173.31	51.53	38.47
Asn 49	-	-	173.26	-	38.38
Lys 50	119.05	8.27	172.44	50.49	36.01
Gly 51	-	-	-	-	
Val 52	-	-	-	-	-
Phe 53	-	-	-	-	-
Gln 54	-	-	174.47	-	29.68
Gly 55	108.95	8.31	171.34	42.62	
Val 56	118.95	7.76	173.34	59.46	29.82
His 57	122.82	8.4	172.12	52.97	27.51
Asp 58	-	-	-	-	-
Ser 59	-	-	-	-	-
Ala 60	-	-	-	-	-
Glu 61	-	-	-	-	-
Lys 62	-	-	-	-	-
Gly 63	-	-	-	-	
Lys 64	-	-	173.69	-	30.21
Asp 65	120.99	8.32	173.26	51.68	38.38
Asn 66	119.05	8.27	172.36	50.49	36.16
Ala 67	124.15	8.24	175.17	50.15	16.31
Glu 68	119.56	8.29	174.57	54.12	27.23
Gly 69	-	-	-	-	
Gln 70	-	-	173.84	-	26.49
Gly 71	109.87	8.4	171.42	42.62	
Glu 72	120.58	8.28	173.96	53.71	27.66
Ser 73	116.91	8.38	172.09	55.42	61

Residue	N	HN	CO	CA	CB
Leu 74	124.25	8.27	174.94	52.73	39.28
Ala 75	123.74	8.14	175.25	50.24	16.2
Asp 76	118.74	8.1	173.96	52.02	38.15
Gln 77	119.86	8.08	173.38	53.55	26.39
Ala 78	123.64	8.11	175.29	50.06	16.09
Arg 79	119.36	8	173.49	53.55	27.95
Asp 80	120.07	8.16	173.61	51.53	38.09
Tyr 81	120.27	7.97	173.55	55.72	35.57
Met 82	-	-	174.47	-	30.12
Gly 83	109.77	8.37	171.34	42.62	
Ala 84	123.54	8.02	175.05	49.75	16.38
Ala 85	122.62	8.15	173.65	50.16	27.79
Lys 86	122.52	8.29	174.31	53.57	30.09
Ser 87	-	-	-	-	-
Lys 88	-	-	-	-	-
Leu 89	-	-	-	-	-
Asn 90	-	-	172.16	-	36
Asp 91	120.48	8.13	173.18	51.68	38.31
Ala 92	123.54	8.03	174.94	49.68	16.44
Val 93	118.95	7.92	173.34	59.61	29.96
Glu 94	-	-	173.73	-	27.57
Tyr 95	121.8	8.41	172.98	55.15	36
Val 96	122.62	7.93	173.2	59.45	30.15
Ser 97	-	-	172.44	-	60.98
Gly 98	110.59	8.3	171.23	42.44	
Arg 99	120.48	8.08	173.71	53.4	30.25
Val 100	-	-	173.26	-	29.82
His 101	123.13	8.41	172.83	53.41	27.5
Gly 102	110.79	8.32	171.23	42.49	
Glu 103	120.48	8.25	173.73	53.52	27.53
Glu 104	-	-	-	-	-
Asp 105	-	-	-	-	-
Pro106	-	-	-	-	-
Thr 107	-	-	-	-	-
Lys 108	-	-	-	-	-
Lys 109	-	-	-	-	-

10 References

Abragam, A. (1961) *The Principles of Nuclear Magnetism*. Clarendon Press, Oxford.

Adams, J.M. and Cory, S. (1998) The Bcl-2 protein family: Arbiters of cell survival. *Science*, **281**, 1322-1326.

Adzhubei, A.A. and Sternberg, M.J. (1993) Left-handed polyproline II helices commonly occur in globular proteins. *J. Mol. Biol.*, **229**, 472-493.

Akalin, A., Elmore, L.W., Forsythe, H.L., Amaker, B.A., McCollum, E.D., Nelson, P.S., Ware, J.L. and Holt, S.E. (2001) A novel mechanism for chaperone-mediated telomerase regulation during prostate cancer progression. *Cancer Res.*, **61**, 4791-4796.

Aloy, P., Bottcher, B., Ceulemans, H., Leutwein, C., Mellwig, C., Fischer, S., Gavin, A.C., Bork, P., Superti-Furga, G., Serrano, L. and Russell, R.B. (2004) Structure-based assembly of protein complexes in yeast. *Science*, **303**, 2026-2029.

Anfinsen, C.B. (1973) Principles That Govern Folding of Protein Chains. *Science*, **181**, 223-230.

Anfinsen, C.B., Haber, E., Sela, M. and White, F.H. (1961) Kinetics of Formation of Native Ribonuclease During Oxidation of Reduced Polypeptide Chain. *Proc. Natl. Acad. Sci. U. S. A.*, **47**, 1309-1312.

Appella, E. and Anderson, C.W. (2001) Post-translational modifications and activation of p53 by genotoxic stresses. *Eur. J. Biochem.*, **268**, 2764-2772.

Arrowsmith, C.H. and Morin, P. (1996) New insights into p53 function from structural studies. *Oncogene*, **12**, 1379-1385.

Ashcroft, M., Kubbutat, M.H.G. and Vousden, K.H. (1999) Regulation of p53 function and stability by phosphorylation. *Mol. Cell. Biol.*, **19**, 1751-1758.

Ashkenazi, A. and Dixit, V.M. (1998) Death receptors: Signaling and modulation. *Science*, **281**, 1305-1308.

Ayed, A., Mulder, F.A.A., Yi, G.S., Lu, Y., Kay, L.E. and Arrowsmith, C.H. (2001) Latent and active p53 are identical in conformation. *Nat. Struct. Biol.*, **8**, 756-760.

Bai, Y.W., Milne, J.S., Mayne, L. and Englander, S.W. (1993) Primary Structure Effects On Peptide Group Hydrogen-Exchnage. *Proteins*, **17**, 75-86.

Bain, A.D. (2003) Chemical exchange in NMR. *Prog. Nucl. Magn. Reson. Spectrosc.*, **43**, 63-103.

Balagurumoorthy, P., Sakamoto, H., Lewis, M.S., Zambrano, N., Clore, G.M., Gronenborn, A.M., Appella, E. and Harrington, R.E. (1995) Four p53 DNA-binding domain peptides bind natural p53-response elements and bend the DNA. *Proc. Natl. Acad. Sci. U. S. A.*, **92**, 8591-8595.

Balint, E., Bates, S. and Vousden, K.H. (1999) MDM2 binds p73 alpha without targeting degradation. *Oncogene*, **18**, 3923-3929.

Basser, P.J. (1995) Inferring microstructural features and the physiological state of tissues from diffusion-weighted images. *NMR Biomed.*, **8**, 333-344.

Bax, A., Griffey, R.H. and Hawkins, B.L. (1983) Correlation of Proton and N-15 Chemical-Shifts by Multiple Quantum NMR. *J. Magn. Reson.*, **55**, 301-315.

Beere, H.M. and Green, D.R. (2001) Stress management - heat shock protein-70 and the regulation of apoptosis. *Trends Cell Biol.*, **11**, 6-10.

Bell, S., Klein, C., Müller, L., Hansen, S. and Buchner, J. (2002) p53 contains large unstructured regions in its native state. *J. Mol. Biol.*, **322**, 917-927.

Beloborodov, I.S., Orekhov, V.Y. and Arseniev, A.S. (1998) Effect of Coupling between Rotational and Translational Brownian Motions on NMR Spin Relaxation: Consideration Using Green Function of Rigid Body Diffusion. *J. Magn. Reson.*, **132**, 328-329.

Bénard, J., Douc-Rasy, S. and Ahomadegbe, J.-C. (2003) TP53 Family Members and Human Cancers. *Hum. Mutat.*, **21**, 182-191.

Bergerat, A., deMassy, B., Gadelle, D., Varoutas, P.C., Nicolas, A. and Forterre, P. (1997) An atypical topoisomerase II from archaea with implications for meiotic recombination. *Nature*, **386**, 414-417.

Berman, A.E., Kozlova, N.I. and Morozevich, G.E. (2003) Integrins: Structure and Signaling. *Biochemistry (Moscow)*, **68**, 1248-1299.

Blees, M.H. (1994) The Effect of Finite Duration of Gradient Pulses on the Pulsed-Field Gradient NMR Method of Studying Restricted Diffusion. *J. Magn. Reson.*, **A109**, 203-209.

Bloomfield, V.A., Dalton, W.O. and Holde, K.E.V. (1967a) Frictional Coefficients of Multisubunit Structures. I. Theory. *Biopolymers*, 135-148.

Bloomfield, V.A., Dalton, W.O. and Holde, K.E.V. (1967b) Frictional Coefficients of Multisubunit Structures. II. Application to Proteins and Viruses. *Biopolymers*, **5**, 149-159.

Bodenhausen, G. and Ruben, D.J. (1980) Natural Abundance N-15 NMR by Enhanced Heteronuclear Spectroscopy. *Chem. Phys. Lett.*, **69**, 185-189.

Boisvert, D.C., Wang, J.M., Otwinowski, Z., Horwich, A.L. and Sigler, P.B. (1996) The 2.4 angstrom crystal structure of the bacterial chaperonin GroEL complexed with ATP gamma S. *Nat. Struct. Biol.*, **3**, 170-177.

Bolivar, F. and Backman, K. (1979) Plasmids of Escherichia coli as cloning vectors. *Methods Enzymol.*, **68**, 245-267.

Bose, S., Weikl, T., Bugl, H. and Buchner, J. (1996) Chaperone function of Hsp90-associated proteins. *Science*, **274**, 1715-1717.

Böttger, A., Böttger, V., Garcia-Echeverria, C., Chene, P., Hochkeppel, H.K., Sampson, W., Ang, K., Howard, S.F., Picksley, S.M. and Lane, D.P. (1997) Molecular characterization of the HDM2-p53 interaction. *J. Mol. Biol.*, **269**, 744-756.

Böttger, V., Böttger, A., Howard, S.F., Picksley, S.M., Chene, P., Garcia-Echeverria, C., Hochkeppel, H.K. and Lane, D.P. (1996) Identification of novel MDM2 binding peptides by phage display. *Oncogene*, **13**, 2141-2147.

Boyer, H.W. and Roulland-Dussoix, D. (1969) A complementation analysis of the restriction and modification of DNA in Escherichia coli. *J. Mol. Biol.*, **41**, 459-472.

Bradford, M.M. (1976) A rapid and sensitive method for the quantitation of microgram quantities of protein utilizing the principle of protein-dye binding. *Anal. Biochem.*, **72**, 248-254.

Branden, C.-I. and Tooze, J. (1998) *Introduction to Protein Structure*. Garland Publishing, Inc., New York.

Brinkmann, U., Mattes, R.E. and Buckel, P. (1989) High-level expression of recombinant genes in Escherichia coli is dependent on the availability of the DnaY gene product. *Gene*, **85**, 109-114.

Brünger, A.T. (1992) *X-PLOR Version 3.1 A System for X-ray Crystallography and NMR*. Yale University Press, New Haven, London.

Buchner, J. (1996) Supervising the fold: functional principles of molecular chaperones. *FASEB J.*, **10**, 10-19.

Buchner, J. (1999) Hsp90 & Co. - a holding for folding. *Trends Biochem. Sci.*, **24**, 136-141.

Buchner, J. and Kiefhaber, T. (1990) Folding Pathway Enigma. *Nature*, **343**, 601-602.

Buey, R.M., Diaz, J.F., Andreu, J.M., O'Brate, A., Giannakakou, P., Nicolaou, K.C., Sasmal, P.K., Ritzen, A. and Namoto, K. (2004) Interaction of epothilone analogs with the paclitaxel binding site: Relationship between binding affinity, microtubule stabilization, and cytotoxicity. *Chem. Biol.*, **11**, 225-236.

Bullock, A.N. and Fersht, A.R. (2001) Rescuing the function of mutant p53. *Nat. Rev. Cancer*, **1**, 68-76.

Bullock, A.N., Henckel, J. and Fersht, A.R. (2000) Quantitative analysis of residual folding and DNA binding in mutant p53 core domain: definition of mutant states for rescue in cancer therapy. *Oncogene*, **19**, 1245-1256.

Burl, M. and Young, I.R. (1996) Eddy Currents and Their Control. In Grant, D.M. and Harris, R.K. (eds.), *Encyclopedia of Nuclear Magnetic Resonance*. Wiley, New York, Vol. 3, pp. 1841-1846.

Burstein, D. (1996) Stimulated Echos: Description, Applications, Practical Hints. *Concepts Magn. Resonance*, **8**, 269-278.

Buszko, M. and Maciel, G.E. (1994) Magnetic-Field-Gradient-Coil System for Solid-State MAS and CRAMPS NMR Imaging. *J. Magn. Reson. Ser. A*, **107**, 151-157.

Byrd, C.A., Bornmann, W., Erdjument-Bromage, H., Tempst, P., Pavletich, N., Rosen, N., Nathan, C.F. and Ding, A. (1999) Heat shock protein 90 mediates macrophage activation by Taxol and bacterial lipopolysaccharide. *Proc. Natl. Acad. Sci. U. S. A.*, **96**, 5645-5650.

Callaghan, P.T. (1993) *Principles of Nuclear Magnetic Resonance Microscopy*. Oxford Univ. Press, Oxford.

Callaghan, P.T., Coy, A., Macgowan, D., Packer, K.J. and Zelaya, F.O. (1991) Diffraction-Like Effects in NMR Diffusion Studies of Fluids in Porous Solids. *Nature*, **351**, 467-469.

Callaghan, P.T., Eccles, C.D., Haskell, T.G., Langhorne, P.J. and Seymour, J.D. (1998) Earth's field NMR in Antarctica: A pulsed gradient spin echo NMR study of restricted diffusion in sea ice. *J. Magn. Reson.*, **133**, 148-154.

Callaghan, P.T., Godefroy, S. and Ryland, B.N. (2003) Use of the second dimension in PGSE NMR studies of porous media. *Magn. Reson. Imaging*, **21**, 243-248.

Campomenosi, P., Monti, P., Aprile, A., Abbondandolo, A., Frebourg, T., Gold, B., Crook, T., Inga, A., Resnick, M.A., Iggo, R. and Fronza, G. (2001) p53 mutants can often transactivate promoters containing a p21 but not Bax or PIG3 responsive elements. *Oncogene*, **20**, 3573-3579.

Canet, D. (1997) Radiofrequency Field Gradient Experiments. *Progr. NMR Spectrosc.*, **30**, 101-135.

Canet, D. and Décorps, M. (1995) Applications of Field Gradients in NMR. In Delpuech, J.-J. (ed.), *Dynamics of Solutions and Fluid Mixtures*. Wiley, New York, pp. 309-343.

Cante, D. (1996) Radiofrequency Gradients Pulses. In Grant, D.M. and Harris, R.K. (eds.), *Encyclopedia of Nuclear Magnetic Resonance*. Wiley, New York, pp. 3938-3944.

Cantor, C.R. and Schimmel, P.R. (1980) Macromolecular Diffusion. In Freeman, W.H. (ed.), *Biophysical Chemistry, Part II: Techniques for the Study of Biological Structure and Function*, New York, Vol. II, pp. 570-590.

Caplan, A.J., Cyr, D.M. and Douglas, M.G. (1993) Eukaryotic Homologs of Escherichia Coli DnaJ - a Diverse Protein Family That Functions with Hsp70 Stress Proteins. *Mol. Biol. Cell*, **4**, 555-568.

Caprihan, A., Wang, L.Z. and Fukushima, E. (1996) A Multiple-Narrow-Pulse Approximation for Restricted Diffusion in a Time-Varying Field Gradient. *J. Magn. Reson.*, **A118**, 94-102.

Carr, H.Y. and Purcell, E.M. (1954) Effects of Diffusion on Free Precession in Nuclear Magnetic Resonance Experiments. *Phys. Rev.*, **94**, 630-638.

Chapman, B. and Mansfield, P. (1986) Double Active Magnetic Screening of Coils in NMR. *J. Phys. D-Appl. Phys.*, **19**, L129-L131.

Chen, A.D., Johnson, C.S., Lin, M. and Shapiro, M.J. (1998) Chemical exchange in diffusion NMR experiments. *J. Am. Chem. Soc.*, **120**, 9094-9095.

Chen, J., Marechal, V. and Levine, A.J. (1993) Mapping of the p53 and MDM2 interaction domains. *Mol. Cell Biol.*, **13**, 4107-4114.

Chen, J.W., Walter, S., Horwich, A.L. and Smith, D.L. (2001) Folding of malate dehydrogenase inside the GroEL-GroES cavity. *Nat. Struct. Biol.*, **8**, 721-728.

Cheng, M.Y., Hartl, F.U., Martin, J., Pollock, R.A., Kalousek, F., Neupert, W., Hallberg, E.M., Hallberg, R.L. and Horwich, A.L. (1989) Mitochondrial Heat-Shock Protein Hsp60 Is Essential for Assembly of Proteins Imported into Yeast Mitochondria. *Nature*, **337**, 620-625.

Chernov, M.V., Bean, L.J.H., Lerner, N. and Stark, G.R. (2001) Regulation of ubiquitination and degradation of p53 in unstressed cells through C-terminal phosphorylation. *J. Biol. Chem.*, **276**, 31819-31824.

Chi, S.W., Ayed, A. and Arrowsmith, C.H. (1999) Solution structure of a conserved C-terminal domain of p73 with structural homology to the SAM domain. *Embo J.*, **18**, 4438-4445.

Chittenden, T., Flemington, C., Houghton, A.B., Ebb, R.G., Gallo, G.J., Elangovan, B., Chinnadurai, G. and Lutz, R.J. (1995) A Conserved Domain in Bak, Distinct from Bh1 and Bh2, Mediates Cell-Death and Protein-Binding Functions. *Embo J.*, **14**, 5589-5596.

Cho, Y., Gorina, S., Jeffrey, P.D. and Pavletich, N.P. (1994) Crystal structure of a p53 tumor suppressor-DNA complex: understanding tumorigenic mutations. *Science*, **265**, 346-355.

Clore, G.M., Ernst, J., Clubb, R., Omichinski, J.G., Kennedy, W.M., Sakaguchi, K., Appella, E. and Gronenborn, A.M. (1995) Refined solution structure of the oligomerization domain of the tumour suppressor p53. *Nat. Struct. Biol.*, **2**, 321-333.

Clore, G.M., Omichinski, J.G., Sakaguchi, K., Zambrano, N., Sakamoto, H., Appella, E. and Gronenborn, A.M. (1994) High-resolution structure of the oligomerization domain of p53 by multidimensional NMR. *Science*, **265**, 386-391.

Cory, S. and Adams, J.M. (2002) The Bcl-2 family: Regulators of the cellular life-or-death switch. *Nat. Rev. Cancer*, **2**, 647-656.

Cotts, R.M., Hoch, M.J.R., Sun, T. and Markert, J.T. (1989) Pulsed Field Gradient Stimulated Echo Methods for Improved NMR Diffusion Measurements in Heterogeneous Systems. *J. Magn. Reson.*, **83**, 252-266.

Counsell, C.J.R., Levitt, M.H. and Ernst, R.R. (1985) The Selection of Coherence-Transfer Pathways by Inhomogeneous Z-Pulses. *J. Magn. Reson.*, **64**, 470-478.

Craig, E., Yan, W. and James, P. (1999) Molecular Chaperones and Folding Catalysts. In Bukau, B. (ed.), *Molecular Chaperones and Folding Catalysts*. Harwood, Amsterdam, pp. 139-162.

Crank, J. (1975) *The Mathmatics of Diffusion*. Claxendon Press, Cambridge.

Cussler, E.L. (1984) *Diffusion: Mass Transfer in Fluid Systems*. Cambridge University Press, Cambridge.

Cyr, D.M., Langer, T. and Douglas, M.G. (1994) DnaJ-Like Proteins - Molecular Chaperones and Specific Regulators of Hsp70. *Trends Biochem. Sci.*, **19**, 176-181.

Dahlman-Wright, K., Baumann, H., McEwan, I.J., Almlof, T., Wright, A.P., Gustafsson, J.A. and Hard, T. (1995) Structural characterization of a minimal functional transactivation domain from the human glucocorticoid receptor. *Proc. Natl. Acad. Sci. U. S. A.*, **92**, 1699-1703.

Dawson, R., Müller, L., Dehner, A., Klein, C., Kessler, H. and Buchner, J. (2003) The N-terminal domain of p53 is natively unfolded. *J. Mol. Biol.*, **332**, 1131-1141.

De Carcer, G., Goes, F.S. and Martin, J. (2001) Hsp90 chaperone complexes are required for the activity and stability of yeast protein kinases Mik1, Wee1 and Swe1. *Eur. J. Biochem.*, **268**, 2281-2289.

Debburman, S.K., Raymond, G.J., Caughey, B. and Lindquist, S. (1997) Chaperone-supervised conversion of prion protein tp its protease-resistent form. *Proc. Natl. Acad. Sci. U. S. A.*, **94**, 13938-13943.

Dehner, A., Furrer, J., Richter, K., Schuster, I., Buchner, J. and Kessler, H. (2003) NMR Chemical Shift Perturbation Study of the N-Terminal Domain of Hsp90 upon Binding of ADP, AMP-PNP, Geldanamycin, and Radicicol. *Chembiochem*, **4**, 870-877.

Dejong, W.W., Leunissen, J.A.M. and Voorter, C.E.M. (1993) Evolution of the Alpha-Crystallin Small Heat-Shock Protein Family. *Mol. Biol. Evol.*, **10**, 103-126.

Delaglio, F., Grzesiek, S., Vuister, G.W., Zhu, G., Pfeifer, J. and Bax, A. (1995) Nmrpipe - a Multidimensional Spectral Processing System Based on Unix Pipes. *J. Biomol. NMR*, **6**, 277-293.

Delsuc, M.A. and Malliavin, T.E. (1998) Maximum entropy processing of DOSY NMR spectra. *Anal. Chem.*, **70**, 2146-2148.

DeMali, K.A., Wennerberg, K. and Burridge, K. (2003) Integrin signaling to the actin cytoskeleton. *Curr. Opin. Cell Biol.*, **15**, 572-582.

Derrick, T.S., McCord, E.F. and Larive, C.K. (2002) Analysis of protein/ligand interactions with NMR diffusion measurements: The importance of eliminating the protein background. *J. Magn. Reson.*, **155**, 217-225.

Dingley, A.J., Mackay, J.P., Chapman, B.E., Morris, M.B., Kuchel, P.W., Hambly, B.D. and King, G.F. (1995) Measuring Protein Self-Association Using Pulsed-Field-Gradient NMR-Spectroscopy - Application to Myosin Light-Chain-2. *J. Biomol. NMR*, **6**, 321-328.

Dingley, A.J., Mackay, J.P., Shaw, G.L., Hambly, B.D. and King, G.F. (1997) Measuring macromolecular diffusion using heteronuclear multiple-quantum pulsed-field-gradient NMR. *J. Biomol. NMR*, **10**, 1-8.

Dohn, M., Zhang, S.Z. and Chen, X.B. (2001) p63 alpha and Delta Np63 alpha can induce cell cycle arrest and apoptosis and differentially regulate p53 target genes. *Oncogene*, **20**, 3193-2105.

Dominguez, C., Boelens, R. and Bonvin, A.M. (2003) HADDOCK: a protein-protein docking approach based on biochemical or biophysical information. *J. Am. Chem. Soc.*, **125**, 1731-1737.

Donaldson, L. and Capone, J.P. (1992) Purification and characterization of the carboxyl-terminal transactivation domain of Vmw65 from herpes simplex virus type 1. *J. Biol. Chem.*, **267**, 1411-1414.

Dunker, A.K., Lawson, J.D., Brown, C.J., Williams, R.M., Romero, P., Oh, J.S., Oldfield, C.J., Campen, A.M., Ratliff, C.M., Hipps, K.W., Ausio, J., Nissen, M.S., Reeves, R., Kang, C.,

Kissinger, C.R., Bailey, R.W., Griswold, M.D., Chiu, W., Garner, E.C. and Obradovic, Z. (2001) Intrinsically disordered protein. *J. Mol. Graph. Model.*, **19**, 26-59.

Dunker, A.K. and Obradovic, Z. (2001) The protein trinity - linking function and disorder. *Nat. Biotechnol.*, **19**, 805-806.

Dutta, R. and Inouye, M. (2000) GHKL, an emergent ATPase/kinase superfamily. *Trends Biochem. Sci.*, **25**, 24-28.

Dyson, H.J. and Wright, P.E. (2002) Coupling of folding and binding for unstructured proteins. *Curr. Opin. Struct. Biol.*, **12**, 54-60.

Edelhoch, H. (1967) Spectroscopic determination of tryptophan and tyrosine in proteins. *Biochemistry*, **6**, 1948-1954.

Ehrnsperger, M., Graber, S., Gaestel, M. and Buchner, J. (1997) Binding of non-native protein to Hsp25 during heat shock creates a reservoir of folding intermediates for reactivation. *Embo J.*, **16**, 221-229.

Ellis, R.E., Yuan, J.Y. and Horvitz, H.R. (1991) Mechanisms and Functions of Cell-Death. *Annu. Rev. Cell Biol.*, **7**, 663-698.

Ellis, R.J. (1990) The molecular chaperone concept. *Semin. Cell Dev. Biol.*, **1**, 1-9.

Ernst, R.R. (1992) Nobel Lecture. Nuclear magnetic resonance Fourier transform spectroscopy. *Biosci. Rep.*, **12**, 143-187.

Ernst, R.R., Bodenhausen, G. and Wokaun, A. (1987) *Principles of Nuclear Magnetic Resonance in One and Two Dimensions*. Oxford University Press, Oxford.

Fares, M.A., Ruiz-Gonzalez, M.X., Moya, A., Elena, S.F. and Barrio, E. (2002) Endosymbiotic bacteria - GroEL buffers against deleterious mutations. *Nature*, **417**, 398-398.

Fersht, A.R. (1995) Characterizing Transition-States in Protein-Folding - an Essential Step in the Puzzle. *Curr. Opin. Struct. Biol.*, **5**, 79-84.

Fields, S. and Jang, S.K. (1990) Presence of a potent transcription activating sequence in the p53 protein. *Science*, **249**, 1049-1052.

Fillippovich, I., Sorokina, N., Gatei, M., Haupt, Y., Hobson, K., Moallem, E., Spring, K., Mould, M., McGuckin, M.A., Lavin, M.F. and Khanna, K.K. (2001) Transactivation-deficient p73 alpha (p73 Delta exon2) inhibits apoptosis and competes with p53. *Oncogene*, **20**, 514-522.

Filson, D.P. and Bloomfield, V.A. (1967) Shell model calculations of translational and rotational frictional coefficients. *J. Polym. Sci. Part C*, **25**, 73-83.

Fink, A.L. (1998) The Hsp70 reaction cycle and its role in protein folding. In Fink, A.L. and Goto, Y. (eds.), *Molecular Chaperones in the Life Cycle of Poteins*. Dekker, New York, pp. 123-150.

Fink, A.L. (1999) Chaperone-Mediated Protein Foldin. *Physiol. Rev.*, **79**, 425-449.

Fischer, E. (2003) Struktur und Funktion von Hsp12 aus der Bäckerhefe S. cerevisiae. *Department Chemie (Thesis)*. Technische Universität München, München.

Fischer, J.J. and Jardetzky, O. (1965) Nuclear Magnetic Relaxation Study of Intermolecular Complexes. The Mechanism of Penicillin Binding to Serum Albumin. *J. Am. Chem. Soc.*, **87**, 3237-3244.

Flaherty, K.M., Deluca-Flaherty, C. and McKay, D.B. (1990) Three-dimensional structure of the ATPase fragment of a 70k heat shock protein. *Nature*, **346**, 623-628.

Flaherty, K.M., McKay, D.B., Kabsch, W. and Holmes, K.C. (1991) Similarity of the 3-Dimensional Structures of Actin and the Atpase Fragment of a 70 kDa Heat-Shock Cognate Protein. *Proc. Natl. Acad. Sci. U. S. A.*, **88**, 5041-5045.

Flores, E.R., Tsai, K.Y., Crowley, D., Sengupta, S., Yang, A., McKeon, F. and Jacks, T. (2002) p63 and p73 are required for p53-dependent apoptosis in response to DNA damage. *Nature*, **416**, 560-564.

Freedman, D.A. and Levine, A.J. (1999) Regulation of the p53 protein by the MDM2 oncoprotein - Thirty-eighth G.H.A. Clowes Memorial Award lecture. *Cancer Res.*, **59**, 1-7.

Friedman, P.N., Chen, X., Bargonetti, J. and Prives, C. (1993) The p53 protein is an unusually shaped tetramer that binds directly to DNA. *Proc. Natl. Acad. Sci. U. S. A.*, **90**, 3319-3323.

Frydman, J., Erdjument-Bromage, H., Tempst, P. and Hartl, F.U. (1999) Co-translational domain folding as the structural basis for the rapid de novo folding of firefly luciferase. *Nat. Struct. Biol.*, **6**, 697-705.

Frydman, J., Nimmesgern, E., Erdjumentbromage, H., Wall, J.S., Tempst, P. and Hartl, F.U. (1992) Function in Protein Folding of Tric, a Cytosolic Ring Complex Containing Tcp-1 and Structurally Related Subunits. *Embo J.*, **11**, 4767-4778.

Furrer, J., Enthart, A., Kühlewein, A., Dehner, A., Klein, C., Hansen, S., Schwaiger, M., Kessler, H. and Gemmecker, G. (2003) Backbone 1H, 13C and 15N resonance assignments for the 25.8 kDa DNA binding domain of the human p63 protein. *J. Biomol. NMR*, **26**, 377-378.

Galigniana, M.D., Harrell, J.M., O'Hagen, H.M., Ljungman, M. and Pratt, W.B. (2004) Hsp90-binding immunophilins link p53 to dynein during p53 transport to the nucleus. *J. Biol. Chem.*, **279**, 22483-22489.

García de la Torre, J. (1989) *Hydrodynamic properties of macromolecular assemblies.* Cambridge University Press, Cambridge.

García de la Torre, J. and Bloomfield, V.A. (1977) Hydrodynamic Properties of Macromolecular Complexes. I. Translation. *Biopolymers*, **16**, 1747-1763.

García de la Torre, J., Huertas, M.L. and Carrasco, B. (2000a) Calculation of Hydrodynamic Properties of Globular Proteins from Their Atomic-Level Structure. *Biophys. J.*, **78**, 719-730.

García de la Torre, J., Huertas, M.L. and Carrasco, B. (2000b) HYDRONMR: prediction of NMR relaxation of globular proteins from atomic-level structures and hydrodynamic calculations. *J. Magn. Reson.*, **147**, 138-146.

García de la Torre, J., Navarro, S., López Martínez, M.C., Díaz, F.G. and López Cascales, J.J. (1994) HYDRO: A computer software for the prediction of hydrodynamic properties of macromolecules. *Biophys. J.*, **67**, 530-531.

García de la Torre, J. and Rodes, V. (1983) Effects from bead size and hydrodynamic interactions on the translational and rotational coefficients of macromolecular bead models. *J. Chem. Phys.*, **79**, 2454-2460.

Gavin, A.C., Bosche, M., Krause, R., Grandi, P., Marzioch, M., Bauer, A., Schultz, J., Rick, J.M., Michon, A.M., Cruciat, C.M., Remor, M., Hofert, C., Schelder, M., Brajenovic, M., Ruffner, H., Merino, A., Klein, K., Hudak, M., Dickson, D., Rudi, T., Gnau, V., Bauch, A., Bastuck, S., Huhse, B., Leutwein, C., Heurtier, M.A., Copley, R.R., Edelmann, A., Querfurth, E., Rybin, V., Drewes, G., Raida, M., Bouwmeester, T., Bork, P., Seraphin, B., Kuster, B., Neubauer, G. and Superti-Furga, G. (2002) Functional organization of the yeast proteome by systematic analysis of protein complexes. *Nature*, **415**, 141-147.

Gavin, A.C. and Superti-Furga, G. (2003) Protein complexes and proteome organization from yeast to man. *Curr. Opin. Chem. Biol.*, **7**, 21-27.

Gee, M.A., Heuser, J.E. and Vallee, R.B. (1997) An extended microtubule-binding structure within the dynein motor domain. *Nature*, **390**, 636-639.

Gemmecker, G., Eberstadt, M., Buhr, A., Lanz, R., Grdadolnik, S.G., Kessler, H. and Erni, B. (1997) Glucose transporter of Escherichia coli: NMR characterization of the phosphocysteine form of the IIBGlc domain and its binding interface with the IIA(Glc) subunit. *Biochemistry*, **36**, 7408-7417.

Gemmecker, G., Jahnke, W. and Kessler, H. (1993) Measurement of Fast Proteon-Exchange Rates in Isotropically Labeled Compounds. *J. Am. Chem. Soc.*, **115**, 11620-11621.

Genini, D., Sheeter, D., Rought, S., Zaunders, J.J., Susin, S.A., Kroemer, G., Richman, D.D., Carson, D.A., Corbeil, J. and Leoni, L.M. (2001) HIV induces lymphocyte apoptosis by a p53-initiated, mitochondrial-mediated mechanism. *Faseb J.*, **15**, 5-6.

Ghibelli, L., Mengoni, F., Lichtner, M., Coppola, S., De Nicola, M., Bergamaschi, A., Mastroianni, C. and Vullo, V. (2003) Anti-apoptotic effect of HIV protease inhibitors via direct inhibition of calpain. *Biochem. Pharmacol.*, **66**, 1505-1512.

Giannakakou, P., Nakano, M., Nicolaou, K.C., O'Brate, A., Yu, I., Blagosklonny, M.V., Greber, U.F. and Fojo, T. (2002) Enhanced microtubule-dependent trafficking and p53 nuclear accumulation by suppression of microtubule dynamics. *Proc. Natl. Acad. Sci. U. S. A.*, **99**, 10855.

Giannakakou, P., Sackett, D.L., Ward, Y., Webster, K.R., Blagosklonny, M.V. and Fojo, T. (2000) p53 is associated with cellular microtubules and is transported to the nucleus by dynein. *Nat. Cell Biol.*, **2**, 709-717.

Gibbs, S.J. and Johnson, C.S. (1991) A PFG NMR Experiment for Accurate Diffusion and Flow Studies in the Presence of Eddy Currents. *J. Magn. Reson.*, **93**, 395-402.

Giot, L., Bader, J.S., Brouwer, C., Chaudhuri, A., Kuang, B., Li, Y., Hao, Y.L., Ooi, C.E., Godwin, B., Vitols, E., Vijayadamodar, G., Pochart, P., Machineni, H., Welsh, M., Kong, Y., Zerhusen, B., Malcolm, R., Varrone, Z., Collis, A., Minto, M., Burgess, S., McDaniel, L., Stimpson, E., Spriggs, F., Williams, J., Neurath, K., Ioime, N., Agee, M., Voss, E., Furtak, K., Renzulli, R., Aanensen, N., Carrolla, S., Bickelhaupt, E., Lazovatsky, Y., DaSilva, A., Zhong, J., Stanyon, C.A., Finley, R.L., White, K.P., Braverman, M., Jarvie, T., Gold, S., Leach, M., Knight, J., Shimkets, R.A., McKenna, M.P., Chant, J. and Rothberg, J.M. (2003) A protein interaction map of Drosophila melanogaster. *Science*, **302**, 1727-1736.

Glover, J.R., Schirmer, E.C., Singer, M.A. and Lindquist, S.L. (1998) Molecular Chaperones in the Life Cacle of Proteins. In Fink, A.L. and Goto, Y. (eds.), *Molecular Chaperones in the Life Cacle of Proteins*. Dekker, New York, pp. 193-224.

Goddard, T.D. and Kneller, D.G. Sparky. University of California, San Francisco.

Gottschalk, K.E. and Kessler, H. (2002) The structures of Integrins and integrin-ligand complexes: Implications for drug design and signal transduction. *Angew. Chem. Int. Ed.*, **41**, 3767-3774.

Gozansky, E.K. and Gorenstein, D.G. (1996) DOSY-NOESY: Diffusion-ordered NOESY. *J. Magn. Reson. Ser. B*, **111**, 94-96.

Green, D.R. and Reed, J.C. (1998) Mitochondria and apoptosis. *Science*, **281**, 1309-1312.

Grenert, J.P., Sullivan, W.P., Fadden, P., Haystead, T.A.J., Clark, J., Mimnaugh, E., Krutzsch, H., Ochel, H.J., Schulte, T.W., Sausville, E., Neckers, L.M. and Toft, D.O. (1997) The amino-terminal domain of heat shock protein 90 (hsp90) that binds geldanamycin is an ATP/ADP switch domain that regulates hsp90 conformation. *J. Biol. Chem.*, **272**, 23843-23850.

Grodberg, J. and Dunn, J.J. (1988) ompT encodes the Escherichia coli outer membrane protease that cleaves T7 RNA polymerase during purification. *J. Bacteriol.*, **170**, 1245-1253.

Grzesiek, S., Bax, A., Clore, G.M., Gronenborn, A.M., Hu, J.S., Kaufman, J., Palmer, I., Stahl, S.J. and Wingfield, P.T. (1996) The solution structure of HIV-1 Nef reveals an unexpected fold and permits delineation of the binding surface for the SH3 domain of Hck tyrosine protein kinase. *Nat. Struct. Biol.*, **3**, 340-345.

Gu, W. and Roeder, R.G. (1997) Activation of p53 sequence-specific DNA binding by acetylation of the p53 C-terminal domain. *Cell*, **90**, 595-606.

Gu, W., Shi, X.L. and Roeder, R.G. (1997) Synergistic activation of transcription by CBP and p53. *Nature*, **387**, 819-823.

Hacker, G. (2000) The morphology of apoptosis. *Cell Tissue Res.*, **301**, 5-17.

Hahn, E.L. (1950) Spin Echoes. *Phys. Rev.*, **80**, 580-594.

Hainaut, P., Soussi, T., Shomer, B., Hollstein, M., Greenblatt, M., Hovig, E., Harris, C.C. and Montesano, R. (1997) Database of p53 gene somatic mutations in human tumors and cell lines: updated compilation and future prospects. *Nucleic Acids Res.*, **25**, 151-157.

Halle, B. and Denisov, V.P. (2001) Magnetic relaxation dispersion studies of biomolecular solutions. In *Nuclear Magnetic Resonance of Biologica Macromolecules, Pt A*, p. 178.

Hargreaves, R., David, C.L., Whitesell, L. and Skibo, E.B. (2003) Design of quinolinedione-based geldanamycin analogues. *Bioorg. Med. Chem. Lett.*, **13**, 3075-3078.

Harris, S.F., Shiau, A.K. and Agard, D.A. (2004) The Crystal Structure of the Carboxy-Terminal Dimerization Domain of htpg, Escherichia coli Hsp90, Reveals a Potential Substrate Binding Site. *Structure*, **12**, 1087-1097.

Harrison, C.J., Hayer-Hartl, M., DiLiberto, M., Hartl, F. and Kuriyan, J. (1997) Crystal structure of the nucleotide exchange factor GrpE bound to the ATPase domain of the molecular chaperone DnaK. *Science*, **276**, 431-435.

Hartl, F.U. (1996) Molecular chaperones in cellular protein folding. *Nature*, **381**, 571-580.

Hartl, F.U., Hlodan, R. and Langer, T. (1994) Molecular Chaperones in Protein-Folding - the Art of Avoiding Sticky Situations. *Trends Biochem. Sci.*, **19**, 20-25.

Haslbeck, M. (2001) Funktion kleiner Hitzschockproteine der Bäckerhefe S. cerevisiae. *Department Chemie (Thesis)*. Technische Universität München, München.

Haslbeck, M., Braun, N., Stromer, T., Richter, B., Model, N., Weinkauf, S. and Buchner, J. (2004) Hsp42 is the general small heat shock protein in the cytosol of Saccharomyces cerevisiae. *Embo J.*, **23**, 638-649.

Haslbeck, M. and Buchner, J. (2002) Chaperone function of sHsps. *Prog. Mol. Subcell. Biol.*, **28**, 37-59.

Haslbeck, M., Walke, S., Stromer, T., Ehrnsperger, M., White, H.E., Chen, S.X., Saibil, H.R. and Buchner, J. (1999) Hsp26: a temperature-regulated chaperone. *Embo J.*, **18**, 6744-6751.

Hayashi, I., Vuori, K. and Liddington, R.C. (2002) The focal adhesion targeting (FAT) region of focal adhesion kinase is a four-helix bundle that binds paxillin. *Nat. Struct. Biol.*, **9**, 101-106.

Heller, M., John, M., Coles, M., Bosch, G., Baumeister, W. and Kessler, H. (2004) NMR studies on the substrate-binding domains of the thermosome: Structural plasticity in the protrusion region. *J. Mol. Biol.*, **336**, 717-729.

Hill, R.B., Flanagan, J.M. and Prestegard, J.H. (1995) H-1 and N-15 Magnetic-Resonance Assignments, Secondary Structure, and Tertiary Fold of Escherichia-Coli DnaK(1-78). *Biochemistry*, **34**, 5587-5596.

Hirao, A., Kong, Y.Y., Matsuoka, S., Wakeham, A., Ruland, J., Yoshida, H., Liu, D., Elledge, S.J. and Mak, T.W. (2000) DNA damage-induced activation of p53 by the checkpoint kinase Chk2. *Science*, **287**, 1824-1827.

Ho, Y., Gruhler, A., Heilbut, A., Bader, G.D., Moore, L., Adams, S.L., Millar, A., Taylor, P., Bennett, K., Boutilier, K., Yang, L.Y., Wolting, C., Donaldson, I., Schandorff, S., Shewnarane, J., Vo, M., Taggart, J., Goudreault, M., Muskat, B., Alfarano, C., Dewar, D., Lin, Z., Michalickova, K., Willems, A.R., Sassi, H., Nielsen, P.A., Rasmussen, K.J., Andersen, J.R., Johansen, L.E., Hansen, L.H., Jespersen, H., Podtelejnikov, A., Nielsen, E., Crawford, J., Poulsen, V., Sorensen, B.D., Matthiesen, J., Hendrickson, R.C., Gleeson, F., Pawson, T., Moran, M.F., Durocher, D., Mann, M., Hogue, C.W.V., Figeys, D. and Tyers, M. (2002) Systematic identification of protein complexes in Saccharomyces cerevisiae by mass spectrometry. *Nature*, **415**, 180-183.

Hofseth, L.J., Hussain, S.P. and Harris, C.C. (2004) p53: 25 years after its discovery. *Trends in Pharma. Sci.*, **25**, 177-181.

Hollstein, M., Rice, K., Greenblatt, M.S., Soussi, T., Fuchs, R., Sorlie, T., Hovig, E., Smith-Sorensen, B., Montesano, R. and Harris, C.C. (1994) Database of p53 gene somatic mutations in human tumors and cell lines. *Nucleic Acids Res.*, **22**, 3551-3555.

Hollstein, M., Sidransky, D., Vogelstein, B. and Harris, C.C. (1991) p53 mutations in human cancers. *Science*, **253**, 49-53.

Holz, M., Heil, S.R. and Sacco, A. (2000) Temperature-dependent self-diffusion coefficients of water and six selected molecular liquids for calibration in accurate H-1 NMR PFG measurements. *Phys. Chem. Chem. Phys.*, **2**, 4740-4742.

Holz, M. and Weingärtner, H. (1991) Calibration in Accurate Spin-Echo Self-Diffusion Measurements Using 1H and Less-Common Nuclei. *J. Magn. Reson.*, **92**, 115-125.

Horwich, A.L. and Saibil, H.R. (1998) The thermosome: chaperonin with a builtin lid. *Nat. Struct. Biol.*, **5**, 333-336.

Hrovat, M.I. and Wade, C.G. (1981a) NMR Pulsed Gradient Diffusion Measurements .II. Residual Gradients and Lineshape Distortions. *J. Magn. Reson.*, **45**, 67-80.

Hrovat, M.I. and Wade, C.G. (1981b) NMR Pulsed-Gradient Diffusion Measurements .I. Spin-Echo Stability and Gradient Calibration. *J. Magn. Reson.*, **44**, 62-75.

Hubbard, S.J. and Thornton, J.M. (1993) NACCESS. Department of Biochemistry and Molecular Biology, University College London, London.

Humphrey, W., Dalke, A. and Schulten, K. (1996) VMD - Visual Molecular Dynamics. *J. Molecul. Graph. Model.*, **14**, 33-38.

Hunt, J.F., Weaver, A.J., Landry, S., Gierasch, L. and Deisenhofer, J. (1994) Progress on the Crystal-Structure Determination of the Gro-Es Chaperonin Protein from Escherichia-Coli. *Biophys. J.*, **66**, A133-A133.

Hupp, T.R. and Lane, D.P. (1994) Allosteric Activation of Latent p53 Tetramers. *Curr. Biol.*, **4**, 865-875.

Hupp, T.R., Meek, D.W., Midgley, C.A. and Lane, D.P. (1992) Regulation of the specific DNA binding function of p53. *Cell*, **71**, 875-886.

Hurd, R.E., Deese, A., O´Neil, M., Sukumar, S. and Van Zijl, P.C.M. (1996) Impact of Differential Linearity in Gradient-Enhanced NMR. *J. Magn. Reson.*, **A119**, 285-288.

Huynen, M.A., Snel, B., von Mering, C. and Bork, P. (2003) Function prediction and protein networks. *Curr. Opin. Cell Biol.*, **15**, 191-198.

Isaacs, J.S., Xu, W. and Neckers, L.M. (2003) Heat shock protein 90 as a molecular target for cancer therapeutics. *Cancer Cell*, **3**, 213-217.

Ito, T., Chiba, T., Ozawa, R., Yoshida, M., Hattori, M. and Sakaki, Y. (2001) A comprehensive two-hybrid analysis to explore the yeast protein interactome. *Proc. Natl. Acad. Sci. U. S. A.*, **98**, 4569-4574.

Itoh, H., Ogura, M., Komatsuda, A., Wakui, H., Miura, A.B. and Tashima, Y. (1999) A novel chaperone-activity-reducing mechanism of the 90 kDa molecular chaperone Hsp90. *Biochem. J.*, **343**, 697-703.

Jakob, U. and Buchner, J. (1994) Assisting Spontaneity - the Role of Hsp90 and Small Hsps as Molecular Chaperones. *Trends Biochem. Sci.*, **19**, 205-211.

Jakob, U., Gaestel, M., Engel, K. and Buchner, J. (1993) Small Heat-Shock Proteins Are Molecular Chaperones. *J. Biol. Chem.*, **268**, 1517-1520.

Jasanoff, A. and Fersht, A.R. (1994) Quantitative determination of helical properties from trifluorethanol titration curves. *Biochemistry*, **33**, 2129-2135.

Jasinski, A., Jakubowski, T., Rydzy, R., Morris, P., Smith, I.C.P., Kozlowski, P. and Saunders, J.K. (1992) Shielded Gradient Coils and Radio Frequency Probes for High-Resolution Imaging of Rat Brains. *Magn. Reson. Med.*, **24**, 29-41.

Jayaraman, L. and Prives, C. (1999) Covalent and noncovalent modifiers of the p53 protein. *Cell. Mol. Life Sci.*, **55**, 76-87.

Jeffrey, P.D., Gorina, S. and Pavletich, N.P. (1995) Crystal structure of the tetramerization domain of the p53 tumor suppressor at 1.7 angstroms. *Science*, **267**, 1498-1502.

Jehenson, P., Westphal, M. and Schuff, N. (1990) Analytical Method for the Compensation of Eddy-Current Effects Induced by Pulsed Magnetic-Field Gradients in NMR Systems. *J. Magn. Reson.*, **90**, 264-278.

Jerschow, A. (2000) Thermal convection currents in NMR: Flow profiles and implications for coherence pathway selection. *J. Magn. Reson.*, **145**, 125-131.

Jerschow, A. and Müller, N. (1996) 3D diffusion-ordered TOCSY for slowly diffusing molecules. *J. Magn. Reson. Ser. A*, **123**, 222-225.

Jerschow, A. and Müller, N. (1997) Suppression of convection artifacts in stimulated-echo diffusion experiments. Double-stimulated-echo experiments. *J. Magn. Reson.*, **125**, 372-375.

Joerger, A.C., Allen, M.D. and Fersht, A.R. (2004) Crystal structure of a superstable mutant of human p53 core domain - Insights into the mechanism of rescuing oncogenic mutations. *J. Biol. Chem.*, **279**, 1291-1296.

Johnson, C.S. (1965) *Advances in Magnetic Resonance*. Academic Press, New York.

Johnson, C.S. (1993) Effects of Chemical-Exchange in Diffusion-Ordered 2d NMR-Spectra. *J. Magn. Reson. Ser. A*, **102**, 214-218.

Johnson, C.S. (1994) *Nuclear Magnetic Resonance Probes of Molecular Dynamics*. Kluwer Academic, Dordrecht.

Johnson, C.S. (1999) Diffusion Ordered Nuclear Magnetic Resonance Spectroscopy: Princeples and Applications. *Prog. Nucl. Magn. Reson. Spectrosc.*, **34**, 203-256.

Jolly, C. and Morimoto, R.I. (2000) Role of the heat shock response and molecular chaperones in oncogenesis and cell death. *J. Natl. Cancer Inst.*, **92**, 1564-1572.

Kaghad, M., Bonnet, H., Yang, A., Creancier, L., Biscan, J.C., Valent, A., Minty, A., Chalon, P., Lelias, J.M., Dumont, X., Ferrara, P., McKeon, F. and Caput, D. (1997) Monoallelically expressed gene related to p53 at 1p36, a region frequently deleted in neuroblastoma and other human cancers. *Cell*, **90**, 809-819.

Kamal, A., Thao, L., Sensintaffar, J., Zhang, L., Boehm, M.F., Fritz, L.C. and Burrows, F.J. (2003) A high-affinity conformation of Hsp90 confers tumour selectivity on Hsp90 inhibitors. *Nature*, **425**, 407-410.

Kampinga, H.H., Brunsting, J.F., Stege, G.J.J., Konings, A.W.T. and Landry, J. (1994) Cells Overexpressing Hsp27 Show Accelerated Recovery from Heat-Induced Nuclear-Protein Aggregation. *Biochem. Biophys. Res. Commun.*, **204**, 1170-1177.

Kane, S.A., Fleener, C.A., Zhang, Y.S., Davis, L.J., Musselman, A.L. and Huang, P.S. (2000) Development of a binding assay for p53/HDM2 by using homogeneous time-resolved fluorescence. *Anal. Biochem.*, **278**, 29-38.

Karlicek, R.F. and Lowe, I.J. (1980) Modified Pulsed Gradient Technique for Measuring Diffusion in the Presence of Large Background Gradients. *J. Magn. Reson.*, **37**, 75-91.

Kartasheva, N.N., Contente, A., Lenz-Stoppler, C., Roth, J. and Dobbelstein, M. (2002) p53 induces the expression of its antagonist p73 Delta N, establishing an autoregulatory feedback loop. *Oncogene*, **21**, 4715-4727.

Kauzmann, W. (1959) Some Factors in the Interpretation of Protein Denaturation. *Adv.Protein Chem.*, **14**, 1-63.

Kay, B.K., Williamson, M.P. and Sudol, M. (2000) The importance of being proline: the interaction of proline-rich motifs in signaling proteins with their cognate domains. *Faseb J.*, **14**, 231-241.

Kay, L.E. and Prestegard, J.H. (1986) An Application of Pulse-Gradient Double-Quantum Spin Echoes to Diffusion Measurements on Molecules with Scalar-Coupled Spins. *J. Magn. Reson.*, **67**, 103-113.

Kiefhaber, T., Rudolph, R., Kohler, H.H. and Buchner, J. (1991) Protein Aggregation Invitro and Invivo - a Quantitative Model of the Kinetic Competition between Folding and Aggregation. *Bio-Technology*, **9**, 825-829.

Kim, K.K., Kim, R. and Kim, S.H. (1998) Crystal structure of a small heat-shock protein. *Nature*, **394**, 595-599.

Kim, R., Lai, L.H., Lee, H.H., Cheong, G.W., Kim, K.K., Wu, Z., Yokota, H., Marqusee, S. and Kim, S.H. (2003) On the mechanism of chaperone activity of the small heat-shock protein of Methanococcus jannaschii. *Proc. Natl. Acad. Sci. U. S. A.*, **100**, 8151-8155.

King, F.W., Wawrzynow, A., Hohfeld, J. and Zylicz, M. (2001) Co-chaperones Bag-1, Hop and Hsp40 regulate Hsc70 and Hsp9O interactions with wild-type or mutant p53. *Embo J.*, **20**, 6297-6305.

Kirkwood, J.G. (1954) The general Theory of Irreversible Processes in Solutions of Macromolecules. *J. Polym. Sci.*, **12**, 1-14.

Klein, C. (2002) Biochemische und strukturelle Untersuchungen an Proteinen des p53 Tumorsuppressor Netzwerks: p53, p63 und MDM2. *Department Chemie (Thesis)*. Technische Universität München, München.

Klein, C., Georges, G., Künkele, A.P., Huber, R., Engh, R.A. and Hansen, S. (2001a) High thermostability and lack of cooperative DNA binding distinguish the p63 core domain from the homologous tumor suppressor p53. *J. Biol. Chem.*, **276**, 37390-37401.

Klein, C., Hesse, F., Dehner, A., Engh, R.A., Schwaiger, M. and Hansen, S. (2004) In vitro folding and characterization of the p53 DNA binding domain. *Biol. Chem.*, **385**, 95-102.

Klein, C., Planker, E., Diercks, T., Kessler, H., Künkele, K.P., Lang, K., Hansen, S. and Schwaiger, M. (2001b) NMR spectroscopy reveals the solution dimerization interface of p53 core domains bound to their consensus DNA. *J. Biol. Chem.*, **276**, 49020-49027.

Kneller, D.G. and Kuntz, I.D. (1993) UCSF Sparky - an NMR Display, Annotation and Assignment Tool. *J. Cell. Biochem.*, 254-254.

Koide, S., Jahnke, W. and Wright, P.E. (1995) Measurement of Intrinsic Exchange-Rates of Amide Protons in a N-15-Labeled Peptide. *J. Biomol. NMR*, **6**, 306-312.

Kopnin, B.P. (2000) Targets of oncogenes and tumor suppressors: Key for understanding basic mechanisms of carcinogenesis. *Biochem.-Moscow*, **65**, 2-27.

Kräger, J., Pfeifer, H. and Heink, W. (1988) *Advances in Magnetic Resonance*. Academic Press, New York.

Kraulis, P.J. (1991) MOLSCRIPT: A Program to Produce Both Detailed and Schematic Plots of Protein Structures. *J. Appl. Crystallogr.*, **24**, 946-950.

Kriwacki, R.W., Hengst, L., Tennant, L., Reed, S.I. and Wright, P.E. (1996) Structural studies of p21Waf1/Cip1/Sdi1 in the free and Cdk2-bound state: conformational disorder mediates binding diversity. *Proc. Natl. Acad. Sci. U. S. A.*, **93**, 11504-11509.

Kroemer, G. (2003) The mitochondrial permeability transition pore complex as a pharmacological target. An introduction. *Curr. Med. Chem.*, **10**, 1469-1472.

Kroemer, G. and Reed, J.C. (2000) Mitochondrial control of cell death. *Nat. Med.*, **6**, 513-519.

Kubbutat, M.H.G., Jones, S.N. and Vousden, K.H. (1997) Regulation of p53 stability by MDM2. *Nature*, **387**, 299-303.

Kubota, H., Hynes, G., Carne, A., Ashworth, A. and Willison, K. (1994) Identification of 6 TCP-1-Related Genes Encoding Divergent Subunits of the TCP-1-Containing Chaperonin. *Curr. Biol.*, **4**, 89-99.

Kussie, P.H., Gorina, S., Marechal, V., Elenbaas, B., Moreau, J., Levine, A.J. and Pavletich, N.P. (1996) Structure of the MDM2 oncoprotein bound to the p53 tumor suppressor transactivation domain. *Science*, **274**, 948-953.

Landry, S.J., Zeilstraryalls, J., Fayet, O., Georgopoulos, C. and Gierasch, L.M. (1993) Characterization of a Functionally Important Mobile Domain of GroES. *Nature*, **364**, 255-258.

Langer, T., Lu, C., Echols, H., Flanagan, J., Hayer, M.K. and Hartl, F.U. (1992) Successive Action of DnaK, DnaJ and GroEL Along the Pathway of Chaperone-Mediated Protein Folding. *Nature*, **356**, 683-689.

Lebrun, A., Lavery, R. and Weinstein, H. (2001) Modeling multi-component protein-DNA complexes: the role of bending and dimerization in the complex of p53 dimers with DNA. *Protein Eng.*, **14**, 233-243.

Lee, S., Sowa, M.E., Choi, J.M. and Tsai, F.T.F. (2004) The ClpB/Hsp104 molecular chaperone - a protein disaggregating machine. *J. Struct. Biol.*, **146**, 99-105.

Lee, W.T., Harvey, T.S., Yin, Y., Yau, P., Litchfield, D. and Arrowsmith, C.H. (1994) Solution Structure of the Tetrameric Minimum Transforming Domain of p53. *Nat. Struct. Biol.*, **1**, 877-890.

Lenk, R. (1986) *Fluctuations, Diffusion and Spin Relaxation*. Elsevier, Amsterdam.

Leu, J.I.J., Dumont, P., Hafey, M., Murphy, M.E. and George, D.L. (2004) Mitochondrial p53 activates Bak and causes disruption of a Bak-Mcl1 complex. *Nat. Cell Biol.*, **6**, 443-450.

Leutner, M., Gschwind, R.M., Liermann, J., Schwarz, C., Gemmecker, G. and Kessler, H. (1998) Automated backbone assignment of labeled proteins using the threshold accepting algorithm. *J. Biomol. NMR*, **11**, 31-43.

Levine, A.J. (1997) p53, the cellular gatekeeper for growth and division. *Cell*, **88**, 323-331.

Lewis, J.M., Truong, T.N. and Schwartz, M.A. (2002) Integrins regulate the apoptotic response to DNA damage through modulation of p53. *Proc. Natl. Acad. Sci. U. S. A.*, **99**, 3627-3632.

Li, S., Armstrong, C.M., Bertin, N., Ge, H., Milstein, S., Boxem, M., Vidalain, P.-O., et al. (2004) A Map of the Interactome Network of the Metazoan C. elegans. *Science*, **303**, 540-543.

Liberek, K., Marszalek, J., Ang, D., Georgopoulos, C. and Zylicz, M. (1991) Escherichia-Coli DnaJ and GrpE Heat-Shock Proteins Jointly Stimulate Atpase Activity of DnaK. *Proc. Natl. Acad. Sci. U. S. A.*, **88**, 2874-2878.

Lilie, H. and Buchner, J. (1995) Interaction of GroEL with a Highly Structured Folding Intermediate - Iterative Binding Cycles Do Not Involve Unfolding. *Proc. Natl. Acad. Sci. U. S. A.*, **92**, 8100-8104.

Lin, J., Chen, J., Elenbaas, B. and Levine, A.J. (1994) Several hydrophobic amino acids in the p53 amino-terminal domain are required for transcriptional activation, binding to mdm-2 and the adenovirus 5 E1B 55-kD protein. *Gene. Dev.*, **8**, 1235-1246.

Lin, M.F., Shapiro, M.J. and Wareing, J.R. (1997) Diffusion-edited NMR-affinity NMR for direct observation of molecular interactions. *J. Am. Chem. Soc.*, **119**, 5249-5250.

Lin, M.F., Shapiro, M.J. and Wareing, J.R. (1997b) Screening mixtures by affinity NMR. *J. Org. Chem.*, **62**, 8930-8931.

Lindquist, S. and Craig, E.A. (1988) The Heat-Shock Proteins. *Annu. Rev. Genet.*, **22**, 631-677.

Linse, P. and Södermann, O. (1995) The Validity of the Short-Gradient-Pulse Approximation in NMR Studies of Restricted Diffusion. Simulations of Molecules Diffusing between Planes, in Cylinders and Spheres. *J. Magn. Reson.*, **A116**, 77-86.

Lipari, G. and Szabo, A. (1981) Nuclear magnetic resonance relaxation in nucleic acid fragments: models for internal motion. *Biochemistry*, **20**, 6250-6256.

Lohrum, M.A.E., Ludwig, R.L., Kubbutat, M.H.G., Hanlon, M. and Vousden, K.H. (2003) Regulation of HDM2 activity by the ribosomal protein L11. *Cancer Cell*, **3**, 577-587.

Los, M., Wesselborg, S. and Schulze-Osthoff, K. (1999) The role of caspases in development, immunity, and apoptotic signal transduction: Lessons from knockout mice. *Immunity*, **10**, 629.

Lu, H., Keller, D., Zeng, X.Y., Goodman, R., Lozano, G. and Zhao, Y.M. (2001) Phosphorylation of the p53 serine 392 by a UV responsive kinase complex containing the transcriptional elongation factor FACT. *Faseb J.*, **15**, A6.

Lu, H. and Levine, A.J. (1995) Human TAFII31 protein is a transcriptional coactivator of the p53 protein. *Proc. Natl. Acad. Sci. U. S. A.*, **92**, 5154-5158.

Lu, H., Zeng, X., Chen, L., Jost, C.A., Maya, R., Keller, D., Wang, X., Kaelin, W.G., Oren, M. and Chen, J. (1999) MDM2 suppresses p73 function without promoting p73 degradation. *Faseb J.*, **13**, A1538.

Luna, R.M.D., Wagner, D.S. and Lozano, G. (1995) Rescue of Early Embryonic Lethality in MDM2-Deficient Mice by Deletion of p53. *Nature*, **378**, 203-206.

Lüttgen, H., Robelek, R., Mühlberger, R., Diercks, T., Schuster, S.C., Köhler, P., Kessler, H., Bacher, A. and Richter, G. (2002) Transcriptional regulation by antitermination. Interaction of RNA with NusB protein and NusB/NusE protein complex of Escherichia coli. *J. Mol. Biol.*, **316**, 875-885.

Maisse, C., Guerrieri, P. and Melino, G. (2003) p73 and p63 protein stability: the way to regulate function. *Biochem. Pharmacol.*, **66**, 1555-1561.

Majors, P.D., Blackley, J.L., Altobelli, S.A., Caprihan, A. and Fukushima, E. (1990) Eddy-Current Compensation by Direct Field Detection and Digital Gradient Modification. *J. Magn. Reson.*, **87**, 548-553.

Maloney, A. and Workman, P. (2002) Hsp90 as a new therapeutic target for cancer therapy: the story unfolds. *Expert Opin. Biol. Th.*, **2**, 3-24.

Mansfield, P. and Chapman, B. (1986a) Active Magnetic Screening of Coils for Static and Time-Dependent Magnetic-Field Generation in NMR Imaging. *J. Phys. E. Sci. Instrum.*, **19**, 540-545.

Mansfield, P. and Chapman, B. (1986b) Active Magnetic Screening of Gradient Coils in NMR Imaging. *J. Magn. Reson.*, **66**, 573-576.

Marchenko, N.D., Zaika, A. and Moll, U.M. (2000) Death signal-induced localization of p53 protein to mitochondria - A potential role in apoptotic signaling. *J. Biol. Chem.*, **275**, 16202-16212.

Marcu, M.G., Chadli, A., Bouhouche, I., Catelli, M. and Neckers, L.M. (2000) The heat shock protein 90 antagonist novobiocin interacts with a previously unrecognized ATP-binding domain in the carboxyl terminus of the chaperone. *J. Biol. Chem.*, **275**, 37181-37186.

Maruya, M., Sameshima, M., Nemoto, T. and Yahara, I. (1999) Monomer arrangement in Hsp90 dimer as determined by decoration with N and C-terminal region specific antibodies. *J. Mol. Biol.*, **285**, 903-907.

May, P. and May, E. (1999) Twenty years of p53 research: structural and functional aspects of the p53 protein. *Oncogene*, **18**, 7621-7636.

Mayer, B.J. (2001) SH3 domains: complexity in moderation. *J. Cell Biol.*, **114**, 1253-1263.

McLure, K.G. and Lee, P.W.K. (1998) How p53 binds DNA as a tetramer. *Embo J.*, **17**, 3342-3350.

McLure, K.G. and Lee, P.W.K. (1999) p53 DNA binding can be modulated by factors that alter the conformational equilibrium. *Embo J.*, **18**, 763-770.

Merritt, E.A. and Bacon, D.J. (1997) Raster3D Version 2.0 - A Program for Photorealistic Molecular Graphics. *Acta Crystallogr.*, **D50**, 869-873.

Meyer, P., Prodromou, C., Hu, B., Vaughan, C., Roe, S.M., Panaretou, B., Piper, P.W. and Pearl, L.H. (2003) Structural and Functional Analysis of the Middle Segment of Hsp90. Implications for ATP Hydrolysis and Client Protein and Cochaperone Interactions. *Mol. Cell*, **11**, 647-658.

Meyer, P., Prodromou, C., Liao, C., Hu, B., Roe, S.M., Vaughan, C., Vlasic, I., Panaretou, B., Piper, P.W. and Pearl, L.H. (2004) Structural basis for recruitment of the ATPase activator Aha1 to the Hsp90 chaperone machinery. *Embo J.*, **23**, 511-519.

Michelini, E.T. and Flynn, G.C. (1999) The unique chaperone operon of Thermotoga maritima: Cloning and initial characterization of a functional Hsp70 and small heat shock protein. *J. Bacteriol.*, **181**, 4237-4244.

Midgley, C.A., Fisher, C.J., Bartek, J., Vojtesek, B., Lane, D. and Barnes, D.M. (1992) Analysis of p53 expression in human tumours: an antibody raised against human p53 expressed in Escherichia coli. *J. Cell Sci.*, **101 (Pt 1)**, 183-189.

Mihara, M. and Moll, U.M. (2003) Detection of mitochondrial localization of p53. *Method. Mol. Biol.*, **234**, 203-209.

Mills, R. (1973) Self-Diffusion in Normal and Heavy Water in the Range 1-45 Degrees. *J. Phys. Chem.*, **77**, 685-688.

Milner, J. (1995) Flexibility - the Key to P53 Function. *Trends in Biochemical Sciences*, **20**, 49.

Minty, A., Dumont, X., Kaghad, M. and Caput, D. (2000) Covalent modification of p73 alpha by SUMO-1 - Two-hybrid screening with p73 identifies novel SUMO-1-interacting proteins and a SUMO-1 interaction motif. *J. Biol. Chem.*, **275**, 36316-36323.

Modig, K., Liepinsh, E., Otting, G. and Halle, B. (2004) Dynamics of protein and peptide hydration. *J. Am. Chem. Soc.*, **126**, 102-114.

Mori, S., Abeygunawardana, C., Johnson, M.O. and Vanzijl, P.C.M. (1995) Improved Sensitivity of HSQC Spectra of Exchanging Protons At Short Interscan Delays Using a New Fast HSQC (FHSQC) Detection Scheme That Avoids Water Saturation. *J. Magn. Reson. Ser. B*, **108**, 94-98.

Morris, K.F. and Johnson, C.S. (1993) Resolution of Discrete and Continuous Molecular-Size Distributions by Means of Diffusion-Ordered 2d NMR-Spectroscopy. *J. Am. Chem. Soc.*, **115**, 4291-4299.

Moseley, M.E., Cohen, Y., Mintorovitch, J., Chileuitt, L., Shimizu, H., Kucharczyk, J., Wendland, M.F. and Weinstein, P.R. (1990) Early detection of regional cerebral ischemia in cats: comparison of diffusion- and T2-weighted MRI and spectroscopy. *Magn. Reson. Med.*, **14**, 330-346.

Muchmore, S.W., Sattler, M., Liang, H., Meadows, R.P., Harlan, J.E., Yoon, H.S., Nettesheim, D., Chang, B.S., Thompson, C.B., Wong, S.L., Ng, S.C. and Fesik, S.W. (1996) X-ray and NMR structure of human Bcl-x(L), an inhibitor of programmed cell death. *Nature*, **381**, 335-341.

Muller, J.J., O., G., Zirwer, D. and Damaschun, G. (1983) Calculation of small-angle x-ray and neutron scattering curves and of translational friction coefficients on the common basis of finite elements. *Stud. Biophys.*, **93**, 39-46.

Munster, P.N., Basso, A., Solit, D., Norton, L. and Rosen, N. (2001) Modulation of Hsp90 function by ansamycins sensitizes breast cancer cells to chemotherapy-induced apoptosis in an RB- and schedule-dependent manner - See The Biology Behind: E. A. Sausville, combining cytotoxics and 17-allylamino, 17-demethoxygeldanamycin: Sequence and tumor biology matters. *Clin. Cancer Res.*, **7**, 2228-2236.

Murday, J.S. (1973) Measurement of magnetic Field Gradient by its Effect on the NMR Free Induction Decay. *J. Magn. Reson.*, **11**, 111-120.

Nagaich, A.K., Zhurkin, V.B., Durell, S.R., Jernigan, R.L., Appella, E. and Harrington, R.E. (1999) p53-induced DNA bending and twisting: p53 tetramer binds on the outer side of a DNA loop and increases DNA twisting. *Proc. Natl. Acad. Sci. U. S. A.*, **96**, 1875-1880.

Nakagawa, T., Takahashi, M., Ozaki, T., Watanabe, K., Hayashi, S., Hosoda, M., Todo, S. and Nakagawara, A. (2003) Negative autoregulation of p73 and p53 by Delta Np73 in regulating differentiation and survival of human neuroblastoma cells. *Cancer Lett.*, **197**, 105-109.

Nakagawa, T., Takahashi, M., Ozaki, T., Watanabe, K., Todo, S., Mizuguchi, H., Hayakawa, T. and Nakagawara, A. (2002) Autoinhibitory regulation of p73 by Delta Np73 to modulate cell survival and death through a p73-specific target element within the Delta Np73 promoter. *Mol. Cell. Biol.*, **22**, 2575-2558.

Narayanan, S., Bosl, B., Walter, S. and Reif, B. (2003) Importance of low-oligomeric-weight species for prion propagation in the yeast prion system Sup35/Hsp104. *Proc. Natl. Acad. Sci. U. S. A.*, **100**, 9286-9291.

Neckers, L. (2002) Heat shock protein 90 inhibition by 17-allylamino-17-demethoxygeldanamycin: A novel therapeutic approach for treating hormone-refractory prostate cancer - Commentary. *Clin. Cancer Res.*, **8**, 962-966.

Neckers, L. and Lee, Y.S. (2003) Cancer - The rules of attraction. *Nature*, **425**, 357-357.

Nicholson, D.W. (1996) ICE/CED3-like proteases as therapeutic targets for the control of inappropriate apoptosis. *Nat. Biotechnol.*, **14**, 297-301.

Nylandsted, J., Wick, W., Hirt, U.A., Brand, K., Rohde, M., Leist, M., Weller, M. and Jaattela, M. (2002) Eradication of glioblastoma, and breast and colon carcinoma xenografts by Hsp70 depletion. *Cancer Res.*, **62**, 7139-7142.

O'Brate, A. and Giannakakou, P. (2003) The importance of p53 location: nuclear or cytoplasmic zip code? *Drug Resist. Update*, **6**, 313-322.

Obermann, W.M.J., Sondermann, H., Russo, A.A., Pavletich, N.P. and Hartl, F.U. (1998) In vivo function of Hsp90 is dependent on ATP binding and ATP hydrolysis. *J. Cell Biol.*, **143**, 901-910.

Okamura, S., Arakawa, H., Tanaka, T., Nakanishi, H., Ng, C.C., Taya, Y., Monden, M. and Nakamura, Y. (2001) p53DINP1, a p53-inducible gene, regulates p53-dependent apoptosis. *Mol. Cell*, **8**, 85-94.

Olivier, M., Eeles, R., Hollstein, M., Khan, M.A., Harris, C.C. and Hainaut, P. (2002) The IARC TP53 database: New Online mutation analysis and recommendations to users. *Hum. Mutat.*, **19**, 607-614.

Orekhov, V.Y., Korzhnev, D.M., Pervushin, K.V., Hoffmann, E. and Arseniev, A.S. (1999) Sampling of protein dynamics in nanosecond time scale by N-15 NMR relaxation and self-diffusion measurements. *J. Biomol. Struct. Dyn.*, **17**, 157-174.

Otting, G. (1997) NMR studies of water bound to biological molecules. *Prog. Nucl. Magn. Reson. Spectrosc.*, **31**, 259-285.

Palmer, A.G. (1997) Probing molecular motion by NMR. *Curr. Opin. Struct. Biol.*, **7**, 732-737.

Panaretou, B., Prodromou, C., Roe, S.M., O'Brien, R., Ladbury, J.E., Piper, P.W. and Pearl, L.H. (1998) ATP binding and hydrolysis are essential to the function of the Hsp90 molecular chaperone in vivo. *Embo J.*, **17**, 4829-4836.

Panaretou, B., Siligardi, G., Meyer, P., Maloney, A., Sullivan, J.K., Singh, S., Millson, S.H., Clarke, P.A., Naaby-Hansen, S., Stein, R., Cramer, R., Mollapour, M., Workman, P., Piper, P.W., Pearl, L.H. and Prodromou, C. (2002) Activation of the ATPase activity of Hsp90 by the stress-regulated cochaperone Aha1. *Mol. Cell*, **10**, 1307-1318.

Parker, W. and Song, P.S. (1992) Protein structures in SDS micell-protein complexes. *Biophys. J.*, **61**, 1435-1439.

Parsell, D.A., Kowal, A.S., Singer, M.A. and Lindquist, S.L. (1994) Protein disaggregation mediated by heat shock protein Hsp104. *Nature*, **372**, 475-478.

Pavletich, N.P., Chambers, K.A. and Pabo, C.O. (1993) The DNA-binding domain of p53 contains the four conserved regions and the major mutation hot spots. *Gene. Dev.*, **7**, 2556-2564.

Pelta, M.D., Barjat, H., Morris, G.A., Davis, A.L. and Hammond, S.J. (1998) Pulse sequences for high-resolution diffusion-ordered spectroscopy (HR-DOSY). *Magn. Reson. Chem.*, **36**, 706-714.

Peng, Y.H., Chen, L.H., Li, C.G., Lu, W.G. and Chen, J.D. (2001) Inhibition of MDM2 by Hsp90 contributes to mutant p53 stabilization. *J. Biol. Chem.*, **276**, 40583-40590.

Perfettini, J.L., Kroemer, R.T. and Kroemer, G. (2004) Fatal liaisons of p53 with Bax and Bak. *Nat. Cell Biol.*, **6**, 386-388.

Peschier, L.J.C., Bouwstra, J.A., deBleyser, J., Junginger, H.E. and Leyte, J.C. (1996) Cross-relaxation effects in pulsed-field-gradient stimulated-echo measurements on water in a macromolecular matrix. *J. Magn. Reson. Ser. B*, **110**, 150-157.

Petros, A.M., Gunasekera, A., Xu, N., Olejniczak, E.T. and Fesik, S.W. (2004a) Defining the p53 DNA-binding domain/Bcl-x(L)-binding interface using NMR. *FEBS Lett.*, **559**, 171-174.

Petros, A.M., Medek, A., Nettesheim, D.G., Kim, D.H., Yoon, H.S., Swift, K., Matayoshi, E.D., Oltersdorf, T. and Fesik, S.W. (2001) Solution structure of the antiapoptotic protein Bcl-2. *Proc. Natl. Acad. Sci. U. S. A.*, **98**, 3012-3017.

Petros, A.M., Olejniczak, T.E. and Fesik, S.W. (2004b) Structural biology of the Bcl-2 family pf proteins. *Biochim. Biophys. Acta*, **1644**, 83-94.

Picksley, S.M., Vojtesek, B., Sparks, A. and Lane, D.P. (1994) Immunochemical analysis of the interaction of p53 with MDM2;--fine mapping of the MDM2 binding site on p53 using synthetic peptides. *Oncogene*, **13**, 2523-2529.

Piotto, M., Saudek, V. and Sklenar, V. (1992) Gradient-Tailored Excitation For Single-Quantum NMR-Spectroscopy of Aqueous-Solutions. *J. Biomol. NMR*, **2**, 661-665.

Pontius, B.W. (1993) Close encounters: why unstructured, polymeric domains can increase rates of specific macromolecular association. *Trends Biochem. Sci.*, **18**, 181-186.

Praekelt, U.M. and Meacock, P.A. (1990) Hsp12, a new small heat shock gene of Saccharomyces cerevisiae: analysis of structure, regulation and function. *Mol. Gen. Gent.*, **223**, 97-106.

Pratt, W.B., Galigniana, M.D., Harrell, J.M. and DeFranco, D.B. (2004) Role of Hsp90 and the Hsp90-binding immunophilins in signalling protein movement. *Cell. Signal.*, **16**, 857-872.

Pratt, W.B. and Toft, D.O. (2003) Regulation of signaling protein function and trafficking by the Hsp90/Hsp70-based chaperone machinery. *Exp. Biol. Med.*, **228**, 111-133.

Price, W.S. (1996) Gradient NMR. In Webb, G.A. (ed.), *Annual Reports on NMR Spectroscopy*. Academic, London, Vol. 35, pp. 51-142.

Price, W.S. (1997a) *NMR Imaging*. Academic Press, London.

Price, W.S. (1997b) Pulsed-field gradient nuclear magnetic resonance as a tool for studying translational diffusion .1. Basic theory. *Concepts Magn. Resonance*, **9**, 299-336.

Price, W.S. (1998) Pulsed-field gradient nuclear magnetic resonance as a tool for studying translational diffusion: Part II. Experimental aspects. *Concepts Magn. Resonance*, **10**, 197-237.

Price, W.S., Chang, W.-T., Kwok, W.-M. and Hwang, L.-P. (1994) Design and Construction of a Pulsed Field Gradient NMR Probe for a High-Field Superconducting Magnet. *J. Chin. Chem. Soc.*, **41**, 119-127.

Price, W.S., E., C.B. and Kuchel, P.W. (1990) Correlation of Viscosity and Conductance with 23Na+ NMR T1 Measurements. *B. Chem. Soc. Jpn.*, **63**, 2961-2965.

Price, W.S. and Kuchel, P.W. (1991) Effect of Nonrectangular Field Gradient Pulses in the Stejskal and Tanner (Diffusion) Pulse Sequence. *J. Magn. Reson.*, **94**, 133-139.

Prives, C. (1994) How loops, beta sheets, and alpha helices help us to understand p53. *Cell*, **78**, 543-546.

Prodromou, C., Panaretou, B., Chohan, S., Siligardi, G., O'Brien, R., Ladbury, J.E., Roe, S.M., Piper, P.W. and Pearl, L.H. (2000) The ATPase cycle of Hsp90 drives a molecular 'clamp' via transient dimerization of the N-terminal domains. *Embo J.*, **19**, 4383-4392.

Prodromou, C., Roe, S.M., Obrien, R., Ladbury, J.E., Piper, P.W. and Pearl, L.H. (1997) Identification and structural characterization of the ATP/ADP- binding site in the Hsp90 molecular chaperone. *Cell*, **90**, 65-75.

Provencher, S.W. (1976a) Eigenfunction Expansion Method for Analysis of Exponential Decay Curves. *J. Chem. Phys.*, **64**, 2773-2777.

Provencher, S.W. (1976b) Fourier Method for Analysis of Exponential Decay Curves. *Biophys. J.*, **16**, 27-41.

Provencher, S.W. and Vogel, R.H. (1983) *Numerical Treatment of Inverse Problems in Differential and Integral Equations*. Birkhauser, Boston.

Qian, Y.Q., Patel, D., Hartl, F.U. and McColl, D.J. (1996) Nuclear magnetic resonance solution structure of the human Hsp40 (HDJ-1) J-domain. *J. Mol. Biol.*, **260**, 224-235.

Queitsch, C., Sangster, T.A. and Lindquist, S. (2002) Hsp90 as a capacitor of phenotypic variation. *Nature*, **417**, 618-624.

Raulet, R., Grandclaude, D., Humbert, F. and Canet, D. (1997) Fast NMR imaging with B1 gradients. *J. Magn. Reson.*, **124**, 259-262.

Ravagnan, L., Roumier, T. and Kroemer, G. (2002) Mitochondria, the killer organelles and their weapons. *J. Cell. Physiol.*, **192**, 131-137.

Raycroft, L., Wu, H.Y. and Lozano, G. (1990) Transcriptional activation by wild-type but not transforming mutants of the p53 anti-oncogene. *Science*, **252**, 1708-1711.

Reed, J.C. (2000) Mechanisms of apoptosis. *Am. J. Pathol.*, **157**, 1415-1430.

Reif, B., Narayanan, S., Bosl, B. and Walter, S. (2004) The yeast prion system: Molecular interactions between Sup35 and Hsp104 characterized by solution state NMR spectroscopy. *Biophys. J.*, **86**, 176A-176A.

Richardson, A., Schwager, F., Landry, S.J. and Georgopoulos, C. (2001) The importance of a mobile loop in regulating chaperonin/co-chaperonin interaction - Humans versus Escherichia coli. *J. Biol. Chem.*, **276**, 4981-4987.

Richter, K. and Buchner, J. (2001) Hsp90: Chaperoning signal transduction. *J. Cell. Physiol.*, **188**, 281-290.

Richter, K., Muschler, P., Hainzl, O. and Buchner, J. (2001) Coordinated ATP hydrolysis by the Hsp90 dimer. *J. Biol. Chem.*, **276**, 33689-33696.

Richter, K., Reinstein, J. and Buchner, J. (2002) N-terminal residues regulate the catalytic efficiency of the Hsp90 ATPase cycle. *J. Biol. Chem.*, **277**, 44905-44910.

Ridley, A.J., Schwartz, M.A., Burridge, K., Firtel, R.A., Ginsberg, M.H., Borisy, G., Parsons, J.T. and Horwitz, A.R. (2003) Cell migration: Integrating signals from front to back. *Science*, **302**, 1704-1709.

Rippin, T.M., Freund, S.M.V., Veprintsev, D.B. and Fersht, A.R. (2002) Recognition of DNA by p53 core domain and location of intermolecular contacts of cooperative binding. *J. Mol. Biol.*, **319**, 351-358.

Riseman, J. and Kirkwood, J.G. (1950) The intrisic Viscosity, translational and rotatory diffusion constants of rod-like Macromolecules in Solution. *J. Chem. Phys.*, **18**, 512-516.

Rodriguez, M.S., Desterro, J.M.P., Lain, S., Midgley, C.A., Lane, D.P. and Hay, R.T. (1999) SUMO-1 modification activates the transcriptional response of p53. *Embo J.*, **18**, 6455-6461.

Roe, S.M., Ali, M.M., Meyer, P., Vaughan, C., Panaretou, B., Piper, P.W., Prodromou, C. and Pearl, L.H. (2004) The mechanism of Hsp90 regulation by the protein kinase-specific cochaperone p50(cdc37). *Cell*, **116**, 87-98.

Roe, S.M., Prodromou, C., O'Brien, R., Ladbury, J.E., Piper, P.W. and Pearl, L.H. (1999) Structural basis for inhibition of the Hsp90 molecular chaperone by the antitumor antibiotics radicicol and geldanamycin. *J. Med. Chem.*, **42**, 260-266.

Roumier, T., Castedo, M., Perfettini, J.-L., Andreau, K., Métivier, D., Zamzami, N. and Kroemer, G. (2003) Mitochondrion-dependent caspase activation by the HIV-1 envelope. *Biochem. Pharmacol.*, **66**, 1321-1329.

Rowan, S., Ludwig, R.L., Haupt, Y., Bates, S., Lu, X., Oren, M. and Vousden, K.H. (1996) Specific loss of apoptotic but not cell-cycle arrest function in a human tumor derived p53 mutant. *Embo J.*, **15**, 827-838.

Rubbi, C.P. and Milner, J. (2003) Disruption of the nucleolus mediates stabilization of p53 in response to DNA damage and other stresses. *Embo J.*, **22**, 6068-6077.

Rutherford, S.L. and Lindquist, S. (1998) Hsp90 as a capacitor for morphological evolution. *Nature*, **396**, 336-342.

Saibil, H.R. (1996) What can electron microscopy tell us about chaperoned protein folding? *Fold. Des.*, **1**, R45-R49.

Saibil, H.R., Horwich, A.L. and Fenton, W.A. (2002) Allostery and protein substrate conformational change during GroEL/GroES-mediated protein folding. In *Protein Folding in the Cell*, p. 45.

Saibil, H.R. and Ranson, N.A. (2002) The chaperonin folding machine. *Trends Biochem. Sci.*, **27**, 627-632.

Sakamuro, D., Sabbatini, P., White, E. and Prendergast, G.C. (1997) The polyproline region of p53 is required to activate apoptosis but not growth arrest. *Oncogene*, **15**, 887-898.

Salek, R.M., Williams, M.A., Prodromou, C., Pearl, L.H. and Ladbury, J.E. (2002) Letter to the editor: Backbone resonance assignments of the 25kD N-terminal ATPase domain from the Hsp90 chaperone. *J. Biomol. NMR*, **23**, 327-328.

Salzmann, M., Pervushin, K., Wider, G., Senn, H. and Wüthrich, K. (1998) TROSY in triple-resonance experiments: New perspectives for sequential NMR assignment of large proteins. *Proc. Natl. Acad. Sci. U. S. A.*, **95**, 13585-13590.

Salzmann, M., Wider, G., Pervushin, K., Senn, H. and Wüthrich, K. (1999) TROSY-type triple-resonance experiments for sequential NMR assignments of large proteins. *J. Am. Chem. Soc.*, **121**, 844-848.

Sambrook, J. and Russell, D.W. (2001) *Molecular Cloning: A laboratory manual*. Cold Spring Harbor Laboratory Press, Cold Spring Harbor, NY, USA.

Sanger, F., Nicklen, S. and Coulson, A.R. (1977) DNA sequencing with chain-terminating inhibitors. *Proc. Natl. Acad. Sci. U. S. A.*, **74**, 5463-5467.

Sattler, M., Liang, H., Nettesheim, D., Meadows, R.P., Harlan, J.E., Eberstadt, M., Yoon, H.S., Shuker, S.B., Chang, B.S., Minn, A.J., Thompson, C.B. and Fesik, S.W. (1997) Structure of Bcl-x(L)-Bak peptide complex: Recognition between regulators of apoptosis. *Science*, **275**, 983-986.

Scheibel, T., Weikl, T. and Buchner, J. (1998) Two chaperone sites in Hsp90 differing in substrate specificity and ATP dependence. *Proc. Natl. Acad. Sci. U. S. A.*, **95**, 1495-1499.

Schroder, H., Langer, T., Hartl, F.U. and Bukau, B. (1993) DnaK, DnaJ and GrpE Form a Cellular Chaperone Machinery Capable of Repairing Heat-Induced Protein Damage. *Embo J.*, **12**, 4137-4144.

Schulte, T.W. and Neckers, L.M. (1998) The benzoquinone ansamycin 17-allylamino-17-demethoxygeldanamycin binds to Hsp90 and shares important biologic activities with geldanamycin. *Cancer Chemother. Pharmacol.*, **42**, 273-279.

Schultz, J., Ponting, C.P., Hofmann, K. and Bork, P. (1997) SAM as a protein interaction domain involved in developmental regulation. *Protein Sci.*, **6**, 249-253.

Schulze-Osthoff, K., Ferrari, D., Los, M., Wesselborg, S. and Peter, M.E. (1998) Apoptosis signaling by death receptors. *Eur. J. Biochem.*, **254**, 439-459.

Schwarz, E., Lilie, H. and Rudolph, R. (1996) The Effect of Molecular Chaperones on in vivo and in vitro folding processes. *Biol. Chem.*, **377**, 411-416.

Seymour, J.D. and Piper, P.W. (1999) Stress induction of Hsp30. the plasma membrane heat shock protein gene of S. cerevisiae, appears not to use known stress-regulated transcription factors. *Microbiology*, **145**, 231-239.

Sheltraw, D. and Kenkre, V.M. (1996) The Memory-Function Technique for the Calculation of Pulsed-Gradient NMR Sognals in Confined Geometries. *J. Magn. Reson.*, **A122**, 126-136.

Shorter, J. and Lindquist, S. (2004) Hsp104 catalyzes formation and elimination of self-replicating Sup35 prion conformers. *Science*, **304**, 1793-1797.

Shuker, S.B., Hajduk, P.J., Meadows, R.P. and Fesik, S.W. (1996) Discovering high-affinity ligands for proteins: SAR by NMR. *Science*, **274**, 1531-1534.

Sklenar, V., Piotto, M., Leppik, R. and Saudek, V. (1993) Gradient-Tailored Water Suppression For H-1-N-15 HSQC Experiments Optimized to Retain Full Sensitivity. *J. Magn. Reson. Ser. A*, **102**, 241-245.

Soga, S., Kozawa, T., Narumi, H., Akinaga, S., Irie, K., Matsumoto, K., Sharma, S.V., Nakano, H., Mizukami, T. and Hara, M. (1998) Radicicol leads to selective depletion of Raf kinase and disrupts K-Ras-activated aberrant signaling pathway. *J. Biol. Chem.*, **273**, 822-828.

Soussi, T. and May, P. (1996) Structural aspects of the p53 protein in relation to gene evolution: a second look. *J. Mol. Biol.*, **260**, 623-637.

Sreedhar, A.S. and Csermely, P. (2004) Heat shock proteins in the regulation of apoptosis: new strategies in tumor therapy - A comprehensive review. *Pharmacol. Ther.*, **101**, 227-257.

Sriram, M., Osipiuk, J., Freeman, B., Morimoto, R. and Joachimiak, A. (1997) Human Hsp70 molecular chaperone binds two calcium ions within the ATPase domain. *Structure*, **5**, 403-414.

Stebbins, C.E., Russo, A.A., Schneider, C., Rosen, N., Hartl, F.U. and Pavletich, N.P. (1997) Crystal structure of an Hsp90-geldanamycin complex: Targeting of a protein chaperone by an antitumor agent. *Cell*, **89**, 239-250.

Stejskal, E.O. (1965) Use of Spin Echoes in a Pulsed Magnetic-Field Gradient to Study Anisotropic Restricted Diffusion and Flow. *J. Chem. Phys.*, **43**, 3597-3597.

Stejskal, E.O. and Tanner, J.E. (1965) Spin Diffusion Measurements - Spin Echoes in Presence of a Time-Dependent Field Gradient. *J. Chem. Phys.*, **42**, 288-288.

Steller, H. (1995) Mechanisms and Genes of Cellular Suicide. *Science*, **267**, 1445-1449.

Stommel, J.M., Marchenko, N.D., Jimenez, G.S., Moll, U.M., Hope, T.J. and Wahl, G.M. (1999) A leucine-rich nuclear export signal in the p53 tetramerization domain: regulation of subcellular localization and p53 activity by NES masking. *Embo J.*, **18**, 1660-1672.

Straubinger, K., Schick, F. and Lutz, O. (1995) Relaxation of AB spin systems in stimulated-echo spectroscopy. *J. Magn. Reson. Ser. B*, **109**, 251-258.

Supko, J.G., Hickman, R.L., Grever, M.R. and Malspeis, L. (1995) Preclinical Pharmacological Evaluation of Geldanamycin as an Antitumor Agent. *Cancer Chemother. Pharmacol.*, **36**, 305-315.

Szyperski, T., Pellecchia, M., Wall, D., Georgopoulos, C. and Wüthrich, K. (1994) NMR Structure Determination of the Escherichia-Coli DnaJ Molecular Chaperone - Secondary Structure and

Backbone Fold of the N-Terminal Region (Residues-2-108) Containing the Highly Conserved J-Domain. *Proc. Natl. Acad. Sci. U. S. A.*, **91**, 11343-11347.

Takekawa, M., Adachi, M., Nakahata, A., Nakayama, I., Itoh, F., Tsukuda, H., Taya, Y. and Imai, K. (2000) p53-inducible Wip1 phosphatase mediates a negative feedback regulation of p38 MAPK-p53 signaling in response to UV radiation. *Embo J.*, **19**, 6517-6526.

Talagala, S.L. and Lowe, I.J. (1991) Introduction to Magnetic Resonance Imaging. *Concepts Magn. Resonance*, **3**, 145-159.

Tanner, J.E. (1970) Use of Stimulated Echo in NMR-Diffusion Studies. *J. Chem. Phys.*, **52**, 2523-2523.

Tanner, J.E. and Stejskal, E.O. (1968) Restricted Self-Diffusion of Protons in Colloidal Systems by Pulsed-Gradient Spin-Echo Method. *J. Chem. Phys.*, **49**, 1768-1768.

Thompson, C.B. (1995) Apoptosis in the Pathogenesis and Treatment of Disease. *Science*, **267**, 1456-1462.

Thut, C.J., Chen, J.L., Klemm, R. and Tjian, R. (1995) p53 transcriptional activation mediated by coactivators TAFII40 and TAFII60. *Science*, **274**, 948-953.

Tompa, P. (2002) Intrinsically unstructured proteins. *Trends Biochem. Sci.*, **27**, 527-533.

Torrey, H.C. (1956) Bloch Equations with Diffusion Terms. *Phys. Rev.*, **104**, 563-565.

Triezenberg, S.J. (1995) Structure and function of transcriptional activation domains. *Curr. Opin. Gene. Dev.*, **5**, 190-196.

Trink, B., Okami, K., Wu, L., Sriuranpong, V., Jen, J. and Sidransky, D. (1998) A new human p53 homologue. *Nat. Med.*, **4**, 747-748.

Tsvetkova, N.M., Horvath, I., Torok, Z., Wolkers, W.F., Balogi, Z., Shigapova, N., Crowe, L.M., Tablin, F., Vierling, E., Crowe, J.H. and Vigh, L. (2002) Small heat-shock proteins regulate membrane lipid polymorphism. *Proc. Natl. Acad. Sci. U. S. A.*, **99**, 13504-13509.

Turner, R. (1986) A Target Field Approach to Optimal Coil Design. *J. Phys. D-Appl. Phys.*, **19**, L147-L151.

Turner, R. and Bowley, R.M. (1986) Passive Screening of Switched Magnetic-Field Gradients. *J. Phys. E-Sci. Instrum.*, **19**, 876-879.

Uesugi, M. and Verdine, G.L. (1999) The alpha-helical FXXPhiPhi motif in p53: TAF interaction and discrimination by MDM2. *Proc. Natl. Acad. Sci. U. S. A.*, **96**, 14801-14806.

Uetz, P., Giot, L., Cagney, G., Mansfield, T.A., Judson, R.S., Knight, J.R., Lockshon, D., Narayan, V., Srinivasan, M., Pochart, P., Qureshi-Emili, A., Li, Y., Godwin, B., Conover, D., Kalbfleisch, T., Vijayadamodar, G., Yang, M.J., Johnston, M., Fields, S. and Rothberg, J.M. (2000) A comprehensive analysis of protein-protein interactions in Saccharomyces cerevisiae. *Nature*, **403**, 623-627.

Uversky, V.N. (2002) What does it mean to be natively unfolded? *Eur. J. Biochem.*, **269**, 2-12.

Vakser, I.A., Matar, O.G. and Lam, C.F. (1999) A systematic study of low-resolution recognition in protein-protein complexes. *Proc. Natl. Acad. Sci. U. S. A.*, **96**, 8477-8482.

Vallee, R.B. and Gee, M.A. (1998) Make room for dynein. *Trends Cell Biol.*, **8**, 490-494.

Van Kampen, N.G. (1981) *Stochastic Processes in Physics and Chemsitry*. CRC Press, Boca Raton, FL.

Van Waals, J.J. and Bergman, A.H. (1990) Optimization of Eddy-Current Compensation. *J. Magn. Reson.*, **90**, 52.

Varela, J.C., Praekelt, U.M., Meacock, P.A., Planta, R.J. and Mager, W.H. (1995) The Saccharomyces cerevisiae Hsp12 gene is activated by the high-osmolarity glycerol pathway and negatively regulated by protein kinase A. *Mol. Cell Biol.*, **15**, 6232-6245.

Varfolomeev, E.E. and Ashkenazi, A. (2004) Tumor necrosis factor: An apoptosis JuNKie? *Cell*, **116**, 491-497.

Venot, C., Maratrat, M., Dureuil, C., Conseiller, E., Bracco, L. and Debussche, L. (1998) The requirement for the p53 proline-rich functional domain for mediation of apoptosis is correlated with specific PIG3 gene transactivation and with transcriptional repression. *Embo J.*, **17**, 4668-4679.

Viitanen, P.V., Lubben, T.H., Reed, J., Goloubinoff, P., Okeefe, D.P. and Lorimer, G.H. (1990) Chaperonin-Facilitated Refolding of Ribulosebisphosphate Carboxylase and ATP Hydrolysis by Chaperonin-60 (GroEL) Are K+ Dependent. *Biochemistry*, **29**, 5665-5671.

Vogelstein, B., Lane, D. and Levine, A.J. (2000) Surfing the p53 network. *Nature*, **408**, 307-310.

Von Meerwall, E. and Kamat, M. (1989) Effect of Residual Field Gradients on Pulsed-Gradient Nmr Diffusion Measurements. *J. Magn. Reson.*, **83**, 309.

Vousden, K. (2003) Regulation and function of the p53 tumour suppressor protein. *Brit. J. Cancer*, **88**, S7-S7.

Vousden, K.H. (2000) p53: Death star. *Cell*, **103**, 691-694.

Vousden, K.H. (2002) Activation of the p53 tumor suppressor protein. *Biochim. Biophys. Acta*, **1602**, 47-59.

Vuori, K. (1998) Integrin signaling: Tyrosine phosphorylation events in focal adhesions. *J. Membr. Biol.*, **165**, 191-199.

Walker, K.K. and Levine, A.J. (1996) Identification of a novel p53 functional domain that is necessary for efficient growth suppression. *Proc. Natl. Acad. Sci. U. S. A.*, **93**, 15335-15340.

Walter, S. and Buchner, J. (2002) Molecular Chaperones - Cellular Machines for Protein Folding. *Angew. Chem. Int. Ed.*, **41**, 1098-1113.

Wang, L.Z., Caprihan, A. and Fukushima, E. (1995a) The Narrow-Pulse Criterion for Pulsed-Gradient Spin-Echo Measurements. *J. Magn. Reson.*, **A117**, 209-219.

Wang, W.K., Bycroft, M., Foster, N.W., Buckle, A.M., Fersht, A.R. and Chen, Y.W. (2001) Structure of the C-terminal sterile alpha-motif (SAM) domain of human p73 alpha. *Acta Crystallogr. Sect. D-Biol. Crystallogr.*, **57**, 545-551.

Wang, Y. and Prives, C. (1995) Increased and Altered DNA-Binding of Human P53 by S and G2/M but Not G1 Cyclin-Dependent Kinases. *Nature*, **376**, 88.

Wang, Y., Schwedes, J.F., Parks, D., Mann, K. and Tegtmeyer, P. (1995b) Interaction of p53 with its consensus DNA-binding site. *Mol. Cell Biol.*, **15**, 2157-2165.

Waterman, M.J.F., Stavridi, E.S., Waterman, J.L.F. and Halazonetis, T.D. (1998) ATM-dependent activation of p53 involves dephosphorylation and association with 14-3-3 proteins. *Nature Genet.*, **19**, 175-178.

Wei, M.C., Zong, W.X., Cheng, E.H.Y., Lindsten, T., Panoutsakopoulou, V., Ross, A.J., Roth, K.A., MacCregor, G.R., Thompson, C.B. and Korsmeyer, S.J. (2001) Proapoptotic BAX and BAK: A requisite gateway to mitochondrial dysfunction and death. *Science*, **292**, 727-730.

Weikl, T., Muschler, P., Richter, K., Veit, T., Reinstein, J. and Buchner, J. (2000) C-terminal regions of Hsp90 are important for trapping the nucleotide during the ATPase cycle. *J. Mol. Biol.*, **303**, 583-592.

Weingärtner, H. (1984) Diffusion in Liquid-Mixtures of Light and Heavy-Water. *Ber. Bunsenges. Phys. Chem.*, **88**, 47-50.

Weinreb, P.H., Zhen, W., Poon, A.W., Conway, K.A. and Lansbury, P.T. (1996) NACP, a protein implicated in Alzheimer´s disease and learning, is natively unfolded. *Biochemistry*, **35**, 13709-13715.

Whitesell, L., Mimnaugh, E.G., Decosta, B., Myers, C.E. and Neckers, L.M. (1994) Inhibition of Heat-Shock Protein Hsp90-Pp60(V-Src) Heteroprotein Complex-Formation By Benzoquinone Ansamycins - Essential Role For Stress Proteins in Oncogenic Transformation. *Proc. Natl. Acad. Sci. U. S. A.*, **91**, 8324-8328.

Wider, G., Dotsch, V. and Wüthrich, K. (1994) Self-Compensating Pulsed Magnetic-Field Gradients for Short Recovery Times. *J. Magn. Reson. Ser. A*, **108**, 255-258.

Williamson, M.P. (1994) The structure and function of proline-rich regions in proteins. *Biochem. J.*, **297 (Pt 2)**, 249-260.

Wishart, D.S., Bigam, C.G., Holm, A., Hodges, R.S. and Sykes, B.D. (1995a) H-1, C-13 and N-15 Random Coil Nmr Chemical-Shifts of the Common Amino-Acids .1. Investigations of Nearest-Neighbor Effects. *J. Biomol. NMR*, **5**, 67-81.

Wishart, D.S., Bigam, C.G., Holm, A., Hodges, R.S. and Sykes, B.D. (1995b) H-1, C-13 and N-15 Random Coil NMR Chemical-Shifts of the Common Amino-Acids. I. Investigations of Nearest-Neighbor Effects. *J. Biomol. NMR*, **5**, 332-332.

Wishart, D.S., Sykes, B.D. and Richards, F.M. (1992) The Chemical-Shift Index - a Fast and Simple Method For the Assignment of Protein Secondary Structure Through Nmr- Spectroscopy. *Biochemistry*, **31**, 1647-1651.

Woessner, D.E. (1961) Effects of Diffusion in Nuclear Magnetic Resonance Spin-Echo Experiments. *J. Chem. Phys.*, **34**, 2057-2057.

Woessner, D.E. (1996) Brownian Motion and Correlation Times. In Grant, D.M. and Harris, R.K. (eds.), *Encyclopedia of Nuclear Magnetic Resonance*. Wiley, New York, pp. 4018-4028.

Wolter, K.G., Hsu, Y.T., Smith, C.L., Nechushtan, A., Xi, X.G. and Youle, R.J. (1997) Movement of Bax from the cytosol to mitochondria during apoptosis. *J. Cell Biol.*, **139**, 1281-1292.

Wong, K.B., DeDecker, B.S., Freund, S.M., Proctor, M.R., Bycroft, M. and Fersht, A.R. (1999a) Hot-spot mutants of p53 core domain evince characteristic local structural changes. *Proc Natl Acad Sci U S A*, **96**, 8438-8442.

Wong, K.B., DeDecker, B.S., Freund, S.M., Proctor, M.R., Bycroft, M. and Fersht, A.R. (1999b) Hot-spot mutants of p53 core domain evince characteristic local structural changes. *Proc. Natl. Acad. Sci. U. S. A.*, **96**, 8438-8442.

Wright, P.E. and Dyson, H.J. (1999) Intrinsically unstructured proteins: re-assessing the protein structure-function paradigm. *J. Mol. Biol.*, **293**, 321-331.

Wu, D.H., Chen, A.D. and Johnson, C.S. (1996) Three-dimensional diffusion-ordered NMR spectroscopy: The homonuclear COSY-DOSY experiment. *J. Magn. Reson. Ser. A*, **121**, 88-91.

Wüthrich, K. (1986) NMR of Proteins and Nucleic Acids. In. Wiley & Sons Inc., New York.

Wüthrich, K. (2003) NMR studies of structure and function of biological macromolecules (Nobel lecture). *Angew. Chem. Int. Ed.*, **42**, 3340-3363.

Wüthrich, K., Billeter, M., Guntert, P., Luginbuhl, P., Riek, R. and Wider, G. (1996) NMR studies of the hydration of biological macromolecules. *Faraday Discuss.*, 245-253.

Wyllie, A.H. (1980) Glucocorticoid-Induced Thymocyte Apoptosis Is Associated with Endogenous Endonuclease Activation. *Nature*, **284**, 555-556.

Xia, Y. (1996) Contrast in NMR Imaging and Microscopy. *Concepts Magn. Resonance*, **8**, 205-225.

Xu, Z.H., Horwich, A.L. and Sigler, P.B. (1997) The crystal structure of the asymmetric GroEL-GroES-(ADP)(7) chaperonin complex. *Nature*, **388**, 741-750.

Yahara, I. (1998) Molecular Chaperones in the Life Cycle of Proteins. In Fink, A.L. and Goto, Y. (eds.), *Molecular Chaperones in the Life Cycle of Proteins*. Dekker, New York, pp. 183-192.

Yang, A., Kaghad, M., Caput, D. and McKeon, F. (2002) On the shoulders of giants: p63, p73 and the rise of p53. *Trends Genet.*, **18**, 90-95.

Yang, A.N., Kaghad, M., Wang, Y.M., Gillett, E., Fleming, M.D., Dotsch, V., Andrews, N.C., Caput, D. and McKeon, F. (1998) p63, a p53 homolog at 3q27-29, encodes multiple products with transactivating, death-inducing, and dominant-negative activities. *Mol. Cell.*, **2**, 305-316.

Young, J.C., Moarefi, I. and Hartl, F.U. (2001) Hsp90: a specialized but essential protein-folding tool. *J. Cell Biol.*, **154**, 267-273.

Zhang, Y.P. and Xiong, Y. (2001) A p53 amino-terminal nuclear export signal inhibited by DNA damage-induced phosphorylation. *Science*, **292**, 1910-1915.

Zhao, K.H., Chai, X.M., Johnston, K., Clements, A. and Marmorstein, R. (2001) Crystal structure of the mouse p53 core DNA-binding domain at 2.7 angstrom resolution. *J. Biol. Chem.*, **276**, 12120-12127.

Zhou, B.P., Liaq, Y., Xia, W.Y., Zou, Y.Y., Spohn, B. and Hung, M.C. (2002) HER-2/neu induces p53 ubiquitination via Akt-mediated MDM2 phosphorylation. *Nat. Cell Biol.*, **4**, 736.

Zhou, X.M., Liu, Y., Payne, G., Lutz, R.J. and Chittenden, T. (2000) Growth factors inactivate the cell death promoter BAD by phosphorylation of its BH3 domain on Ser155. *J. Biol. Chem.*, **275**, 25046-25051.

Zhu, X., Zhao, X., Burkholder, W.F., Gragerov, A., Ogata, C.M., Gottesman, M.E. and Hendrickson, W.A. (1996) Structural analysis of substrate binding by the molecular chaperone DnaK. *Science*, **272**, 1606-1614.

Zimmerman, J.R. and Brittin, W.E. (1957) Nuclear Magnetic Resonance Studies in Multiple Phase System - Lifetime of a Water Molecule in an Adsorbing Phase on Silica Gel. *J. Phys. Chem.*, **61**, 1328-1333.